NUMERICAL METHODS IN ENGINEERING SERIES

Milling Simulation

Metal Milling Mechanics, Dynamics and Clamping Principles

Weihong Zhang and Min Wan

iSTE WILEY

Series Editor
Piotr Breitkopf

Milling Simulation

Metal Milling Mechanics, Dynamics and Clamping Principles

Weihong Zhang
Min Wan

ISTE
WILEY

First published 2016 in Great Britain and the United States by ISTE Ltd and John Wiley & Sons, Inc.

ISTE Ltd
27-37 St George's Road
London SW19 4EU
UK

www.iste.co.uk

John Wiley & Sons, Inc.
111 River Street
Hoboken, NJ 07030
USA

www.wiley.com

Library of Congress Control Number: 2016936179

British Library Cataloguing-in-Publication Data
A CIP record for this book is available from the British Library
ISBN 978-1-78630-015-7

Contents

Preface

Milling is a material removal process used widely for machining metal components made of steel, aluminum alloy and titanium alloy in manufacturing industries. This book focuses on the fundamentals of the metal milling process, based on the research results of the authors and their graduate students. The book contains five parts:

– The introduction reviews mainly the state of the art of research relevant to milling processes, and the main structure and contents of this book are introduced.

– Chapter 1 introduces cutting force modeling methods. Algorithms and procedures for calibrations of cutting force coefficients and cutter runout are described in detail.

– Chapter 2 is focussed on explaining the surface quality of milling processes. Calculation methods for surface errors in milling of thin-walled workpieces and milling surface topography are described.

– Chapter 3 investigates the regenerative chatter in milling processes. An analytical method for calculating the tool point frequency response function is introduced first, and then numerical methods for obtaining stability lobe diagrams are derived in detail.

– Chapter 4 discusses the basic principles in workpiece-fixture system. Analyses of locating scheme correctness, clamping sequences, clamping stability, etc. are mathematically formulated.

This book is not indented to capture all the significant contributions that have been previously reported in the literature of machining science. For the purpose of revealing the mechanisms of milling processes, a key aspect of this book is the inclusion of detailed mathematical models to predict cutting forces, surface errors, chatter stability dynamics and clamping principles. The theoretical parts are derived from experimental observations and are further validated by experiments.

The book can be used as a guideline for graduate students and research engineers who wish to learn the basic theory and principles of milling processes and machine dynamics.

Weihong ZHANG, Min WAN
March 2016

Introduction

Milling is a widely used method to remove materials from the initial configuration of a workpiece for machining monolithic parts in aeronautic, aerospace and automobile manufacturing industries. Due to the characteristics of large size and weak rigidity, cutting deformations and chatter vibrations will be easily induced during the cutting process. As a result, machining accuracy and surface quality of workpieces are not easily achieved and useless products will be produced in the worst case. Traditionally, the usual approach to remedying the machining precision was to validate the NC program by expensive trial and error cutting. Recently, an alternative approach is to numerically simulate the milling process *a priori*. It is desired that a quasi net-shaping will be obtained practically with optimal cutting parameters in perhaps one pass without grinding and polishing. To this end, research on the mechanics and dynamics of milling process is of great significance in developing strategies to guarantee accuracy. Issues such as cutting force modeling, surface quality prediction, chatter stability analysis and clamping scheme design are the key to this aspect.

I.1. Cutting force modeling

Cutting force modeling is the basis of all simulation schemes. In early research [MER 44], the concept of specific cutting energy was employed in cutting force modeling where cutting forces were assumed to be entirely related to shearing and friction effects. Under this assumption, the lumped force model was proposed as a classical one [KOE 61]. It approximates the entire cutting process as an equivalent shearing mechanism. This means that

the cutting forces are supposed to be proportional to the chip load and the proportion scale is named the cutting force coefficient.

Since then, research efforts have been focused on how to effectively determine the cutting force coefficients in the lumped force model. For instance, Kline *et al*. [KLI 82a] and Larue and Anselmetti [LAR 03] treat the coefficients as constants. The former calibrated them by means of measured average cutting forces, whereas measured cutter deflections were used by the latter. Endres *et al.* [END 90] used empirical relations that mapped three independent variables of interest, i.e. instantaneous uncut chip thickness, cutting speed and rake angle, to represent the cutting force coefficients. Altintas and Spence [ALT 91] assumed that the coefficients are a power function of the average chip thickness, determined based on a strict integral technique. Instantaneous models such as the Weilbull function proposed by Ko *et al*. [KO 02] were also used to characterize instantaneous influences of process geometry parameters upon the cutting force coefficients for the lumped cutting force model.

It was, however, recognized by Thomsen [THO 66] that the cutting forces do not converge to zero when the chip thickness approaches zero. This phenomenon is the so-called rubbing effect associated with the clearance face of the flank edge and responsible for cutting process damping [END 95]. Masuko [MAS 56] and Albrecht [ALB 60, ALB 61] proposed the dual-mechanism model to separate the chip removal and flank rubbing mechanisms for the machining process of constant chip thickness. With regard to the milling process of periodically changing chip thickness, Altintas [ALT 12] modeled the chip removal and the flank rubbing effects separately as functions of chip load and chip width, respectively. Meanwhile, Budak *et al.* [BUD 96] calibrated the cutting force coefficients using orthogonal cutting tests with oblique cutting analysis and transformation. Gonzalo *et al*. [GON 10] identified the constant coefficients by means of measured instantaneous cutting force data. Wang and Zheng [WAN 03] used the convolution integration method to identify the cutting force coefficients. However, it is interesting to remark that the methods proposed above were developed for each cutter type individually, e.g. the flat end mill and the ball end mill. To have a unified cutting force model of general end mills, Engin and Altintas [ENG 01] developed a generalized mechanics and dynamics model where cutting force coefficients are predicted from an orthogonal database. Alternatively, Gradisek *et al*. [GRA 04] calibrated the cutting force

coefficients for a general end mill based on the average cutting forces measured.

With respect to the cutting force prediction, however, most work was based on the assumption that machine set-up errors such as cutter tilt and cutter offset runout were ignored. In contrast, a rigid mechanistic cutting force model including the cutter radial runout was proposed by Kline and DeVor [KLI 83]. This model was later extended by Sutherland and DeVor [SUT 86] and a regeneration model was developed to predict the cutting forces in flat end milling, accounting for the cutter flexibility and the cutter runout. In this context, we suppose that the cutter runout parameters are known *a priori*. Wang and Liang [WAN 96] developed an analytical model for the calculation of instantaneous uncut chip thickness and cutting forces.

In fact, the problem also arises of how to figure out the runout parameters and the cutting force coefficients simultaneously based upon the measured cutting forces. For cylindrical end milling, a numerical scheme was proposed by Armarego and Despande [ARM 89], who estimated the runout parameters through a best-fit procedure. Liang, Zheng and Wang *et al.* [LIA 94, ZHE 97, WAN 03] analyzed the influence of the cutter runout on the cutting forces using the convolution integration method. Cutting force coefficients and cutter runout parameters were identified by means of the Fourier series. An alternative approach was suggested by Cho *et al.* [YUN 00, YUN 01] who calibrated the cutting force coefficients and the cutter runout for cylindrical end mills based on the instantaneous cutting forces rather than the average ones. Attention was also received in ball end milling. Feng and Menq [FEN 94a, FEN 94b] calibrated the cutting force coefficients and the runout using the mechanistic approach for the modelling of complicated ball end milling process. Ko and Cho [KO 05] calibrated the instantaneous cutting force coefficients and the runout parameters for ball end milling with the synchronization procedure.

I.2. Surface quality simulation

In a milling process without chatter, the static surface form error caused mainly by elastic deflections of the cutter and of the workpiece is often the dominant defect when milling a thin-walled workpiece made up of titanium or aluminum alloys at a low spindle speed [BUD 95, TSA 99]. The surface

form error is mainly made up of the force-induced deflection, which results in a deviation of the depth of cut. Many research attempts have been focused on this problem. Kline [KLI 82b], Larue [LAR 03], Budak [BUD 94], Shirase [SHI 96], Ryu [RYU 03] and Paksiri [PAK 04] used the cutter deflection to predict the surface form errors; whereas Ratchev *et al.* [RAT 04a, RAT 04b, RAT 06] used the workpiece deflections to calculate surface form error of a flexible workpiece. For example, Kline *et al.* [KLI 82b] studied the prediction of surface form errors in the peripheral milling of a clamped-clamped-clamped-free rectanglular plate. The cutter is modeled as a continuous cantilevered beam and the plate is discretized by the FEM. In the meantime, cutting forces are assumed to be concentrated forces in the calculation of the cutter and workpiece deflections. Budak and Altintas [BUD 94] and Shirase *et al.* [SHI 96] studied the surface form errors uniquely caused by the deflection of the cutter that is modeled as an assemblage of discrete elements with equal length. Thus, cutting forces are discretized onto the element nodes to calculate the deflection of the cutter. This approximation is valid when the workpiece has relatively a large rigidity. Zhang *et al.* [ZHA 01a] determined the surface form errors by evaluating the deflections of both the cutter and the workpiece without considering the coupling effect between cutter and workpiece. To consider this coupling effect in a flexible milling process, many researchers used iteration schemes to predict the cutting forces and the surface form errors [BUD 95, TSA 99]. Budak and Altintas [BUD 95] and Tsai and Liao [TSA 99] developed iteration schemes to retain the coupling effect of deflections between the cutter and workpiece, as well as the rigidity diminution of the workpiece due to material removal. Meanwhile, the workpiece is meshed by one layer of 8-node and 12-node isoparametric volume elements along the thickness direction, respectively. Nevertheless, the generated mesh of the workpiece has to coincide, element to element, with that of the cutter. In addition, the stiffness reduction of the workpiece due to material removal can be simulated by changing nodal coordinates of such a one-layer element. This requirement becomes a major limitation in the modeling step, especially in the modeling process of complex workpieces. In the above work, it can be generally said that the surface form errors were predicted either by means of an analytical/finite element method [LAR 03, BUD 95, RYU 03] or by means of neural networks [PAK 04].

Based on the obtained values of surface form errors, compensation techniques have been widely used to reduce the resulting errors without sacrificing the machining productivity. Depince [DEP 06], Rao [RAO 06], Landon [LAN 03] and Law [LAW 99, LAW 03] studied the cutting-force-induced tool deflection compensation in peripheral milling by the mirror method. Based on the closed loop volumetric error relations, Bohez [BOH 02] proposed a general method to compensate the systematic errors. Cho *et al*. [CHO 03] proposed an integrated error compensation method by the online error measuring method. Paksiri [PAK 04] proposed an error compensation model in a 3-axis CNC milling machine using a back-propagation neural network. Ratchev *et al*. [RAT 06] investigated a multi-level error compensation method for milling low-rigidity parts. With all of these methods, the surface quality can be greatly improved but cannot be ensured in all machining conditions [DEP 06]. Although the errors can be reduced to some degree, the surface form errors may still violate the required tolerance after compensation. Ryu and Chu [RYU 05] proposed a surface form error reduction method through successive down and up milling. Some researchers [BUD 95, ERD 06, YAZ 94] were limited to the feed rate scheduling with the sacrifice of productivity.

With respect to the surface topography, finding the machined surface topography and the geometric shape and texture of the machined surface is essential, because the latter directly affects the surface quality, especially the surface roughness. For a ball end milling process, the surface topography also affects the cutting force and chip load calculations. Simulations of machined surface topography also constitute an active research topic in the manufacturing community. Relevant published research works can be summarized as follows; Kline *et al*. [KLI 82b] discussed the effects of cutter runout on the shape of the tooth marks in end milling process. Jung *et al*. [JUN 05a, JUN 05b] developed the so-called ridge method to predict the characteristic lines of the cut remainder for a disk tool in the ball end milling process, and three types of ridges are defined to this end. Imani *et al*. [IMA 98], Imani and Elbestawi [IMA 01] and Sadeghi *et al*. [SAD 03] used solid modeling techniques and Boolean operations to deal with the geometric simulation of the ball end milling operations. In summary, many researchers employed discretization and interpolation techniques to simulate the machined surface topography. Elbestawi *et al*. [ELB 94] and Ismail *et al*. [ISM 93] studied the trochoid path for surface generation of end milling. The

tool path is discretized into segments to simulate the surface topography. Based on the concepts of parallel reference section levels and elementary linear sections, Bouzakis *et al*. [BOU 03] modeled the workpiece and cutting edge to simulate the topography in the ball end milling process. Furthermore, Ehmann and Hong [EHM 94], Xu *et al.* [XU 01] simulated the topography of the end milling by meshing cutter and workpiece into small elements. Lazoglu [LAZ 03] applied a similar method to the ball end milling process. Li *et al*. [LI 02] formulated the trajectory equations of the cutting edge relative to the workpiece and simulated the surface topography in the end milling process. Antoniadis *et al*. [ANT 03] determined the machined surface roughness for ball end milling, based on shape-function interpolation over a number of finite linear segments of the workpiece. In fact, all of the above methods depend on how the workpiece, cutting edge, and tool path are discretized, and the coherence between these discretizations.

The second class of methods refers to the so-called Z-map modeling method. To use it, the cutting edge is represented by its parametric equation and the tool-cutting rotation motion is discretized. In this manner, the final surface topography is determined by comparing the point on the cutting edge with the node on the workpiece surface in the height direction. For example, Soshi *et al*. [SOS 04] applied such a method to predict surface topography in five-axis ball end milling without considering the cutter runout and wear. In contrast, only the runout effect was considered in the work of Zhao *et al*. [ZHA 03b]. More importantly, both runout and wear were taken into account by Liu *et al*. [LIU 06] and Sriyotha *et al*. [SRI 06]. The topography was studied experimentally by Toh [TOH 04] in high-speed milling of inclined hardened steel surfaces.

I.3. Chatter stability analysis

Chatter is a form of self-excited vibration due to the dynamic interaction between the cutter and the workpiece. The occurrence of chatter vibration leads to poor surface finish and in the worst case may damage the machine spindle or the cutter. In practice, to achieve high material removal rate and high machining quality, the milling process must be conducted in stable state. Thus, the problem arises of how to evaluate whether the selected cutting parameters will lead to stable milling or not. The challenge is to develop a

suitable dynamic model that can reflect the chatter mechanism in milling. Many research efforts have been focused on this issue.

Altintas [ALT 12, ALT 92, ALT 95, ALT 99b, MER 04, ALT 08] is one of the pioneers who studied the dynamic behavior of the milling process. Research results in [ALT 12, ALT 92, ALT 95, ALT 99b, MER 04, ALT 08] pointed out that when the cutting forces create a relative displacement between the cutter and the workpiece at the cutting point, the chip thickness experiences waves on the inner and outer surfaces due to present and past vibrations. The gain and the phase shift between the inner and outer waves may lead to exponential growing chips and hence very large forces until the cutter jumps out of the cut. The above phenomenon is the well known chip-regenerative chatter. From this basic physical understanding, it can be found that there exist delayed position variables which could be used to couple the cutting forces to the cutter motion. The mathematical models developed to explain these phenomena correspond to delay differential equations (DDEs). Based on this important discovery, extensive efforts have been carried out to model the dynamic milling process and to develop stability lobe diagrams that can distinguish chatter-free operations from unstable operations.

In early decades, Koenigsberger and Tlusty [KOE 67] used an orthogonal cutting model to analyze the milling stability. Later, Altintas and co-workers [ALT 12, ALT 92, ALT 95, ALT 99b, MER 04, ALT 08] developed a stability method which leads to the analytical determination of stability lobes directly in the frequency domain. This method, known as zero-order approximation, can achieve reasonably accurate predictions for processes where the cutting forces vary relatively little, e.g. the case of large radial immersions. However, if the process is highly intermittent, e.g. the case of small radial immersion, a zero-order approximation will lead to unacceptable results. To improve the prediction accuracy in this case, a higher order solution was suggested to predict the stability by Budak and Altintas [BUD 98a, BUD 98b]. Alternatively, Tlusty and Ismail [TLU 81] pointed out that the time domain simulation would be a good choice for accurate stability predictions in milling. The closed-form for expressing the dynamics of milling systems in the time domain was formulated by Sridhar *et al*. [SRI 68], but its analytical solution was firstly accomplished by Minis *et al*. [MIN 90], who used the famous Floquet theory [KOL 86, LAK 88]. Zhao and Balachandran [ZHA 01b] numerically determined the stability boundary using the time

domain simulations. Later, Mann *et al*. [BAY 03, MAN 04] proposed a temporal finite element analysis for solving the delayed equations written in the form of a state space model, whereas Insperger and Stepan [INS 04] employed the semi-discretization scheme to solve the stability in the discrete time domain. Other research efforts mainly extended the application of the above principal solutions in the frequency and time domain. For example, Merdol and Altintas [MER 08] planned the milling process by using the stability results in the frequency domain. Patel *et al*. [PAT 08] implemented the temporal finite element method to detect the island phenomena in milling. Note that these islands were first found by Zatarain *et al*. [ZAT 06]. Tois [TOT 09] developed a probabilistic algorithm for a robust analysis of stability in milling based on the basic principles of the semi-discretization scheme. Campomanes and Altintas [CAM 03] proposed an improved time domain simulation method for analyzing the stability at small radial immersions. Gradisek *et al*. [GRA 05] investigated the stability boundaries for variable radial immersions by both the zero-order method and the semi-discretization method.

It is worth noting that the above works were conducted under the assumption that there is only one delay term. The delay is often assumed to be constant and has the value of the tooth passing period. This is true for ideal milling operations with a constant pitch cutter. However, in practice, the time delay is basically determined by the rotation of the cutter, but it is also affected by the current and the delayed position of the cutting edge. That is, the time delay may be state-dependent. Insperger *et al*. [INS 07, INS 08a] analyzed such state-dependent delays for the turning process. As with milling, due to the effect of cutter runout or unpitched space angles, the appearance of state-dependent delays directly leads to the existence of multiple delayed terms:

– the occurrence of cutter runout will lead to the explicit phenomenon that the current cutting point on the inner surface wave may be to remove the outer surface wave generated by its l-th previous tooth. Here, l may be more than one. As a result, many delays may occur;

– the adoption of a variable pitch cutter will also lead to variable delays. If cutter runout does not occur, any cutting point is always to remove the surface left by its first previous tooth. In this case, the delay term corresponding to the cutting points on the same tooth is identical. However, due to the unevenly pitched space angles, the delay corresponding to different teeth will

be different. If cutter runout occurs, the delay will be influenced by both the cutter runout and the space angle. In summary, there might also exist more than one delay in this case.

Insperger *et al*. [INS 08b] systematically studied the frequency characteristic for an evenly pitched milling cutter with runout in the time domain. Their results showed that cutter runout will shift the frequency content of the cutting force signal away from the tooth passing frequency and towards the spindle rotation frequency. The principal period of runout-milling process is equal to the spindle rotation period. Although this understanding was achieved, their research was still carried out under the assumption that the delay can be approximated as the tooth passing period. This hypothesis will have a good prediction accuracy when the runout is relatively small. If the cutter runout is large, some accuracy may be lost in the actual process. Altintas and Budak *et al.* [ALT 99a, BUD 03a, BUD 03b] studied the stability of the variable pitch milling cutter in the frequency domain. Their works showed that the pitch angles have a great effect on the stability boundary. Sims *et al*. [SIM 08] proposed a time-averaged semi-discretization method to study the chatter stability for variable pitch and variable helix milling cutters. However, the above methods [ALT 99a, BUD 03a, BUD 03b, SIM 08] were not suitable for the case when cutter runout occurs.

I.4. Clamping system design

Fixtures are generally mechanical devices used to assist machining, assembly, inspection, welding and other manufacturing operations. The functions of such devices aim to locate and ensure the desired positions and orientations of workpieces during the manufacturing process. By definition, the machining dimensions of a workpiece are those parameters that describe the machining features and have to be ensured during the machining operation. For this reason, it is desired to determine the constrained DOFs (hereafter called theoretical constrained DOFs) that will be used to design the corresponding locating scheme, i.e. to design both the locator number and positions. Actually, fixture locating scheme design has been receiving much attention and the experienced locating scheme, e.g. 3-2-1 locating rule, was taken into account [HOF 91, RON 99, RON 05, NEE 05, NEE 95].

Fixture design is an important issue before the locating scheme can be designed. After plenty of studies and practices, many experts and skilled

workers have accumulated much experience in fixture design, and have established some empirical principles [HOF 91]. A drawing of fixture design is often prepared based on the operation plan and the workpiece information. Since the 1980s, Computer Aided Fixture Design (CAFD) techniques have been extensively developed. As a result, the period of fixture design is shortened and some burdensome tasks such as consulting handbooks of jig and fixture design, drawing all assembly views and compiling technical documentation become greatly simplified [LI 01]. In addition, the quality and efficiency of fixture design are improved to a certain extent. However, the fixture specification for the machining is strongly dependent upon the designer's experience and knowledge so that an optimum solution of fixture design is generally difficult to obtain [RON 02]. Many existing works were mainly restricted to the layout design of contact points. The design of locators' dimensions and locations are not simultaneously involved in the model. Although Guo *et al*. [GUO 01] presented the basic concepts of the robustness of the fixture positioning scheme to study the influence of locator dimensions, rule function and restraint conditions, the relationship between the localization error and its causes was still underdeveloped and thus needs to be investigated.

Once a workpiece is completely located and restrained by the locators and clamps of the machining fixture, the workpiece will be machined or processed to generate required geometric features according to the process plan. However, the inherent geometrical and mechanical nature of a workpiece-fixture system, e.g. the geometric defaults of locator dimensions, the inconsistent datum error (IDE) of a workpiece, the compliance, will all affect the final workpiece position. Experimental results showed that such source errors are the major fixturing errors influencing the workpiece accuracy and can amount to 20–60 percent of the total machining error in an extreme case [WU 97]. Therefore, performance evaluations of the workpiece-fixture system constitute a significant task for fixture design optimization and control of machining error. Fixture design performance may principally include locating correctness for constraining DOFs of a workpiece in specific directions, workpiece stability for guaranteeing the workpiece in static equilibrium condition and machining error analysis for ensuring tolerance requirements of a product design.

During a machining process, since a workpiece is subject to cutting forces and torques, a fixture must be used to restrain the workpiece in the correct

location so that the manufacturing process can be carried out according to design specifications. A fixture basically consists of clamps and locators. The function of locators is to provide a workpiece with the desired location. However, due to the effect of gravity and the machining forces exerted on the workpiece, locators alone are usually insufficient to constrain the workpiece. Clamps are thus utilized to provide extra constraints to counteract an eventual movement of the workpiece. Therefore, fixturing the workpiece in an equilibrium state has a significant impact on the machining quality and production safety. This is the implication of the stability. In fact, stability analysis is one of the essential tasks in the fixture design that started inevitably from "closure analysis" including form-closure and force-closure. It is therefore noted that form-closure can be viewed as a particular force-closure with frictionless contacts only [WU 97]. Practically, it is more significant to investigate the force-closure.

Due to the presence of friction at the contact points between the workpiece and fixture, the clamping sequence greatly influences the final distribution of contact forces in the workpiece-fixture system when multiple clamps are applied sequentially. Thus, the clamping sequence has to be appropriately planned at the machining fixture design stage. Traditionally, the mounting process of a fixture is to immobilize the workpiece with negligent effects of contact forces on displacements and rotations of the workpiece. Recently, a deluge of studies has been carried out for the contact force synthesis, and two basic modeling approaches were proposed: a kinematic model and FEM model. However, little research has been carried out concerning basic theories, mathematical modeling and computing methods of the clamping sequence.

I.5. Purpose of this book

The main contents of this book include the following:

1) a series of new methods for calibrating the cutting force coefficients and cutter runout parameters are described in detail [WAN 06a, YAN 13, WAN 07a, WAN 07b, WAN 09a, DAN 10, WAN 09b, WAN 14, YAN 11]. Typical characteristics of these kinds of methods lie in that they can be applied within a great range of cutting conditions although calibrations are carried out with a few cutting tests under a specific regime;

2) methods for the prediction and control of surface quality are described [WAN 05, WAN 06b, WAN 08, GAO 06, ZHA 08]. For example, numerical algorithms for predicting surface form errors in peripheral milling of thin-walled workpieces using irregular finite element method are proposed, and bi-parameter algorithms are proposed to control surface form errors. Approaches for calculating the surface topography of both three-axis and multi-axis ball end milling processes are also developed without the requirement of discretizing the cutting edge and meshing the workpiece;

3) to have a unified model, new methods [WAN 10b, WAN 11, WAN 15] are presented to determine the stability lobe for the milling process with multiple delays in the time domain by improving the semi-discretization method [INS 04, INS 02]. The advantage of the proposed method lies in the fact that the algorithms performed in instantaneous consideration of every possible delay can be applied to a great range of actual milling processes. It can be used to study the stability of the milling process both with and without runout. It is also suitable for the milling cutter with either constant or nonconstant pitch angle. Emphasis is also placed on how to effectively incorporate the instantaneous cutting force model into the prediction procedure of stability lobes, by numerically predicting the vibration time history of the cutter motion;

4) a series of analyses are conducted to solve the clamping principles of the workpiece-fixture system [QIN 07b, QIN 06a, QIN 08, QIN 06b, QIN 07a]. The main efforts are focused on key issues, such as the design of the locator number and positions satisfying the machining dimensions of the workpiece, workpiece position error in fixture locating schemes, the relationship between the workpiece position error and its source errors, machining error in terms of both geometric default and compliance of the workpiece-fixture system, workpiece stability, and design optimization of the clamping sequence.

1

Cutting Forces in Milling Processes

1.1. Formulations of cutting forces

Milling is a cutting operation which is generally used to remove materials from the blank for the purpose of achieving parts with the desired shape and surface quality. Cutting mechanics of the milling process includes the shearing effect between the cutting edge and the workpiece, the friction effect between the rake face and chip, as well as the ploughing effect between the clearance surface and the machined surface. The combined influence of the three effects lead to the generation of cutting forces, which can result in cutting deflections and can further damage the surface quality of the machined parts. Study of the mechanics of the milling process is of great significance to control surface errors and to plan stable cutting strategy. Milling is a typical multipoint tool operation, whose cutting mechanism involves elastic-plastic mechanics and thermal dynamics. Specific analyses for a detailed understanding of the behavior of temperature and strain rate fields are not covered in this text. In this chapter, we will discuss the generation mechanism of cutting forces, and then detail a series of methods for calibrating the cutting force coefficients which enable us to accurately predict cutting forces.

1.1.1. *Mechanics of orthogonal cutting*

Orthogonal cutting is usually used to explain the mechanism of material removal, and the three-dimensional oblique cutting process can be evaluated by geometrical and kinematic transformation models, as reported by Altintas [ALT 12]. Without the loss of generality, the orthogonal cutting process is

Milling Simulation: *Metal Milling Mechanics, Dynamics and Clamping Principles*,
First Edition. Weihong Zhang and Min Wan.

adopted to formulate the cutting forces. Figure 1.1 shows the relationship of cutting forces in the cross-sectional view of an orthogonal cutting process. The cutting edge is assumed to be a sharp one so that the shearing effect occurs at a plane without thickness. Two cutting force components exist between the chip and tool (i.e. the normal F_{n} and the friction F_{f} components). They are in balance with the normal and shearing force components related to the shear plane, i.e. F_{nshear} and F_{shear}, as shown in Figure 1.1(a).

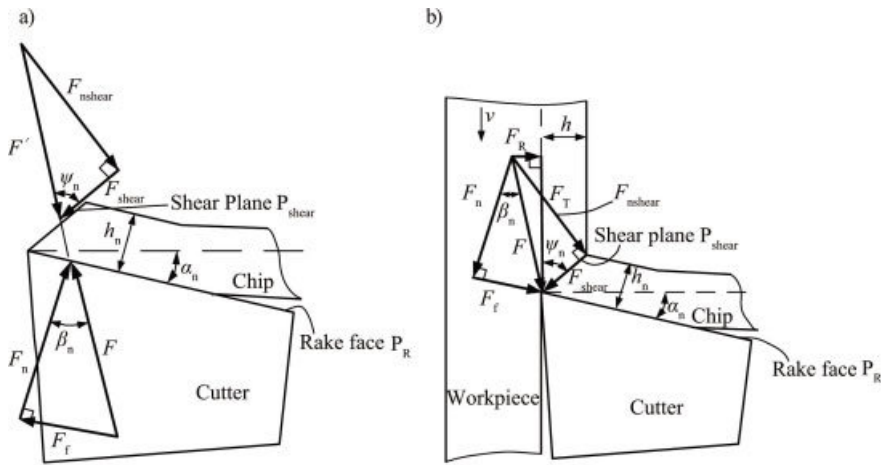

Figure 1.1. *Cutting forces in the orthogonal cutting process*

Shearing force F_{shear} can be expressed as

$$F_{\mathrm{shear}} = \tau_{\mathrm{s}} bh / \sin\psi_{\mathrm{n}} \qquad [1.1]$$

where h is the instantaneous uncut chip thickness and b is the chip width. τ_{s} is the yield shearing stress of the workpiece material. ψ_{n} is the shearing angle defined as the angle between the shear plane and the cutting speed.

From Figure 1.1, it can be observed that

$$F_{\mathrm{shear}} = F\cos(\psi_{\mathrm{n}} + \beta_{\mathrm{n}} - \alpha_{\mathrm{n}}) \qquad [1.2]$$

where F is the resultant cutting force and β_n is the friction angle, measured as the angle between F and F_n, α_n is the normal rake angle of the cutter.

Combination of equation [1.1] and equation [1.2] gives rise to

$$F = \frac{\tau_s bh}{\sin\psi_n \cos(\psi_n + \beta_n - \alpha_n)} \quad [1.3]$$

At the same time, F can be also split into tangential force F_T parallel to the cutting speed direction, and component F_R normal to the cutting speed direction.

$$\begin{aligned} F_T &= F\cos(\beta_n - \alpha_n) \\ F_R &= F\sin(\beta_n - \alpha_n) \end{aligned} \quad [1.4]$$

The substitution of equation [1.3] into equation [1.4] produces

$$\begin{aligned} F_T &= K_T bh \\ F_R &= K_R bh \end{aligned} \quad [1.5]$$

with

$$\begin{aligned} K_T &= \frac{\tau_s \cos(\beta_n - \alpha_n)}{\sin\psi_n \cos(\psi_n + \beta_n - \alpha_n)} \\ K_R &= \frac{\tau_s \sin(\beta_n - \alpha_n)}{\sin\psi_n \cos(\psi_n + \beta_n - \alpha_n)} \end{aligned} \quad [1.6]$$

Equation [1.5] means that the cutting forces can be evaluated by multiplying bh, the cross area of the chip, by the cutting force coefficients K_T or K_R expressed by equation [1.6], derived from the shearing mechanism. In the actual cutting experience, the total cutting forces are contributed by the shearing effect related to the primary and secondary deformation zones, and the "ploughing" or "rubbing" effect at the flank of the cutting edge, which is associated with the tertiary deformation zone. Due to this fact, there are two widely used cutting force models depending upon whether the rubbing effect is included or not. The first one is the so-called lumped mechanism model

that shares the same mathematical equation as equation [1.5]. As its name suggests, the shearing on the rake face and the rubbing at the cutting edge are merged as a single coefficient. The second model is the dual mechanism model, which calculates the cutting forces as a superposition of shearing and edge forces with

$$\begin{aligned} F_{\mathrm{T}} &= K_{\mathrm{Tc}} bh + K_{\mathrm{Te}} b \\ F_{\mathrm{R}} &= K_{\mathrm{Rc}} bh + K_{\mathrm{Re}} b \end{aligned} \qquad [1.7]$$

where K_{Tc} or K_{Rc} represents the cutting coefficient due to shearing effect, while K_{Te} or K_{Re} stands for the edge coefficient that does not contribute to the shearing. The first term of the right-hand side of equation [1.7] is obtained by applying the same mechanism of orthogonal cutting mechanics as explained in equation [1.5].

It is noted that equation [1.6] is derived from the orthogonal cutting operation. In the oblique cutting process, cutting force coefficients are calculated by the orthogonal-to-oblique method. Readers are referred to the well-known formulas developed in [ALT 12] for the details of the orthogonal-to-oblique method.

If the materials property parameter τ_{s}, cutter geometrical parameter α_{n}, process geometrical parameters ψ_{n} and β_{n}, and the cutting condition parameters b and h are known in advance, the values of cutting force coefficients K_{T} and K_{R} (or K_{Tc} and K_{Rc}) can be calculated by using the analytical equation [1.6]. Alternatively, K_{T} and K_{R} (or K_{Tc} and K_{Rc}, and K_{Te} and K_{Re}) can also be mechanistically identified based on the measured cutting forces. The following contents will detail the modeling of cutting forces in the milling process and the related methods for obtaining the values of cutting force coefficients.

1.1.2. *Cutting force model for a general milling cutter*

A general end milling cutter with helical flutes is shown in Figure 1.2. XYZ is the coordinate system, with the positive direction of axes Y and X being aligned with the normal direction of the machined surface and the feed direction, respectively. D, R, R_{r}, R_{z}, α_1, α_2 and H are seven geometric

parameters [ENG 01, GRA 04] used to describe the cutter envelope. Note that in Figure 1.2, M_z, N_z, M_r and N_r are geometrical parameters that can be calculated by these seven parameters. As explained in [ENG 01], distinct cutter geometries can be deduced from the general end mill model when particular values are attributed to these parameters. For example, parameters $\{D, R, R_r, R_z, \alpha_1, \alpha_2, H\}$ will be chosen as $\{D, 0, D/2, 0, 0, 0, H\}$ and $\{D, D/2, 0, D/2, 0, 0, H\}$ for the flat end and ball end mills, respectively.

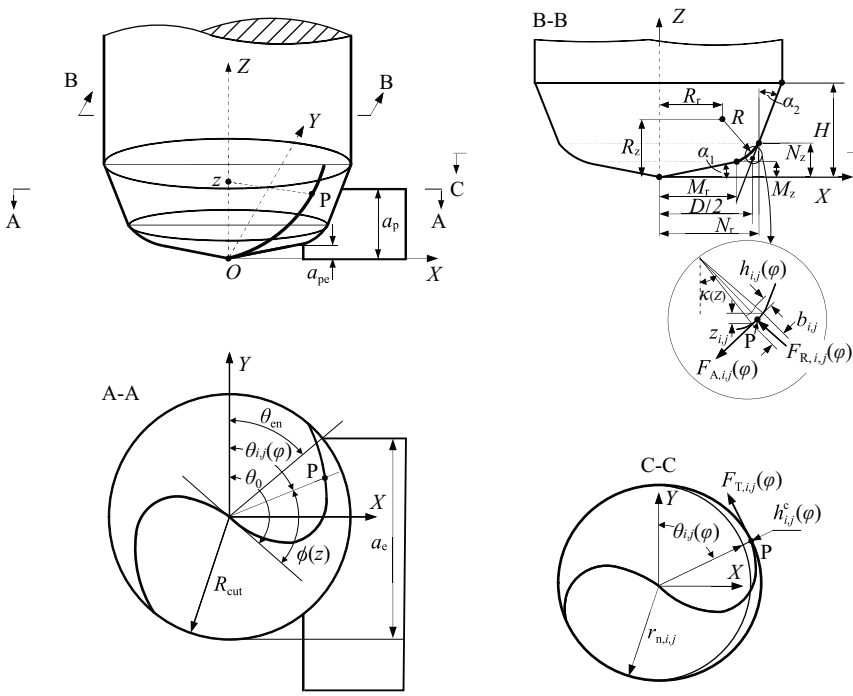

Figure 1.2. *Geometric model of a general end mill and the cutting process*

For the convenience of cutting force calculation, the cutting edges are divided into a finite number of co-axial disk elements with equivalent axial length. For convenience, the axial length of the *j*th axial disk element of the *i*th flute is symbolized as $z_{i,j}$. It should be noted that $z_{i,j}$=$z_{i,k}$ (k=1, 2, ...). The total cutting forces are summed axially along the sliced disk elements from the bottom of the flute to the final axial depth of cut. The cutting forces

contributed by the *j*th axial disk element of the *i*th flute (e.g. the element P shown in Figure 1.2) at an arbitrary cutter rotation angle φ can be expressed by the lumped or dual mechanism models.

Lumped mechanism model

$$\begin{aligned} F_{\mathrm{T},i,j}(\varphi) &= K_{\mathrm{T}} h_{i,j}(\varphi) b_{i,j} \\ F_{\mathrm{R},i,j}(\varphi) &= K_{\mathrm{R}} h_{i,j}(\varphi) b_{i,j} \\ F_{\mathrm{A},i,j}(\varphi) &= K_{\mathrm{A}} h_{i,j}(\varphi) b_{i,j} \end{aligned} \quad [1.8]$$

with

$$\begin{aligned} h_{i,j}(\varphi) &= h^{\mathrm{c}}_{i,j}(\varphi) \sin \kappa(z) \\ b_{i,j} &= z_{i,j} / \sin \kappa(z) \end{aligned} \quad [1.9]$$

where K_{T}, K_{R}, K_{A} are three cutting force coefficients in tangential, radial and axial directions. $h_{i,j}(\varphi)$ and $\kappa(z)$ are the instantaneous uncut chip thickness at the current cutter rotation angle φ and the tool cutting edge angle related to the *j*th axial disk element of the *i*th flute, respectively. z is the axial coordinate of the *j*th axial disk element of the *i*th flute. Based on the geometric definition of the general end mill, $\kappa(z)$ can be expressed as follows [GRA 04].

Case 1: if $z \leq M_{\mathrm{z}}$,

$$\begin{aligned} \kappa(z) &= \alpha_1 \\ \phi(z) &= \ln[z / \tan \alpha_1] \tan \beta / \cos \alpha_1 \end{aligned} \quad [1.10]$$

where $\phi(z)$ is the radial lag angle at z due to the cutter helix angle β.

Case 2: if $M_{\mathrm{z}} < z \leq N_{\mathrm{z}}$,

$$\begin{aligned} \kappa(z) &= \arcsin \sqrt{1 - [(R_{\mathrm{z}} - z)/R]^2} \\ \phi(z) &= (z - M_{\mathrm{z}}) \tan \beta / R + \ln(M_{\mathrm{r}}) \tan \beta / \cos \alpha_1 \end{aligned} \quad [1.11]$$

Case 3: if $N_{\mathrm{z}} < z$,

$$\kappa(z) = \pi/2 - \alpha_2$$

if $\alpha_2 \neq 0$

$$\phi(z) = \phi_0 + \ln[(N_\mathrm{r} + z - N_\mathrm{z}) \tan \alpha_2] \tan \beta / \sin \alpha_2 - \ln(N_r) \tan \beta / \sin \alpha_2$$

if $\alpha_2 = 0$

$$\phi(z) = \phi_0 + (z - N_\mathrm{z}) \tan \beta / N_\mathrm{r}$$

$$\phi_0 = (N_\mathrm{z} - M_\mathrm{z}) \tan \beta / R + \ln(M_\mathrm{r}) \tan \beta / \cos \alpha_1 \qquad [1.12]$$

Dual mechanism model

$$\begin{aligned} F_{\mathrm{T},i,j}(\varphi) &= K_{\mathrm{Tc}} h_{i,j}(\varphi) b_{i,j} + K_{\mathrm{Te}} b_{i,j} \\ F_{\mathrm{R},i,j}(\varphi) &= K_{\mathrm{Rc}} h_{i,j}(\varphi) b_{i,j} + K_{\mathrm{Re}} b_{i,j} \\ F_{\mathrm{A},i,j}(\varphi) &= K_{\mathrm{Ac}} h_{i,j}(\varphi) b_{i,j} + K_{\mathrm{Ae}} b_{i,j} \end{aligned} \qquad [1.13]$$

where K_{qc} and K_{qe} (q=T, R or A) are the force coefficients corresponding to the chip shearing and the edge rubbing, respectively.

Once three force components are obtained from equation [1.8] or equation [1.13], they can be mapped along the X, Y and Z directions as

$$\begin{bmatrix} F_{\mathrm{X},i,j}(\varphi) \\ F_{\mathrm{Y},i,j}(\varphi) \\ F_{\mathrm{Z},i,j}(\varphi) \end{bmatrix} = g(\theta_{i,j}(\varphi)) \mathbf{T}(\theta_{i,j}(\varphi)) \begin{bmatrix} F_{\mathrm{T},i,j}(\varphi) \\ F_{\mathrm{R},i,j}(\varphi) \\ F_{\mathrm{A},i,j}(\varphi) \end{bmatrix} \qquad [1.14]$$

with

$$\mathbf{T}(\theta_{i,j}(\varphi)) = \begin{bmatrix} -\cos\theta_{i,j}(\varphi) & -\sin\kappa(z)\sin\theta_{i,j}(\varphi) & -\cos\kappa(z)\sin\theta_{i,j}(\varphi) \\ \sin\theta_{i,j}(\varphi) & -\sin\kappa(z)\cos\theta_{i,j}(\varphi) & -\cos\kappa(z)\cos\theta_{i,j}(\varphi) \\ 0 & \cos\kappa(z) & -\sin\kappa(z) \end{bmatrix}$$

where $\theta_{i,j}(\varphi)$ is the cutter position angle related to the jth axial disk element of the ith flute at cutter rotation angle φ, and is defined as the clockwise angle determined from axis Y to the disk element. $g(\theta_{i,j}(\varphi))$ is the window function used to identify whether the disk element is in cut or not.

$$g(\theta_{i,j}(\varphi)) = \begin{cases} 1, & \theta_{\mathrm{en},i,j}(\varphi) \leq \theta_{i,j}(\varphi) \leq \theta_{\mathrm{ex},i,j}(\varphi) \\ 0, & \text{otherwise} \end{cases} \qquad [1.15]$$

where $\theta_{\text{en},i,j}(\varphi)$ and $\theta_{\text{ex},i,j}(\varphi)$ are entry and exit angles related to the *j*th axial disk element of the *i*th flute, which are geometrically defined in Figure 1.3

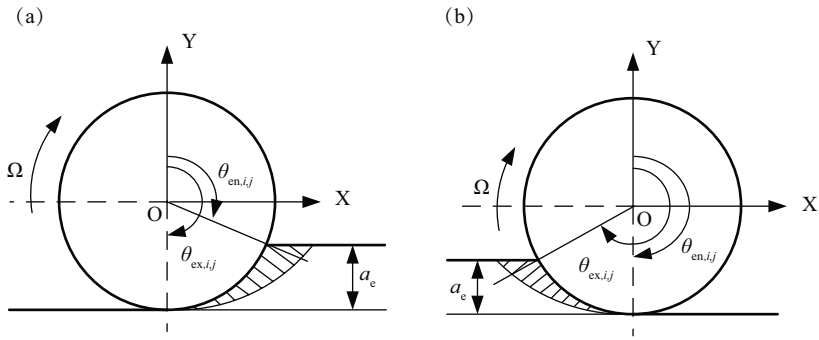

Figure 1.3. *Definition of entry and exit angles: a) down milling; b) up milling*

Subsequently, the total cutting force components $F_s(\varphi)$ (s=X, Y or Z) at any cutter rotation angle φ can be evaluated by summing the forces acting on all flutes and disk elements:

$$F_s(\varphi) = \sum_{i,j} F_{s,i,j}(\varphi)\ , \quad s = \text{X, Y or Z} \qquad [1.16]$$

1.2. Milling process geometry

1.2.1. *Calculations of uncut chip thickness*

As illustrated in Figure 1.4, at an instantaneous cutting position of the *j*th axial disk element of the *i*th flute, the equivalent chip thickness $h^c_{i,j}(\varphi)$ refers to the distance in the radial direction of the cutter between the tooth path to be generated by the cutter element, and the surface left by the *j*th axial disk element of the (*i*-*m*)th flute. The occurrence of cutter runout will lead to $m \neq 1$. Due to the deflections of the cutter and workpiece, the cutter axis shifts from its nominal position. As a result, two adjacent tooth paths will deviate from the desired paths. So, $h^c_{i,j}(\varphi)$ will be different from the nominal value. Based on

the circular tooth path assumption [MAR 45] shown in Figure 1.4(a), $h^{c}_{i,j}(\varphi)$ is calculated as follows

$$h^{c}_{i,j}(\varphi) = r_{i,j} - l_{i,j} \qquad [1.17]$$

where $l_{i,j}$ is an intermediate variable, as shown in Figure 1.4. $r_{i,j}$ is the actual radius of the circular tooth path generated by the *j*th axial disk element of the *i*th flute at cutter rotation angle φ. In this section, $r_{i,j}$ will be calculated by using equation [1.18] based on the radial cutter runout model, which is widely used by many researchers [WAN 03, ARM 89, LIA 94, FEN 94a, FEN 94b, WAN 07a, AKS 98, AZE 04, CHE 97, SEE 99, SHI 97, WAN 07b, WAN 94].

$$r_{i,j} = r_{\mathrm{n},i,j} + \rho\cos[\lambda - \phi(z) - 2(i-1)\pi/N] \qquad [1.18]$$

where $r_{\mathrm{n},i,j}$ is the nominal cutting radius of the *j*th axial disk element of the *i*th flute. N is the total number of cutting teeth of the cutter. ρ and λ are the geometrical parameters in the radial cutter runout model, in which the cutter axis is assumed to be parallel to the centerline of the machine spindle, as defined in Figure 1.5. Geometrically, ρ is the cutter axis offset, defined as the distance between the rotation center of the spindle and the geometric center of the cutter, while λ is location angle measured as the angle between the direction of the offset and the tip of the nearest tooth (tooth 1).

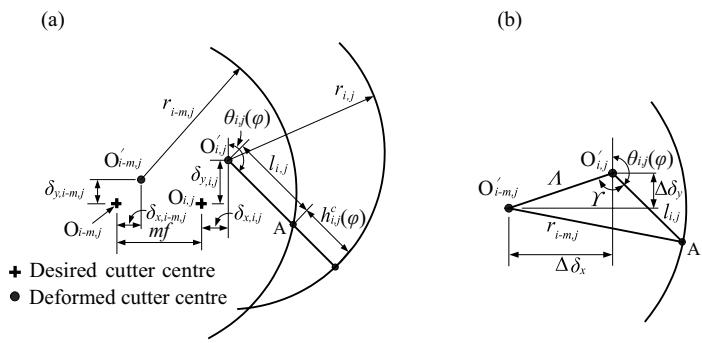

Figure 1.4. *Geometric illustration of equivalent chip thickness: a) geometric definition; b) close-up view of sub-figure (a)*

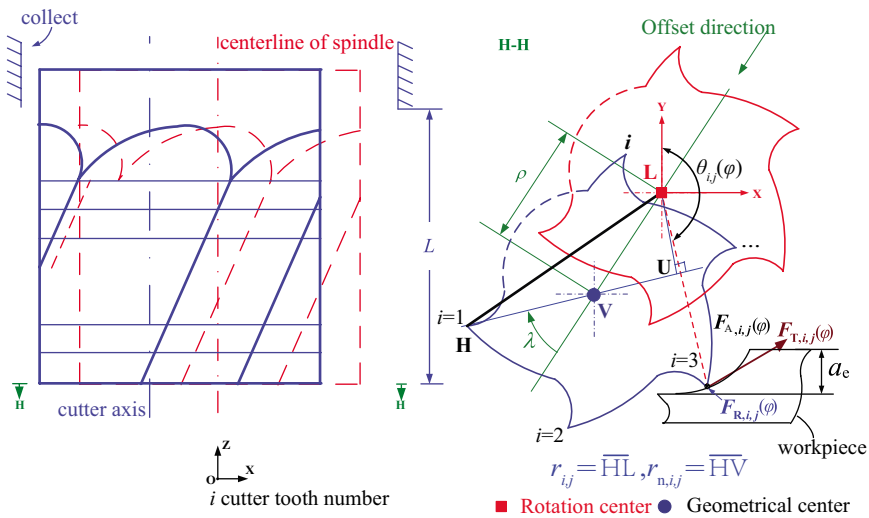

Figure 1.5. *Definition of radial cutter runout. For a color version of this figure, see www.iste.co.uk/zhang/milling.zip*

Using the law of cosines, a geometric relation exists between the cutter centre of the current tooth path and that of the past tooth path in Figure 1.4(b).

$$r_{i-m,j}^2 = \Lambda^2 + {l_{i,j}}^2 - 2\Lambda\, l_{i,j} \cos \Upsilon \qquad [1.19]$$

in which

$$\Lambda = \sqrt{\Delta\delta_x^2 + \Delta\delta_y^2} \qquad [1.20]$$

with

$$\Delta\delta_x = mf + \delta_{x,i,j} - \delta_{x,i-m,j};\ \Delta\delta_y = \delta_{y,i,j} - \delta_{y,i-m,j} \qquad [1.21]$$

Notice that ($\delta_{x,i,j}$, $\delta_{y,i,j}$) and($\delta_{x,i-m,j}$, $\delta_{y,i-m,j}$) correspond to offset values of cutter centres of the current tooth and the m-past tooth from their

desired positions, respectively. f is the feed per tooth. Obviously, the following relation holds.

$$\Upsilon = \pi - \theta_{i,j}(\varphi) + \arccos(\frac{\Delta\delta_y}{\Lambda}) \quad [1.22]$$

By solving equation [1.19], $l_{i,j}$ is obtained as

$$l_{i,j} = \Lambda\cos\Upsilon + \sqrt{r_{i-m,j}^2 - \Lambda^2\sin^2\Upsilon} \quad [1.23]$$

By substituting equation [1.23] into equation [1.17], $h_{i,j}^{c}$ is derived as

$$h_{i,j}^{c}(\varphi) = -\Lambda\cos\Upsilon + r_{i,j} - \sqrt{r_{i-m,j}^2 - \Lambda^2\sin^2\Upsilon} \quad [1.24]$$

Due to the fact that $r_{i-m,j} >> \Delta\delta_x$ and $r_{i-m,j} >> \Delta\delta_y$, it follows that $r_{i-m,j} >> \Lambda\sin\Upsilon$ from equation [1.20]. Thus, equation [1.24] can be approximated by

$$\begin{aligned} h_{i,j}^{c}(\varphi) &= -\Lambda\cos\Upsilon + r_{i,j} - r_{i-m,j} \\ &\approx mf\sin\theta_{i,j}(\varphi) + r_{i,j} - r_{i-m,j} \end{aligned} \quad [1.25]$$

Note that if a negative value of $h_{i,j}^{c}(\varphi)$ is obtained by equation [1.24] or equation [1.25], $h_{i,j}^{c}(\varphi)$ is set to be zero.

Physically, a static milling process free of vibration implies that cutting forces must have stabilized themselves after a few tooth periods. In other words, the cutting forces obtained from two adjacent tooth periods must be equal, as assumed by Budak [BUD 92]. The implication of this stability condition requires that the volume of materials cut off by the current tooth should be identical to that cut off by the previous tooth with the negligence of runout, i.e. m =1 and $r_{i,j} = r_{i-1,j}$ in equation [1.25]. Now, suppose that $F_i(\theta_{i,j}(\varphi))$ represents the resultant cutting force vector associated with the cutter position angle $\theta_{i,j}(\varphi)$, then

$$\mathbf{F}_i(\theta_{i,j}(\varphi)) = \mathbf{F}_{i-1}(\theta_{i-1,j}(\varphi)) \quad [1.26]$$

Likewise, cutter deflections of the concerned cutter segment also remain unchanged between two adjacent teeth, so that following equations hold

$$\boldsymbol{\delta}_{\mathrm{t},i,j} = \boldsymbol{\delta}_{\mathrm{t},i-1,j} \qquad [1.27]$$

where $\boldsymbol{\delta}_{\mathrm{t},i,j} = (\delta_{\mathrm{t,X},i,j}, \delta_{\mathrm{t,Y},i,j}, \delta_{\mathrm{t,Z},i,j})$ is the cutter deflection vector corresponding to the *j*th axial disk element of the *i*th flute. It is evaluated based on the cantilevered beam model [SUT 86, BUD 95, SHI 96].

Concerning the cutter center offset values ($\delta_{x,i,j}$,$\delta_{y,i,j}$,$\delta_{x,i-1,j}$,$\delta_{y,i-1,j}$), because of $\delta_{x,i,j} = \delta_{\mathrm{t,X},i,j}$ and $\delta_{y,i,j} = \delta_{\mathrm{t,Y},i,j}$, the following important relations can be derived:

– from equation [1.27],

$$\delta_{x,i,j} = \delta_{x,i-1,j}, \quad \delta_{y,i,j} = \delta_{y,i-1,j} \qquad [1.28]$$

– from equation [1.21],

$$\Delta\delta_x = f, \quad \Delta\delta_y = 0 \qquad [1.29]$$

– from equation [1.22],

$$\beta = {}^{3\pi}\!/_{2} - \theta_{i,j}(\varphi) \qquad [1.30]$$

By reviewing the above relations, equation [1.25] can be further simplified as

$$h^{\mathrm{c}}_{i,j}(\varphi) = f \sin\theta_{i,j}(\varphi) \qquad [1.31]$$

Obviously, equation [1.31] indicates that $h^{\mathrm{c}}_{i,j}$ converges to its nominal value of $f \sin\theta_{i,j}(\varphi)$ in a static milling process. It gives the theoretical explanation why the nominal value of the equivalent chip thickness, $f \sin\theta_{i,j}(\varphi)$, is widely used by many researchers to establish the cutting force model.

1.2.2. *Determination of entry and exit angles*

Equation [1.15] shows that cutting force prediction is dependent on the entry, θ_{en}, and the exit, θ_{ex}, angles. In the case of a milling workpiece with

simple geometry, both angles can be calculated analytically. For instance, in flat end milling of a plane, the entry and exit angles can be mathematically expressed as

$$\begin{aligned} \theta_{\text{en}} &= \frac{\pi}{2} + \arcsin\frac{(D-2a_{\text{e}})}{D},\ \theta_{\text{ex}} = \pi, && \text{for down milling} \\ \theta_{\text{en}} &= \pi,\ \theta_{\text{ex}} = \frac{\pi}{2} - \arcsin\frac{(D-2a_{\text{e}})}{D}, && \text{for up milling} \end{aligned} \quad [1.32]$$

where a_{e} stands for the radial depth of cut.

For a milling workpiece with complex geometry, a complicated cutter geometry and process geometry make it very difficult to analytically determine the entry and exit angles. Alternatively, researchers propose that through extracting the cutter-workpiece engagement (CWE) region, i.e. the engagement domain of each axial disk along the tool axis, the entry and exit angles can be correspondingly calculated. A literature review shows that existing CWE extracting methods have the following characteristics:

– for a discrete method [CHO 97, LAZ 03, FUS 03, ROT 07, LI 10, ZHA 11, ARA 11, KIM 06, LI 08, KAR 10], the achievement of high accuracy computing of CWE requires a high resolution of workpiece decomposition, large store memory and long computing time;

– for a solid modeling-based method [FER 08b, LAZ 11, SPE 94, IMA 98, ELM 98, SPE 00, YIP 06], Boolean operations for implementing surface/surface intersection algorithms are greatly time-consuming because CWE maps are extracted from the in-process workpiece. Meanwhile, as the data structure size quickly increases during simulation, numerical inaccuracies of the workpiece's model will be stacked and thus topological errors may occur.

This section proposes a solid trimming method by which CWE maps are extracted from the removal volume of multi-axis milling rather than from the in-process workpiece (IPW). In this method, both the workpiece and tool surfaces are described by a B-rep solid modeler.

CWE is geometrically defined as the instantaneous engagement region when flutes enter into and leave a workpiece. In other words, it is the contact area between the tool envelope surface and the workpiece, and can be treated

as a function of cutter's axial height. The calculation of CWE thus depends upon both the geometry complexities of the cutter and workpiece as well as the relative location between the cutter and workpiece. It is independent of tool flute numbers and cutting parameters. The proposed method is schematically depicted in Figure 1.6. It can be seen that the calculation of CWE maps is based on the removal volume, rather than the entire in-process workpiece, as reported in [ARA 08]. This allows the subsequent operations to be performed on a simple data structure. Detailed explanations of the key steps are described below.

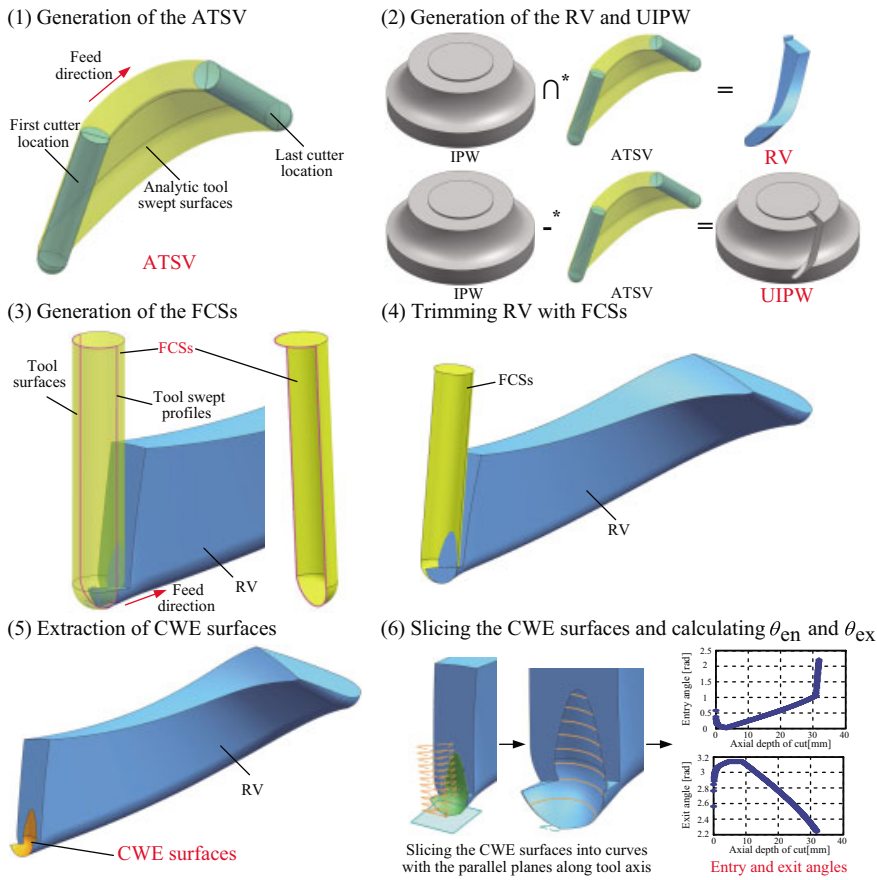

Figure 1.6. *The whole procedure of CWE extraction. For a color version of this figure, see www.iste.co.uk/zhang/milling.zip*

1.2.2.1. *Generation of analytic tool swept volume, removal volume and updated in-process workpiece*

This section corresponds to steps (1) and (2) in Figure 1.6. The main content of both steps are as follows:

i) Generation of the analytic tool swept volume (ATSV) by the method reported in [WEI 04]. This step is often performed by sewing the analytic tool swept surface, $\{\text{Faces}\}_{\text{Swept}}$, the ingress part of the tool surface, $\{\text{Faces}\}_{\text{Ingress}}$, at the first cutter location and the egress part of the tool surface, $\{\text{Faces}\}_{\text{Egress}}$, at the($N_{CL}$-1)th cutter location,

$$E_{\text{Swept}}=\{\text{Faces}\}_{\text{Swept}}+\{\text{Faces}\}_{\text{Ingress}}+\{\text{Faces}\}_{\text{Egress}} \quad [1.33]$$

where E_{Swept} denotes the solid model of analytic tool swept volume. N_{CL} denotes the number of cutter locations.

In this work, the analytic tool swept surface is obtained by employing the analytic method proposed in [GON 09].

ii) With the ATSV obtained above, the removal volume (RV) and updated in-process workpiece (UIPW) are obtained by performing Boolean operations between the ATSV and the in-process workpiece (IPW):

$$\text{RV} = \text{ATSV}\bigcap^{*}\text{IPW} \quad [1.34]$$

$$\text{UIPW} = \text{IPW}-^{*}\text{ATSV} \quad [1.35]$$

where $\bigcap^{*}$ and $-^{*}$ denote the Boolean intersection and subtraction operator, respectively. Notice that UIPW becomes IPW for the next tool path segments.

Traditionally, equation [1.34] is carried out based on the tool swept volume obtained with Boolean union operation among the cutter solid models at all cutter locations along the tool path [FER 08a]. Because there are many small edges and faces in the tool swept volume, the calculation of RV needs many surface/surface intersection calculations between the IPW and the tool swept volume, whereas the method proposed here determines RV by using the ATSV, which involves at most nine surfaces. As a result, abundant surface/surface intersection calculations are avoided in the calculation procedure of RV and UIPW. Correspondingly, the simple data structure of the ATSV results in a

simple data structure of the RV and UIPW. This favors the efficient CWE extraction described in the following sections.

1.2.2.2. *Generation of the feasible contact surfaces*

In the actual milling process, only partial tool surfaces may make contact with the workpiece, as illustrated in Figure 1.7(a). These surfaces are named feasible contact surfaces (FCSs) according to [ARA 08]. Mathematically, the angle between the tool surface normal $\mathbf{N}(u, v, t)$ and the instantaneous velocity $\mathbf{V}(u, v, t)$ at any point on FCSs of a tool should be a sharp or a right angle at most. That is,

$$\mathbf{N}(u, v, t) \cdot \mathbf{V}(u, v, t) \geq 0 \qquad [1.36]$$

where u and v are two variables in the parameter equations of the tool surfaces. t is the instantaneous cutting time variable corresponding to the given cutter location. If a set of points meet the condition $\mathbf{N}(u, v, t) \cdot \mathbf{V}(u, v, t) = 0$, these points will constitute closed curves, named tool swept profiles, which define the critical boundaries of FCSs, as shown in Figure 1.7(b). Then, the FCSs are obtained by following the two steps below. First, split the tool surfaces into two parts by the tool swept profiles. Second, select the part satisfying equation [1.36] as the required feasible contact surfaces $\{\text{Faces}\}_{\text{FCS},k}$, where k means the kth cutter location along the tool path.

1.2.2.3. *Trimming removal volume with feasible contact surfaces*

CWE surfaces are usually extracted by subtracting the tool movements from the solid model of the workpiece or the removal volume [LAZ 11]. As illustrated in Figure 1.8, some materials which should be removed from the workpiece are not actually cut, due to the inaccurate calculations of tool movements in 5-axis milling. This results in bodies with many small edges and surfaces being produced at each cutter location. As the cutter advances, these edges and faces will be accumulated along the tool path so that the model data structure and computing time will increase during the whole simulation procedure. Meanwhile, topological errors easily occur because of the stacked numerical inaccuracies induced by these small edges and faces.

Here the proposed method is to extract the CWE surfaces directly based on the removal volume and feasible contact surfaces obtained above. As shown in

Figure 1.9, the trimming operation related to the kth cutter location is described below:

1) compute the intersection curves between the FCSs and boundary surfaces of RV;

2) split FCSs and the boundary surfaces of RV by the intersection curves obtained above;

3) reconstruct the remaining removal volume with the split boundary surfaces obtained above.

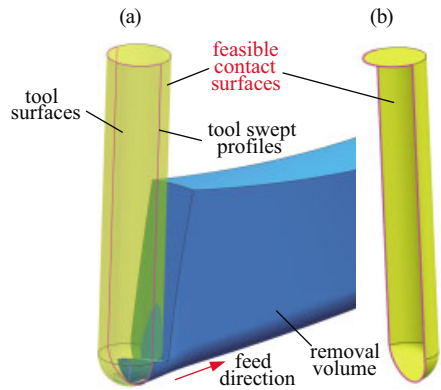

Figure 1.7. *Illustration of feasible contact surfaces: a) tool surfaces contacting with the RV; b) feasible contact surfaces at specific cutter location. For a color version of this figure, see www.iste.co.uk/zhang/milling.zip*

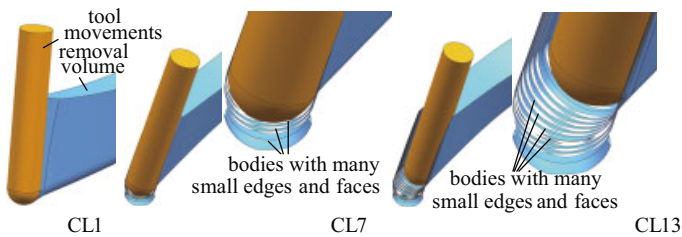

Figure 1.8. *Production of bodies with many small edges and surfaces when the tool movements are subtracted from the removal volume. For a color version of this figure, see www.iste.co.uk/zhang/milling.zip*

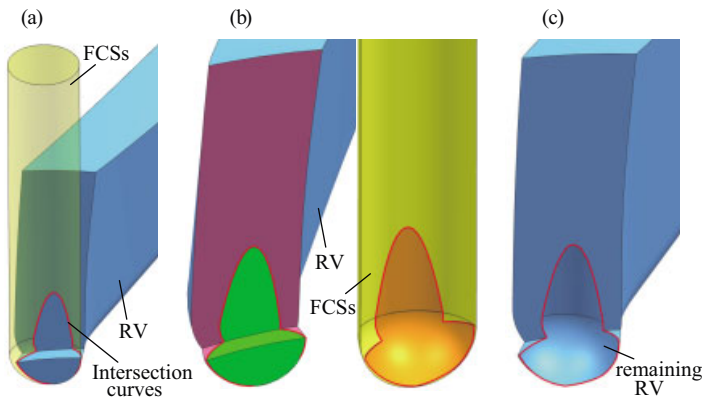

Figure 1.9. *The illustration of the trimming operation: a) computing the intersection curves; b) splitting the boundary surfaces; c) reconstructing the remaining RV. For a color version of this figure, see www.iste.co.uk/zhang/milling.zip*

In this way, a large number of bodies with small edges and faces can be avoided as the cutter moves along the tool path. Because only the FCSs of the tool surfaces may make contact with the workpiece in the actual milling process, the CWE surfaces are actually the subsets of the FCSs. Keeping this idea in mind, the CWE surfaces can be obtained through trimming the removal volume by the FCSs at each cutter location. With this operation, the CWE surfaces are directly imprinted on the remaining removal volume once the materials between the previous and the current FCSs are discarded. Following this procedure, CWE surfaces at the kth cutter location, $\{\text{Faces}\}_{\text{CWE},k}$, can thus be expressed as

$$\{\text{Faces}\}_{\text{CWE},k} = \{\text{Faces}\}_{\text{RV},k} \cap^* \{\text{Faces}\}_{\text{FCS},k} \qquad [1.37]$$

where $\{\text{Faces}\}_{\text{RV},k}$ denotes all boundary surfaces of the remaining removal volume RV_{k+1} at the kth cutter location, and RV_{k+1} denotes the solid model of the remaining removal volume after the trimming operation at the kth cutter location. Figure 1.10 illustrates the CWE surfaces extraction procedure associated with two adjacent cutter locations.

In fact, in B-rep solid modeler, the CWE surfaces constitute partial boundary surfaces of the remaining removal volume. Once the cutter moves

to a new cutter location, CWE surfaces on the removal volume related to the previous cutter location are removed, and newly generated CWE surfaces will be updated as the boundary surfaces of the remaining removal volume, as shown in Figure 1.10(b) and (d). This can avoid generating abundant small edges and faces. In addition, the number of boundary surfaces of the removal volume does not always increase. Benefiting from this steady data structure, the proposed method is efficient without stacked numerical inaccuracies and topological errors.

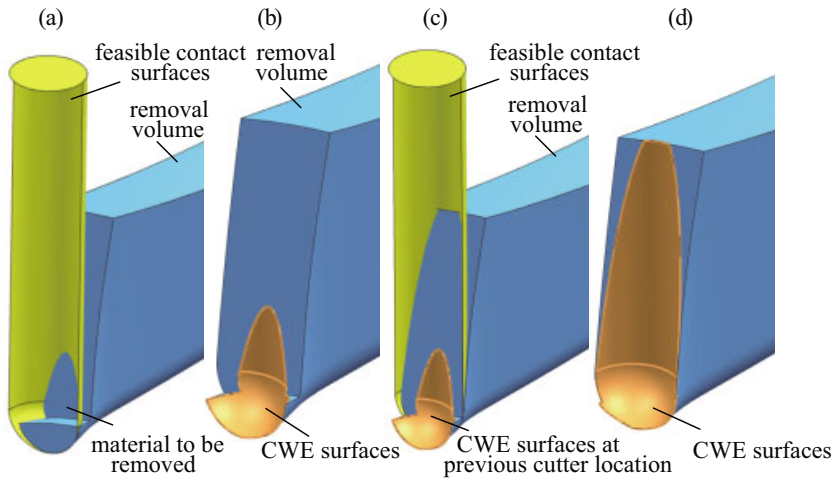

Figure 1.10. *Illustration of trimming procedure: a) and c); instantaneous trimming status at the 1st and 2nd cutter locations; b) and d); remaining removal volume after trimming at the 1st and 2nd cutter locations. For a color version of this figure, see www.iste.co.uk/zhang/milling.zip*

1.2.2.4. *Extraction of the CWE surfaces from the removal volume*

As described above, because CWE surfaces imprinted on some boundary surfaces of the remaining RV are generated by the FCSs, they have the same attributes as the tool surfaces, such as surface type, center point and axis direction. This means that these attributes can be used to identify and extract the CWE surfaces from the remaining RV. The detailed algorithm is described as follows.

Step 1: search all boundary surfaces of the remaining removal volume RV_{k+1} at the kth cutter location and save them as $\{\mathrm{Faces}\}_{\mathrm{RV},k}$.

Step 2: identify the surface attributes of all $\{\mathrm{Faces}\}_{\mathrm{RV},k}$.

Step 3: if the attributes of each $\{\mathrm{Faces}\}_{\mathrm{RV},k}$ are consistent with those of the tool surface, append the surface into the sequence of the CWE surfaces $\{\mathrm{Faces}\}_{\mathrm{CWE},k}$ at the kth cutter location.

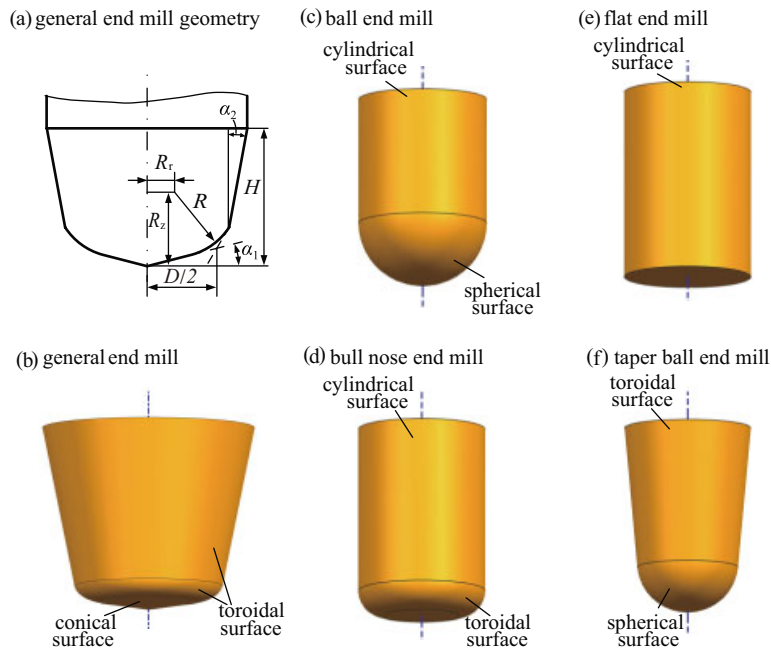

Figure 1.11. *General tool geometry and surfaces of different end mills*

For the different end mills shown in Figure 1.11, the types of tool surfaces can be classified as cylindrical, conical, toroidal and spherical surfaces, which include the attributes of axis, spherical center or radius, as listed in Table 1.1. With this information, one can perform Step 3 to identify the CWE surfaces. To have a clear understanding of the above method, the pseudo-codes corresponding to these milling cutters are described below.

Input:
RV_{k+1} : *the remaining removal volume after trimming operation at the kth cutter location, where* $k = 1, 2, ..., N_{CL} - 1$.
$[\mathbf{P}_{\mathrm{c},k}, \mathbf{n}_k]$: *the cutter location data at the kth cutter location;* $\mathbf{P}_{\mathrm{c},k}$ *denotes the cutter tip coordinate*; $\mathbf{n}_k$ *denotes the tool orientation vector.*
ϵ : *tolerance for comparing the constructive features of the surface and the cutter location.*
$\{D, R, R_{\mathrm{r}}, R_{\mathrm{z}}, \alpha_1, \alpha_2, H\}$: *tool geometry parameters as shown in Figure 1.11(a).*
Output:
$\{\mathrm{Faces}\}_{\mathrm{CWE},k}$: *the CWE surfaces at the kth cutter location.*
Step 1:
Search all boundary surfaces of the remaining removal volume RV_{k+1} *at the kth cutter location and save them as* $\{Faces\}_{RV,k}$ *temporarily.*
Step 2:
FOR (each surface in $\{\mathrm{Faces}\}_{\mathrm{RV},k}$)
{*Identify the type of the surface, the axis of the revolution surface of the cutter body* $\mathbf{n}_{\mathrm{s}}$, *and the sphere center of the revolution surface of the cutter body* $\mathbf{C}_{\mathrm{s}}$.}
Step 3:
FOR (each surface in $\{\mathrm{Faces}\}_{\mathrm{RV},k}$)
{
IF (face type == cylindrical surface *or* face type == conical surface *or* face type == toroidal surface)
{
IF

$$\|\mathbf{n}_{\mathrm{s}} - \mathbf{n}_k\|_\infty < \epsilon \; or \; \|\mathbf{n}_{\mathrm{s}} + \mathbf{n}_k\|_\infty < \epsilon \qquad [1.38]$$

{ Append the surface into the sequence of the cutter-workpiece engagement surfaces $\{\mathrm{Faces}\}_{\mathrm{CWE},k}$ }
ELSE IF (face type == spherical surface)
{
Calculate the ball center $\mathbf{C}_{\mathrm{B},k}$ of the ball end mill or taper ball end mill with the cutter location data and tool geometry parameters, where

$$\mathbf{C}_{\mathrm{B},k} = \mathbf{P}_{\mathrm{c},k} - R\mathbf{n}_k \qquad [1.39]$$

IF

$$(\|\mathbf{C}_{\mathrm{s}} - \mathbf{C}_{\mathrm{B},k}\|_\infty < \epsilon) \qquad [1.40]$$

{ Append the surface into the sequence of the cutter-workpiece engagement surfaces $\{\text{Faces}\}_{\text{CWE},k}$ } }
}.
OUTPUT *the CWE surfaces* $\{\text{Faces}\}_{\text{CWE},k}$ *at the kth cutter location.*

Mill type	*Surface type*	*Surface attributes*
general end mill	toroidal surface conical surface	axis ($\mathbf{n}_k$) axis ($\mathbf{n}_k$)
ball end mill	cylindrical surface spherical surface	axis ($\mathbf{n}_k$) spherical center ($\mathbf{C}_{\text{B},k}$)
bull nose end mill	cylindrical surface toroidal surface	axis ($\mathbf{n}_k$) axis ($\mathbf{n}_k$)
flat end mill	cylindrical surface	axis ($\mathbf{n}_k$)
taper ball end mill	toroidal surface spherical surface	axis ($\mathbf{n}_k$) spherical center ($\mathbf{C}_{\text{B},k}$)

Table 1.1. *Surface attributes for different end mills*

1.2.2.5. *Procedure for calculating entry and exit angles*

The whole procedure for calculating the entry and exit angles for a specified workpiece model and cutter location (CL) file is summarized as follows:

1) read the information about cutter location, cutter geometry parameters and machine coordinate system from the CL file;

2) establish the solid model of the workpiece in the CAD/CAM system;

3) construct the analytical tool swept volume using equation [1.33];

4) calculate the removal volume and updated in-process workpiece with equation [1.34] and equation [1.35];

5) set $k = 1$ and $\text{RV}_1 = \text{RV}$. RV_k represents the solid model of the remaining removal volume after the trimming operation at the (k-1)th cutter location and to be cut at the kth cutter location;

6) generate the feasible contact surfaces $\{\text{Faces}\}_{\text{FCS},k}$ using equation [1.36] at the kth cutter location;

7) trim the solid model RV_k by $\{\text{Faces}\}_{\text{FCS},k}$. Save the remaining part of RV_k along the feed direction as RV_{k+1};

8) search all boundary surfaces of RV_{k+1} and save them as $\{\text{Faces}\}_{\text{RV},k}$;

9) if the surface attributes of each $\{\text{Faces}\}_{\text{RV},k}$ are consistent with the surface attributes of the tool surface, append the surface into the sequence of the CWE surfaces $\{\text{Faces}\}_{\text{CWE},k}$ at the kth cutter location and repeat this step until all surfaces are considered;

10) calculate the intersection arcs in $\{\text{Faces}\}_{\text{CWE},k}$ related to a set of discretized horizontal planes, which are perpendicular to the tool orientation and equivalently placed with equivalent length Δz along the tool orientation from the tool tip. Here, Δz is set to be $z_{i,j}$, i.e. the axial length of each edge disk of the cutter, as described in section 1.1.2;

Here, the intersection arcs include entry end point $\mathbf{P}_{k,\text{en}}$, exit end point $\mathbf{P}_{k,\text{ex}}$ and center point $\mathbf{C}_k$ of arcs at the kth cutter location;

11) calculate the entry and exit angles at the kth cutter location using the following equations and the intersection arc data obtained from step (10):

$$\theta_{\text{en}} = \arcsin(\mathbf{f}_k \cdot \mathbf{r}_{k,\text{en}}),\ \theta_{\text{ex}} = \arcsin(\mathbf{f}_k \cdot \mathbf{r}_{k,\text{ex}}) \qquad [1.41]$$

where $\mathbf{f}_k$ is the feed direction vector at the kth cutter location, calculated using the CL data in step (1). $\mathbf{r}_{k,\text{en}} = \mathbf{P}_{k,\text{en}} - \mathbf{C}_k$ and $\mathbf{r}_{k,\text{ex}} = \mathbf{P}_{k,\text{ex}} - \mathbf{C}_k$. $\mathbf{P}_{k,\text{en}}$, $\mathbf{P}_{k,\text{ex}}$ and $\mathbf{C}_k$ are the coordinates of the entry end point, exit end point and center point obtained from step (10), respectively;

12) if $k < N_{\text{CL}} - 1$, set $k = k + 1$ and go to step (6). Otherwise, stop the procedure.

1.2.2.6. *Numerical simulations*

A ball end milling of an impeller is adopted to numerically check the validity of the method. An extraction algorithm is coded using C# and the application programming interface NX Open of SIEMENS NX 7.5. Instantaneous entry and exit angles are shown in Figure 1.12. During the engaging stage of the first-cut, the cutter-workpiece engagement area expands from the tip to the middle of the cutter until the continuous cutting stage starts. Corresponding to most parts of the cutter, engagement angles associated with following-cut are smaller than those related to first-cut, as shown in Figure 1.12. However, with respect to the ball end part, it follows the reverse conclusion due to the fact that the small radius at the ball end makes the cutting like a slot milling. Meanwhile, the efficiency of the proposed method is compared with the existing method described in [LAZ 11]. When 929 CL points in the above ball end milling are simulated,

the cost of the proposed method is about 424.2 seconds, while the cost of the method in [LAZ 11] is about 1716 seconds. This means the proposed method is more time-efficient.

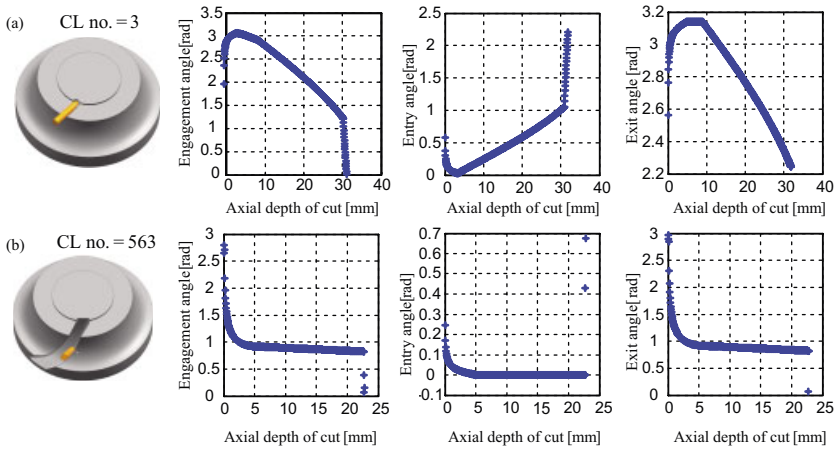

Figure 1.12. *Ball end milling of an impeller at two different cutter locations*

1.3. Identification of the cutting force coefficients

In order to efficiently predict the cutting forces, it is of great importance to calibrate the values of cutting force coefficients and the cutter runout parameters *a priori*. In this book, four types of methods developed by the authors will be described in detail.

1.3.1. *Calibration method for general end mills*

This is a unified method suited to general end mills, such as flat end mill, bull nose end mill, ball end mill, etc. The cutter is firstly discretized into a finite number of disk elements. The total cutting forces are then obtained by summing the elemental forces acting on all sliced disk elements.

1.3.1.1. *Identification of the cutting force coefficients*

This scheme is generally developed based on the measured cutting forces. For a general end mill shown in Figure 1.2, at the cutting instant of angular

position $\theta_{i,j}(\varphi)$ for the *j*th axial disk element of the *i*th flute, the cyclic symmetry of the cutter flutes ensures that the *j*th axial disk element of the (*i*+*k*)th flute will have the same angular position, i.e. $\theta_{i+k,j}(\varphi + 2k\pi/N)) = \theta_{i,j}(\varphi)$ after a cutter rotation of $2k\pi/N$. As a result, the sum of the cutting forces acting on the *j*th axial disk element of the *i*th (*i*=1, 2, ..., *N*) flute at the angular position $\theta_{i,j}(\varphi)$ can be expressed as

$$\begin{bmatrix} F_{\mathrm{X},j}(\varphi) \\ F_{\mathrm{Y},j}(\varphi) \\ F_{\mathrm{Z},j}(\varphi) \end{bmatrix} = \mathbf{T}(\theta_{i,j}(\varphi)) \begin{bmatrix} K_{\mathrm{T}} \sum_{i=1}^{N} (h_{i,j}(\varphi) b_{i,j}) \\ K_{\mathrm{R}} \sum_{i=1}^{N} (h_{i,j}(\varphi) b_{i,j}) \\ K_{\mathrm{A}} \sum_{i=1}^{N} (h_{i,j}(\varphi) b_{i,j}) \end{bmatrix} \quad [1.42]$$

By reviewing equation [1.9] and equation [1.25] together with $b_{i,j} = b_{k,j}$ $(i, k = 1, 2, ..., N)$, we can obtain

$$\sum_{i=1}^{N} (h_{i,j}(\varphi) b_{i,j}) = z_{i,j} \{ N f \sin \theta_{i,j}(\varphi) + \sum_{i=1}^{N} [r_{i,j} - r_{i-m,j}] \} \quad [1.43]$$

with $r_{i-m,j} = r_{N,j}$ if $i - m = 0$.

Because of $\sum_{i=1}^{N} [r_{i,j} - r_{i-m,j}] = 0$, the runout effect related to the last summation term of equation [1.43] can be naturally annulled so that

$$\sum_{i=1}^{N} (h_{i,j}(\varphi) b_{i,j}) = N z_{i,j} f \sin \theta_{i,j}(\varphi) \quad [1.44]$$

Furthermore, by substituting equation [1.44] into equation [1.42] and then dividing equation [1.42] by *N*, we can obtain force components defined as

$$\begin{bmatrix} \overline{F}_{\mathrm{X},j}(\varphi) \\ \overline{F}_{\mathrm{Y},j}(\varphi) \\ \overline{F}_{\mathrm{Z},j}(\varphi) \end{bmatrix} = \frac{1}{N} \begin{bmatrix} \sum_{i=1}^{N} F_{\mathrm{X},j}(\varphi) \\ \sum_{i=1}^{N} F_{\mathrm{Y},j}(\varphi) \\ \sum_{i=1}^{N} F_{\mathrm{Z},j}(\varphi) \end{bmatrix} = z_{i,j} f \sin \theta_{i,j}(\varphi) \mathbf{T}(\theta_{i,j}(\varphi)) \begin{bmatrix} K_{\mathrm{T}} \\ K_{\mathrm{R}} \\ K_{\mathrm{A}} \end{bmatrix} \quad [1.45]$$

From the above relation, it follows that $\overline{F}_{s,j}(\varphi)$ (s = X, Y or Z) is independent of the cutter runout. In other words, equation [1.45] is just the nominal components of the cutting forces associated with the jth disk element of all flutes no matter what the cutter runout is.

Correspondingly, the total nominal cutting forces corresponding to $\theta_{i,j}(\varphi)$ can be obtained by adding equation [1.45] along z

$$\begin{bmatrix}\overline{F}_{\mathrm{X}}(\varphi)\\ \overline{F}_{\mathrm{Y}}(\varphi)\\ \overline{F}_{\mathrm{Z}}(\varphi)\end{bmatrix}=\frac{1}{N}\begin{bmatrix}\sum_{i=1}^{N}[F_{\mathrm{X}}(\varphi+2(i-1)\pi/N)]\\ \sum_{i=1}^{N}[F_{\mathrm{Y}}(\varphi+2(i-1)\pi/N)]\\ \sum_{i=1}^{N}[F_{\mathrm{Z}}(\varphi+2(i-1)\pi/N)]\end{bmatrix}=f\,\mathbf{T}_1(\theta_{i,j}(\varphi))\begin{bmatrix}K_{\mathrm{T}}\\ K_{\mathrm{R}}\\ K_{\mathrm{A}}\end{bmatrix} \quad [1.46]$$

where

$$\mathbf{T}_1(\theta_{i,j}(\varphi))=\begin{bmatrix}-\sum_{i,j}(z_{i,j}B_2) & -\sum_{i,j}(C_1B_1) & -\sum_{i,j}(C_2B_1)\\ \sum_{i,j}(z_{i,j}B_1) & -\sum_{i,j}(C_1B_2) & -\sum_{i,j}(C_2B_2)\\ 0 & \sum_{i,j}[C_2\sin\theta_{i,j}(\varphi)] & -\sum_{i,j}[C_1\sin\theta_{i,j}(\varphi)]\end{bmatrix} \quad [1.47]$$

with

$$\begin{aligned}B_1&=\sin^2\theta_{i,j}(\varphi), \quad & B_2&=\sin\theta_{i,j}(\varphi)\cos\theta_{i,j}(\varphi)\\ C_1&=z_{i,j}\sin\kappa(z), & C_2&=z_{i,j}\cos\kappa(z)\end{aligned} \quad [1.48]$$

Here, the nominal cutting forces $\overline{F}_s(\varphi)$ (s = X, Y or Z) are expressed as a linear function of the cutting force coefficients. Assume that $F_s^{\mathrm{M}}(\varphi)$ (s = X, Y or Z) denotes measured values of cutting forces at cutter rotation angle φ. Following equation [1.46], $\overline{F}_s(\varphi)$ can be approximated by averaging the measured values over one cutter revolution.

$$\overline{F}_s(\varphi)=\frac{1}{N}\sum_{i=1}^{N}[F_s^{\mathrm{M}}(\varphi+2(i-1)\pi/N)], \quad s=\mathrm{X,\ Y\ or\ Z} \quad [1.49]$$

Finally, with the known values of $\overline{F}_s(\varphi)$ (s = X, Y or Z), K_q (q = T, R or A) can be deduced immediately from equation [1.46] by the inverse of $\mathbf{T}_1(\theta_{i,j}(\varphi))$. Compared with existing methods, the main features of the proposed approach are twofold. On the one hand, a concise formulation independent of the cutter radial runout is established for the determination of cutting force coefficients. On the other hand, instantaneous values of the nominal cutting force components provide the possibility to investigate the instantaneous variation of the cutting force coefficients.

1.3.1.2. *Identification of the cutter runout parameters*

Under the assumption of $m = 1$, the substitution of equation [1.18] into equation [1.25] will give rise to the following equation

$$h^c_{i,j}(\varphi) = f \sin\theta_{i,j}(\varphi) + [-2\rho \sin({}^{\pi}\!/_{N}\,) \sin(\lambda - \phi(z) - {}^{(2i-3)\pi}\!/_{N}\,)] \quad [1.50]$$

The condition $m = 1$ implies that the current tooth removes the materials being left just by the previous one. Furthermore, by considering equations [1.50], [1.9], [1.8] and [1.14] together, equation [1.16] can be further developed as

$$\begin{aligned}\begin{bmatrix} F_{\mathrm{X}}(\varphi) \\ F_{\mathrm{Y}}(\varphi) \\ F_{\mathrm{Z}}(\varphi) \end{bmatrix} &= f\mathbf{T}_1(\theta_{i,j}(\varphi)) \begin{bmatrix} K_{\mathrm{T}} \\ K_{\mathrm{R}} \\ K_{\mathrm{A}} \end{bmatrix} + \mathbf{T_2}(\theta_{i,j}(\varphi)) \begin{bmatrix} \rho\cos\lambda \\ \rho\sin\lambda \end{bmatrix} \\ &= \begin{bmatrix} \overline{F}_{\mathrm{X}}(\varphi) \\ \overline{F}_{\mathrm{Y}}(\varphi) \\ \overline{F}_{\mathrm{Z}}(\varphi) \end{bmatrix} + \mathbf{T_2}(\theta_{i,j}(\varphi)) \begin{bmatrix} \rho\cos\lambda \\ \rho\sin\lambda \end{bmatrix}\end{aligned} \quad [1.51]$$

with

$$\mathbf{T}_2(\theta_{i,j}(\varphi)) = \sin({}^{\pi}\!/_{N}\,) \begin{bmatrix} A_{11}(\theta_{i,j}(\varphi)) & A_{12}(\theta_{i,j}(\varphi)) \\ A_{21}(\theta_{i,j}(\varphi)) & A_{22}(\theta_{i,j}(\varphi)) \\ A_{31}(\theta_{i,j}(\varphi)) & A_{32}(\theta_{i,j}(\varphi)) \end{bmatrix}$$

$$\begin{aligned}A_{11}(\theta_{i,j}(\varphi)) = \sum_{i,j} 2z_{i,j} \sin\gamma_{i,j} [&K_{\mathrm{T}} \cos\theta_{i,j}(\varphi) + K_{\mathrm{R}} \sin\kappa(z) \sin\theta_{i,j}(\varphi) \\ &+ K_{\mathrm{A}} \cos\kappa(z) \sin\theta_{i,j}(\varphi)]\end{aligned}$$

$$A_{12}(\theta_{i,j}(\varphi)) = \sum_{i,j} 2z_{i,j}\cos\gamma_{i,j}[K_{\mathrm{T}}\cos\theta_{i,j}(\varphi) + K_{\mathrm{R}}\sin\kappa(z)\sin\theta_{i,j}(\varphi) + K_{\mathrm{A}}\cos\kappa(z)\sin\theta_{i,j}(\varphi)]$$

$$A_{21}(\theta_{i,j}(\varphi)) = \sum_{i,j} 2z_{i,j}\sin\gamma_{i,j}[-K_{\mathrm{T}}\sin\theta_{i,j}(\varphi) + K_{\mathrm{R}}\sin\kappa(z)\cos\theta_{i,j}(\varphi) + K_{\mathrm{A}}\cos\kappa(z)\cos\theta_{i,j}(\varphi)]$$

$$A_{22}(\theta_{i,j}(\varphi)) = \sum_{i,j} 2z_{i,j}\cos\gamma_{i,j}[-K_{\mathrm{T}}\sin\theta_{i,j}(\varphi) + K_{\mathrm{R}}\sin\kappa(z)\cos\theta_{i,j}(\varphi) + K_{\mathrm{A}}\cos\kappa(z)\cos\theta_{i,j}(\varphi)]$$

$$A_{31}(\theta_{i,j}(\varphi)) = \sum_{i,j} 2z_{i,j}\sin\gamma_{i,j}[-K_{\mathrm{R}}\cos\kappa(z) + K_{\mathrm{A}}\sin\kappa(z)]$$

$$A_{32}(\theta_{i,j}(\varphi)) = \sum_{i,j} 2z_{i,j}\cos\gamma_{i,j}[-K_{\mathrm{R}}\cos\kappa(z) + K_{\mathrm{A}}\sin\kappa(z)]$$

$$\gamma_{i,j} = -\phi(z) - {}^{(2i-3)\pi}\!/_{N}$$

The first term of the right-hand side in equation [1.51] refers to a nominal component independent of cutter runout whereas the second term refers to the perturbation component due to cutter runout.

By combining equation [1.51] with equation [1.46], we can obtain

$$\mathbf{T_2}(\theta_{i,j}(\varphi))\begin{bmatrix}\rho\cos\lambda\\ \rho\sin\lambda\end{bmatrix} = \begin{bmatrix}F_{\mathrm{X}}(\varphi)\\ F_{\mathrm{Y}}(\varphi)\\ F_{\mathrm{Z}}(\varphi)\end{bmatrix} - \begin{bmatrix}\overline{F}_{\mathrm{X}}(\varphi)\\ \overline{F}_{\mathrm{Y}}(\varphi)\\ \overline{F}_{\mathrm{Z}}(\varphi)\end{bmatrix} \quad [1.52]$$

Obviously, with the measured cutting forces assigned to $F_{\mathrm{X}}(\varphi)$, $F_{\mathrm{Y}}(\varphi)$ and $F_{\mathrm{Z}}(\varphi)$ and the known values of K_{T}, K_{R} and K_{A} calibrated based on equation [1.46], cutter runout parameters ρ and λ can be evaluated

immediately by virtue of equation [1.52]. However, as the measured data often involve noise signals that may perturb $F_{\mathrm{X}}(\varphi)$, $F_{\mathrm{Y}}(\varphi)$ and $F_{\mathrm{Z}}(\varphi)$, the accuracy of ρ and λ may be strongly deteriorated if equation [1.52] is directly used. Moreover, since the cutter runout leads to a redistribution of the cutting forces over different tooth periods, it is necessary to choose the measured cutting forces in different tooth periods when solving ρ and λ. In this way, the influence of the noise signals may be weaken to the lower degree. To do this, the force component that has the largest peak value, e.g. $F_{\mathrm{Y}}(\varphi)$, is generally adopted.

Using equation [1.52] and F_{Y} at the cutter rotation angles $\varphi_i = \varphi + 2(i-1)/N$ (i=1, 2, ..., N), we can obtain

$$\mathbf{T_3}\begin{bmatrix} g_1 \\ g_2 \end{bmatrix} = \mathbf{F_0} \qquad [1.53]$$

with

$$\mathbf{T_3} = \begin{bmatrix} A_{21}(\theta_{i,j}(\varphi_1)) & A_{22}(\theta_{i,j}(\varphi_1)) \\ \vdots & \vdots \\ A_{21}(\theta_{i,j}(\varphi_i)) & A_{22}(\theta_{i,j}(\varphi_i)) \\ \vdots & \vdots \\ A_{21}(\theta_{i,j}(\varphi_N)) & A_{22}(\theta_{i,j}(\varphi_N)) \end{bmatrix}$$

$$g_1 = \rho\cos\lambda$$

$$g_2 = \rho\sin\lambda$$

$$\mathbf{F_0} = \begin{bmatrix} F_Y(\varphi_1) - \overline{F}_Y(\varphi) \\ \vdots \\ F_Y(\varphi_i) - \overline{F}_Y(\varphi) \\ \vdots \\ F_Y(\varphi_N) - \overline{F}_Y(\varphi) \end{bmatrix}$$

By means of the least square theory, g_1 and g_2 can be determined by

$$\begin{bmatrix} g_1 \\ g_2 \end{bmatrix} = \left[\mathbf{T_3^T T_3}\right]^{-1}\left[\mathbf{T_3^T F_0}\right] \qquad [1.54]$$

Therefore, it turns out that when $m = 1$, we have

$$\begin{aligned} &\lambda = \arctan(g_2/g_1) \\ &\rho = g_1/\cos\lambda \quad \text{or} \quad \rho = g_1/\sin\lambda \end{aligned} \qquad [1.55]$$

Note that the correct λ should give rise to a positive value of ρ. However, from the above procedure, we can see that a set of ρ and λ can be available for each value of cutter rotation angle. For this reason, the real set of runout parameter is selected to be such a one that minimizes the squared difference between the simulated and measured cutting forces at all sampling instants.

In the particular case of $N = 2$, $\mathbf{T_3^T T_3}$ will become singular in equation [1.54]. ρ and λ can be optimally selected to be those that satisfy equation [1.53] and minimize the squared difference between the simulated and measured cutting forces at all sampled instants. For a single flute cutter with $N = 1$, the cutting forces are not influenced by cutter runout.

1.3.1.3. *Selection of cutting parameters*

As stated above, the identification procedure of ρ and λ is based on the assumption of single tooth engagement (STE). That is, only one flute is in cut at any cutter rotation angle. This condition can be easily satisfied with a reasonable selection of radial depth of cut, a_e, and axial depth of cut, a_p. Critical values of a_e and a_p can be defined by the following cutting conditions: whenever the current tooth disengages from the workpiece, the next tooth has to be engaged with the workpiece immediately. This means that with critical a_e and a_p, any increase of a_e or a_p will lead to multiple teeth engagement (MTE), i.e. an engagement of at least two teeth simultaneously at some cutter rotation angles. For a general end mill, the condition of STE can be mathematically written as

$$\phi(a_p) - \phi(a_{pe}) + \frac{\pi}{2} + \arcsin\left(\frac{a_e - R_{cut}}{R_{cut}}\right) < \frac{2\pi}{N} \qquad [1.56]$$

where a_{pe} and R_{cut} are the pseudo axial depth of cut that is not engaged and the maximum radius of the cutting edge point that is engaged with the workpiece, respectively, as defined in Figure 1.2.

This is the critical condition characterizing the dependence between critical values of a_e and a_p. Critical conditions are now illustrated for a three-fluted flat end mill, three-fluted bull nose end mill and four-fluted ball end mill in Figures 1.13(a), (b) and (c). Equation [1.56] can be applied to design the experimental set-up for calibration of instantaneous cutting force coefficients. If the measured signals of the cutting forces are not bright enough to clearly identify the case of STE, we can appropriately reduce values of a_e or a_p.

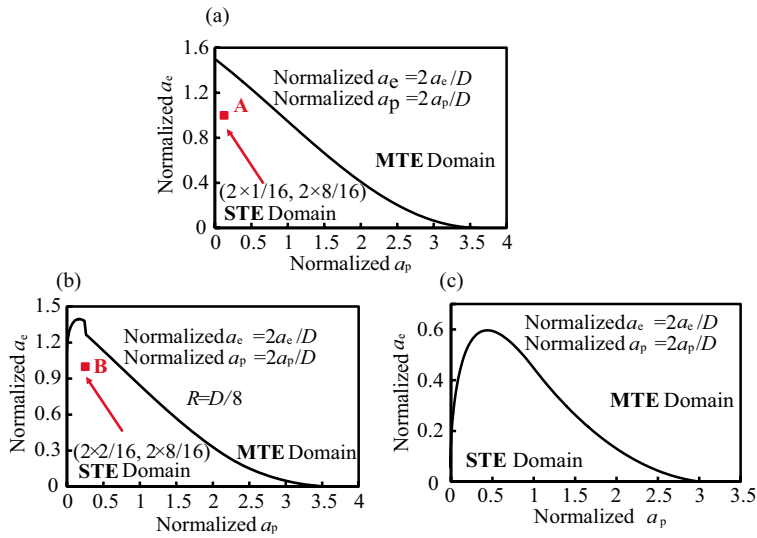

Figure 1.13. *Critical curves describing the engagement of a single flute; a) Three-fluted flat end mill with a helix angle of* $30°$*; b) Three-fluted bull nose end mill with a helix angle of* $30°$*; c) Four-fluted ball end mill with a helix angle of* $35°$

However, one must keep in mind that equation [1.56] is derived with the negligence of the cutter runout. Practically, if one tooth is engaged in cut with an immersed axial length more than its nominal value due to runout, there must be at least another tooth that will be in cut with an immersed axial length less than its nominal value after some cutter rotation angles. As a result, STE will appear. Therefore, as long as a_e and a_p satisfy equation [1.56], the cutting test is in the state of STE regardless of the cutter runout.

1.3.1.4. *Test applications*

To apply the above procedure, a series of cutting tests are performed in milling aluminum alloy 2618 with a vertical CNC milling machine. Three-component dynamometer Kistler 9255B is used to measure the cutting forces. A three-fluted carbide flat end mill with a diameter of 16mm and a helix angle of 30° is studied, respectively. A test with $a_p = 1$ mm, $a_e = 8$ mm and $f = 0.05$ mm/tooth is used to calibrate the cutting force coefficients as well as the runout parameters. The identified cutting force coefficients are plotted versus the instantaneous average chip thickness (IACT) $\overline{h}(\phi)$, as shown in Figure 1.14.

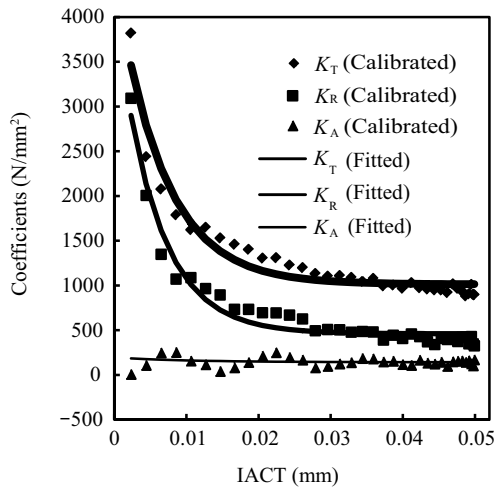

Figure 1.14. *Calibrated cutting force coefficients*

In Figure 1.14, we can see that an exponent-like relation exists between cutting force coefficients K_q (q = T, R or A) and $\overline{h}(\varphi)$. For this reason, the relationship between K_q and $\overline{h}(\varphi)$ is interpolated by the following nonlinear fitting function

$$K_q = W_{q1} + W_{q2} e^{[W_{q3}\overline{h}(\varphi)]}, \quad (q = \mathrm{T}, \mathrm{R} \text{ or } \mathrm{A}) \qquad [1.57]$$

where W_{q1}, W_{q2} and W_{q3} are constants determined by the fitting procedure. The fitted cutting force coefficients are also illustrated in Figure 1.14 for

comparison with calibrated discrete values. With fitted values of K_q, runout parameters ρ and λ are then identified. Results are: $\rho = 5$ μm and $\lambda = 60°$. Another test with $a_p = 1.3$ mm, $a_e = 8$ mm and $f = 0.1$ mm/tooth is used to verify the accuracy of calibrated cutting force model. From Figure 1.15, it can be seen that a good agreement exists between the predicted and measured cutting forces.

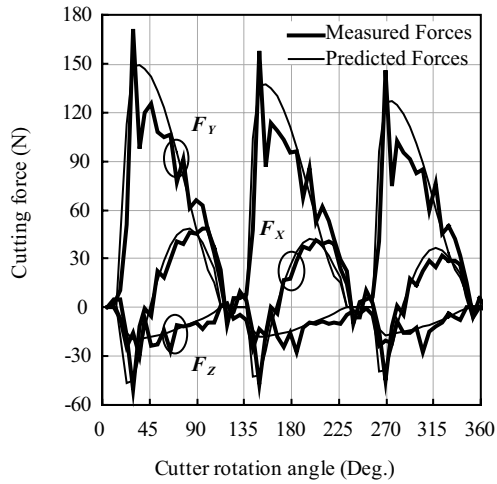

Figure 1.15. *Comparison of measured and predicted cutting forces*

1.3.2. *Calibration method in the frequency domain*

The cutting forces given in equation [1.8] are in the angle domain. Under the constant assumption of K_T and K_R, and $m = 1$ in equation [1.25], the cutting forces can be expanded as follows in frequency domain through convolution analysis [LIA 94]

$$\begin{bmatrix} F_X(\varphi) \\ F_Y(\varphi) \end{bmatrix} = \sum_{k=-\infty}^{+\infty} \left\{ \begin{bmatrix} \mathbf{A}_X[Nk] \\ \mathbf{A}_Y[Nk] \end{bmatrix} e^{JNk\varphi} + \begin{bmatrix} \mathbf{A}_{XO}[Nk+1] \\ \mathbf{A}_{YO}[Nk+1] \end{bmatrix} e^{J(Nk+1)\varphi} + \begin{bmatrix} \mathbf{A}_{XO}[Nk-1] \\ \mathbf{A}_{YO}[Nk-1] \end{bmatrix} e^{J(Nk-1)\varphi} \right\} \quad [1.58]$$

with

$$\begin{bmatrix}\mathbf{A}_{\mathrm{X}}[Nk]\\ \mathbf{A}_{\mathrm{Y}}[Nk]\end{bmatrix}=\frac{N}{2\pi}\begin{bmatrix}-K_{\mathrm{T}} & -K_{\mathrm{R}}\\ -K_{\mathrm{R}} & K_{\mathrm{T}}\end{bmatrix}\mathbf{P}_{\mathrm{e}}(Nk)CWD(Nk)$$

$$\begin{bmatrix}\mathbf{A}_{\mathrm{XO}}[Nk+1]\\ \mathbf{A}_{\mathrm{YO}}[Nk+1]\end{bmatrix}=\frac{N}{2\pi}J\rho\sin\frac{\pi}{N}e^{-J(\lambda+\frac{\pi}{N})}\begin{bmatrix}-K_{\mathrm{T}} & -K_{\mathrm{R}}\\ -K_{\mathrm{R}} & K_{\mathrm{T}}\end{bmatrix}\mathbf{P}_{\mathrm{o}}(Nk+1)CWD(Nk)$$

$$\begin{bmatrix}\mathbf{A}_{\mathrm{XO}}[Nk-1]\\ \mathbf{A}_{\mathrm{YO}}[Nk-1]\end{bmatrix}=-\frac{N}{2\pi}J\rho\sin\frac{\pi}{N}e^{J(\lambda+\frac{\pi}{N})}\begin{bmatrix}-K_{\mathrm{T}} & -K_{\mathrm{R}}\\ -K_{\mathrm{R}} & K_{\mathrm{T}}\end{bmatrix}\mathbf{P}_{\mathrm{o}}(Nk-1)CWD(Nk)$$

$$CWD(Nk)=\frac{D\sin\frac{Nka_{\mathrm{p}}\tan\beta}{D}}{Nk\tan\beta}e^{-JNk\frac{a_{\mathrm{p}}\tan\beta}{D}}$$

$$\mathbf{P}_{\mathrm{e}}(Nk)=\begin{bmatrix}P_1[Nk]\\ P_2[Nk]\end{bmatrix}=f\int_{\theta_{\mathrm{en}}}^{\theta_{\mathrm{ex}}}\begin{bmatrix}\sin\theta\cos\theta\\ \sin^2\theta\end{bmatrix}e^{-JNk\theta}d\theta$$

$$\mathbf{P}_{\mathrm{o}}(Nk)=\begin{bmatrix}P_3[Nk]\\ P_4[Nk]\end{bmatrix}=\int_{\theta_{\mathrm{en}}}^{\theta_{\mathrm{ex}}}\begin{bmatrix}\cos\theta\\ \sin\theta\end{bmatrix}e^{-JNk\theta}d\theta$$

where $\mathbf{A}_s[Nk]$, $\mathbf{A}_{s\mathrm{O}}[Nk+1]$ and $\mathbf{A}_{s\mathrm{O}}[Nk-1]$ ($s=\mathrm{X},\mathrm{Y}$) are the parameters related to the harmonics of the cutting forces predicted by equation [1.16]. J is unity of imaginary number.

In this section, the convolution theory-based method is described for the identification of the cutting force coefficients and radial cutter runout parameters, i.e. ρ and λ defined in Figure 1.5, for flat end mill. Details are explained and listed as follows.

$F_{\mathrm{X}}(\varphi)$ and $F_{\mathrm{Y}}(\varphi)$ can be expressed as

$$\begin{bmatrix}F_{\mathrm{X}}(\varphi)\\ F_{\mathrm{Y}}(\varphi)\end{bmatrix}=\begin{bmatrix}H_1(\varphi) & H_2(\varphi)\\ -H_2(\varphi) & H_1(\varphi)\end{bmatrix}\begin{bmatrix}K_{\mathrm{T}}\\ K_{\mathrm{R}}\end{bmatrix} \qquad [1.59]$$

with

$$\begin{aligned}H_1(\varphi)&=-\sum_{i,j}z_{i,j}h_{i,j}(\varphi)\cos\theta_{i,j}(\varphi)\\ H_2(\varphi)&=-\sum_{i,j}z_{i,j}h_{i,j}(\varphi)\sin\theta_{i,j}(\varphi)\end{aligned} \qquad [1.60]$$

The Fourier series expansion of equation [1.59] can be written as

$$\begin{bmatrix} F_{\mathrm{X}}(\varphi) \\ F_{\mathrm{Y}}(\varphi) \end{bmatrix} = \left\{ \sum_{\omega=-\infty}^{+\infty} \begin{bmatrix} \mathrm{Q}_1[\omega] & \mathrm{Q}_2[\omega] \\ -\mathrm{Q}_2[\omega] & \mathrm{Q}_1[\omega] \end{bmatrix} e^{J\omega\varphi} \right\} \begin{bmatrix} K_{\mathrm{T}} \\ K_{\mathrm{R}} \end{bmatrix} \quad [1.61]$$

where $\mathrm{Q}_1[\omega]$ and $\mathrm{Q}_2[\omega]$ are the Fourier Transformations of $H_1(\varphi)$ and $H_2(\varphi)$, respectively. Based on equation [1.58], the measured cutting forces $F_s^{\mathrm{M}}(\varphi)$ (s=X, Y) can be expanded as follows using Discrete Fourier Transformation.

$$\begin{bmatrix} F_{\mathrm{X}}^{\mathrm{M}}(\varphi) \\ F_{\mathrm{Y}}^{\mathrm{M}}(\varphi) \end{bmatrix} = \sum_{k=-\infty}^{+\infty} \left\{ \begin{bmatrix} \mathbf{A}_{\mathrm{X}}^{\mathrm{M}}[Nk] \\ \mathbf{A}_{\mathrm{Y}}^{\mathrm{M}}[Nk] \end{bmatrix} e^{JNk\varphi} + \begin{bmatrix} \mathbf{A}_{\mathrm{XO}}^{\mathrm{M}}[Nk+1] \\ \mathbf{A}_{\mathrm{YO}}^{\mathrm{M}}[Nk+1] \end{bmatrix} e^{J(Nk+1)\varphi} + \begin{bmatrix} \mathbf{A}_{\mathrm{XO}}^{\mathrm{M}}[Nk-1] \\ \mathbf{A}_{\mathrm{YO}}^{\mathrm{M}}[Nk-1] \end{bmatrix} e^{J(Nk-1)\varphi} \right\} \quad [1.62]$$

By combining equation [1.61] with equation [1.62] at $\omega = Nk$, the following relation can be obtained

$$\mathbf{B}[K_{\mathrm{T}}, K_{\mathrm{R}}]^{\mathrm{T}} = \mathbf{b} \quad [1.63]$$

with

$$\mathbf{b} = \left[\mathrm{Re}(\mathbf{A}_{\mathrm{X}}^{\mathrm{M}}[Nk]), \mathrm{Im}(\mathbf{A}_{\mathrm{X}}^{\mathrm{M}}[Nk]), \mathrm{Re}(\mathbf{A}_{\mathrm{Y}}^{\mathrm{M}}[Nk]), \mathrm{Im}(\mathbf{A}_{\mathrm{Y}}^{\mathrm{M}}[Nk])\right]^{\mathrm{T}}$$

$$\mathbf{B} = \begin{bmatrix} \mathrm{Re}\,(\mathrm{Q}_1[Nk]) & \mathrm{Re}\,(\mathrm{Q}_2[Nk]) \\ \mathrm{Im}\,(\mathrm{Q}_1[Nk]) & \mathrm{Im}\,(\mathrm{Q}_2[Nk]) \\ -\mathrm{Re}\,(\mathrm{Q}_2[Nk]) & \mathrm{Re}\,(\mathrm{Q}_1[Nk]) \\ -\mathrm{Im}\,(\mathrm{Q}_2[Nk]) & \mathrm{Im}\,(\mathrm{Q}_1[Nk]) \end{bmatrix} \quad [1.64]$$

where Re(*) and Im(*) indicate the real and imaginary parts of a complex number.

With the aid of equations [1.58] and [1.62], K_{T}, K_{R}, ρ and λ can be obtained using the method proposed by Liang and Wang [LIA 94].

$$\begin{bmatrix} K_T \\ K_R \end{bmatrix} = \begin{bmatrix} -P_1(0) & -P_2(0) \\ P_2(0) & -P_1(0) \end{bmatrix}^{-1} \begin{bmatrix} \mathbf{A}_{\mathrm{X}}^{\mathrm{M}}[0] \\ \mathbf{A}_{\mathrm{Y}}^{\mathrm{M}}[0] \end{bmatrix} \begin{bmatrix} \frac{N}{2\pi} CWD(0) \end{bmatrix}^{-1}$$

$$\rho = \frac{\left|\mathbf{A}_{\mathrm{YO}}^{\mathrm{M}}[1]\right|}{\sin(\pi/N)(N/2\pi)a_{\mathrm{p}}\left|K_{\mathrm{T}}P_4(1) - K_{\mathrm{R}}P_3(1)\right|} \qquad [1.65]$$

$$\lambda = \frac{\pi}{2} - \frac{\pi}{N} - \angle\mathbf{A}_{\mathrm{YO}}^{\mathrm{M}}[1] + \angle[K_{\mathrm{T}}P_4(1) - K_{\mathrm{R}}P_3(1)]$$

Details of this method and the definitions of $P_1(0)$, $P_2(0)$, $CWD(0)$, $P_3(1)$ and $P_4(1)$, are given in [LIA 94].

The accuracy of equation [1.65] relies on the following two preconditions:

– the medial parameters involved in equation [1.62], e.g. $\mathbf{A}_{\mathrm{X}}^{\mathrm{M}}[Nk]$, $\mathbf{A}_{\mathrm{Y}}^{\mathrm{M}}[Nk]$, $\mathbf{A}_{\mathrm{YO}}^{\mathrm{M}}[Nk+1]$, etc., depend on the entry and exit angles, i.e. θ_{en} and θ_{ex}, which are calculated using equation [1.32] derived with nominal cutting parameters;

– it is derived by assuming that $m = 1$.

However, the occurrence of cutter runout will greatly affect the actual cutting radius as well as θ_{en} and θ_{ex}. This means that the above two preconditions are not strictly satisfied when runout occurs. As a result, some accuracy will be lost if equation [1.65] is directly used. Note that, the larger the value of ρ, the greater the inaccuracy. To improve the calibration accuracy of equation [1.65], a new method is presented below.

With the aid of equation [1.63], an optimal selection procedure can be used to determine K_q ($q = \mathrm{T},\ \mathrm{R}$), ρ and λ according to the following steps:

Step 1: Set $\rho = \rho_0$ and $\lambda = \lambda_0$. ρ_0 and λ_0 are initially set by using equation [1.65].

Step 2: Calculate $h_{i,j}(\varphi)$ by

$$h_{i,j}(\varphi) = \min_{m=1\ to\ N} \{h_{i,j}(\varphi) = mf\sin\theta_{i,j}(\varphi) + r_{i,j} - r_{i-m,j}\} \qquad [1.66]$$

where $r_{i,j}$ and $r_{i-m,j}$ are obtained by equation [1.18].

Step 3: Calculate $\mathrm{Q}_1[\omega]$ and $\mathrm{Q}_2[\omega]$ based on equations [1.60] and [1.66].

Step 4: Calculate $\mathbf{B}$ using equation [1.64]. Then, by using the linear least square method, K_T and K_R can be immediately obtained by

$$\begin{bmatrix} K_\mathrm{T} \\ K_\mathrm{R} \end{bmatrix} = \left(\mathbf{B}^\mathrm{T}\mathbf{B}\right)^{-1}\mathbf{B}^\mathrm{T}\mathbf{b} \qquad [1.67]$$

Step 5: Substitute K_T and K_R obtained from equation [1.67] into equation [1.59]. Then, calculate the minimum square deviation $\delta(\rho,\lambda)$ between $F_s^\mathrm{M}(\varphi)$ and $F_s(\varphi)$ ($s = \mathrm{X}, \mathrm{Y}$) by

$$\delta(\rho,\lambda) = \sum_{\varphi=0}^{2\pi}\left(\left|F_\mathrm{X}^\mathrm{M}(\varphi) - F_\mathrm{X}(\varphi)\right|^2 + \left|F_\mathrm{Y}^\mathrm{M}(\varphi) - F_\mathrm{Y}(\varphi)\right|^2\right) \qquad [1.68]$$

Step 6: If $\delta(\rho,\lambda)$ achieves the level of minimum among all cases of different ρ and λ, set K_T and K_R, ρ and λ as the final results of cutting force coefficients and runout parameters. Otherwise, repeat the above Steps 2 to 6 by setting ρ and λ to other values ρ_* and λ_*.

The key issue of the above steps is to optimally select ρ_* and λ_*. Generally, for every possible pairs of ρ_* and λ_* with $\rho_{\min} \le \rho_* \le \rho_{\max}$ and $\lambda_{\min} \le \lambda_* \le \lambda_{\max}$, Step 2 to Step 6 will be performed. Here, $\rho_{\max}$ and $\rho_{\min}$ denote the maximum and minimum possible values of ρ_*; $\lambda_{\max}$ and $\lambda_{\min}$ denote the maximum and minimum possible values of λ_*. The case which has the minimum $\delta(\rho,\lambda)$ corresponds to the final result.

Obviously, this parametric study must sweep all cases in the feasible domain. To increase the computing efficiency, an automatical searching procedure will be described here.

The key is to approximately develop the explicit expressions that relate ρ and λ to $F_s^\mathrm{M}(\varphi)$ and $F_s(\varphi)$. For this reason, it is interesting to study the following test case. The distributions of $|\mathbf{A}_\mathrm{Y}[1]|$ and $\angle\mathbf{A}_\mathrm{Y}[1]$ vs. ρ and λ are considered. $\mathbf{A}_\mathrm{Y}[1]$ is obtained from $F_\mathrm{Y}(\varphi)$ using the Fourier transformation.

$F_{\mathrm{Y}}(\varphi)$ should be calculated from Step 5 for every selected set of ρ and λ. ρ and λ are chosen to vary from $10^{-6}\mu\mathrm{m}$ to 35 $\mu\mathrm{m}$ and from 40° to 60°, respectively. The simulation results are shown in Figure 1.16. It can be found that both $|\mathbf{A}_{\mathrm{Y}}[1]|$ and $\angle\mathbf{A}_{\mathrm{Y}}[1]$ are approximately distributed in a planar surface over the considered region. This phenomenon indicates that $|\mathbf{A}_{\mathrm{Y}}[1]|$ and $\angle\mathbf{A}_{\mathrm{Y}}[1]$ can be locally treated as linear functions of ρ and λ. The same observations can also be made in other cutting conditions and regions of ρ and λ. Thus, following relations hold.

$$\begin{aligned} |\mathbf{A}_{\mathrm{Y}}[1]| &= E_{11}\rho + E_{12}\lambda + E_{13} \\ \angle\mathbf{A}_{\mathrm{Y}}[1] &= E_{21}\rho + E_{22}\lambda + E_{23} \end{aligned} \tag{1.69}$$

where $E_{uv}\,(u = 1, 2, v = 1, 2, 3)$ are unknown coefficients that can be determined using the finite difference scheme in the following way.

$$\begin{aligned} E_{11} &= (|\mathbf{A}_{\mathrm{Y}}[1]|_3 - |\mathbf{A}_{\mathrm{Y}}[1]|_1)/\Delta\rho_1 \\ E_{12} &= (|\mathbf{A}_{\mathrm{Y}}[1]|_2 - |\mathbf{A}_{\mathrm{Y}}[1]|_1)/\Delta\lambda_1 \\ E_{13} &= |\mathbf{A}_{\mathrm{Y}}[1]|_1 - (E_{11}\rho_1 + E_{12}\lambda_1) \\ E_{21} &= [(\angle\mathbf{A}_{\mathrm{Y}}[1])_3 - (\angle\mathbf{A}_{\mathrm{Y}}[1])_1]/\Delta\rho_1 \\ E_{22} &= [(\angle\mathbf{A}_{\mathrm{Y}}[1])_2 - (\angle\mathbf{A}_{\mathrm{Y}}[1])_1]/\Delta\lambda_1 \\ E_{23} &= (\angle\mathbf{A}_{\mathrm{Y}}[1])_1 - (E_{21}\rho_1 + E_{22}\lambda_1) \end{aligned} \tag{1.70}$$

where ρ_1, λ_1 is a set of selected values satisfying $\rho_{\min} \le \rho_1, \rho_2 \le \rho_{\max}$ and $\lambda_{\min} \le \lambda_1, \lambda_2 \le \lambda_{\max}$. Assume that $\rho_2 = \rho_1 + \Delta\rho_1$, $\lambda_2 = \lambda_1 + \Delta\lambda_1$. With the aid of Steps 2 to 5, we can obtain $|\mathbf{A}_{\mathrm{Y}}[1]|_1$ and $(\angle\mathbf{A}_{\mathrm{Y}}[1])_1$ related to ρ_1 and λ_1. $|\mathbf{A}_{\mathrm{Y}}[1]|_2$ and $(\angle\mathbf{A}_{\mathrm{Y}}[1])_2$ related to ρ_1 and λ_2, $|\mathbf{A}_{\mathrm{Y}}[1]|_3$ and $(\angle\mathbf{A}_{\mathrm{Y}}[1])_3$ related to ρ_2 and λ_1.

Now, ρ_* and λ_* can be easily obtained by relating equation [1.69] to the experimental values of $\left|\mathrm{A}_{\mathrm{Y}}^{\mathrm{M}}[1]\right|$ and $\angle\mathrm{A}_{\mathrm{Y}}^{\mathrm{M}}[1]$ through

$$\begin{bmatrix} \rho_* \\ \lambda_* \end{bmatrix} = \begin{bmatrix} E_{11} & E_{12} \\ E_{21} & E_{22} \end{bmatrix}^{-1} \begin{bmatrix} \mathrm{A}_{\mathrm{Y}}^{\mathrm{M}}[1] - E_{13} \\ \angle\mathrm{A}_{\mathrm{Y}}^{\mathrm{M}}[1] - E_{23} \end{bmatrix} \tag{1.71}$$

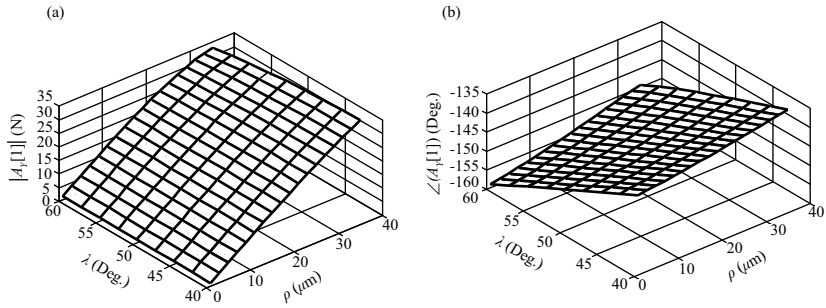

Figure 1.16. *Distribution of* $|\mathbf{A}_Y[1]|$ *and* $\angle\mathbf{A}_Y[1]$ *v.s.* ρ *and* λ*; a)* $|\mathbf{A}_Y[1]|$ *v.s.* ρ *and* λ*; b)* $\angle\mathbf{A}_Y[1]$ *v.s.* ρ *and* λ

It is worth noting that as $|\mathbf{A}_Y[1]|$ and $\angle\mathbf{A}_Y[1]$ are linearly approximated over a local region, it is necessary to update the approximation on the new design point in an iterative way. This means that the coefficients E_{uv} involved in equation [1.70] need to be re-evaluated iteratively. As a result, $K_q\,(q = \mathrm{T},\ \mathrm{R})$, ρ and λ should be iteratively determined according to the following steps:

Step a: Set $\rho_1 = \rho_0$ and $\lambda_1 = \lambda_0$.

Step b: Calculate E_{uv} by means of equation [1.70].

Step c: Calculate ρ_* and λ_* using equation [1.71].

Step d: Set $\rho = \rho_*$ and $\lambda = \lambda_*$. Then, repeat Steps 2 to 5.

Step e: If the error between two iterative results of $\delta(\rho, \lambda)$ attains the prescribed tolerance, stop the iteration. Otherwise, repeat the above Steps b to e by attributing ρ_* and λ_* to ρ_1 and λ_1.

1.3.3. *Calibration method involving four cutter runout parameters*

This method is mainly developed for the cutting force model, in which the cutting force coefficients are expressed as the exponential function of the

instantaneous uncut chip thickness. That is, the elemental cutting forces related to the *j*th disk element of the *i*th flute are expressed as

$$\begin{aligned} F_{\mathrm{T},i,j}(\varphi) &= K_{\mathrm{T}} h_{i,j}(\varphi) z_{i,j} \\ F_{\mathrm{R},i,j}(\varphi) &= K_{\mathrm{R}} h_{i,j}(\varphi) z_{i,j} \\ F_{\mathrm{A},i,j}(\varphi) &= K_{\mathrm{A}} h_{i,j}(\varphi) z_{i,j} \end{aligned} \quad [1.72]$$

with

$$\begin{aligned} K_{\mathrm{T}} &= k_{\mathrm{T}} [h_{i,j}(\varphi)]^{-m_{\mathrm{T}}} \\ K_{\mathrm{R}} &= k_{\mathrm{R}} [h_{i,j}(\varphi)]^{-m_{\mathrm{R}}} \\ K_{\mathrm{A}} &= k_{\mathrm{A}} [h_{i,j}(\varphi)]^{-m_{\mathrm{A}}} \end{aligned} \quad [1.73]$$

where k_{T}, k_{R}, k_{A}, m_{T}, m_{R} and m_{A} are constants required to be determined from experiments.

Total cutting force components at cutter rotation angle φ can be obtained by

$$\begin{bmatrix} F_{\mathrm{X}}(\varphi) \\ F_{\mathrm{Y}}(\varphi) \\ F_{\mathrm{Z}}(\varphi) \end{bmatrix} = \sum_{i,j} \left\{ \mathbf{T}_{i,j}(\varphi) \begin{bmatrix} F_{\mathrm{T},i,j} \\ F_{\mathrm{R},i,j} \\ F_{\mathrm{Z},i,j} \end{bmatrix} \right\} \quad [1.74]$$

with

$$\mathbf{T}_{i,j}(\varphi) = \begin{bmatrix} -\cos\theta_{i,j}(\varphi) & -\sin\theta_{i,j}(\varphi) & 0 \\ \sin\theta_{i,j}(\varphi) & -\cos\theta_{i,j}(\varphi) & 0 \\ 0 & 0 & 1 \end{bmatrix} \quad [1.75]$$

It should be noted that $h_{i,j}(\varphi)$ is calculated by equations [1.9] and [1.25], in which the calculation of the actual radius $r_{i,j}$ of the circular tooth path includes the influence of cutter runout. In this section, two types of cutter runout models, i.e. radial and tilt cutter runout models, will be involved to reveal this effect:

– *radial cutter runout model*: its geometrical definition is given in section 1.2.1. In this model, $r_{i,j}$ can be calculated by using equation [1.18];

– *tilt cutter runout model*: in this model, the actual installation state of the cutter is considered. That is, besides axis offset, there exists more or less axis tilt after the cutter is completely amounted in spindle, as shown in Figure 1.17. The geometry of this kind of cutter runout is characterized by four parameters, i.e. ρ_{T}, λ_{T}, τ_{T} and ϑ. Here, ρ_{T} and τ_{T} are the axial offset and tilt angle between the cutter axis and the centerline of the spindle, respectively. λ_{T} is the location angle measured as the angle between the direction of the offset and the tip of the nearest tooth (tooth 1). ϑ is the locating angle of tilt, which is defined as the angle between the direction of axis tilt and the direction of axial offset ρ_{T}. Note that L labeled in Figure 1.17 means the cantilevered length of cutter after installation. As shown in Figure 1.17, tilt cutter runout makes $r_{i,j}$ change from $\overline{\mathrm{AF}}$ to $\overline{\mathrm{OF}}$. Under this understanding, $r_{i,j}$ can be calculated by

$$r_{i,j} = \{\rho_{\mathrm{T}}^2 + r_{\mathrm{n},i,j}^2 + (L - jz_{i,j})^2 \sin^2\tau_{\mathrm{T}} + 2r_{\mathrm{n},i,j}\rho_{\mathrm{T}}\cos(-\lambda_{\mathrm{T}} + \phi(z) + \frac{2(i-1)\pi}{N}) + 2((L - jz_{i,j})\sin\tau_{\mathrm{T}}[\rho_{\mathrm{T}}\cos(\phi) + r_{\mathrm{n},i,j}\cos(\vartheta - \lambda_{\mathrm{T}} + \phi(z) + \frac{2(i-1)\pi}{N})])\}^{\frac{1}{2}} \quad [1.76]$$

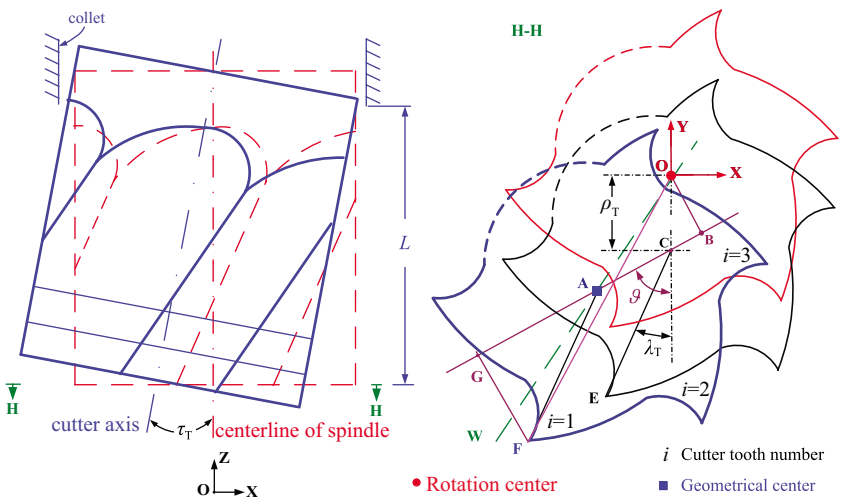

Figure 1.17. *Definition of tilt cutter runout. For a color version of this figure, see www.iste.co.uk/zhang/milling.zip*

By using the cutting forces measured from two milling tests, which satisfy the following two conditions, a new scheme will be proposed for calibrating the values of k_q, m_q (q=T, R, A) and ρ_{T}, λ_{T}, τ_{T} and ϑ:

– radial and axial depths of cut of the first test, i.e. a_{e} and a_{p}, should satisfy equation [1.56] so that only one tooth is in contact with the workpiece at any cutter rotation angle φ. At the same time, a_{p} should be so small that $z_{i,j}$ can be set to be a_{p};

– a_{p} of the second test should be large enough, and generally it can be set to be the value greater than D. At the same time, a_{e} should be relatively small so that the cutter cannot be broken under the combination of a_{e} and a_{p}.

Because a_{p} in the first test is small, its cutter runout state in the range of $0-a_{\mathrm{p}}$ along the cutter axis can be approximately treated as a radial cutter runout model. Consequently, the first test is adopted to calibrate k_q, m_q ($q=$T, R, A) and ρ, λ. Then, ρ_{T}, λ_{T}, τ_{T} and ϑ are calibrated based on the second test and the calibrated results from the first test. Detailed procedures are as follows.

1.3.3.1. *Calibration of k_q, m_q ($q=T,R,A$) and ρ, λ*

Under the cutting condition of the first test, the cutting forces acting on the *i*th flute at an arbitrary cutter rotation angle φ constitute the total forces of the cutter. With this idea in mind, one can have

$$\begin{aligned} a_{\mathrm{p}}\begin{bmatrix} k_{\mathrm{T}}[h_{i,1}(\varphi)]^{1-m_{\mathrm{T}}} \\ k_{\mathrm{R}}[h_{i,1}(\varphi)]^{1-m_{\mathrm{R}}} \\ k_{\mathrm{A}}[h_{i,1}(\varphi)]^{1-m_{\mathrm{A}}} \end{bmatrix} &= [\mathbf{T}_{i,1}(\varphi)]^{-1}\begin{bmatrix} F_{\mathrm{X}}^{\mathrm{M}}(\varphi) \\ F_{\mathrm{Y}}^{\mathrm{M}}(\varphi) \\ F_{\mathrm{A}}^{\mathrm{M}}(\varphi) \end{bmatrix} \\ &\triangleq \begin{bmatrix} F_{\mathrm{T},i,1}^{\mathrm{M}}(\varphi) \\ F_{\mathrm{R},i,1}^{\mathrm{M}}(\varphi) \\ F_{\mathrm{A},i,1}^{\mathrm{M}}(\varphi) \end{bmatrix} \end{aligned} \qquad [1.77]$$

With the aids of equation [1.77], k_q and m_q (q = T, R, A), ρ_1 and λ_1 can be determined following the steps below:

Step 1: Set $r=0$ and set $\rho^{(r)}=\rho_*$ and $\lambda^{(r)}=\lambda_*$. ρ_* and λ_* are the initially selected values. Practically, ρ_* and λ_* can be set to be the values close to zero. Here, r means the iteration step number.

Step 2: Calculate $h_{i,1}^{(r)}(\varphi_k)$ for all cutter rotation angle φ_k $\left(k = 1,\ 2,\ \ldots,\ N_{\text{sp}}\right)$ related to all sampled cutting forces. N_{sp} is the number of sampling points.

$$h_{i,1}^{(r)}(\varphi_k) = \min_{m=1}^{N} \left\{ mf \sin\theta_{i,1}(\varphi_k) + r_{i,1}^{(r)} - r_{i-m,1}^{(r)} \right\} \qquad [1.78]$$

where $r_{i,1}^{(r)}$ is calculated by equation [1.18].

Step 3: Establish the following relationship based on equations [1.77] and [1.78].

$$\mathbf{B}[k_{\text{t}}, m_{\text{T}}, k_{\text{r}}, m_{\text{R}}, k_{\text{a}}, m_{\text{A}}]^{\text{T}} = \mathbf{b} \qquad [1.79]$$

with $k_{\text{t}} = \ln(k_{\text{T}})$,$k_{\text{r}} = \ln(k_{\text{R}})$,$k_{\text{a}} = \ln(k_{\text{A}})$

$$\mathbf{B} = \begin{bmatrix}
1 & \ln[h_{i,1}^{(r)}(\varphi_1)] & 0 & 0 & 0 & 0 \\
1 & \ln[h_{i,1}^{(r)}(\varphi_2)] & 0 & 0 & 0 & 0 \\
\vdots & \vdots & \vdots & \vdots & \vdots & \vdots \\
1 & \ln[h_{i,1}^{(r)}(\varphi_{N_{\text{sp}}})] & 0 & 0 & 0 & 0 \\
0 & 0 & 1 & \ln[h_{i,1}^{(r)}(\varphi_1)] & 0 & 0 \\
0 & 0 & 1 & \ln[h_{i,1}^{(r)}(\varphi_2)] & 0 & 0 \\
\vdots & \vdots & \vdots & \vdots & \vdots & \vdots \\
0 & 0 & 1 & \ln[h_{i,1}^{(r)}(\varphi_{N_{\text{sp}}})] & 0 & 0 \\
0 & 0 & 0 & 0 & 1 & \ln[h_{i,1}^{(r)}(\varphi_1)] \\
0 & 0 & 0 & 0 & 1 & \ln[h_{i,1}^{(r)}(\varphi_2)] \\
\vdots & \vdots & \vdots & \vdots & \vdots & \vdots \\
0 & 0 & 0 & 0 & 1 & \ln[h_{i,1}^{(r)}(\varphi_{N_{\text{sp}}})]
\end{bmatrix} \qquad [1.80]$$

$$\mathbf{b}=\begin{bmatrix}\ln[F^{\mathrm{M}}_{\mathrm{T},i,1}(\varphi_1)]-\ln[h^{(r)}_{i,1}(\varphi_1)]-\ln(a_{\mathrm{p}})\\ \ln[F^{\mathrm{M}}_{\mathrm{T},i,1}(\varphi_2)]-\ln[h^{(r)}_{i,1}(\varphi_2)]-\ln(a_{\mathrm{p}})\\ \vdots\\ \ln[F^{\mathrm{M}}_{\mathrm{T},i,1}(\varphi_{N_{\mathrm{sp}}})]-\ln[h^{(r)}_{i,1}(\varphi_{N_{\mathrm{sp}}})]-\ln(a_{\mathrm{p}})\\ \ln[F^{\mathrm{M}}_{\mathrm{R},i,1}(\varphi_1)]-\ln[h^{(r)}_{i,1}(\varphi_1)]-\ln(a_{\mathrm{p}})\\ \ln[F^{\mathrm{M}}_{\mathrm{R},i,1}(\varphi_2)]-\ln[h^{(r)}_{i,1}(\varphi_2)]-\ln(a_{\mathrm{p}})\\ \vdots\\ \ln[F^{\mathrm{M}}_{\mathrm{R},i,1}(\varphi_{N_{\mathrm{sp}}})]-\ln[h^{(r)}_{i,1}(\varphi_{N_{\mathrm{sp}}})]-\ln(a_{\mathrm{p}})\\ \ln[F^{\mathrm{M}}_{\mathrm{A},i,1}(\varphi_1)]-\ln[h^{(r)}_{i,1}(\varphi_1)]-\ln(a_{\mathrm{p}})\\ \ln[F^{\mathrm{M}}_{\mathrm{A},i,1}(\varphi_2)]-\ln[h^{(r)}_{i,1}(\varphi_2)]-\ln(a_{\mathrm{p}})\\ \vdots\\ \ln[F^{\mathrm{M}}_{\mathrm{A},i,1}(\varphi_{N_{\mathrm{sp}}})]-\ln[h^{(r)}_{i,1}(\varphi_{N_{\mathrm{sp}}})]-\ln(a_{\mathrm{p}})\end{bmatrix} \quad [1.81]$$

where $\ln(*)$ indicates the natural logarithm operation. Note that if $h^{(r)}_{i,1}(\varphi_k)=0$ or $F^{\mathrm{M}}_{q,i,1}(\varphi_k)<0$, the corresponding row should be canceled from equation [1.79]

Step 4: Determine k_{T}, m_{T}, k_{R}, m_{R}, k_{A} and m_{A} by

$$\begin{aligned}&[k_{\mathrm{t}},m_{\mathrm{T}},k_{\mathrm{r}},m_{\mathrm{R}},k_{\mathrm{a}},m_{\mathrm{A}}]^{\mathrm{T}}=\left(\mathbf{B}^{\mathrm{T}}\mathbf{B}\right)^{-1}\mathbf{B}^{\mathrm{T}}\mathbf{b}\\ &k_{\mathrm{T}}=e^{k_{\mathrm{t}}},k_{\mathrm{R}}=e^{k_{\mathrm{r}}},k_{\mathrm{A}}=e^{k_{\mathrm{a}}}\end{aligned} \quad [1.82]$$

Step 5: Substitute k_q and m_q obtained from equation [1.82] into equation [1.74]. Then, calculate $\Delta^{(r)}$ by

$$\Delta^{(r)}=\sum_{s=\mathrm{X,Y,Z}}\sum_{k=1}^{N_{\mathrm{sp}}}\left|F^{\mathrm{M}}_{s}(\varphi_k)-F_s(\varphi_k)\right|^2 \quad [1.83]$$

Step 6: If $\Delta^{(r)}$ achieves the level of minimum among all cases of $\rho^{(r)}$ and $\lambda^{(r)}$, set k_q, m_q, $\rho^{(r)}$ and $\lambda^{(r)}$ as the final results of cutting force coefficients

and radial cutter runout parameters ρ and λ. Otherwise, repeat the above Step 2 to Step 6 by setting $\rho^{(r)}$ and $\lambda^{(r)}$ to other values.

To increase the computing efficiency, an optimization algorithm, i.e. the Nelder-Mead simplex method [LAG 98, NEL 65], is adopted to select the best $\rho^{(r)}$ and $\lambda^{(r)}$ without the requirements of calculating the numerical or analytic gradients. The major idea about this algorithm is as follows. An initial simplex is firstly constructed. Then at each step of the search, a new point in or near the current simplex is generated. The function value at the new point is compared with the function's values at the vertices of the simplex and, usually, one of the vertices is replaced by the new point, giving a new simplex. This step is repeated until the diameter of the simplex is less than the specified tolerance. For details about this algorithm, one can refer to [LAG 98, NEL 65].

It is worth noting that in the above procedure a_{p} should be generally in the interval of [1 mm, 2 mm]. If a_{p} is too large, it can not be approximated by one disk element. If a_{p} is too small, $F_s^{\mathrm{M}}(\varphi)$ (s=X,Y,Z) will be greatly influenced by the noise signals. As a result, equation [1.77] may lose validity.

1.3.3.2. *Calibration of ρ_{T}, λ_{T}, τ_{T} and ϑ*

If one treats the cutter installation state shown in Figure 1.17 as a radial cutter runout model, the following important relationship between tilt and radial cutter runout models can be obtained.

$$\begin{aligned}
&\rho{=}\overline{\mathrm{OA}} = \sqrt{\overline{\mathrm{OB}}^2 + \overline{\mathrm{BA}}^2} = \sqrt{\overline{\mathrm{OB}}^2 + \left(\overline{\mathrm{BC}} + \overline{\mathrm{CA}}\right)^2} \\
&\lambda = -\angle\mathrm{FAW} \\
&\angle\mathrm{FAG} = \angle\mathrm{ECG}
\end{aligned} \qquad [1.84]$$

with

$$\begin{aligned}
&\overline{\mathrm{OB}} = \rho_{\mathrm{T}} \sin\vartheta \\
&\overline{\mathrm{BC}} = \rho_{\mathrm{T}} \cos\vartheta \\
&\overline{\mathrm{CA}} = (L - j z_{i,j}) \sin\tau_{\mathrm{T}}
\end{aligned}$$

Note that in this book the positive directions of λ_{T} and λ are defined as the clockwise direction. According to this definition, λ given in equation [1.84] is

negative. Further analysis of the geometry in Figure 1.17 gives the following relationship

$$\begin{aligned}
&\angle\text{FAG} = \angle\text{FAW} + \angle\text{WAG} = \angle\text{FAW} + \angle\text{OAB} \\
&= \angle\text{FAW} + \sin\left(\frac{\overline{\text{OB}}}{\overline{\text{OA}}}\right) \\
&\angle\text{ECG} = \vartheta - \lambda_{\text{T}}
\end{aligned} \tag{1.85}$$

By considering equations [1.84] and [1.85] together, one can obtain the following expressions

$$\begin{aligned}
&\rho^2 = (\rho_{\text{T}} \sin\vartheta)^2 + (\rho_{\text{T}} \cos\vartheta + (L - jz_{i,j}) \sin\tau_{\text{T}})^2 \\
&\arcsin\left(\frac{\rho_{\text{T}} \sin\vartheta}{\rho}\right) - \lambda = \vartheta - \lambda_{\text{T}}
\end{aligned} \tag{1.86}$$

Because $z_{i,j} = a_{\text{p}}$ in the first cutting test, $j = 1$ can be achieved. With this idea in mind, equation [1.86] can be further simplified as.

$$\begin{aligned}
&{\rho_{\text{T}}}^2 + 2\rho_{\text{T}}(L - a_{\text{p}}) \sin\tau_{\text{T}} \cos\vartheta + (L - a_{\text{p}})^2 \sin^2\tau_{\text{T}} - \rho^2 = 0 \\
&\lambda_{\text{T}} = \vartheta + \lambda - \sin\left(\frac{\rho_{\text{T}} \sin\vartheta}{\rho}\right)
\end{aligned} \tag{1.87}$$

By solving the above quadratic equation, the following results are obtained

$$\begin{aligned}
&\rho_{\text{T}} = \frac{-a + \sqrt{a^2 - 4c}}{2} \\
&\lambda_{\text{T}} = \vartheta + \lambda - \sin\left(\frac{\rho_{\text{T}} \sin\vartheta}{\rho}\right)
\end{aligned} \tag{1.88}$$

with

$$\begin{aligned}
&a = 2(L - a_{\text{p}}) \sin\tau_{\text{T}} \cos\vartheta \\
&c = (L - a_{\text{p}})^2 \sin^2\tau_{\text{T}} - \rho^2
\end{aligned}$$

Based on equation [1.88], ρ_{T}, λ_{T}, τ_{T} and ϑ are calibrated based on k_q, m_q (q = T, R, A) and ρ, λ calibrated from section 1.3.3.1 and $F_s^{\mathrm{M}}(\varphi)$ measured from the second test.

Step 1: Set $r = 0$ and set $\vartheta^{(r)} = \vartheta_*$, $\tau_{\mathrm{T}}^{(r)} = \tau_{\mathrm{T},*}$. ϑ_* and $\tau_{\mathrm{T},*}$ are initial values usually close to zero.

Step 2: Calculate ${\rho_{\mathrm{T}}}^{(r)}$ and ${\lambda_{\mathrm{T}}}^{(r)}$ by using

$$\begin{gathered}{\rho_{\mathrm{T}}}^{(r)} = \frac{-a + \sqrt{a^2 - 4c}}{2},\ {\lambda_{\mathrm{T}}}^{(r)} = \vartheta^{(r)} + \lambda - \arcsin\left(\frac{{\rho_{\mathrm{T}}}^{(r)} \sin\vartheta^{(r)}}{\rho}\right) \\ a = 2(L - a_{\mathrm{p}}) \sin {\tau_{\mathrm{T}}}^{(r)} \cos\vartheta^{(r)},\ c = (L - a_{\mathrm{p}})^2 \sin^2 {\tau_{\mathrm{T}}}^{(r)} - \rho^2\end{gathered} \quad [1.89]$$

Step 3: Calculate $h_{i,j}^{(r)}(\varphi_k)$ for all cutter rotation angle φ_k (k=1, 2, …, N_{sp}).

$$h_{i,j}^{(r)}(\varphi_k) = \min_{m=1}^{N} \left\{ mf \sin\theta_{i,j}(\varphi_k) + r_{i,j}^{(r)} - r_{i-m,j}^{(r)} \right\} \quad [1.90]$$

where $r_{i,j}^{(r)}$ is calculated by equation [1.76].

Step 4: Substitute k_q, m_q and $h_{i,j}^{(r)}(\varphi_k)$ into equations [1.72] and [1.74] to predict $F_s(\varphi_k)$. Then, calculate $\Delta^{(r)}$ with equation [1.83].

Step 5: If $\Delta^{(r)}$ achieves the level of minimum among all cases of $\vartheta^{(r)}$ and $\tau_{\mathrm{T}}^{(r)}$, set $\rho_{\mathrm{T}}^{(r)}$, $\lambda_{\mathrm{T}}^{(r)}$, $\tau_{\mathrm{T}}^{(r)}$ and $\vartheta^{(r)}$ as the final results of ρ_{T}, λ_{T}, τ_{T} and ϑ. Otherwise, set $r = r+1$ and the above Step 2 to Step 5 by setting $\vartheta^{(r)}$ and $\tau_{\mathrm{T}}^{(r)}$ to other values.

Similarly, to determine the values of $\vartheta^{(r)}$ and $\tau_{\mathrm{T}}^{(r)}$, Nelder-Mead simplex method [LAG 98, NEL 65] is used. This idea together with Nelder-Mead simplex method can avoid the complex solving of nonlinear equations.

It is also worth noting that the proposed calibration procedures implies the following important understanding:

a) if tilt cutter runout model is considered, sections 1.3.3.1 and 1.3.3.2 should be combined to calibrate k_q, m_q (q = T, R, A) and ρ_{T}, λ_{T}, τ_{T}, ϑ. In this case, two cutting tests are needed;

b) whereas, if radial cutter runout model is considered, the calibration of k_q, $m_q (q = T, R, A)$ and ρ, λ can be completed only by using section 1.3.3.1. In this case, only the first cutting test is needed.

1.3.3.3. *Model verification*

Using the tests listed in the title of Table 1.2, the cutting force coefficients and runout parameters based on two cutter runout models are calculated and listed in Table 1.2. It is worth noting that with the procedures described in section 1.3.3.2, the calibrations of ρ_{T}, λ_{T}, τ_{T} and ϑ for tilt cutter runout model converge within 38 iteration steps. However, if we use one degree as the step length of ϑ ($0 \leq \vartheta \leq 360°$) and 0.001 degree as the step length of τ ($0 \leq \tau \leq 0.06°$, $0.06°$ is an artificially given maximum bound) for parametric study, it requires about 360×60 (= 21600) iteration steps. Furthermore, the calibrated results of ρ_{T}, λ_{T}, τ_{T} and ϑ from parametric study are: $\rho_{\mathrm{T}} = 14.53$ μm, $\lambda_{\mathrm{T}} = 132.79°$, $\tau_{\mathrm{T}} = 0.028°$ and $\vartheta = 72°$. They are very close to those listed in Table 1.2.

	Radial cutter runout model	Tilt cutter runout model
k_{T} $(\mathrm{N/mm^2})$	758.17	758.17
m_{T}	0.1723	0.1723
k_{R} $(\mathrm{N/mm^2})$	86.10	86.10
m_{R}	0.6609	0.6609
k_{A} $(\mathrm{N/mm^2})$	143.10	143.10
m_{A}	0.1555	0.1555
Runout parameters	$\rho = 32.84$ μm	$\rho_{\mathrm{T}} = 14.50$ μm
	$\lambda = 85.69°$	$\lambda_{\mathrm{T}} = 131.95°$
		$\tau_{\mathrm{T}} = 0.02779°$
		$\vartheta = 70.85°$
Result source	Calibrated from Test 1	Calibrated from Tests 1 and 2

Table 1.2. *Calibrated results of cutting force coefficients and runout parameters based on different cutter runout models (for Test 1: $a_e = 8$ mm, $a_p = 2$ mm, f = 0.1667 mm/tooth, spindle speed=1200 RPM; for Test 2: $a_e = 0.8$ mm, $a_p = 25$ mm, $f = 0.1$ mm/tooth, spindle speed = 1000 RPM)*

1.3.4. *Identification of shear stress, shear angle and friction angle using milling tests*

According to the oblique theory proposed by [ARM 85], the milling mechanism of the *j*th disk of the *i*th flute can be treated as an oblique cutting

process, as shown in Figure 1.18. From the viewpoint of the principle of force equilibrium, K_{T}, K_{R} and K_{A} can be derived as [ALT 12]

$$\begin{aligned} K_{\mathrm{T}} &= \frac{\tau_s}{\sin\psi_n}\frac{\cos(\beta_n-\alpha_n)+\tan\beta\tan\eta\sin\beta_n}{\sqrt{\cos^2(\psi_n+\beta_n-\alpha_n)+\tan^2\eta\sin^2\beta_n}} \\ K_{\mathrm{R}} &= \frac{\tau_s}{\sin\psi_n\cos\beta}\frac{\sin(\beta_n-\alpha_n)}{\sqrt{\cos^2(\psi_n+\beta_n-\alpha_n)+\tan^2\eta\sin^2\beta_n}} \\ K_{\mathrm{A}} &= \frac{\tau_s}{\sin\psi_{\mathrm{n}}}\frac{\cos(\beta_n-\alpha_n)\tan\beta-\tan\eta\sin\beta_n}{\sqrt{\cos^2(\psi_n+\beta_n-\alpha_{\mathrm{n}})+\tan^2\eta\sin^2\beta_{\mathrm{n}}}} \end{aligned} \quad [1.91]$$

where η is chip flow angle. Equation [1.91] is a key bridge of orthogonal-to-oblique method that relates the cutting forces to the process geometric and physical parameters, i.e. τ_{s}, ψ_{n}, β_{n}, α_{n} and η. More details on this derivation can be found in [ALT 12, BUD 96]. However the determination of shear stress τ_s, shear angle ψ_n and friction angle β_n involved in the cutting force model still resorted to abundant orthogonal cutting tests. For example, as reported in [ALT 12, BUD 96], more than 180 turning experiments were used for determination procedure. Instead of orthogonal turning, milling experiments are directly designed to determine shear stress, shear angle and friction angle in this section, and only a few milling tests are required for the determination procedure.

1.3.4.1. *Determination of normal friction angle* β_{n}

Figure 1.19(a) shows the geometric relations of cutting forces in normal plane $\mathrm{P_n}$. It can be found that

$$\tan(\beta_{\mathrm{n}}-\alpha_{\mathrm{n}})=\tan\varphi_{\mathrm{n}}=\frac{F_{\mathrm{Rn},i,j}(\varphi)}{F_{\mathrm{Tn},i,j}(\varphi)} \text{ or } \beta_{\mathrm{n}}=\alpha_{\mathrm{n}}+\tan^{-1}\frac{F_{\mathrm{Rn},i,j}(\varphi)}{F_{\mathrm{Tn},i,j}(\varphi)} \quad [1.92]$$

with

$$\alpha_{\mathrm{n}}=\tan^{-1}(\tan\alpha_{\mathrm{r}}\cos\beta) \quad [1.93]$$

where α_{r} is radial rake angle of cutting edge. $F_{\mathrm{Rn},i,j}(\varphi)$ and $F_{\mathrm{Tn},i,j}(\varphi)$ are projections of $F_{\mathrm{R},i,j}(\varphi)$, $F_{\mathrm{T},i,j}(\varphi)$ and $F_{\mathrm{A},i,j}(\varphi)$ onto normal plane $\mathrm{P_n}$, which is vertical to the cutting edge, as shown in Figures 1.18 and 1.19. Obviously,

if the values of $F_{\mathrm{Rn},i,j}(\varphi)$ and $F_{\mathrm{Tn},i,j}(\varphi)$ are available, β_{n} can immediately be determined by using equation [1.92]. According to the theory in [ALT 12, BUD 96], cutting is uniform along the cutting edge in orthogonal turning process. Hence, $F_{\mathrm{Rn},i,j}(\varphi)$ and $F_{\mathrm{Tn},i,j}(\varphi)$ related to all disk elements are equal and collinear with the fixed thrust and feed directions. Thus, in turning process, β_{n} can be determined by directly replacing $F_{\mathrm{Rn},i,j}(\varphi)$ and $F_{\mathrm{Tn},i,j}(\varphi)$ with the total cutting forces measured experimentally. However, in milling process, it is practically difficult to determine β_{n} strictly from the measured cutting forces because of the following two factors. First, even at the same cutting instant, cutting forces associated with each disk element are different in magnitude and direction. Second, the measured cutting forces using dynamometer are available only in form of total cutting forces $F_s\,(\varphi)$ (s = X, Y, Z) and cannot be decomposed into force components related to each single disk element, i.e. $F_{\mathrm{Rn},i,j}(\varphi)$ and $F_{\mathrm{Tn},i,j}(\varphi)$. Therefore, a new approach is proposed below.

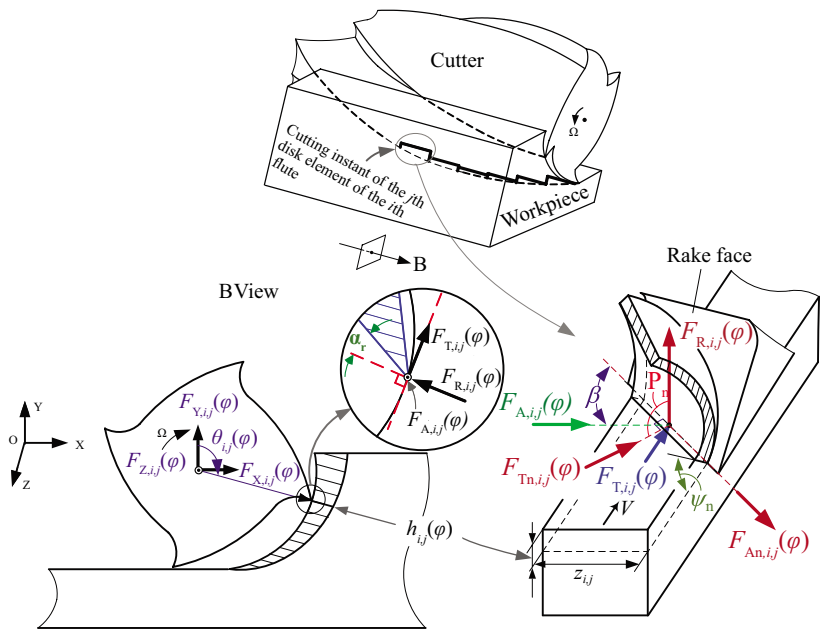

Figure 1.18. *Geometries and mechanics of flat end milling process. For a color version of this figure, see www.iste.co.uk/zhang/milling.zip*

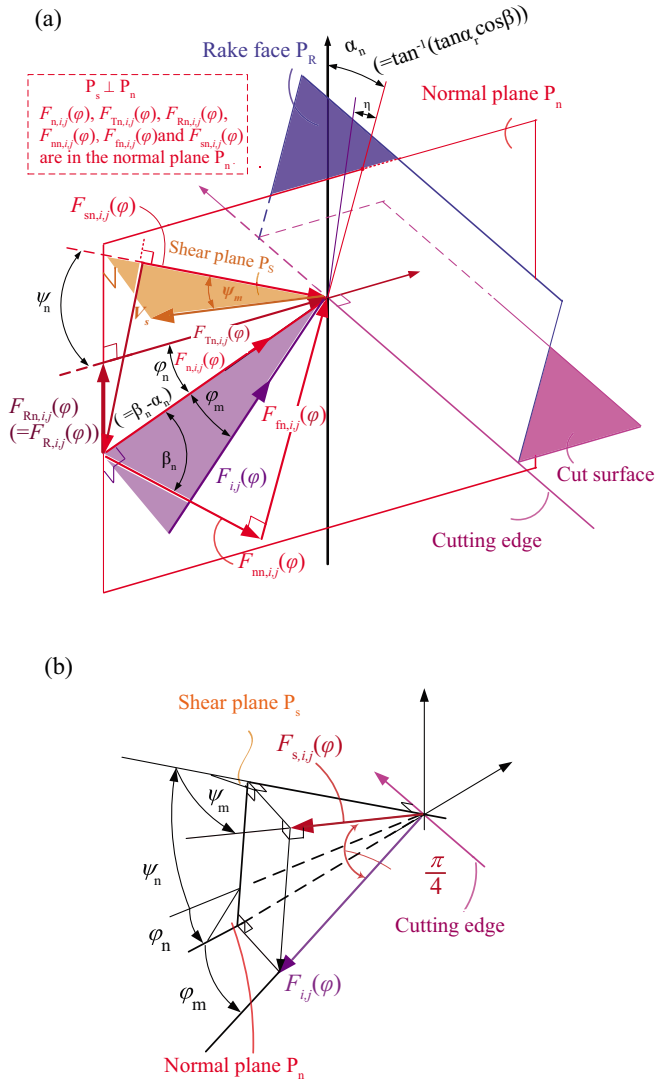

Figure 1.19. *Cutting forces related to the jth axial disk element of the ith flute; a) General relationship in equivalent oblique cutting; b) Relative geometrical diagram. For a color version of this figure, see www.iste.co.uk/zhang/milling.zip*

Total cutting forces can be deemed to be contributed by a single disk element under the following two conditions:

1) axial and radial depths of cut a_{p} and a_{e} satisfy equation [1.56]. That is, only one flute remains to be in cut at any engagement instant;

2) a_{p} is small enough so that it can be directly assigned to $z_{i,j}$. Generally, a_{p} can be selected within the range of 1–2 mm.

Based on a test under the above two conditions, $F_{\mathrm{Rn},i,1}(\varphi)$, $F_{\mathrm{Tn},i,1}(\varphi)$ and $F_{\mathrm{An},i,1}(\varphi)$ shown in Figures 1.18 and 1.19 are then determined according to the following steps:

1) measure the total cutting forces $\mathbf{F}^{\mathrm{M}}_{\mathrm{XYZ}}(\varphi)$ using a force dynamometer;

2) assume that $[F_{\mathrm{X},i,1}(\varphi), F_{\mathrm{Y},i,1}(\varphi), F_{\mathrm{Z},i,1}(\varphi)]^{\mathrm{T}} = \mathbf{F}^{\mathrm{M}}_{\mathrm{XYZ}}(\varphi)$;

3) transform the measured forces $\mathbf{F}^{\mathrm{M}}_{\mathrm{XYZ}}(\varphi)$ into tangential, radial and axial components by using the following equation:

$$[F_{\mathrm{T},i,1}(\varphi), F_{\mathrm{R},i,1}(\varphi), F_{\mathrm{A},i,1}(\varphi)]^{\mathrm{T}} = [\mathbf{T}(\theta_{i,1}(\varphi))]^{-1}\mathbf{F}^{\mathrm{M}}_{\mathrm{XYZ}}(\varphi) \qquad [1.94]$$

4) calculate $F_{\mathrm{Rn},i,1}(\varphi)$, $F_{\mathrm{Tn},i,1}(\varphi)$ and $F_{\mathrm{An},i,1}(\varphi)$ based on the geometric relationship shown in Figure 1.18:

$$[F_{\mathrm{Tn},i,1}(\varphi), F_{\mathrm{Rn},i,1}(\varphi), F_{\mathrm{An},i,1}(\varphi)]^{\mathrm{T}} = \mathbf{T}(\beta)[F_{\mathrm{T},i,1}(\varphi), F_{\mathrm{R},i,1}(\varphi), F_{\mathrm{A},i,1}(\varphi)]^{\mathrm{T}} \qquad [1.95]$$

Finally, β_{n} can be determined by substituting $F_{\mathrm{Rn},i,j}(\varphi)$ and $F_{\mathrm{Tn},i,j}(\varphi)$ obtained from equation [1.95] into equation [1.92].

1.3.4.2. *Determination of shear angle ψ_{n} and chip flow angle η*

The maximum shear stress principle indicates that shear occurs in the direction of maximum shear stress, where the angle between the shear velocity and the resultant force is $\pi/4$. The application of this principle to the milling process of the *j*th disk element of the *i*th flute leads to the reslutant force $F_{i,j}(\varphi)$ making a $\pi/4$ acute angle with the shear direction V_{s}, as shown in Figure 1.19(b). Mathematically, following relation holds for the shear force

$F_{\mathrm{s},i,j}(\varphi)$.

$$\begin{aligned} F_{\mathrm{s},i,j}(\varphi) &= F_{i,j}(\varphi)(\cos\varphi_{\mathrm{m}}\cos(\varphi_{\mathrm{n}}+\psi_{\mathrm{n}})\cos\psi_{\mathrm{m}}+\sin\varphi_{\mathrm{m}}\sin\psi_{\mathrm{m}}) \\ &= F_{i,j}(\varphi)\cos\frac{\pi}{4} \end{aligned} \quad [1.96]$$

Furthermore, because $F_{\mathrm{s},i,j}(\varphi)$ is the maximum shear force on the shear plane, the component of the resultant force in the direction normal to the shear on the shear plane must be zero.

$$F_{i,j}(\varphi)(\cos\varphi_{\mathrm{m}}\cos(\varphi_{\mathrm{n}}+\psi_{\mathrm{n}})\sin\psi_{\mathrm{m}}-\sin\varphi_{\mathrm{m}}\cos\psi_{\mathrm{m}})=0 \quad [1.97]$$

Solutions of equations [1.96] and [1.97] give

$$\sin\psi_{\mathrm{m}}=\sqrt{2}\sin\varphi_{\mathrm{m}} \quad [1.98]$$

$$\cos(\psi_{\mathrm{n}}+\varphi_{\mathrm{n}})=\frac{\tan\varphi_{\mathrm{m}}}{\tan\psi_{\mathrm{m}}} \quad [1.99]$$

Besides, according to [ALT 12], following geometric relations exist.

$$\sin\varphi_{\mathrm{m}}=\sin\beta_{\mathrm{a}}\sin\eta \quad [1.100]$$

$$\tan(\varphi_{\mathrm{n}}+\alpha_{\mathrm{n}})=\tan\beta_{\mathrm{a}}\cos\eta \quad \text{or} \quad \tan\beta_{\mathrm{n}}=\tan\beta_{\mathrm{a}}\cos\eta \quad [1.101]$$

where β_{a} is the actual friction angle on the rake face. Chip flow angle η is generally assumed to equal helix angle β according to the chip flow rule proposed by [ALT 12].

Using β_{n} obtained in section 1.3.4.1 as the initial value, solutions of ψ_{n}, φ_{m} and φ_{n} can be achieved by combining equations [1.98] to [1.101].

1.3.4.3. *Determination of shear stress* τ_{s}

Based on ψ_{n}, φ_{m} and φ_{n} determined above, shear stress τ_{s} can be calculated as

$$\begin{aligned}\tau_{\mathrm{s}} &= \frac{F_{\mathrm{s},i,1}(\varphi)}{A_{\mathrm{s},i,1}(\varphi)} \\ &= \frac{F_{i,1}(\varphi)(\cos\varphi_{\mathrm{m}}\cos(\varphi_{\mathrm{n}}+\psi_{\mathrm{n}})\cos\psi_{\mathrm{m}}+\sin\varphi_{\mathrm{m}}\sin\psi_{\mathrm{m}})}{A_{\mathrm{s},i,1}(\varphi)}\end{aligned} \quad [1.102]$$

where $F_{i,1}(\varphi)$ is obtained by substituting the components of the measured forces $\mathbf{F}_{\mathrm{M,XYZ}}(\varphi)$ into the following equation.

$$F_{i,1}(\varphi) = \sqrt{\left(F^{\mathrm{M}}_{\mathrm{X},i,1}(\varphi)\right)^2 + \left(F^{\mathrm{M}}_{\mathrm{Y},i,1}(\varphi)\right)^2 + \left(F^{\mathrm{M}}_{\mathrm{Z},i,1}(\varphi)\right)^2} \quad [1.103]$$

$A_{\mathrm{s},i,1}(\varphi)$ is calculated by

$$A_{\mathrm{s},i,1}(\varphi) = \frac{a_{\mathrm{p}}}{\cos\beta}\frac{h_{i,1}(\varphi)}{\sin\psi_{\mathrm{n}}} \quad [1.104]$$

in which $h_{i,1}(\varphi)$ can be calculated by using equations [1.9] and [1.25] if radial cutter runout parameters ρ and λ have been identified in advance. Alternatively, to ignore the effect of cutter runout, both $F_{i,1}(\varphi)$ and $h_{i,1}(\varphi)$ can be calculated using the nominal components.

As φ varies, the milling cutter undergoes a trochoidal motion that yields a continuous variation of chip thickness from zero to its maximum value, which in turn leads to the instantaneous cutting forces over a wide range of chip thickness. With these values, explicit expressions of τ_{s}, β_{n} and ψ_{n} can be established by treating τ_{s}, β_{n} and ψ_{n} as the functions of instantaneous uncut chip thickness.

The relations shown in Figure 1.20 are identified from two milling tests using carbide flat end mill and 7050 aluminum alloy. It can obviously be seen that β_{n} and ψ_{n} are the functions of uncut chip thickness. Figure 1.21 compares the measured cutting forces with the predicted ones by using the results from Figure 1.20.

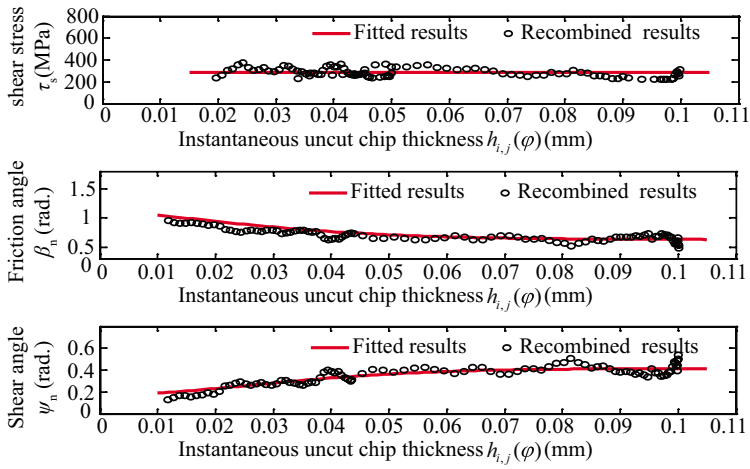

Figure 1.20. *Results of stress, friction angle and shear angle. For a color version of this figure, see www.iste.co.uk/zhang/milling.zip*

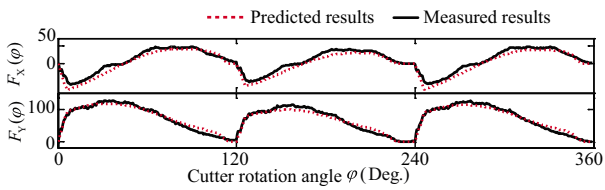

Figure 1.21. *Comparisons of measured and predicted cutting forces. For a color version of this figure, see www.iste.co.uk/zhang/milling.zip*

1.4. Ternary cutting force model including bottom edge cutting effect

A typical milling process of flat end mill is shown in Figure 1.22, from which it can be seen that both the flank edge and the bottom edge can be engaged with the workpiece during the actual cutting process. Thus, the calculation of the total cutting forces should include the contributions of the flank edge cutting and the bottom edge cutting effects. An illustration of

the force components is also shown in Figure 1.22. The total cutting forces can be expressed as

$$\mathbf{F}(\varphi) = \mathbf{F}_{\mathrm{F}}(\varphi) + \mathbf{F}_{\mathrm{B}}(\varphi) \qquad [1.105]$$

where $\mathbf{F}_{\mathrm{F}}(\varphi)$ and $\mathbf{F}_{\mathrm{B}}(\varphi)$ are the cutting force vectors induced by flank and bottom edges at the cutter rotation angle φ. More details for the procedure of calculating $\mathbf{F}_{\mathrm{F}}(\varphi)$ and $\mathbf{F}_{\mathrm{B}}(\varphi)$ are given in the following.

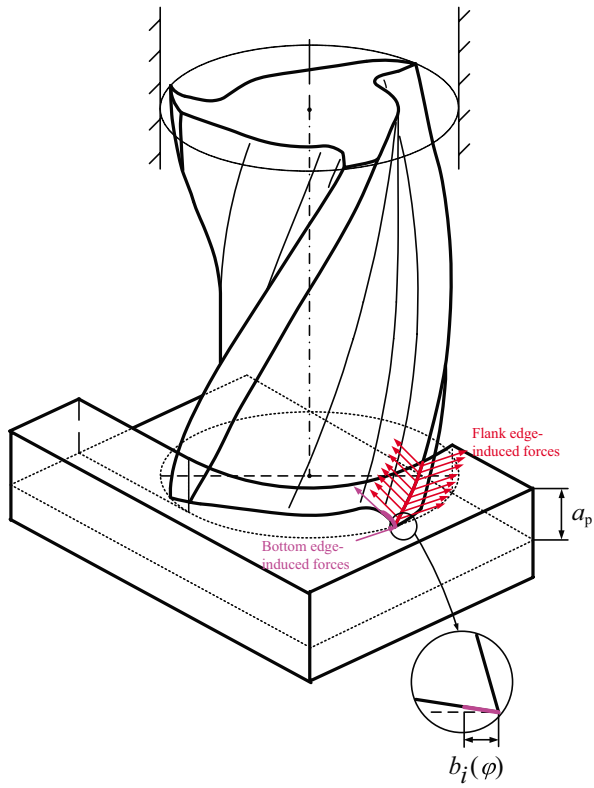

Figure 1.22. *Flat end milling process. For a color version of this figure, see www.iste.co.uk/zhang/milling.zip*

1.4.1. *Calculations of* $\mathbf{F}_{B}(\varphi)$

The calculation of $\mathbf{F}_{\mathrm{F}}(\varphi)$ can be carried out according to

$$\mathbf{F}_{\mathrm{F}}(\varphi) = \begin{bmatrix} F_{\mathrm{X,F}}(\varphi) \\ F_{\mathrm{Y,F}}(\varphi) \end{bmatrix} \quad [1.106]$$

$$\begin{aligned} F_{\mathrm{X,F}}(\varphi) &= \sum_{i,j} \{g(\theta_{i,j}(\varphi))[-F_{\mathrm{T,F},i,j}(\varphi)\cos\theta_{i,j}(\varphi) - F_{\mathrm{R,F},i,j}(\varphi)\sin\theta_{i,j}(\varphi)]\} \\ F_{\mathrm{Y,F}}(\varphi) &= \sum_{i,j} \{g(\theta_{i,j}(\varphi))[F_{\mathrm{T,F},i,j}(\varphi)\sin\theta_{i,j}(\varphi) - F_{\mathrm{R,F},i,j}(\varphi)\cos\theta_{i,j}(\varphi)]\} \end{aligned} \quad [1.107]$$

with

$$\begin{aligned} F_{\mathrm{T,F},i,j}(\varphi) &= K_{\mathrm{Tc}} h_{\mathrm{F},i,j}(\varphi) z_{i,j} + K_{\mathrm{Te}} z_{i,j} \\ F_{\mathrm{R,F},i,j}(\varphi) &= K_{\mathrm{Rc}} h_{\mathrm{F},i,j}(\varphi) z_{i,j} + K_{\mathrm{Re}} z_{i,j} \\ h_{\mathrm{F},i,j}(\varphi) &= \max\{0, \min_{m=1,2,\ldots,N} [mf\sin\theta_{i,j}(\varphi) + r_{i,j} - r_{i-m,j}]\} \end{aligned} \quad [1.108]$$

Note that in equation [1.108], the cutting mechanism of flank edge is characterized by dual mechanism model, in which the shearing effect and the rubbing effect of the flank edge are described separately.

1.4.2. *Calculations of* $\mathbf{F}_{B}(\varphi)$

The cutting mechanism of the bottom edge is likely the rubbing effect of the bottom edge rather than the shearing effect. Hence, the tangential force $F_{\mathrm{T,B},i}(\varphi)$ and the radial force $F_{\mathrm{R,B},i}(\varphi)$ related to the *i*th flute can be written as

$$\begin{aligned} F_{\mathrm{T,B},i}(\varphi) &= K_{\mathrm{T,B}} b_i(\varphi) \\ F_{\mathrm{R,B},i}(\varphi) &= K_{\mathrm{R,B}} b_i(\varphi) \end{aligned} \quad [1.109]$$

where $K_{\mathrm{T,B}}$ and $K_{\mathrm{R,B}}$ are tangential and radial coefficients related to the bottom cutting effect of the bottom edge. $b_i(\varphi)$ is the bottom uncut chip width

related to the *i*th bottom edge at the cutter rotation angle φ, as shown in Figure 1.22. Based on equation [1.109], $\mathbf{F}_{\mathrm{B}}(\varphi)$ can be calculated by

$$\mathbf{F}_{\mathrm{B}}(\varphi) = \begin{bmatrix} F_{\mathrm{X,B}}(\varphi) \\ F_{\mathrm{Y,B}}(\varphi) \end{bmatrix} \qquad [1.110]$$

with

$$\begin{aligned} F_{\mathrm{X,B}}(\varphi) &= g(\theta_{i,0}(\varphi))[-F_{\mathrm{T,B},i}(\varphi)\cos\theta_{i,0}(\varphi) \\ &\quad - F_{\mathrm{R,B},i}(\varphi)\sin\theta_{i,0}(\varphi)] \\ F_{\mathrm{Y,B}}(\varphi) &= g(\theta_{i,0}(\varphi))[F_{\mathrm{T,B},i}(\varphi)\sin\theta_{i,0}(\varphi) \\ &\quad - F_{\mathrm{R,B},i}(\varphi)\cos\theta_{i,0}(\varphi)] \end{aligned} \qquad [1.111]$$

where $\theta_{i,0}(\varphi)$ is the angular position related to the *i*th flank edge tip at the cutter rotation angle φ.

Without the loss of generality, model calibration will be illustrated for equations [1.108] and [1.109]. Methods for the calibration of $K_{q\mathrm{c}}$, $K_{q\mathrm{e}}$ and $K_{q,\mathrm{B}}$ ($q = \mathrm{T}, \mathrm{R}$) are now described in detail.

1.4.3. *Calibration of* $K_{q\mathbf{c}}$ ($\mathbf{q} = T, R$)

As long as the cutting is a single tooth engagement test with a_{p} being in the range of 1–2 mm, the total cutting forces measured in Cartesian X- and Y-directions can be transformed into tangential and radial components with good precision. Transformed tangential and radial forces show that they can linearly be approximated with respect to chip load $\sum_{i,j}[h_{\mathrm{F},i,j}(\varphi)z_{i,j}]$. This implies that the cutting force coefficients related to chip removal effect can be treated as constants. Based on this fact, $K_{q\mathrm{c}}$ is calibrated by virtue of the transformed tangential and radial forces in following steps:

1) select experimental parameters under the condition that the axial depth of cut a_{p} is in the range of 1–2 mm;

2) identify radial cutter runout parameters ρ and λ experimentally or numerically;

3) measure the total cutting forces in X- and Y-directions by a force dynamometer;

4) calculate $h_{\mathrm{F},i,j}(\varphi)$ in terms of ρ and λ using equation [1.108];

5) calculate chip load $\sum_{i,j}[h_{\mathrm{F},i,j}(\varphi)z_{i,j}]$;

6) transform the measured X- and Y-forces $\mathbf{F}_{\mathrm{XY}}^{\mathrm{M}}(\varphi) = [\mathbf{F}_{\mathrm{X}}^{\mathrm{M}}(\varphi), \mathbf{F}_{\mathrm{Y}}^{\mathrm{M}}(\varphi)]^{\mathrm{T}}$ into tangential and radial components by;

$$\mathbf{F}_{\mathrm{TR}}^{\mathrm{M}}(\varphi) = [\mathbf{T}(\theta_{i,0}(\varphi))]^{-1}\mathbf{F}_{\mathrm{XY}}^{\mathrm{M}}(\varphi) \qquad [1.112]$$

where $\mathbf{F}_{\mathrm{TR}}^{\mathrm{M}}(\varphi) = [\mathbf{F}_{\mathrm{T}}^{\mathrm{M}}(\varphi), \mathbf{F}_{\mathrm{R}}^{\mathrm{M}}(\varphi)]^{\mathrm{T}}$.

7) plot $F_q^{\mathrm{M}}(\varphi)$ ($q = \mathrm{T}, \mathrm{R}$) obtained from Step (6) as a function of chip load for each tooth;

8) use linear function to fit the relationship between $F_q^{\mathrm{M}}(\varphi)$ and chip load for each tooth. The slope of each fitted line is symbolized as $k_{i,q}$ ($i = 1, 2, ..., N$, $q = \mathrm{T}, \mathrm{R}$);

9) calculate $K_{q\mathrm{c}}$ by means of

$$K_{q\mathrm{c}} = \sum_{i=1}^{N} k_{i,q}/N \qquad [1.113]$$

1.4.4. *Calibrations of* $K_{q,B}$ ($\mathbf{q} = T, R$)

Based on equation [1.106] and $K_{q\mathrm{c}}$ ($q = \mathrm{T}, \mathrm{R}$) calibrated above, the cutting force $\mathbf{F}_{\mathrm{Fc}}(\varphi)$, which is related to shearing effect, can be calculated and then used together with the measured forces $\mathbf{F}_{\mathrm{XY}}^{\mathrm{M}}(\varphi)$ to obtain the following components.

$$\mathbf{F}_{\mathrm{BFTR}}^{\mathrm{M}}(\varphi) = [\mathbf{T}(\theta_{i,0}(\varphi))]^{-1}[\mathbf{F}_{\mathrm{XY}}^{\mathrm{M}}(\varphi) - \mathbf{F}_{\mathrm{Fc}}(\varphi)] \qquad [1.114]$$

where $\mathbf{F}_{\mathrm{BFTR}}^{\mathrm{M}}(\varphi) = [\mathrm{F}_{\mathrm{BFT}}^{\mathrm{M}}(\varphi), \mathrm{F}_{\mathrm{BFR}}^{\mathrm{M}}(\varphi)]^{\mathrm{T}}$ stands for the experimental force component that only contains the flank rubbing and bottom edge cutting

effects. Combining this component with the prediction expression leads to the following equation.

$$\left[\sum_{i,j} z_{i,j}\ b_i(\varphi)\right]\begin{bmatrix} K_{q\mathrm{e}} \\ K_{q,\mathrm{B}} \end{bmatrix} = \mathrm{F}^{\mathrm{M}}_{\mathrm{BF}q}(\varphi), q = \mathrm{T},\ \mathrm{R} \qquad [1.115]$$

At all sampling instants of the full engagement period, equation [1.115] can be expressed as

$$\mathbf{B}\left[K_{\mathrm{Te}},\ K_{\mathrm{T,B}},\ K_{\mathrm{Re}},\ K_{\mathrm{R,B}}\right]^{\mathrm{T}} = \mathbf{b} \qquad [1.116]$$

with

$$\mathbf{B} = \begin{bmatrix} \sum_{i,j} z_{i,j}(\varphi_1) & b_i(\varphi_1) & 0 & 0 \\ \vdots & \vdots & \vdots & \vdots \\ \sum_{i,j} z_{i,j}(\varphi_n) & b_i(\varphi_{N_{\mathrm{sap}}}) & 0 & 0 \\ 0 & 0 & \sum_{i,j} z_{i,j}(\varphi_1) & b_i(\varphi_1) \\ \vdots & \vdots & \vdots & \vdots \\ 0 & 0 & \sum_{i,j} z_{i,j}(\varphi_n) & b_i(\varphi_{N_{\mathrm{sap}}}) \end{bmatrix} \qquad [1.117]$$

$$\mathbf{b} = \begin{bmatrix} \mathrm{F}^{\mathrm{M}}_{\mathrm{BFT}}(\varphi_1) \\ \vdots \\ \mathrm{F}^{\mathrm{M}}_{\mathrm{BFT}}(\varphi_{N_{\mathrm{sap}}}) \\ \mathrm{F}^{\mathrm{M}}_{\mathrm{BFR}}(\varphi_1) \\ \vdots \\ \mathrm{F}^{\mathrm{M}}_{\mathrm{BFR}}(\varphi_{N_{\mathrm{sap}}}) \end{bmatrix} \qquad [1.118]$$

Based on equation [1.116], $K_{q\mathrm{e}}$ and $K_{q,\mathrm{B}}$ ($q = \mathrm{T}, \mathrm{R}$) can be determined by means of least-square fitting method.

$$\left[K_{\mathrm{Te}},\ K_{\mathrm{T,B}},\ K_{\mathrm{Re}},\ K_{\mathrm{R,B}}\right]^{\mathrm{T}} = \left[\mathbf{B}^{\mathrm{T}}\mathbf{B}\right]^{-1}\left[\mathbf{B}^{\mathrm{T}}\,\mathbf{b}\right] \qquad [1.119]$$

1.4.5. *Experimental work*

Experiments are performed in a three-axis CNC vertical machining center for a three-fluted $\phi 16$ Carbide end mill/aluminum AL 2618-T6 couple. The cutter is normal right-handed mill with helix angle of 30°. By using the above procedure, final results of the corresponding coefficients are as follows.

$$[K_{\mathrm{Tc}}, K_{\mathrm{Rc}}, K_{\mathrm{Te}}, K_{\mathrm{Re}}, K_{\mathrm{T,B}}, K_{\mathrm{R,B}}]^{\mathrm{T}} = [690.89\mathrm{N/mm}^2, 179.32\mathrm{N/mm}^2, 10.22\mathrm{N/mm}, 10.20\mathrm{N/mm}, 100.58\mathrm{N/mm}, 66.54\mathrm{N/mm}]^{\mathrm{T}} \quad [1.120]$$

Figure 1.23 shows the predicted cutting forces by using the model described in this section and the one given in section 1.3.1. It can be found that the proposed model holds the same order of prediction accuracy as the lumped force model described in section 1.3.1.

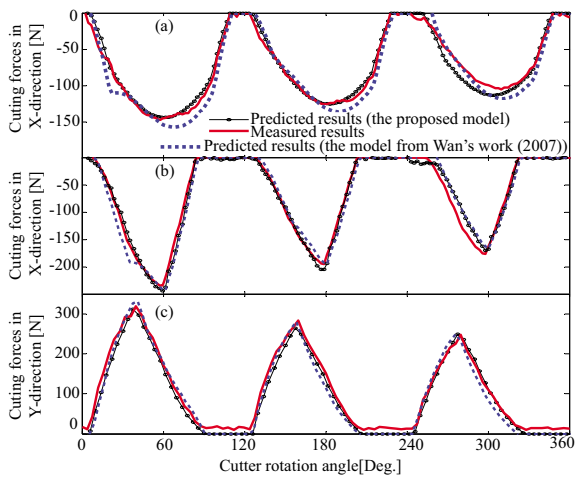

Figure 1.23. *Comparisons of cutting forces predicted by two method. For a color version of this figure, see www.iste.co.uk/zhang/milling.zip*

1.5. Cutting force prediction in peripheral milling of a curved surface

A typical peripheral milling of a curved surface is illustrated in Figure 1.24. XYZ is a globally stationary coordinate system attached to the

table, in which the workpiece boundary, the geometry of desired surface and the tool path are described. $X_S Y_S Z_S$ is a locally moving coordinate system attached to the spindle of the machine tool with its origin O_S at the center of the spindle. $O_S X_S$ is aligned with the instantaneous feed direction of the theoretical tool path. $O_S Z_S$ points upward along the spindle axis. $O_S Y_S$ is the normal to the feed direction and follows the definition of right-hand coordinate system. Then $X_S Y_S Z_S$ will move as the tool moves along the tool path. $\theta_f(t)$ represents the angular location of the instantaneous feed direction $O_S X_S$ and is measured anti-clockwise from the positive direction of X-axis at the sampling instant t. $O_{TP}(t)$ and $R_{TP}(t)$ denote the center of curvature and the radius of curvature related to tool position $O_S(t)$ on the theoretical tool path, respectively.

Generally speaking, the tool position depends upon the parametric equation of theoretical tool path. The actual tool path generally used in NC machining is made up of a series of straight line segments and circular arc segments generated by the integrated CAM software, no matter how complex the theoretical tool path is. One such approximation can easily be used to determine the tool position without solving nonlinear equations and the computing time is largely saved. Mathematically, the actual tool position $\mathbf{p}_a(t)$ is iteratively updated as

$$\mathbf{p}_a(t+T_s)=\begin{cases}\mathbf{p}_a(t)+V_f T_s \mathbf{f}_a(t) & \text{, for linear tool path segment}\\ [\mathbf{R}]\,(\mathbf{p}_a(t)-\mathbf{o}_{CTP})+\mathbf{o}_{CTP}, & \text{for circular tool path segment}\end{cases} \quad [1.121]$$

with

$$\mathbf{f}_a(t)=\frac{\mathbf{p}_{en}-\mathbf{p}_{st}}{|\mathbf{p}_{en}-\mathbf{p}_{st}|},$$

$$[\mathbf{R}]=\begin{bmatrix}\cos\alpha_s & -\sin\alpha_s & 0\\ \sin\alpha_s & \cos\alpha_s & 0\\ 0 & 0 & 1\end{bmatrix},$$

$$\alpha_s=\frac{V_f T_s}{R_{CTP}}$$

where $\mathbf{p}_a(t) = [X_a(t), Y_a(t), 0]^T$ is the tool position on the actual tool path. T_s is a given sampling time interval. V_f is the feed rate defined as the distance that the mill feeds as the spindle rotates one radian. $\mathbf{f}_a(t)$ is feed direction

of the cutter. $\mathbf{o}_{\mathrm{CTP}}$ and R_{CTP} are center point and radius of a circular tool path segment. $\mathbf{p}_{\mathrm{st}}$ and $\mathbf{p}_{\mathrm{en}}$ are start point and end point of a linear tool path segment.

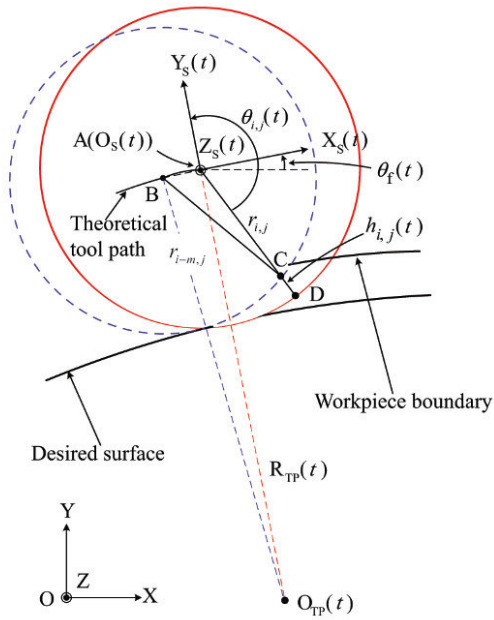

Figure 1.24. *Representation of typical peripheral milling of a curved surface*

Theoretically, the feed direction along the actual tool path might be easily determined by finding the tangential direction of the actual tool path. Nevertheless, if the tool position strides over the joint of two adjacent tool path segments, e.g. the joint of a straight line and a circle, as stated by Wei *et al.* [WEI 10], the feed direction, the exterior normal direction and the curvature of the actual tool path may be abruptly changed. In this section, the problem is avoided based on the concept of equivalent point obtained by mapping the tool position from the actual tool path to the theoretical one. The detailed procedures is presented below.

As shown in Figure 1.25, $\mathbf{p}_{\mathrm{e}}(t) = [X_{\mathrm{e}}(u(t)), Y_{\mathrm{e}}(u(t)), 0]^{\mathrm{T}}$ is the equivalent tool position on the theoretical tool path defined by the intersection

point between the theoretical tool path and the normal of the actual tool path at $\mathbf{p}_{\mathrm{a}}(t)$.

$$(\mathbf{p}_{\mathrm{e}}(t) - \mathbf{p}_{\mathrm{a}}(t)) \times \mathbf{n}_{\mathrm{a}}(t) = \mathbf{0} \qquad [1.122]$$

where $\mathbf{n}_{\mathrm{a}}(t)$ is the exterior normal of the actual tool path. $u(t)$ is the parameter variable of the theoretical tool path.

$$\mathbf{n}_{\mathrm{a}}(t) = \begin{cases} \begin{bmatrix} 0 & 0 & 1 \end{bmatrix}^{\mathrm{T}} \times \mathbf{f}_{\mathrm{a}}(t), & \text{for linear tool path segment} \\ \mathbf{p}_{\mathrm{a}}(t) - \mathbf{o}_{\mathrm{CTP}}, & \text{for circular tool path segment (convex)} \\ \mathbf{o}_{\mathrm{CTP}} - \mathbf{p}_{\mathrm{a}}(t), & \text{for circular tool path segment (concave)} \end{cases} \qquad [1.123]$$

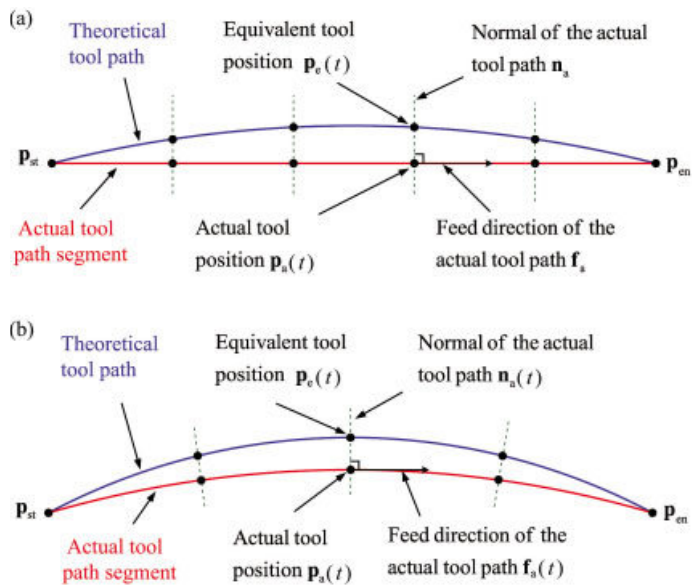

Figure 1.25. *Interpolated tool position on the actual tool path: a) linear tool path segment and b) circular tool path segment*

Geometrically, the equivalent feed direction of the cutter $\mathbf{f}_{\mathrm{e}}(t)$ can be defined as the tangential direction at $\mathbf{p}_{\mathrm{e}}(t)$. It can be easily obtained by means of the value of $u(t)$ solved from equation [1.122]. With $\mathbf{f}_{\mathrm{e}}(t)$ and $u(t)$, the

exterior normal direction $\mathbf{n}_{\mathrm{e}}(t)$ and curvature $K_{\mathrm{e}}(t)$ related to $\mathbf{p}_{\mathrm{e}}(t)$ are thus calculated by

$$\mathbf{n}_{\mathrm{e}}(t) = \begin{bmatrix} 0 & 0 & 1 \end{bmatrix}^{T} \times \mathbf{f}_{\mathrm{e}}(t) \qquad [1.124]$$

$$K_{\mathrm{e}}(t) = \frac{X_{\mathrm{e}}{}'(u(t))\, Y_{\mathrm{e}}{}''(u(t)) - X_{\mathrm{e}}{}''(u(t))\, Y_{\mathrm{e}}{}'(u(t))}{\left(\left(X_{\mathrm{e}}{}'(u(t))\right)^2 + \left(Y_{\mathrm{e}}{}'(u(t))\right)^2 \right)^{\frac{3}{2}}} \qquad [1.125]$$

In the following presentation, $\mathbf{f}_{\mathrm{e}}(t)$, $\mathbf{n}_{\mathrm{e}}(t)$ and $K_{\mathrm{e}}(t)$ are treated as the equivalent feed direction, equivalent exterior normal direction and equivalent curvature for the actual tool position $\mathbf{p}_{\mathrm{a}}(t)$.

Besides, the angular location of the feed direction, i.e. $\theta_{\mathrm{f}}(t)$, is calculated by the method reported in [WEI 10]

$$\theta_{\mathrm{f}}(t) = \arccos\left(\frac{\mathbf{f}_{\mathrm{e}}(t) \cdot \mathbf{I}_{\mathrm{X}}}{|\mathbf{f}_{\mathrm{e}}(t)|} \right) \qquad [1.126]$$

where $\mathbf{I}_{\mathrm{X}} = \begin{bmatrix} 1 & 0 & 0 \end{bmatrix}^{\mathrm{T}}$ is the unit direction vector of X-axis.

Based on the geometries described above, the instantaneous uncut chip thickness and the entry and exit angles can be calculated as follows. Note that for the convenience of study, the cutter is discretized into disc elements with equal axial length $z_{i,j}$.

1.5.1. *Calculations of instantaneous uncut chip thickness*

In case of zero cutter runout, instantaneous uncut chip thickness can be expressed as an explicit function of feed per tooth and tooth positioning angle of the cutting point [KLI 82a, ALT 91, BUD 96, FEN 94a]. Conversely, instantaneous uncut chip thickness will be greatly redistributed in the presence of cutter runout and is generally calculated as the distance between two points, i.e. the cutting point related to the current circular path and the corresponding one at the previous circular path [KLI 83, SUT 86]. Explicit expressions relating the cutting parameters to cutter runout parameters were derived [KOE 61, SUT 86] only for straight surface milling. Here, an explicit

expression of instantaneous uncut chip thickness including the effect of cutter runout is derived for the milling of curved surface with variable curvature. For the milling of convex surfaces illustrated in Figure 1.24, suppose that the current cutting point D related to the *j*th disk element of the *i*th flute, is removing the surface left by the *m*th previous tooth. At the *m*th circular tooth path, the cutting point related to D is symbolized by C. The tool positions related to D and C are denoted by A and B, respectively. By definition, instantaneous uncut chip thickness related to the *j*th disc element of the *i*th flute can be expressed as

$$h_{i,j}(t,m) = L_{\mathrm{CD}} = r_{i,j} - L_{\mathrm{AC}} \qquad [1.127]$$

with $r_{i,j}$ being calculated by equation [1.18].

Equation [1.127] indicates that the value of $h_{i,j}(t,m)$ depends on L_{AC} whose calculation is as follows.

According to the triangle geometry relationship in $\triangle$ABC, L_{AC} can be mathematically derived as:

$$L_{\mathrm{AC}} = \sqrt{r_{i-m,j}^2 - \left(2R_{\mathrm{TP}}(t)\sin\left(\frac{mf}{2R_{\mathrm{TP}}(t)}\right)\cos\left(\frac{mf}{2R_{\mathrm{TP}}(t)} + \theta_{i,j}(t)\right)\right)^2} - 2R_{\mathrm{TP}}(t)\sin\left(\frac{mf}{2R_{\mathrm{TP}}(t)}\right)\sin\left(\frac{mf}{2R_{\mathrm{TP}}(t)} + \theta_{i,j}(t)\right) \qquad [1.128]$$

where $R_{\mathrm{TP}}(t)$ stands for the curvature related to arc. Theoretically, the radii of curvature and the centers of curvature related to tool positions A and B may be different due to the variable curvature of the theoretical tool path. Nevertheless, as the feed per tooth used is relatively small in practical milling and the curvature of arc between two adjacent tool positions A and B has a very mild variation, the curvature of the arc can be assumed to be a constant value equal to $K_{\mathrm{e}}(t)$ and both A and B have the same curvature center $\mathrm{O}_{\mathrm{TP}}(t)$. Mathematically, we have

$$R_{\mathrm{TP}}(t) = \frac{1}{|K_{\mathrm{e}}(t)|} \qquad [1.129]$$

Notice that the corresponding $R_{\mathrm{TP}}(t)$ should be recalculated by equations [1.125] and [1.129] once the tool position changes.

With the aid of equations [1.127] and [1.128], the instantaneous uncut chip thickness can be calculated by [DES 09]

$$h_{i,j}(t) = \max\left[0, \min_{m=1,2,\ldots,N}\left(h_{i,j}(t,m)\right)\right] \qquad [1.130]$$

Note that instantaneous uncut chip thickness can be obtained in a similar way in the case of milling of concave surfaces.

1.5.2. *Calculations of entry and exit angles*

The presence of cutter runout not only influences instantaneous uncut chip thickness but also the entry/exit angles in the milling of curved surface. Desai *et al.* [DES 09] studied one such influence. In their computing of entry/exit angles, the intersection point between the tooth path and the theoretical workpiece boundary is obtained as long as the workpiece boundary is the parallel offset of the geometry of desired surface. However, when the workpiece boundary is not parallel to the geometry of desired surface, e.g. at the disengaging stage, results of entry or exit angles will be erroneous. Wei *et al.* [WEI 10] replaced the theoretical workpiece boundary with a set of straight line and circular arc segments, which are the parallel offset of tool path in pre-machining, i.e. the so-called actual workpiece boundary. Unfortunately, the influence of cutter runout was not considered in their work.

In this section, improvements are made on the calculation of exit angle at the engaging or disengaging stage including the influence of cutter runout. In the case of continuous engagement, entry and exit angles are obtained using the method in [DES 09]. At the engaging stage, as shown Figure 1.26, the exit angle can be obtained by

$$\theta_{\mathrm{ex},i,j}(t) = \min_{m=1,2,\ldots,N}\left(\theta_{\mathrm{ex},i,j}(t,m), \theta_{\mathrm{B,ex},i,j}(t)\right) \qquad [1.131]$$

in which $\theta_{\mathrm{ex},i,j}(t,m)$ means the angle related to the intersection point of the current tooth path and the mth previous tool path corresponding to the *j*th disc element of the *i*th flute. It can be obtained by adopting the exit angle calculating method in [DES 09]. $\theta_{\mathrm{B,ex},i,j}(t)$ is the angle related to the possible exit point,

which is the intersection of the current tooth path and the actual workpiece boundary.

$$\theta_{\mathrm{B,ex},i,j}(t) = \arccos\left(\frac{\left(\mathbf{p}_{\mathrm{w}}\left(v_{\mathrm{B,ex},i,j}(t)\right) - \mathbf{p}_{\mathrm{a}}(t)\right) \cdot \mathbf{n}_{\mathrm{e}}(t)}{\left|\mathbf{p}_{\mathrm{w}}\left(v_{\mathrm{B,ex},i,j}(t)\right) - \mathbf{p}_{\mathrm{a}}(t)\right| \left|\mathbf{n}_{\mathrm{e}}(t)\right|}\right) \qquad [1.132]$$

where $\mathbf{p}_{\mathrm{w}}(v_{\mathrm{B,ex},i,j}(t)) = [X_{\mathrm{w}}(v_{\mathrm{B,ex},i,j}(t)) \;\; Y_{\mathrm{w}}(v_{\mathrm{B,ex},i,j}(t)) \;\; 0]^{\mathrm{T}}$ means the parametric equations of actual workpiece boundary with $v_{\mathrm{B,ex},i,j}(t)$ being the parameter variable of the workpiece boundary corresponding to the *j*th disc element of the *i*th flute. Although the rotation radius of the concerned disc element will deviate from its nominal value to $r_{i,j}$ due to cutter runout [KLI 83, SUT 86, DES 09], the entry angle can still be obtained according to the method in [DES 09], as long as the rotation radius is replaced by $r_{i,j}$.

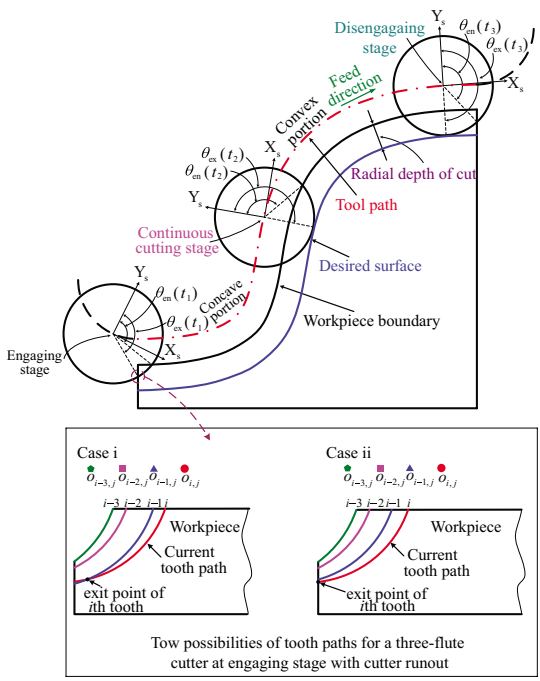

Figure 1.26. *Entry/exit angles at different stages. For a color version of this figure, see www.iste.co.uk/zhang/milling.zip*

Substitution of the instantaneous uncut chip thickness $h_{i,j}(t)$ into equation [1.8] or equation [1.13] leads to the cutting force components $F_{\mathrm{T},i,j}(t)$ and

$F_{\mathrm{R},i,j}(t)$, and then the total cutting force in locally moving coordinate system can be calculated as

$$\begin{aligned} F_{\mathrm{X_S}}(t) &= \sum_{i,j} g(\theta_{i,j}(t)) \left[-F_{\mathrm{T},i,j}(t)\cos\theta_{i,j}(t) - F_{\mathrm{R},i,j}(t)\sin\theta_{i,j}(t)\right] \\ F_{\mathrm{Y_S}}(t) &= \sum_{i,j} g(\theta_{i,j}(t)) \left[F_{\mathrm{T},i,j}(t)\sin\theta_{i,j}(t) - F_{\mathrm{R},i,j}(t)\cos\theta_{i,j}(t)\right] \end{aligned} \quad [1.133]$$

where $g(\theta_{i,j}(t))$ is obtained by substituting the entry angle $\theta_{\mathrm{en},i,j}(t)$ and exit angle $\theta_{\mathrm{ex},i,j}(t)$ into equation [1.15]. Due to the mobility of $\mathrm{X_S Y_S Z_S}$, the transformation into the globally stationary XYZ coordinate system corresponds to

$$\begin{aligned} F_{\mathrm{X}}(t) &= F_{\mathrm{X_S}}(t)\cos\theta_{\mathrm{f}}(t) - F_{\mathrm{Y_S}}(t)\sin\theta_{\mathrm{f}}(t) \\ F_{\mathrm{Y}}(t) &= F_{\mathrm{X_S}}(t)\sin\theta_{\mathrm{f}}(t) + F_{\mathrm{Y_S}}(t)\cos\theta_{\mathrm{f}}(t) \end{aligned} \quad [1.134]$$

Based on the above procedure, the predicted cutting forces are plotted in Figure 1.27 along the entire tool path where the outline of the extreme value variations of the predicted cutting forces indicates that no abrupt change occurs along the entire tool path.

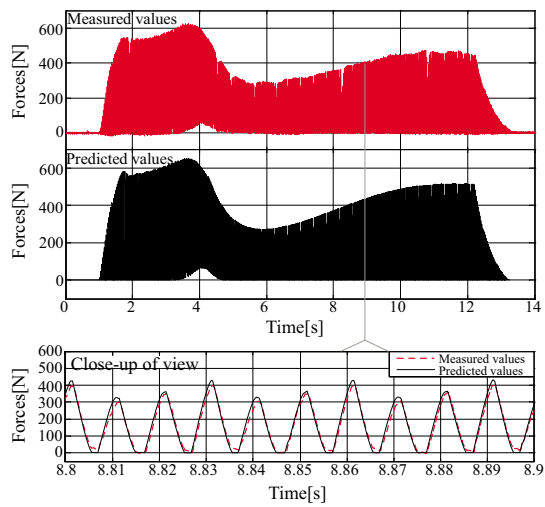

Figure 1.27. *Comparison of the measured and predicted cutting forces in Y-direction vs. time for the entire tool path in test 2($a_p = 10$ mm, $a_e = 3$ mm, $S = 2000$ RMP, $f = 0.05$ mm/tooth). For a color version of this figure, see www.iste.co.uk/zhang/milling.zip*

2

Surface Accuracy in Milling Processes

2.1. Predictions of surface form errors

Advanced manufacturing technologies constitute a basis for productivity improvements in aeronautical and aerospace manufacturing industries. The peripheral milling of thin-walled structural components such as entire girders, aero-engine blades and turbine disks is an important machining process in these industries. Due to the weak rigidity of workpieces, deflections induced by cutting forces inevitably cause surface form errors that will severely deteriorate the accuracy and quality of the workpiece. If the form errors seriously violate the dimensional tolerance, the milling process will lead to waste products. Therefore, reliable machining technologies must be employed to obtain consistent part shapes and the machining accuracy. This can be realized efficiently by numerical simulations combining the finite element method with cutting mechanics, and furthermore by optimizing cutting parameters to improve the cutting process.

In this section, to suit the geometric complexity of the workpiece, it is modeled with irregular finite element meshes that can be generated independently of the cutter. Additionally, based on the idea of the artificial power law used in structural topology optimization, the rigidity variation of the workpiece due to the material removal is updated without remeshing. The proposed approach is finally integrated with an available finite element analysis package. A general approach is developed with an enhancement of the robustness of the numerical procedure and iterative algorithms.

Milling Simulation: *Metal Milling Mechanics, Dynamics and Clamping Principles*,
First Edition. Weihong Zhang and Min Wan.

To be able to calculate the deflections of complex structures in a practical milling process, it is necessary to have a flexible and reliable modeling scheme. The cutter and the workpiece will be modeled independently, i.e. coordinate systems, meshing methods and element types are selected separately according to their own structure characteristics. Suppose XYZ is a local coordinate system which moves with the cutter. Axes Y and Z are aligned with the normal direction of the machined surface and the cutter axis, respectively. Here, the flat helical end mill is modeled as an equivalent cantilevered beam with identical elements along the axial direction [KOP 90]. Notation (i, j) designates the cutter node which is the intersection between one horizontal mesh line and the *i*th cutting edge, while notation $\{i, j\}$ means the *j*th disk element of the *i*th cutting edge, which is the cutting edge segment between cutter node (i, j) and cutter node $(i, j + 1)$, as shown in Figure 2.1. Note that N_e in Figure 2.1 is the total number of cutter elements.

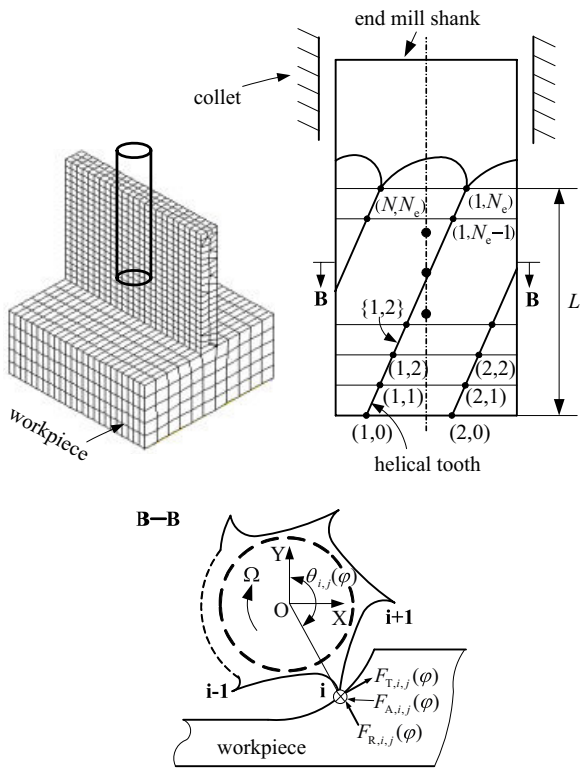

Figure 2.1. *Modeling of the cutter and the workpiece*

The coordinate system of the workpiece can be defined arbitrarily and is independent of that of the cutter. Three dimensional irregular finite element meshes and element types such as tetrahedral elements, prism elements, hexahedral elements or a combination of them can be freely used to discretize the workpiece, e.g. the structure of the workpiece in Figure 2.1. Due to the independent modeling of the cutter and workpiece, a coherence description is made to determine their relative position so that a geometric relationship between the cutting edge and machined surface can be easily identified for the cutting force discretization [WAN 05].

2.1.1. *Calculation of cutting forces and process geometries*

2.1.1.1. *Calculation of cutting forces*

Once three force components related to the cutter element $\{i, j\}$, i.e. $F_{\mathrm{T},i,j}(\varphi)$, $F_{\mathrm{R},i,j}(\varphi)$ and $F_{\mathrm{A},i,j}(\varphi)$, are obtained from equation [1.8] or [1.13], they can be mapped along X, Y and Z directions

$$\begin{bmatrix} F_{\mathrm{X},i,j}(\varphi) \\ F_{\mathrm{Y},i,j}(\varphi) \\ F_{\mathrm{Z},i,j}(\varphi) \end{bmatrix} = g(\theta_{i,j}(\varphi))u_{i,j}\mathbf{T}(\theta_{i,j}(\varphi)) \begin{bmatrix} F_{\mathrm{T},i,j}(\varphi) \\ F_{\mathrm{R},i,j}(\varphi) \\ F_{\mathrm{A},i,j}(\varphi) \end{bmatrix} \quad [2.1]$$

where $g(\theta_{i,j}(\varphi))$ and $\mathbf{T}(\theta_{i,j}(\varphi))$ are calculated by equations [1.15] and [1.75], respectively. $u_{i,j}$ is a correction factor of cutter element $\{i, j\}$ defined as

$$u_{i,j} = z'_{i,j}/z_{i,j} \quad [2.2]$$

with $z'_{i,j}$ being the axial length of cutter element $\{i, j\}$ in contact. For example, one has $u_{i,j} = \overline{\mathrm{EC}}/\overline{\mathrm{ED}}$ for the correction factor of AB shown in Figure 2.2.

After cutting forces are obtained for all engaged cutter elements, they will then be discretized averagely to their adjacent cutter nodes. The obtained nodal forces are further applied equivalently to the workpiece by projecting them onto the nodes of the machined surface.

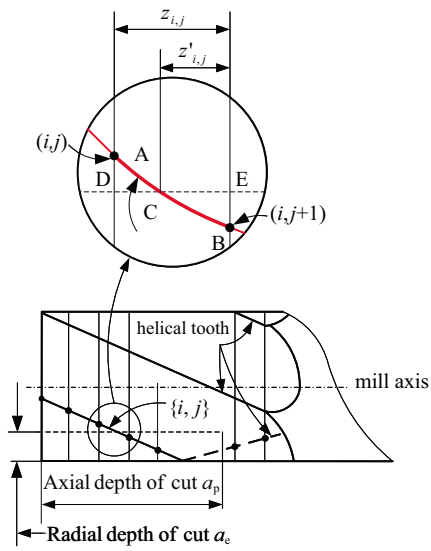

Figure 2.2. *Illustrations of correction factor of the cutting forces*

The discretized cutting force $\bar{\mathbf{f}}_{i,j}$ acting on cutter node (i,j) is approximately obtained as follows

$$\begin{cases} \bar{\mathbf{f}}_{i,j} = \mathbf{F}_{i,j}/2, & j = 0 \\ \bar{\mathbf{f}}_{i,j} = \mathbf{F}_{i,j}/2 + \mathbf{F}_{i,j-1}/2, & j = 1, ..., N_e - 1 \\ \bar{\mathbf{f}}_{i,j} = \mathbf{F}_{i,j-1}/2, & j = N_e \end{cases} \quad [2.3]$$

where $\mathbf{F}_{i,j} = [F_{X,i,j}(\varphi), F_{Y,i,j}, F_{Z,i,j}(\varphi)]$ is the cutting force associated with cutter element $\{i,j\}$, and obtained by equation [2.1]. Hereinto, the first and third expressions correspond to two extreme nodes of the concerned cutter element.

To transfer cutting forces from the cutter to the workpiece, the correspondence between each immersion cutter node and the machined surface node of the workpiece has to be identified instantaneously. This can be done either by finding v numbers of surface nodes of the workpiece, which are near to the immersion cutter node or by identifying on the workpiece a proper v-node grid, to which the immersion cutter node is projected. In this

way, the cutting forces acting on the immersion cutter node are discretized onto the v numbers of nodes of the machined surface. For the purpose of convenience, two approximation schemes are used here to interpolate cutting forces instead of using finite element shape functions.

Distance-based discretization scheme

As shown in Figure 2.3, an immersion cutter node (j, p) is surrounded by v numbers of surface nodes with $v = 4$. According to the distance of the immersion cutter node to the v numbers of surface nodes of the workpiece, the cutting force is discretized approximately by

$$\mathbf{F}_i = \frac{\frac{1}{d_{i,j,p}}}{\sum \frac{1}{d_{k,j,p}}} \overline{\mathbf{f}}_{j,p} \qquad [2.4]$$

in which $d_{i,j,p}$ denotes the distance from the immersion cutter node (j, p) to node i of the workpiece and $\mathbf{F}_i$ denotes the cutting force on the ith surface node after discretization.

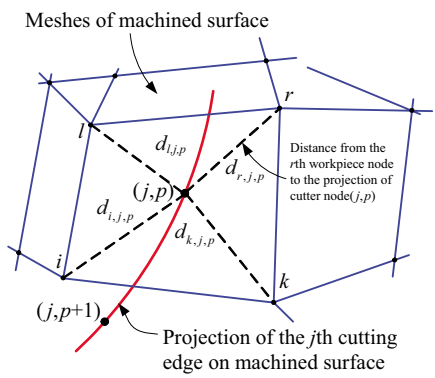

Figure 2.3. *Cutting force discretization*

Averaging force discretization scheme

If the FE model of the workpiece is established with a refined FE mesh, the cutting force can be discretized averagely with a sufficient accuracy by

$$\mathbf{F}_i = \frac{\overline{\mathbf{f}}_{j,p}}{v} \qquad [2.5]$$

However, it is known that deflections of the cutter and of the workpiece as well as the rigidity change of the workpiece strongly influence the cutting forces in the practical milling of thin-walled workpieces. To ensure the computing accuracy, the following studies are performed to suit the complexity of the problem.

2.1.1.2. *Calculation of $\theta_{i,j}(\varphi)$ and $u_{i,j}$*

Obviously, values of $\theta_{i,j}(\varphi)$ and $u_{i,j}$ must be known in advance before computing the cutting forces. To do this, it is necessary to judge whether the concerned cutter element is engaged with the workpiece.

With a given initial configuration of the cutter in the milling process, e.g. down milling shown in Figure 2.4(a), we can see that cutter nodes may be in contact with the workpiece only when rotating to the right side of axis Y. Hence, an angular zone can be defined for each cutter node (i, j) by

$$[\Theta_{\mathrm{l},i,j}, \Theta_{\mathrm{u},i,j}] \qquad [2.6]$$

where $\Theta_{\mathrm{l},i,j}$ and $\Theta_{\mathrm{u},i,j}$ are the entering and leaving angles of cutter node (i, j) with respect to the right side of axis Y, respectively. Note that both bounds will remain unchanged provided that the cutter rotates with entire periods. As shown in Figure 2.4, the initial position of cutter node A(i,j) can be geometrically described by $\xi_{i,j}$ that is defined as an anticlockwise rotation angle from the positive direction of Y to the negative direction of X, whether it is concerned with down milling or up milling. $\xi_{i,j}$ reads

$$\xi_{i,j} = \xi_{1,0} + 2\pi(i-1)/N + jz_{i,j}2\tan\beta/D \qquad [2.7]$$

where N is the tooth number, and $\xi_{1,0}$ is the angular value of node (1,0) in the initial configuration of the cutter. Clearly, the determination of $\Theta_{\mathrm{l},i,j}$ and $\Theta_{\mathrm{u},i,j}$ depends upon $\xi_{i,j}$ and can be made as follows:

a) *Down milling process*

– if cutter node (i, j) is to the left side of axis Y, e.g. at node A in Figure 2.4(a) with $\xi_{i,j} \leq \pi$, then

$$\Theta_{\mathrm{l},i,j} = \xi_{i,j} \qquad \Theta_{\mathrm{u},i,j} = \xi_{i,j} + \pi \qquad [2.8]$$

– if cutter node (i, j) is to the right side of axis Y, e.g. at node A' in Figure 2.4(a) with $\xi_{i,j} > \pi$, then two solutions exist

$$\Theta_{\mathrm{l},i,j} = \xi_{i,j} \qquad \Theta_{\mathrm{u},i,j} = 2\pi \qquad [2.9]$$

and

$$\Theta_{\mathrm{l},i,j} = 0 \qquad \Theta_{\mathrm{u},i,j} = \xi_{i,j} - \pi \qquad [2.10]$$

b) *Up milling process*

The angular zone in the up milling is to the left side of axis Y, as shown in Figure 2.4 (b). We have then

$$\Theta_{\mathrm{l},i,j} = \alpha_{i,j} - \pi \qquad \Theta_{\mathrm{u},i,j} = \xi_{i,j}, \quad \text{if} \quad \xi_{i,j} \geq \pi \qquad [2.11]$$

or alternatively

$$\Theta_{\mathrm{l},i,j} = 0 \qquad \Theta_{\mathrm{u},i,j} = \xi_{i,j}, \quad \text{if} \quad \xi_{i,j} < \pi \qquad [2.12]$$

and

$$\Theta_{\mathrm{l},i,j} = \xi_{i,j} + \pi \qquad \Theta_{\mathrm{u},i,j} = 2\pi, \quad \text{if} \quad \xi_{i,j} < \pi \qquad [2.13]$$

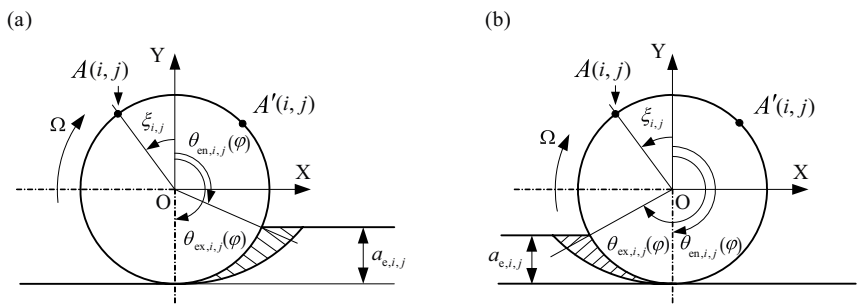

Figure 2.4. *Definitions of contact zones: a) down milling; b) up milling*

Now, it becomes easier to determine whether the cutter element $\{i, j\}$ is engaged with the workpiece. Since the cutter rotation angle φ is periodic, it is limited to $\varphi \in [0,2\pi]$. Therefore, if $\Theta_{\mathrm{l},i,j} \leq \varphi \leq \Theta_{\mathrm{u},i,j}$, it means that cutter

node (i, j) may be engaged with the workpiece. Cutter node (i, j) is therefore engaged with the workpiece provided that

$$\theta_{\mathrm{en},i,j}(\varphi) \leq \theta_{\mathrm{n},i,j}(\varphi) \leq \theta_{\mathrm{ex},i,j}(\varphi) \quad [2.14]$$

where $\theta_{\mathrm{n},i,j}(\varphi)$ means the angle measured clockwise from axis Y to the current position of cutter node (i, j). Specifically, calculations of $\theta_{\mathrm{n},i,j}(\varphi)$ can be performed as follows:

– in down milling, when equation [2.8] or equation [2.9] is retained, one has

$$\theta_{\mathrm{n},i,j}(\varphi) = \varphi - \xi_{i,j} \quad [2.15]$$

Alternatively, if equation [2.10] is verified, one has

$$\theta_{\mathrm{n},i,j}(\varphi) = \varphi - \xi_{i,j} + 2\pi \quad [2.16]$$

As shown in Figure 2.4(a), $\theta_{\mathrm{ex},i,j}(\varphi) = \pi$ while $\theta_{\mathrm{en},i,j}(\varphi)$ depends on the radial depth of cut $a_{\mathrm{e},i,j}$ related to cutter node (i, j).

$$\theta_{\mathrm{en},i,j}(\varphi) = \arccos \frac{2a_{\mathrm{e},i,j} - D}{D} \quad [2.17]$$

– in up milling, one has

$$\theta_{\mathrm{en},i,j}(\varphi) = \pi \qquad \theta_{\mathrm{ex},i,j}(\varphi) = 2\pi - \arccos \frac{2a_{\mathrm{e},i,j} - D}{D} \quad [2.18]$$

If equation [2.11] or equation [2.12] is retained, one has

$$\theta_{\mathrm{n},i,j}(\varphi) = \varphi - \xi_{i,j} + 2\pi \quad [2.19]$$

Otherwise, if equation [2.13] is retained, one has

$$\theta_{\mathrm{n},i,j}(\varphi) = \varphi - \xi_{i,j} \quad [2.20]$$

Therefore, it concludes that cutter element $\{i, j\}$ contacts the workpiece as long as both cutter nodes (i, j) and $(i, j + 1)$ are engaged with the workpiece. Then, following relations hold

$$\theta_{i,j}(\varphi) = \theta_{\mathrm{n},i,j}(\varphi) - \frac{z_{i,j}\tan\beta}{D} \qquad [2.21]$$

and

$$u_{i,j} = 1 \qquad [2.22]$$

If neither cutter node (i, j) nor $(i, j + 1)$ is engaged with the workpiece, cutting forces will not be necessarily computed since $u_{i,j} = 0$. If only cutter node (i, j) contacts the workpiece instead of $(i, j + 1)$, it implies that cutter element $\{i, j\}$ is partially engaged with the workpiece so that $z'_{i,j}$ can be obtained approximately by

$$z'_{i,j} = \frac{(\theta_{\mathrm{n},i,j}(\varphi) - \theta_{\mathrm{en},i,j}(\varphi))D}{2\tan\beta} \qquad [2.23]$$

If cutter node $(i, j + 1)$ contacts the workpiece instead of (i, j), then

$$z'_{i,j} = \frac{(\theta_{\mathrm{ex},i,j+1}(\varphi) - \theta_{\mathrm{n},i,j}(\varphi))D}{2\tan\beta} \qquad [2.24]$$

Finally, note that $u_{i,j}$ and $\theta_{i,j}(\varphi)$ will still be evaluated by means of equation [2.2] and equation [2.21], respectively when the cutter element is partially engaged in last two cases.

2.1.1.3. *Correction of workpiece rigidity due to material removal*

To consider the rigidity change of the workpiece due to the material removal, the idea of softening materials as used in structural topology optimization is implemented [ZHA 03a]. This technique is to correct the element stiffness matrix in terms of its volume variation without remeshing so that

$$K_{\mathrm{st},k} = \varrho_k \overline{K}_{\mathrm{st},k} \qquad [2.25]$$

where $\overline{K}_{\mathrm{st},k}$ is the nominal stiffness matrix of the *k*th element. ϱ_k denotes the ratio of volume variation of the *k*th element after sweeping with

$$\varrho_k = \frac{\Delta V_k}{V_k}, \qquad (10^{-6} = \varepsilon_1 \leq \varrho_k \leq 1) \tag{2.26}$$

in which ΔV_k and V_k designate the remaining and nominal volume of the *k*th element before and after cutting, respectively. Here, a lower bound ε_1 is used to prevent the singularity of the element stiffness matrix when the material is completely removed in milling. The determination of ϱ_k is made in two basic steps:

1) *Identification of the element status of the workpiece*

An element status depends on its relative position with respect to actual radial cutting depth. For an element, if distances calculated from all its nodes to the machined surface are less than the actual radial cutting depths at corresponding machined surface positions, it means that this element is cut off completely; if distances are more than the corresponding radial cutting depths, the element is not cut off at all; if only some distances are less than the corresponding radial cutting depths, the element is cut off partially. As shown in Figure 2.5, distances of nodes P_0 and P_1 to the machined surface are d_0 and d_1, respectively. P_0 and P_1 have a common projection to P_n so that the same radial cutting depth a_e can be used. In this case, the k_1th element is cut off completely with $\varrho_{k_1} = \varepsilon_1$ because distances of all attached nodes are less than corresponding radial depths. The k_2th element is partially cut off because $d_0 < a_\mathrm{e}$ and $d_1 > a_\mathrm{e}$. The k_3th element is not cut at all so that $\varrho_{k_3} = 1$.

2) *Identification of the cutting boundary for partially cut-off elements*

Based on the obtained radial cutting depths from equation [2.29], the cutting boundary can be determined by finding its intersection with all edges of elements being partially cut off. For example, when it is concerned with edge $\overline{\mathrm{P}_0\mathrm{P}_1}$ of the k_2th element, we can write

$$a_\mathrm{e} = d_0 + (d_1 - d_0)\varsigma \qquad \text{with} \qquad 0 < \varsigma < 1 \tag{2.27}$$

If such a parameter ς exists, the intersection point is then

$$\mathbf{P} = \mathbf{P}_0 + (\mathbf{P}_1 - \mathbf{P}_0)\varsigma \tag{2.28}$$

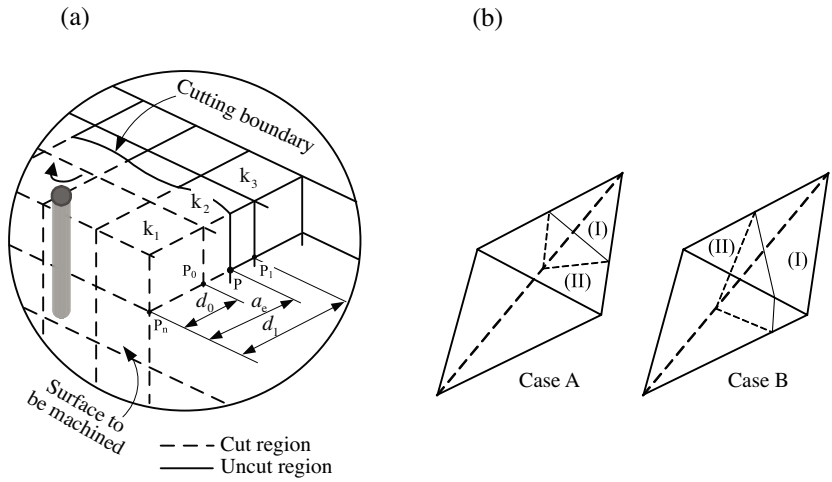

Figure 2.5. *Correction of workpiece rigidity due to material removal; a) corrections of the element stiffness; b) partially cut-off cases for tetrahedral element*

As illustrated in Figure 2.5(b), a summary of all possible cutting cases is presented for tetrahedral elements. Each element is partitioned into (I) and (II), and either of two parts can be retained as the remaining one.

To simplify the calculation of volume variations, it is necessary to remark that element edges will be approximated by straight-line segments when they are curved ones. After the rigidity of the workpiece is modified, the same numerical procedure that stabilizes oscillations as described above will be used to evaluate the actual cutting forces.

2.1.2. *Iterative algorithms of surface form errors*

2.1.2.1. *Development of algorithms*

As shown in Figure 2.6, due to the existence of deflections caused by the cutting forces, the ideal contact curve AB will be shortened to QB. Meanwhile, the nominal intersection line DF between the cutter and the workpiece will be shifted to EH. As a result, for any engaged cutter node, the radial depth of cut, instantaneous uncut chip thickness and the immersion angle will be deviated from their nominal values.

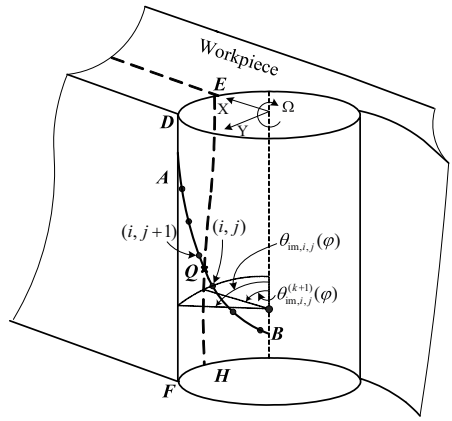

Figure 2.6. *Illustration of immersion angle. Note that $\theta_{\mathrm{im},i,j}(\varphi)$ is the immersion angle related to cutter node (i,j)*

From this point of view, for cutter node (i,j) at any cutting position, the radial depth of cut is corrected by

$$a_{\mathrm{e},i,j}^{(k+1)} = a_{\mathrm{e},i,j} - [\delta_{\mathrm{t,Y},i,j}^{(k)} + \delta_{\mathrm{w,Y},i,j}^{(k)}]$$
$$s.t. \qquad [2.29]$$
$$\left| a_{\mathrm{e},i,j}^{(k+1)} - a_{\mathrm{e},i,j}^{(k)} \right| \leq \varepsilon_2 \qquad k = 0, 1, \cdots, n$$

where $a_{\mathrm{e},i,j}^{(k+1)}$ and $a_{\mathrm{e},i,j}$ are the corrected and radial depths of cut for cutter node (i,j). k stands for the number of iterations. $\delta_{\mathrm{t,Y},i,j}^{(k)}$ and $\delta_{\mathrm{w,Y},i,j}^{(k)}$ denote the normal deflections of cutter node (i,j) and the workpiece at the cutting position after the kth iteration, respectively. ε_2 is the prescribed tolerance to control the iteration process.

As shown in Figure 2.6, due to the deflection, a certain number of cutter disk elements that should be completely in cut becomes now partially engaged, e.g. $\{i,j\}$. The actual contact axial length $z'^{(k+1)}_{i,j}$ can be written as

$$z'^{(k+1)}_{i,j} = u_{i,j}^{(k+1)} z_{i,j}$$

where $u_{i,j}^{(k+1)}$ denotes the correction factor in the (k+1)th iteration defined as

$$u_{i,j}^{(k+1)} = \frac{(\theta_{\mathrm{im},i,j}^{(k+1)}(\varphi) + \theta_{\mathrm{n},i,j}(\varphi) - \pi)D}{2z_{i,j}\tan\beta} \quad [2.30]$$

where $\theta_{\mathrm{im},i,j}^{(k+1)}(\varphi)$ denotes the variation of the immersion angle related to cutter node (i, j) and it can be evaluated in terms of $a_{\mathrm{e},i,j}^{(k+1)}$ by

$$\theta_{\mathrm{im},i,j}^{(k+1)}(\varphi) = \arccos(1 - \frac{a_{\mathrm{e},i,j}^{(k+1)}}{r_{i,j}}) \quad [2.31]$$

The instantaneous uncut chip thickness is iterated as

$$h_{i,j}^{(k+1)}(\varphi) = -\Lambda^{(k)}\cos\Upsilon^{(k)} + r_{i,j} - r_{i-m,j} \quad [2.32]$$

with

$$\Lambda^{(k)} = \sqrt{(mf + \delta_{\mathrm{t,X},i,j}^{(k)} - \delta_{\mathrm{t,X},i-m,j}^{(k)})^2 + (\delta_{\mathrm{t,Y},i,j}^{(k)} - \delta_{\mathrm{t,Y},i-m,j}^{(k)})^2} \quad [2.33]$$

$$\Upsilon^{(k)} = \pi - \theta_{i,j}(\varphi) + \arccos\left(\frac{\delta_{\mathrm{t,Y},i,j}^{(k)} - \delta_{\mathrm{t,Y},i-m,j}^{(k)}}{\Lambda^{(k)}}\right) \quad [2.34]$$

Equation [2.32] is the so-called numerical scheme for regeneration phenomenon simulation. During the iteration procedure of equation [2.29], numerical oscillations may however occur because the variation of radial cutting depth is found to be very practical. The increase of radial cutting depth in the previous iteration will directly lead to an increase of cutting forces and deflections in the current iteration. Consequently, the radial cutting depth will decrease after one iteration step. In the subsequent iterative steps, such a decrease will lead to the increase of radial depth. These phenomena can be seen schematically in Table 2.1. Therefore, the iteration scheme of equation [2.29] may be divergent and values of the radial cutting depth will be in oscillation. The similar phenomenon can also be found in equation [2.32].

Iteration No.	Variation tendency of cutting forces	Variation tendency of $a_{e,i,j}^{(k)}$
1	-	$\downarrow$
2	$\downarrow$	$\uparrow$
3	$\uparrow$	$\downarrow$
4	$\downarrow$	$\uparrow$
...	...	...

Table 2.1. *Variations of cutting forces and radial depth of cut*

To avoid the divergence, following sub-iteration algorithms are adopted:

– a relatively small change of the chip thickness is used

$$\tilde{h}_{i,j}^{(k+1)}(\varphi) = \epsilon_1 \cdot (h_{i,j}^{(k+1)}(\varphi) - \tilde{h}_{i,j}^{(k)})(\varphi) + \tilde{h}_{i,j}^{(k)}(\varphi) \qquad 0 < \epsilon_1 \leq 1 \qquad [2.35]$$

where $\tilde{h}_{i,j}^{(k+1)}(\varphi)$ is the corrected value of the uncut instantaneous chip thickness for cutting force calculation in the (k+1)th iteration. $h_{i,j}^{(k+1)}(\varphi)$ is the value of the instantaneous uncut chip thickness. ϵ_1 is the weighted parameter given *a priori*.

– the oscillation of radial depth of cut is presented as follows.

Case 1: *Single cutter element in oscillation*

As shown in Figure 2.7, suppose that the cutter element $\{i, j\}$ is engaged partially in contact with the workpiece. Because cutter/workpiece deflections lead to a relatively large variation of radial depth of cut $a_{e,i,j}^{(k)}$, the correction factor $u_{i,j}$ defined in equation [2.2] may be divergent as illustrated in Figure 2.8. To solve this problem, a sub-iterative scheme is firstly adopted to stabilize $u_{i,j}$.

$$\begin{aligned}
&\tilde{u}_{i,j}^{(k+1)} = \epsilon_2 \cdot (u_{i,j}^{(k+1)} - \tilde{u}_{i,j}^{(k)}) + \tilde{u}_{i,j}^{(k)} \\
&u_{i,j}^{(k+1)} = \frac{z_{i,j}^{(k+1)}}{z_{i,j}} \\
&s.t. \\
&0 < \epsilon_2 \leq 1 \\
&\left| \tilde{u}_{i,j}^{(k+1)} - u_{i,j}^{(k+1)} \right| \leq \varepsilon_3
\end{aligned} \qquad [2.36]$$

where $\tilde{u}_{i,j}^{(k+1)}$ is the corrected value of the correction factor for cutting force calculation in the (k+1)th iteration. $u_{i,j}^{(k+1)}$ and $z_{i,j}^{(k+1)}$ are the actual values of the correction factor and the axial contacting length related to cutter element $\{i, j\}$, respectively. ϵ_2 is the weighted parameter given *a priori*. ε_3 is the prescribed tolerance to control the iteration.

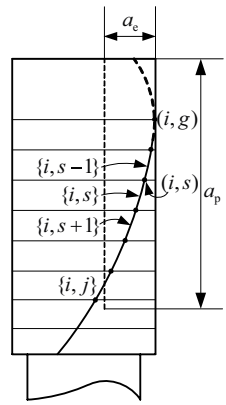

Figure 2.7. *Illustration of partially engaged cutter elements*

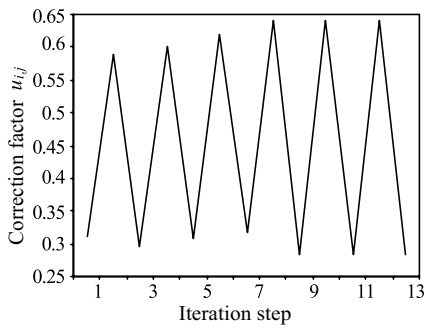

Figure 2.8. *Oscillation of a single correction factor* $u_{i,j}$

Case 2: *Multiple cutter elements in oscillation*

Some cutter elements, e.g. $\{i, s\}$,$\{i, s + 1\}$,...,$\{i, j\}$ shown in Figure 2.7, may also be engaged in cutting in the current iteration and disengaged in

the next one. In this case, the following procedure is proposed to ensure the convergence of the iteration scheme:

a) Assume that cutter elements from $\{i, s+1\}$ to $\{i, j\}$ are not engaged in cutting. So, set $a_{\mathrm{e},i,l}^{(k)} = 0$ for all $(s+1 \leq l \leq j)$;

b) Start the iterative process of equations [2.35] and [2.36] for the cutter element $\{i, s\}$ with $\tilde{u}_{i,s}^{(k+1)}$until the convergence is reached;

c) If $0 \leq \tilde{u}_{i,s}^{(k+1)} < 1$, the convergence achieves for all cutter elements and stop the iteration. Otherwise, continue step (b) by setting $s = s+1$ and $a_{\mathrm{e},i,s}^{(k)} = a_{\mathrm{e},i,s-1}^{(k)}$.

After $\tilde{u}_{i,s}^{(k+1)}$ is updated, the axial depth of the cut will be corrected correspondingly. Note that Case 1 and Case 2 discussed above correspond to the down milling process. In the up milling process, Case 1 is still applicable. Instead, the oscillation will happen for cutter elements near the cutter tip in Case 2. Therefore, oscillating cutter elements, e.g. $\{i, s\}, \{i, s-1\}, ..., \{i, j\}$ are needed to be identified sequentially as performed in down milling.

Note that after the radial dept of cut is corrected, the axial depth of the cut will be corrected correspondingly. The surface form error can be defined as the normal deviation of the final machined surface from the desired machined surface. In the peripheral milling process, the cutter/workpiece deflections in the direction normal to the machined surface constitute the form errors. At a certain position P, as shown in Figure 2.9, the surface form error e_{P} is evaluated by

$$e_{\mathrm{P}} = \delta_{\mathrm{t,Y},i,j} + \delta_{\mathrm{w,Y},i,j} \qquad [2.37]$$

where the cutter deflection $\delta_{\mathrm{t,Y},i,j}$ is calculated according to cantilevered beam theory, while the deflection of the workpiece, $\delta_{\mathrm{w,Y},i,j}$, is calculated using the finite element analysis (FEA) method. It should be mentioned that in fact, as the presence of cutter runout leads to the non-uniform distributions of cutting forces in different tooth periods, the cutting force-induced deflections will be different in different tooth period. Therefore, the combination effect of error curves associated with each tooth period must be considered in the determination of final surface dimensional error distribution. To do this, the final surface dimensional error is achieved by

finding the maximal value envelope from the error superposition curve section of all teeth, as illustrated in Figure 2.10.

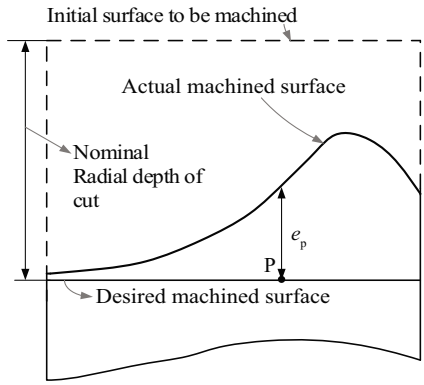

Figure 2.9. *Definition of the surface form error*

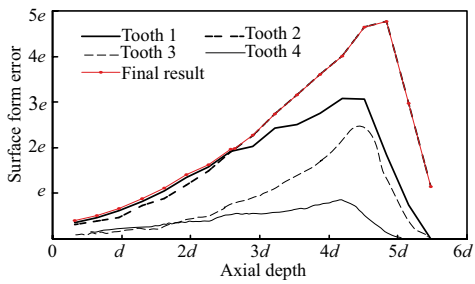

Figure 2.10. *Constitution of the surface form error for a four-fluted end mill. For a color version of this figure, see www.iste.co.uk/zhang/milling.zip*

To estimate values of surface form errors along the tool path, the milling trajectory is firstly split into a sequence of discrete cutting locations. Surface form errors along each surface generation line will be calculated at the current cutting location before the cutter shifts to the next one. At the same time, rigidities of elements swept between these two adjacent locations are corrected as illustrated in the previous section. This routine continues until analyses of all locations are finished.

It is well recognized that the cutting forces are strongly influenced by the deflections of cutter and workpiece as well as the rigidity variation of the workpiece due to material removal. In different situations, two available models are selected to calculate the form errors:

1) *Rigid model*: it is a simplified model in which the cutter/workpiece deflections and the workpiece rigidity change caused by the material removal are ignored. The form errors will be calculated directly based on the nominal cutting parameters.

2) *Flexible model*: both the cutter/workpiece deflections and the workpiece rigidity change induced by material removal are taken into account. At any cutting instant, the proposed iteration algorithm is used to correct the radial depth of cut and the instantaneous uncut chip thickness.

2.1.2.2. *Example and experimental verification*

A carbide flat end mill with identical diameter of 20 mm and a helix angle of 30° is adopted to cut aluminum alloy 7050. Note that the cutter is a single-fluted flat end mill, which is designed to eliminate the runout effect on form error distributions. A cantilever plate with a dimension of $102\ \text{mm} \times 29.4\ \text{mm} \times 2.21\ \text{mm}$ is used to validate the proposed cutting force model. 3D finite element meshes are used to discretize the workpiece. The cutter has a tool gauge length of 61 mm and is discretized into 61 axial elements. The Young's moduli of the cutter and the workpiece are 600 GPa and 71.7 GPa, respectively. The flexibility of the plate is considerable when the cutting is carried out with a radial depth of 0.95 mm and axial depth of cut of 29 mm. Cutting forces are measured with a Kistler 9255B dynamometer.

Figure 2.11 shows the form errors along the cutter axial direction at two feed stations of both plates predicted by the present simulation model and measured by experiment. It can be seen that the results predicted by the rigid model and the flexible model have a good coherence in the variation tendency when compared with the experimental data. In particular, the flexible model is shown to be more reliable because the material removal and the coupling effect are considered. By comparing Figure 2.11(a) with Figure 2.11(b), it is found that both predicted and measured results indicate increasing trend in the form error amplitudes in the feed direction. This is due to the decreasing stiffness of the workpiece as a result of material removal. Additionally, the iteration history of correction factor $u_{1,16}$ in down milling is shown in

Figure 2.12 when the cutter has a rotation of 26.65° from the feed position 42 mm. The iteration scheme is very efficient because it is stabilized after only a few steps.

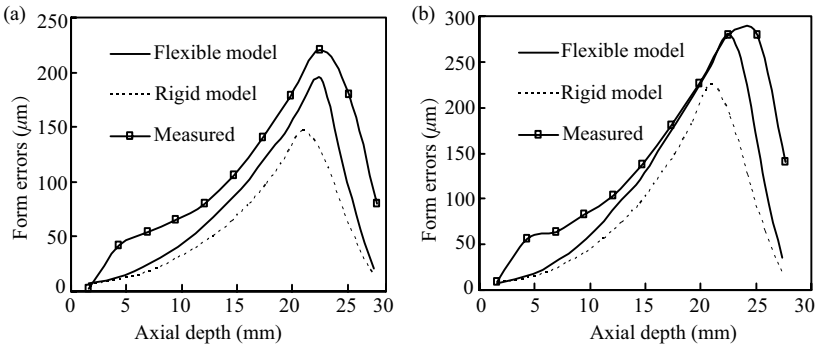

Figure 2.11. *Surface form errors: a) when the cutter feeds 42mm; b) when the cutter feeds 90 mm*

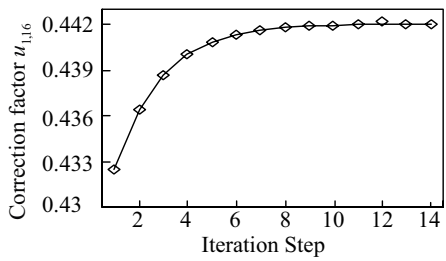

Figure 2.12. *Iteration history of correction factor* $u_{1,16}$

2.2. Control strategy of surface form error

2.2.1. *Development of control strategy*

The aim is to develop method for the reduction of the surface form error so that the surface quality could meet the requirement of the prescribed tolerance. Traditionally, this is done by using mirror error compensation

method to correct the nominal cutter path. According to this method, as shown in Figure 2.13, if the cutter deflection is e, the nominal cutter path will be offset to a distance of e in the opposite direction of the deflection. However, this kind of method may still be unable to ensure that the maximum and minimum values of the surface form errors is in the range of error tolerance.

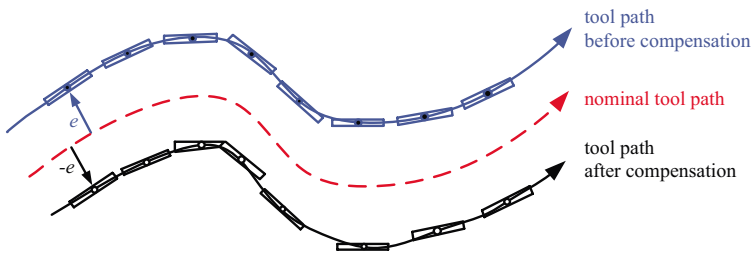

Figure 2.13. *Mirror compensation method*

In fact, to solve this problem, the key issue is to ensure the machining precision and the productivity by optimally selecting the feed rate and radial depth of cut for the maximum feed per tooth and tolerance feasibility. In the following content, a bi-parameter-based optimization will be described in detail. The aim is to increase the cutting efficiency and satisfy the tolerance in the meantime. Mathematically, the design model is to find optimal values of f and a_e that maximize f subjected to the tolerance condition and parameter bounds.

$$\begin{aligned} &\min \quad -f \\ &s.t. \\ &c_{\min} \le e_{\max} \le c_{\max} \\ &c_{\min} \le e_{\min} \le c_{\max} \\ &f_{\min} \le f \le f_{\max} \\ &a_{e,\min} \le a_e \le a_{e,\max} \end{aligned} \qquad [2.38]$$

where $c_{\max}$ and $c_{\min}$ denote the given maximum and minimum bounds of the surface form error tolerance. $f_{\max}$ and $f_{\min}$ are the upper and lower bounds of f, respectively. $a_{e,\max}$ and $a_{e,\min}$ are the upper and lower bounds of a_e, respectively.

To solve this problem, the key is to approximately develop the explicit expressions of $e_{\max}$ and $e_{\min}$ in terms of f and a_{e}. For this reason, it is interesting to study the following test case. Consider a three-fluted flat end mill with a diameter of 16 mm and a helix angle of 30° to cut aluminum alloy 7050. Dynamometer Kistler 9255B is used to measure the cutting forces. Cutting conditions are listed in Table 2.2. All tests are realized without coolant. Test 1 is used to cut a thick block for calibrating the cutting force coefficients and cutter runout. Test 2 and Test 3 are selected for model verification with the flexible cantilever rectangle plate of dimension 107.7 mm $\times$ 29 mm $\times$ 1.85 mm. The cutter runout offset ρ and its location angle λ are calibrated as 28.85 μm and 91.12°, respectively.

Test No.	Wokpiece material	Feed per tooth f (mm/tooth)	Axial depth of cut a_{p} (mm)	Radial depth of cut a_{e} (mm)
1	AL 7050	0.133	1	8
2	AL 7050	0.02	28	0.8
3	AL 7050	0.00487	28	0.855

Table 2.2. *Cutting conditions*

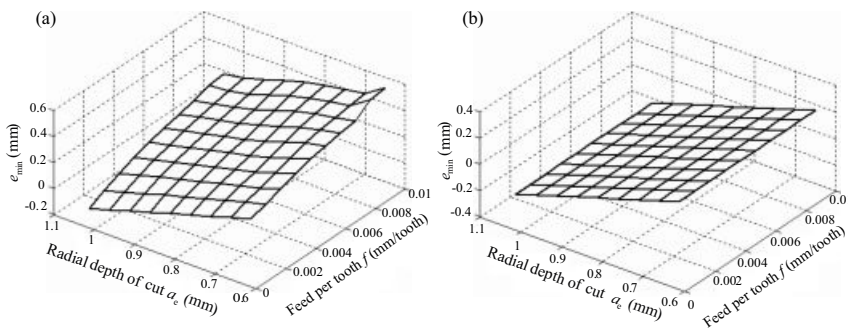

Figure 2.14. *The distributions of $e_{\max}$ and $e_{\min}$ v.s. a_{e} and f; a) $e_{\max}$ and b) $e_{\min}$*

The initial and the desired dimensions of the workpiece used in Test 2 are considered as the machining requirements to show the distributions of $e_{\max}$ and $e_{\min}$ vs. f and a_{e}. a_{e} and f are chosen to vary from 0.65 mm to 1.05 mm and from 10^{-6} mm/tooth to 0.01 mm/tooth, respectively. The simulation results corresponding to the surface generation line where the cutter feeds 3 mm are shown in Figure 2.14. It can be found that both $e_{\max}$ and $e_{\min}$ are

approximately distributed in a planar surface over the considered region. This phenomenon indicates that $e_{\max}$ and $e_{\min}$ can be locally treated as linear functions of a_e and f. The same observations can also be made in other cutting conditions and feed positions. Thus, following relations hold.

$$\begin{aligned} e_{\max} &= A_{11} f + A_{12} a_e + A_{13} \\ e_{\min} &= A_{21} f + A_{22} a_e + A_{23} \end{aligned} \qquad [2.39]$$

where A_{ij}(i=1,2; j=1,2,3) are unknown coefficients that can be determined using the finite difference scheme in the following way.

$$\begin{aligned} A_{11} &= (e_{\max 3} - e_{\max 1})/\Delta f_1 \\ A_{12} &= (e_{\max 2} - e_{\max 1})/\Delta a_{e,1} \\ A_{13} &= e_{\max 1} - (A_{11} f_1 + A_{12} a_{e,1}) \\ A_{11} &= (e_{\min 3} - e_{\min 1})/\Delta f_1 \\ A_{12} &= (e_{\min 2} - e_{\min 1})/\Delta a_{e,1} \\ A_{23} &= e_{\min 1} - (A_{21} f_1 + A_{22} a_{e,1}) \end{aligned} \qquad [2.40]$$

where $a_{e,1}$ and f_1 are selected radial depth of cut and feed rate satisfying $a_{e,\min} \leq a_{e,1}, a_{e,2} \leq a_{e,\max}$ and $f_{\min} \leq f_1, f_2 \leq f_{\max}$. Assume that $a_{e,2} = a_{e,1} + \Delta a_{e,1}$, $f_2 = f_1 + \Delta f_1$. Note that $e_{\max 1}$ and $e_{\min 1}$ are related to $a_{e,1}$ and f_1; $e_{\max 2}$ and $e_{\min 2}$ are related to $a_{e,2}$ and f_1; $e_{\max 3}$ and $e_{\min 3}$ are related to $a_{e,1}$ and f_2.

Based on equation [2.39], equation [2.38] can be easily solved as a linear programming problem. Note that, as mentioned above, $e_{\max}$ and $e_{\min}$ are linearly approximated over a local design region; hence, it is necessary to update the approximation on the new design point in an iterative way. This means that the coefficients A_{ij} involved in equation [2.39] need to be re-evaluated iteratively. Detailed optimization procedure is shown in Figure 2.15, whose key steps are summarized below:

1) set the initial values of $a_{e,1}$ and f_1;

2) calculate A_{ij} by means of equation [2.40];

3) solve equation [2.38] as a linear programming problem;

4) attribute the obtained a_e and f to $a_{e,1}$ and f_1 for the next iteration;

5) repeat Steps(2) and (3);

6) steps (2) to (5) are repeated until the error between two iterative results of f attains the prescribed precision.

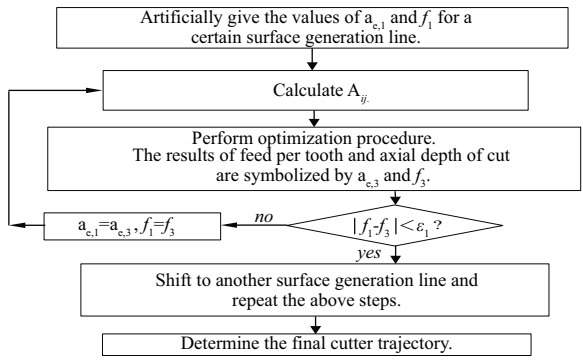

Figure 2.15. *Optimization algorithm for surface form error control*

2.2.2. *Verification of control strategy*

The cutting conditions given in Table 2.2 are used to validate the control strategy. The nominal radial depth of cut is 0.8 mm. The tolerance parameters $c_{\max}$ and $c_{\min}$ are set to be +0.2 mm and -0.05 mm, respectively. Test 2 is carried out with the nominal radial depth of cut, i.e. 0.8 mm, and the initial value of feed per tooth being 0.02 mm/tooth. Test 3 is carried out with the optimized radial depth of cut and the feed per tooth. For the proposed method, suppose that $f_{\max} = 0.01$ mm/tooth, $f_{\min} = 0$ mm/tooth, $a_{e,\max} = 1.05$ mm, $a_{e,\min} = 0.65$mm, $\Delta f_1 = 0.005$ mm/tooth and $\Delta a_{e,1} = 0.03$ mm.

The iteration histories of a_e and f are illustrated in Figure 2.16. It can be seen that the control strategy is time-saving due to the automatic optimization. After convergence, the optimal results are: $a_e = 0.856$ mm and $f = 0.00675$ mm/tooth. Note that Figure 2.16 just corresponds to the surface generation line when the cutter feeds 3 mm. For the whole milling surface of the workpiece, all surface generation lines must be considered. Instead of interpolation, the

radial depth of cut along the cutter trajectory is set to be the minimum value of the optimized results, i.e. $a_e = 0.855$ mm, for the sake of simplification. The final result of f equals 0.00487 mm/tooth. These are set to be the cutting parameters of Test 3.

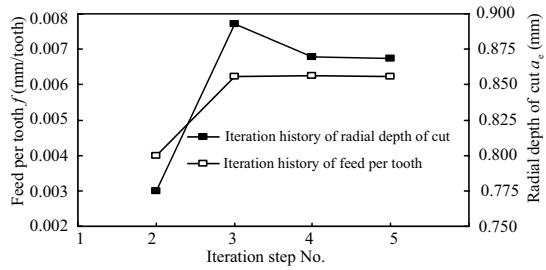

Figure 2.16. *Iteration histories of a_e and f*

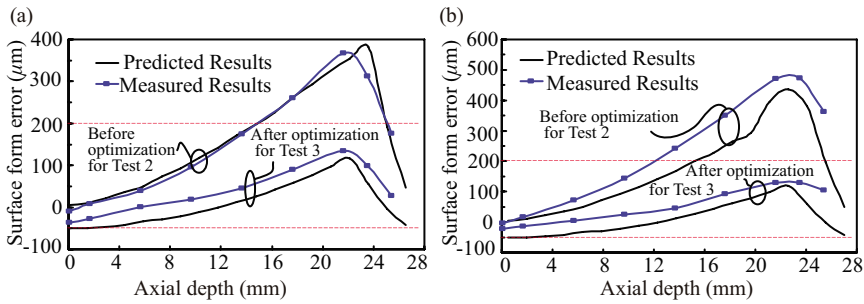

Figure 2.17. *Distributions of surface form errors at the specified surface generation lines; a) when the cutter feeds 20 mm; b) when the cutter feeds 80 mm. For a color version of this figure, see www.iste.co.uk/zhang/milling.zip*

Figure 2.17 shows the predicted and measured surface form errors along the cutter axial depth at two feed positions of Test 2 and Test 3 before and after optimization. It can be seen that the predicted results have a relative good coherence in the variation tendency and magnitude when compared with the experimental data. This turns out that the error model proposed in section 2.2.1 is reliable. It can be seen that all errors are in the tolerance interval after optimization. This means that the proposed strategy is able to find the best

appropriate cutting parameters for the requirements of tolerance and productivity.

2.3. Surface topography in milling processes

In the milling simulation, finding the machined surface topography, the geometric shape and texture of machined surface, is essential since the latter affects directly the surface quality, especially the surface roughness. For a ball end milling process, the surface topography also affects the cutting force and chip load calculations.

This chapter presents a general numerical method to simulate the machined surface topography and roughness in milling process. The key issue related to the proper parameter initialization and computing scheme is investigated to ensure the convergence and efficiency of the iteration process. Effects of milling parameters upon the surface roughness are analyzed. This method has the advantage of simplicity and it is a mesh-independent direct computing method over the traditional interpolation scheme. Firstly, the trajectory equation system of the cutting edge relative to the workpiece in the milling process is formulated with the illustration of the height of the cut remainder. Then, numerical methods are developed to solve the equation system for end and ball end milling. Finally, some examples are studied to evaluate the topography and roughness. Results are compared with corresponding experimental ones. In addition, the developed algorithm also has the advantage of determining the tool position whenever the machined surface is generated in any desired node. This will be helpful in the prediction of form errors due to machining deformation.

In the milling process, the machined surface quality depends upon a variety of factors, e.g. tool geometry, tool path, cutter runout, material properties of the workpiece, vibration of the overall machine system, etc. In this chapter, an analytical model is proposed for the prediction of the topography of the generated surface.

Firstly, consider an arbitrary contour mill and machined surface illustrated in Figure 2.18. Under the premise of disregarding the influence of material properties of the workpiece and the tool, vibration of the machine system, the machined surface topography mainly depends on the tool geometry, tool path and cutter runout. In order to facilitate the description of the relative motion

relationship between the blade of the cutter and workpiece in the milling process, a set of coordinate systems are established *a priori*, as shown in Figure 2.18.

1) $O_W X_W Y_W Z_W$ represents a reference coordinate system fixed on the workpiece;

2) $O_A X_A Y_A Z_A$ is the local coordinate system fixed on the spindle of the milling machine;

3) $O_C X_C Y_C Z_C$ is the local coordinate system fixed on the cutter. The cutter revolves round the spindle, i.e. axis Z_A, with the angle speed Ω;

4) $O_C X_i Y_i Z_i$ is defined as the local coordinate system attached to the ith cutting edge;

5) $O_N X_N Y_N Z_N$ is the local coordinate system whose origin is located at node O_N on the machined surface with axis Z_N being the normal vector of the machined surface at O_N.

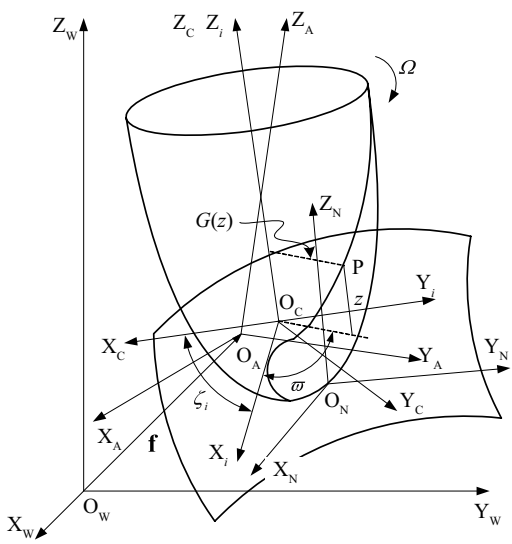

Figure 2.18. *Coordinate systems in the milling process*

In addition, **f** is the feed vector. ζ_j is the angle between the axis X_i and axis X_C. In the coordinate system $O_C X_i Y_i Z_i$, let ϖ and z be curvilinear parameters,

then the coordinates of a given point P on the ith cutting edge can be expressed by [XU 01]

$$(G(z(\varpi))\cos\varpi, G(z(\varpi))\sin\varpi, z(\varpi)) \quad [2.41]$$

where $G(z)$ is parametric equation of the generator.

Based on these coordinate systems and the expression in equation [2.41], the trajectory equations of point P in the local coordinate system $O_N X_N Y_N Z_N$ can be obtained through a series of coordinate transformations as follows

$$\begin{cases} x = x(\varpi, t) \\ y = y(\varpi, t) \\ z = z(\varpi, t) \end{cases} \quad [2.42]$$

Based on the geometrical characteristics of the cutting edge and the tool path, the topography corresponds to the z-value with such ϖ and time t satisfying the following equation system

$$\begin{cases} x(\varpi, t) = 0 \\ y(\varpi, t) = 0 \end{cases} \quad [2.43]$$

Generally, because solutions of ϖ and t are not unique, multiple values of z can be obtained after substituting ϖ and t into $z = z(\varpi, t)$. By definition, the topography value that we have to evaluate refers to the minimum of z. In the following sections, discussions will focus on the topography simulations of end milling and ball end milling processes, respectively.

2.3.1. *Prediction method for flat-end milling*

2.3.1.1. *Derivation of a simulation algorithm*

In this section, numerical simulation and prediction method for flat end milling are investigated in detail. Without the loss of generality, the effect of spindle runout is included in the topography simulation. Based on the above rule, the involved set of coordinate systems is established, as shown in Figure 2.19:

1) $O_W X_W Y_W Z_W$ represents a reference coordinate system attached to the workpiece;

2) $O_A X_A Y_A Z_A$ is the local coordinate system attached to the main-shaft of the mill machine. Axis Z_A is along the main-shaft. Axes X_A and Y_A are parallel to axes X_W and Y_W, respectively. $\mathbf{T}(x_T, y_T, z_T)$ is the initial position of the origin O_A;

3) $O_C X_C Y_C Z_C$ is the local coordinate system fixed on the cutter. Axis Y_C and the vector of spindle runout, ρ, are superposed. The cutter revolves with the angle speed Ω round the spindle, i.e. axis Z_A. The angle between axis Y_C and Y_A is $\Omega t + \Omega_I$, with Ω_I being the initial angle;

4) $O_C X_i Y_i Z_i$ denotes the local coordinate system attached to the ith cutting edge. Axis X_i intersects with the ith cutting edge and the angle between axis X_i and X_C is ζ_j;

5) $O_N X_N Y_N Z_N$ is the local coordinate system of the given node O_N (x_N, y_N, z_N)on the machined surface. Axis Y_N is along the feed direction.

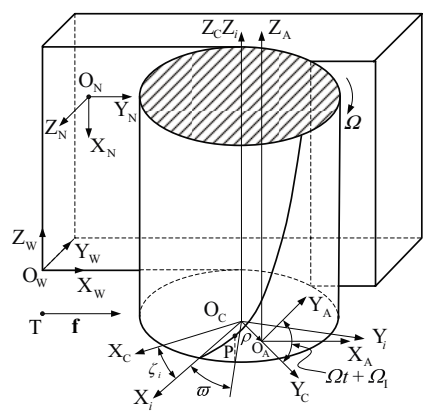

Figure 2.19. *Coordinate systems in end milling process*

In the coordinate system $O_C X_i Y_i Z_i$, consider an arbitrary point P on the ith cutting edge, whose coordinates are expressed as

$$[x \quad y \quad z \quad 1]_i^T = [\frac{D\cos\varpi}{2} \quad \frac{D\sin\varpi}{2} \quad \frac{D\varpi}{2\tan\beta} \quad 1]_i^T \qquad [2.44]$$

The latter can be expressed in the coordinate system $O_N X_N Y_N Z_N$ through coordinate transformation.

$$[x \quad y \quad z \quad 1]_{\mathrm{N}}^{\mathrm{T}} = \mathbf{T}_{\mathrm{M}} [x \quad y \quad z \quad 1]_i^{\mathrm{T}} \qquad [2.45]$$

with $\mathbf{T}_{\mathrm{M}}$ being the overall transformation matrix

$$\mathbf{T}_{\mathrm{M}} = \begin{bmatrix} 0 & 0 & -1 & -z_T + z_N \\ -\sin(\Omega t + \Omega_{\mathrm{I}} - \zeta_j) & \cos(\Omega t + \Omega_{\mathrm{I}} - \zeta_j) & 0 & \rho\cos(\Omega t + \Omega_{\mathrm{I}}) + f_{\mathrm{t}} t + y_{\mathrm{T}} - y_{\mathrm{N}} \\ \cos(\Omega t + \Omega_{\mathrm{I}} - \zeta_j) & \sin(\Omega t + \Omega_{\mathrm{I}} - \zeta_j) & 1 & \rho\sin(\Omega t + \Omega_{\mathrm{I}}) + x_{\mathrm{T}} - x_{\mathrm{N}} \\ 0 & 0 & 0 & 1 \end{bmatrix} \qquad [2.46]$$

where f_{t} means the feed rate, mm/s.

By inserting equation [2.44] and equation [2.46] into equation [2.45], the equation system reads

$$\begin{bmatrix} x \\ y \\ z \end{bmatrix} = \begin{bmatrix} \frac{-D\varpi}{2\tan\beta} - z_{\mathrm{T}} + z_{\mathrm{N}} \\ -R\sin(\Omega t + \Omega_{\mathrm{I}} - \zeta_i - \varpi) + \rho\cos(\Omega t + \Omega_{\mathrm{I}}) + f_{\mathrm{t}} t + y_{\mathrm{T}} - y_{\mathrm{N}} \\ R\cos(\Omega t + \Omega_{\mathrm{I}} - \zeta_i - \varpi) + \rho\sin(\Omega t + \Omega_{\mathrm{I}}) + x_{\mathrm{T}} - x_{\mathrm{N}} \end{bmatrix} \qquad [2.47]$$

To evaluate the minimum value of z for the topography, ϖ will be firstly obtained in a closed form by solving $x(\varpi, t) = 0$. From equation [2.47], one can have

$$\varpi = \frac{2\,(z_{\mathrm{N}} - z_{\mathrm{T}})\tan\beta}{D} \qquad [2.48]$$

Therefore, node O_N is cut by such particular points P of all cutting edges, having the same parameter ϖ (independent of *i*).

As shown in Figure 2.20, for a workpiece section with $x\,(\varpi) = 0$, the trajectory of the point P in the Y–Z plane with respect to the given node O_N on the workpiece is trochoid. Here, the gray and hatched parts represent the workpiece and the remainder cut by one tooth, respectively. In this case, the z value of point A with $y\,(\varpi, t) = 0$ is what one should evaluate.

Due to the nonlinearity of equation [2.47], it is impossible to give rise to the analytic expression of time t. Here, parameter t is derived numerically. To

stabilize the iteration process, the initial value t_0 is set to be the parameter of a particular point B (see Figure 2.20), satisfying following conditions,

$$\begin{cases} \left.\dfrac{\partial z}{\partial t}\right|_{t=t_0} = 0 \\ \left.\dfrac{\partial^2 z}{\partial t^2}\right|_{t=t_0} \geq 0, \quad |y(\varpi, t_0)| \leq \dfrac{Nf}{2} \end{cases} \qquad [2.49]$$

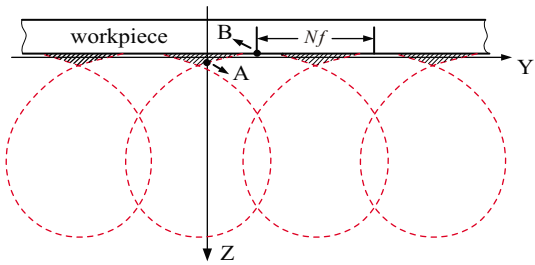

Figure 2.20. *Trajectory of the point on the* i*th cutting edge*

From the first equation in equation [2.49], it follows that

$$t_0 = -\frac{1}{\Omega}\left(\Omega_{\mathrm{I}} - \arctan\frac{\frac{D}{2}\sin(\zeta_i + \varpi) + \rho}{\frac{D}{2}\cos(\zeta_i + \varpi)}\right) + k\pi, \qquad k \in \mathbb{Z} \quad [2.50]$$

Note that k is an integer whose value is determined by the second equation in equation [2.49].

Consequently, the value of t satisfying $y(\varpi, t) = 0$ can be obtained by means of the Newton–Raphson method that proves to be highly convergent in our applications. Note that according to equation [2.49], for any cutting edge i, the initial value and solution of t are both unique. Hence, for any node on the machined surface, the number of calculating $z's$ is equal to the number of cutter teeth N.

2.3.1.2. *Simulation examples and experimental verifications*

Numerical examples are considered and the surface topography of end milling processes is numerically simulated. $\mathrm{R_a}$ or the Root Mean Square

(RMS) is evaluated to characterize the machined surface roughness quantitatively. A Taylor-Hobson contour device is used to measure the roughness of the machined surface for comparison with the simulation results. The surface roughness is measured along the feed direction for the end milling process.

Cutting conditions are described in Table 2.3. Simulation results given in Figure 2.21 show that the up and down milling processes result in different surface textures. From Table 2.4, it is noticed that the simulated R_a associated with the up milling is less than that of the down milling and is very similar to the measured outcome. This result agrees with the basic knowledge of machining experiences.

D	N	β	S	f	a_e	ρ
6 mm	3	30°	800 rpm	0.167 mm/tooth	1 mm	0.012 mm

Table 2.3. *Cutting conditions in flat end milling process*

Milling type	Measured R_a	Simulated R_a	Relative error
Up milling	2.075 μm	2.368 μm	14.1%
Down milling	2.225 μm	2.495 μm	12.1%

Table 2.4. *Simulation results in flat end milling process*

The comparison of the profile between the simulation and experimental results is shown in Figure 2.22. Obviously, the simulation curve is periodic since the roughness is predicted kinematically without considerations of vibration, tool wear and other factors. The correlation between these results is evident.

2.3.2. *Prediction method for multi-axis ball end milling*

2.3.2.1. *Derivation of simulation algorithm*

In this section, different coordinate systems related to multi-axis ball end milling are established first. Then the trajectory equation of the cutting edge relative to the workpiece is formulated. Due to the mathematical complexity, a numerical iterative algorithm is developed to solve the trajectory equation. As we are focused on the finish milling process with the depth of cutting

being small, effect of machining temperature, the cutter-workpiece flexibility and the dynamic property of the machine system are ignored.

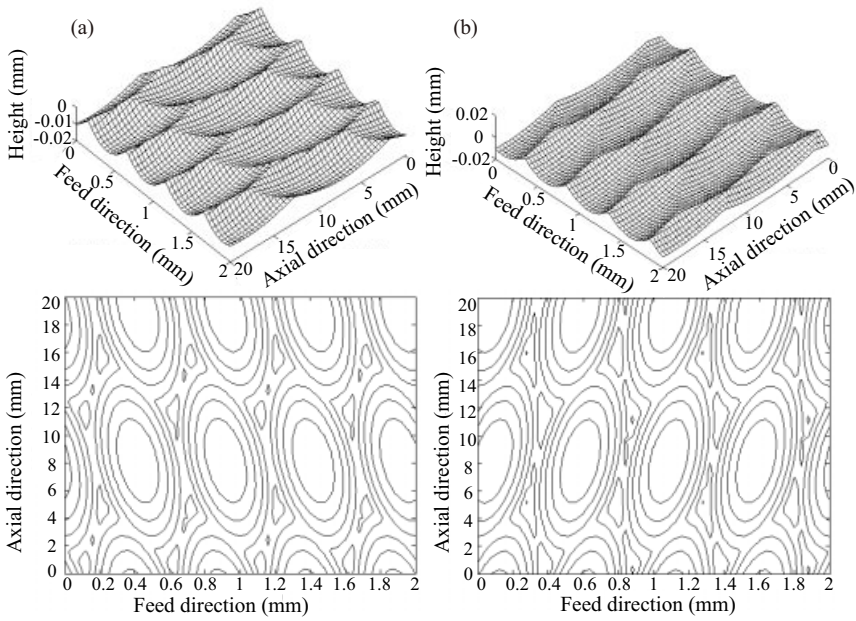

Figure 2.21. *Simulation results in end milling process: a) up milling; b) down milling*

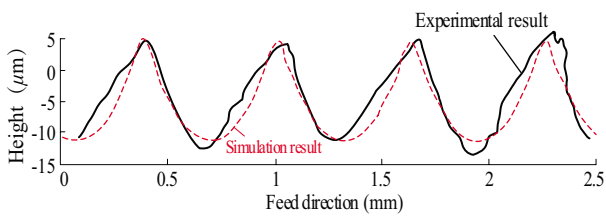

Figure 2.22. *Comparison of the profile between simulation and experimental results. For a color version of this figure, see www.iste.co.uk/zhang/milling.zip*

For an arbitrary linear feed portion of the whole tool trajectory, the involved set of coordinate systems shown in Figure 2.23 is established in order to obtain

the parametric trajectory equation of the cutting edge relative to an arbitrary point, O_N, on the workpiece:

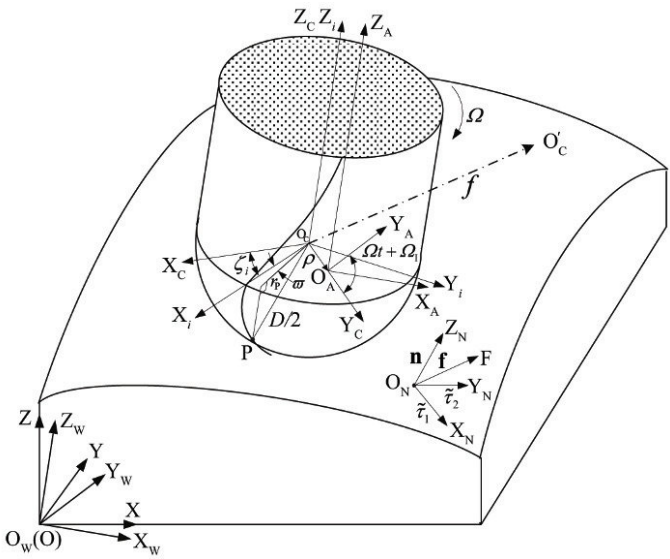

Figure 2.23. *Coordinate systems in the ball end milling process*

1) OXYZ: global coordinate system in which the workpiece machining surface and the tool path are described;

2) $O_W X_W Y_W Z_W$: simulation coordinate system attached to the workpiece with the axis Z_W being parallel to the tool axis Z_A;

3) $O_A X_A Y_A Z_A$: local coordinate system attached to the spindle of the mill machine and moves in pure translation of feed speed f_t relative to the workpiece. Axis Z_A is along the spindle. Axes X_A and Y_A are parallel to axes X_W and Y_W, respectively;

4) $O_C X_C Y_C Z_C$: local coordinate system fixed on the cutter. Axis Y_C and the vector of spindle run-out, ρ, are aligned. The cutter revolves around the spindle at the angle speed. The angle between Y_C and Y_A is $\Omega t + \Omega_I$ with Ω_I being the initial eccentricity angle;

5) $O_C X_i Y_i Z_i$: local coordinate system attached to the ith cutting edge. Axis X_i intersects with the ith cutting edge and has an angle ζ_i with axis X_C;

6) $O_N X_N Y_N Z_N$: local coordinate system of any given node on the machined surface. $O_N Z_N$ is the normal direction of node O_N. Note that axis $O_N F$ is parallel to the linear feed velocity vector $\mathbf{f}$. All axes can be derived below.

$$\begin{aligned} &O_N X_N = \tilde{\tau}_1 \left(x_{\tilde{\tau}_1}, y_{\tilde{\tau}_1}, z_{\tilde{\tau}_1}\right) = \tilde{\tau}_1 / ||\tilde{\tau}_1||, \quad \tilde{\tau}_1 = \mathbf{f} \times \mathbf{n} \\ &O_N Y_N = \tilde{\tau}_2 \left(x_{\tilde{\tau}_2}, y_{\tilde{\tau}_2}, z_{\tilde{\tau}_2}\right) = \tilde{\tau}_2 / ||\tilde{\tau}_2||, \quad \tilde{\tau}_2 = \mathbf{n} \times \tilde{\tau}_1 \\ &O_N Z_N = \mathbf{n} \left(x_n, y_n, z_n\right) = \mathbf{n} / ||\mathbf{n}|| \end{aligned} \tag{2.51}$$

where $\tilde{\tau}_1$, $\tilde{\tau}_2$ and $\mathbf{n}$ stand for the direction vectors of axes X_N, Y_N and Z_N, as illustrated in Figure 2.23. Let ϖ and z be the curvilinear parameters denoting the position angle of the cutter and the z coordinate of the given point on the cutting edge, respectively. Then coordinates of point P on the *i*th cutting edge can be expressed as

$$[x, y, z, 1]_i^{\mathrm{T}} = [r_P \cos \varpi, r_P \sin \varpi, z, 1]_i^{\mathrm{T}} \tag{2.52}$$

in which $r_P = \frac{D\sqrt{\tan^2\beta - \varpi^2}}{2\tan\beta}$ and $z = -\frac{D\varpi}{2\tan\beta}$, $0 \leq \varpi \leq \tan\beta$.

After multiple coordinate system transformations, the overall transformation matrix, denoted by $\mathbf{T}_{M_{iN}}$, from coordinate $O_C X_i Y_i Z_i$ to coordinate $O_N X_N Y_N Z_N$ consists of

$$\mathbf{T}_{M_{iN}} = \mathbf{T}_{M_{WN}} \mathbf{T}_{M_{AW}} \mathbf{T}_{M_{CA}} \mathbf{T}_{M_{iC}} \tag{2.53}$$

in which $\mathbf{T}_{M_{iC}}$, $\mathbf{T}_{M_{CA}}$, $\mathbf{T}_{M_{AW}}$ and $\mathbf{T}_{M_{WN}}$ denote the transformation matrix from $O_C X_i Y_i Z_i$ to $O_C X_C Y_C Z_C$, $O_C X_C Y_C Z_C$ to $O_A X_A Y_A Z_A$, $O_A X_A Y_A Z_A$ to $O_W X_W Y_W Z_W$ and $O_W X_W Y_W Z_W$ to $O_N X_N Y_N Z_N$ for each of them.

Hence, in $O_N X_N Y_N Z_N$, the trajectory equation of a given point on the *i*th cutting edge relative to the workpiece is written as:

$$\begin{bmatrix} x \\ y \\ z \end{bmatrix}_N = \mathbf{T}_{M_{iN}} \begin{bmatrix} x \\ y \\ z \end{bmatrix}_i = \begin{bmatrix} x_{T1} \\ y_{T1} \\ z_{T1} \end{bmatrix} \tag{2.54}$$

with

$$x_{\mathrm{T1}} = C_{\tilde{\tau}_1} r_{\mathrm{P}} \cos(\Omega t + \Omega_{\mathrm{I}} - \zeta_i - \varpi + \gamma_{\tilde{\tau}_1}) - z_{\tilde{\tau}_1} \frac{D\varpi}{2\tan\beta}$$
$$- C_{\tilde{\tau}_1} \rho \sin(\Omega t + \Omega_{\mathrm{I}} + \gamma_{\tilde{\tau}_1}) + d_{\tilde{\tau}_1}$$
$$y_{\mathrm{T1}} = C_{\tilde{\tau}_2} r_{\mathrm{P}} \cos(\Omega t + \Omega_{\mathrm{I}} - \zeta_i - \varpi + \gamma_{\tilde{\tau}_2}) - z_{\tilde{\tau}_2} \frac{D\varpi}{2\tan\beta}$$
$$- C_{\tilde{\tau}_2} \rho \sin(\Omega t + \Omega_{\mathrm{I}} + \gamma_{\tilde{\tau}_2}) + d_{\tilde{\tau}_2} + (x_{\tilde{\tau}_2} x_{\mathrm{f}} + y_{\tilde{\tau}_2} y_{\mathrm{f}} + z_{\tilde{\tau}_2} z_{\mathrm{f}})\, t$$
$$z_{\mathrm{T1}} = C_{\mathrm{n}} r_{\mathrm{P}} \cos(\Omega t + \Omega_{\mathrm{I}} + \zeta_j - \varpi + \gamma_{\mathrm{n}}) - z_{\mathrm{n}} \frac{D\varpi}{2\tan\beta}$$
$$- C_{\mathrm{n}} \rho \sin(\Omega t + \Omega_{\mathrm{I}} + \gamma_{\mathrm{n}}) + d_{\mathrm{n}} + (x_{\mathrm{n}} x_{\mathrm{f}} + y_{\mathrm{n}} y_{\mathrm{f}} + z_{\mathrm{n}} z_{\mathrm{f}})\, t$$

$$C_c = \sqrt{x_c^2 + y_c^2}, \cos\gamma_c = x_c / C_c, \sin\gamma_c = y_c / C_c$$
$$d_c = x_c\,(x_{\mathrm{A}} - x_{\mathrm{N}}) + y_c\,(y_{\mathrm{A}} - y_{\mathrm{N}}) + z_c\,(z_{\mathrm{A}} - z_{\mathrm{N}})\ (c = \tilde{\tau}_1, \tilde{\tau}_2, \mathrm{n})$$

where $\zeta_i = \zeta_1 - (i-1)2\pi/N$ $(i = 1, 2, ..., N)$. $(x_{\mathrm{f}}, y_{\mathrm{f}}, z_{\mathrm{f}})$ means the direction vector of the feed velocity. $[x_{\mathrm{N}}, y_{\mathrm{N}}, z_{\mathrm{N}}]$ denotes the coordinates of node, $\mathrm{O_N}$, in $\mathrm{O_W X_W Y_W Z_W}$, and $[x_{\mathrm{A}}, y_{\mathrm{A}}, z_{\mathrm{A}}]$ denotes the coordinates of cutter center, $\mathrm{O_A}$, in $\mathrm{O_W X_W Y_W Z_W}$.

In fact, equation [2.54] holds under the assumption that the local coordinate system $\mathrm{O_A X_A Y_A Z_A}$ is parallel to the global coordinate system OXYZ. However, in most cases, the axes of and $\mathrm{O_W X_W Y_W Z_W}$ are not parallel in multi-axis ball end milling. Namely, the tool cutter axis is typically inclined with respect to the normal of the workpiece machining surface and moves ahead with varying angles in the feed direction and pick-feed (cross-feed) direction. As the workpiece and tool paths are described under the global coordinate system OXYZ, we have to determine $[x_{\mathrm{N}}, y_{\mathrm{N}}, z_{\mathrm{N}}]$, $[x_{\mathrm{A}}, y_{\mathrm{A}}, z_{\mathrm{A}}]$ and the normal at point $\mathrm{O_N}$ involved in equation [2.54] in advance by means of coordinate transformation from $\mathrm{OXY}Z$ into $\mathrm{O_W X_W Y_W Z_W}$.

As shown in Figure 2.24, such a transformation constitutes two steps in a 5-axis ball end milling: (1) OXYZ revolves around axis Y with an angle γ_{I} to $\mathrm{O_W X'Y'Z'}$. (2) $\mathrm{O_W X'Y'Z'}$ revolves around axis $\mathrm{X'}$ with an angle η_{T} to

$O_W X_W Y_W Z_W$. It is noticed that $O_W Z_W$ is parallel to the cutter axis and the signs of γ_I and η_T are determined using the right hand helix rule. Denote $\mathbf{T}_{M_1}$ and $\mathbf{T}_{M_2}$ to be the transformation matrices of the circumrotation around axis Y and axis X′, respectively, one can have

$$\mathbf{T}_{M_1} = \begin{bmatrix} \cos\gamma_I & 0 & -\sin\gamma_I \\ 0 & 1 & 0 \\ \sin\gamma_I & 0 & \cos\gamma_I \end{bmatrix} \quad [2.55]$$

$$\mathbf{T}_{M_2} = \begin{bmatrix} 1 & 0 & 0 \\ 0 & \cos\eta_T & \sin\eta_T \\ 0 & -\sin\eta_T & \cos\eta_T \end{bmatrix} \quad [2.56]$$

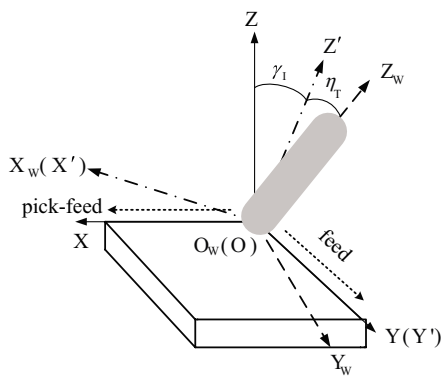

Figure 2.24. *Coordinate system transformation in multi-axis ball end milling*

Consequently, the overall transformation matrix $\mathbf{T}_M$ from OXYZ to $O_W X_W Y_W Z_W$ is written as

$$\mathbf{T}_M = \mathbf{T}_{M_2}\mathbf{T}_{M_1} = \begin{bmatrix} \cos\gamma_I & 0 & -\sin\gamma_I \\ \sin\eta_T\sin\gamma_I & \cos\eta_T & \sin\eta_T\cos\gamma_I \\ \cos\eta_T\sin\gamma_I & -\sin\eta_T & \cos\eta_T\cos\gamma_I \end{bmatrix} \quad [2.57]$$

From equation [2.54], it can be seen that when parameters D, β, Ω, Ω_I, ρ and ζ_i are given in advance, the trajectory equation is a nonlinear system in

function of both parameters ϖ and t. When a considered point on the workpiece is in cut, the general form of the trajectory equation written in $O_N X_N Y_N Z_N$ is

$$\begin{cases} x(\varpi, t) = 0 \\ y(\varpi, t) = 0 \end{cases} \qquad [2.58]$$

ϖ and t will be evaluated numerically due to the implicit relations. Their substitution into the z expression of equation [2.54] will thereafter give rise to the remainder height of the considered point being in cut. The resulting topography value of this point then corresponds to the minimum of all remainder heights formed by all cutting edges. Here, the key issue associated with topography simulation is how to solve equation [2.58] in an efficient way. The Newton–Raphson iteration scheme is employed in this work and the appropriate selection of the starting iteration point is investigated below. Firstly, the curve defined by equation [2.58] with ρ=0 is plotted in Figure 2.25. It can be seen that $x(\varpi, t)|_{\rho=0} = 0$ is a periodical function of parameter t with the periodicity being $2\pi/\Omega$.

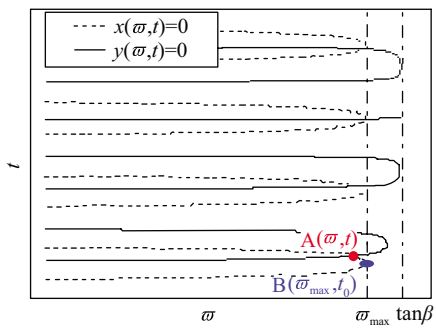

Figure 2.25. *Isovalue curves of equation system without cutter runout (ρ=0)*

Now, the aim is to determine firstly ϖ and t at the intersection point between two families of curves and thereafter the corresponding z-value. Without the loss of generality, consider point A in Figure 2.25. Suppose

$$p = \cos(\Omega t + \Omega_I - \zeta_i - \varpi + \gamma_{\tilde{r}_1}) \qquad p \in [-1\ ,1] \qquad [2.59]$$

by solving $x(\varpi, t)|_{\rho=0} = 0$, the following equation is obtained.

$$\varpi = \frac{2z_{\tilde{\tau}_1} d_{\tilde{\tau}_1} + 2C_{\tilde{\tau}_1} |p| \sqrt{\left(z_{\tilde{\tau}_1}^2 + p^2 C_{\tilde{\tau}_1}^2\right)\left(\frac{D}{2}\right)^2 - d_{\tilde{\tau}_1}^2}}{D\left(z_{\tilde{\tau}_1}^2 + p^2 C_{\tilde{\tau}_1}^2\right)} \tan\beta \qquad [2.60]$$

As shown in Figure 2.26, ϖ is symmetrical with respect to p and each bifurcation is monotone. Accordingly, when p takes the extreme value with

$$|p| = |\cos(\Omega t + \Omega_{\mathrm{I}} - \zeta_i - \varpi + \gamma_{\tilde{\tau}_1})| = 1 \qquad [2.61]$$

the maximum value of ϖ occurs with

$$\varpi_{\max} = \frac{z_{\tilde{\tau}_1} d_{\tilde{\tau}_1} + C_{\tilde{\tau}_1} \sqrt{\left(z_{\tilde{\tau}_1}^2 + C_{\tilde{\tau}_1}^2\right)\left(\frac{D}{2}\right)^2 - d_{\tilde{\tau}_1}^2}}{\frac{D}{2}\left(z_{\tilde{\tau}_1}^2 + C_{\tilde{\tau}_1}^2\right)} \tan\beta \qquad [2.62]$$

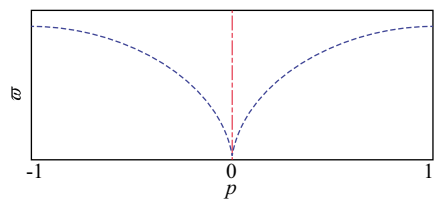

Figure 2.26. *Relationship between ϖ and p*

Furthermore, in the specific coordinate system $\mathrm{O_N X_N Y_N Z_N}$, due to the fact that

$$z_{\tilde{\tau}_1}^2 + C_{\tilde{\tau}_1}^2 = z_{\tilde{\tau}_1}^2 + \left(x_{\tilde{\tau}_1}^2 + y_{\tilde{\tau}_1}^2\right) = \|\tilde{\tau}_1\|^2 = 1 \qquad [2.63]$$

equation [2.62] can be simplified as

$$\varpi_{\max} = \frac{2z_{\tilde{\tau}_1} d_{\tilde{\tau}_1} + 2C_{\tilde{\tau}_1} \sqrt{\left(\frac{D}{2}\right)^2 - d_{\tilde{\tau}_1}^2}}{D} \tan\beta \qquad [2.64]$$

Such a $\varpi_{\max}$ is, in fact, the parameter of the extreme point B shown in Figure 2.25. To ensure the convergence of the iteration, the initialization is made by setting $\varpi_0 = \varpi_{\max}$.

By inserting equation [2.64] into $x(\varpi, t)|_{\rho=0} = 0$ of equation [2.54], the corresponding analytical value of t_0 reads

$$t_0 = \frac{1}{\Omega}\left[\cos^{-1}\frac{z_{\tilde{\tau}_1} D\varpi_0 - 2d_{\tilde{\tau}_1}\tan\beta}{C_{\tilde{\tau}_1} D\sqrt{\tan^2\beta - \varpi_0^2}} - (\Omega_{\mathrm{I}} - \zeta_i - \varpi_0 + \gamma_{\tilde{\tau}_1}) + 2k\pi\right], k \in \mathbb{Z} \quad [2.65]$$

According to equation [2.61], equation [2.65] can be further simplified as

$$t_0 = (\cos^{-1} q - (\Omega_{\mathrm{I}} - \zeta_i - \varpi_0 + \gamma_{\tilde{\tau}_1}) + 2k\pi)/\Omega, \quad k \in \mathbb{Z} \quad [2.66]$$

with

$$q = \begin{cases} 1, & z_{\tilde{\tau}_1} D\varpi_0 - 2d_{\tilde{\tau}_1}\tan\beta \geq 0 \\ -1, & z_{\tilde{\tau}_1} D\varpi_0 - 2d_{\tilde{\tau}_1}\tan\beta < 0 \end{cases}$$

A different k gives a different t_0. Hence, the latter together with the given ϖ_0 will result in a set of z-values whose minimum is the desired topography value. From such a starting point B (ϖ_0,t_0), usually the iteration process converges quickly to point A following numerical experiences. Likewise, when the cutter runout exists initial parameter values given above are also reliable to stabilize the iteration process because of $\rho \ll \frac{D}{2}$. In addition, numerical experience confirms that the convergence is not influenced by other parameters, such as feed rate and spindle speed.

It is important to remark that since all developments are concerned with an arbitrary feed direction and an arbitrary node on the machined surface, the proposed method is therefore applicable to any machined curved surface.

With the starting point (ϖ_0, t_0), the solution of equation [2.58] can be quickly obtained. In the Newton–Raphson iteration, the convergence will be controlled when $x(\varpi, t) \leq \varepsilon_4$ and $y(\varpi, t) \leq \varepsilon_4$ are satisfied. Here, ε_4 is the

prescribed tolerance. Simulation examples demonstrate that a suitable value of ε_4 is needed to ensure both the precision and the computing efficiency. To have an overall idea, the following procedure is provided to show how the final topography of an arbitrary machined surface is evaluated in multi-axis ball end milling.

Step 1: input the tool paths, cutting parameters and the geometrical surface model of the workpiece to be machined;

Step 2: determine the linear feed velocity vector, $\mathbf{f}$, of each segmented linear feed path and then carry out coordinate transformation by means of equation [2.57];

Step 3: determine the cutting areas swept along this linearized tool path according to the cutting depth and cutter radius;

Step 4: calculate the cutter remainder height of the considered point inside the workpiece cutting areas swept by the current cutting edge following equation [2.54] and [2.58];

Step 5: calculate the cutter remainder height for the next cutting edge and update the cutter remainder height by comparing the relative magnitude between the current value and the existing one;

Step 6: repeat steps 4 and 5 for all cutting edges and calculate the remainder cutter height of the next point on the workpiece until all the points in the cut are calculated;

Step 7: repeat steps 2-6 and treat the following linear tool path until the whole cutting process is carried out;

Step 8: output the final topography and roughness of the simulation process.

Alternatively, the time step method [SOS 04, ZHA 03b, LIU 06, SRI 06, YAN 01] is a straightforward one. In such a method, the concept of a discrete cutting tooth is employed to denote a tool model. Time steps are used to index both the cutter's forward motion and tool rotation. The important thing is how to determine the time step, the axial slice thickness and the tolerance that considerably affect the accuracy and the computing time. The first parameter should satisfy the condition that the feeding distance formed by a time step is less than the basic grid length along the feed direction. As the final cutter

remainder height of a node is finally determined by the lowest axial slice that sweeps this node, the second parameter should take a value small enough for the trade-off between the accuracy and computing time. Comparatively, the proposed iterative method is an indirect method, whose result accuracy is merely affected by the tolerance. However, due to the discretization of the workpiece surface and the tool-cutting motion, the simulation results of both the iterative method and time step method could not accurately represent the surface characteristics at the microscale.

To clarify, consider the simulation case where the workpiece is meshed into a 34×34 grid and the basic grid length is 0.03 mm. Assume that the roughness computation accuracy is 0.001 mm. Then, the axial slice thickness used in the time step method should be less than 0.001 mm. As a result, the computing time is 514 seconds and 246 seconds when the time step method and the iterative method are used, respectively. Therefore, in the same condition, the iterative method proposed is much faster.

2.3.2.2. *Simulation examples and experimental verifications*

Several simulation examples are illustrated for both plane milling and sculptured surface milling. Influences of the feed rate, cutting modes, inclination direction and inclination angle of the cutter upon the surface topography and roughness are studied. The maximum peak value of the machined surface topography, R_Z, is evaluated to characterize the surface roughness. To validate the simulation accuracy, experimental tests are performed on the machine bed of a Mikron 1350ucp machine center with coolant. The ball end mill is a four-fluted HSS (high-speed steel) cutter with a 30° helix angle and 10 mm diameter. The pick-feed is set to be 0.5 mm. The workpiece material is al7075-T6. R_Z is measured by a Taylor–Hobson contour device. The micrograph of the machined surface is taken by a Nikon SMZ800 microscope.

As shown in Figures 2.27(a)–(c), each represents the unidirectional up milling, unidirectional down milling and bidirectional milling modes, respectively when the cutter-axis has an inclined angle γ_I in the pick-feed direction. Similarly, in Figures 2.27(d)–(e), each case corresponds to the cutter-axis of an inclined angle η_T in the feed direction. When both angles, γ_I and η_T take no zero values simultaneously, this becomes the case of a 5-axis milling, as shown in Figure 2.24. In fact, any kinematics of 5-axis milling

modes can be described by a proper combination of the above single inclined angle cases given in Figure 2.27.

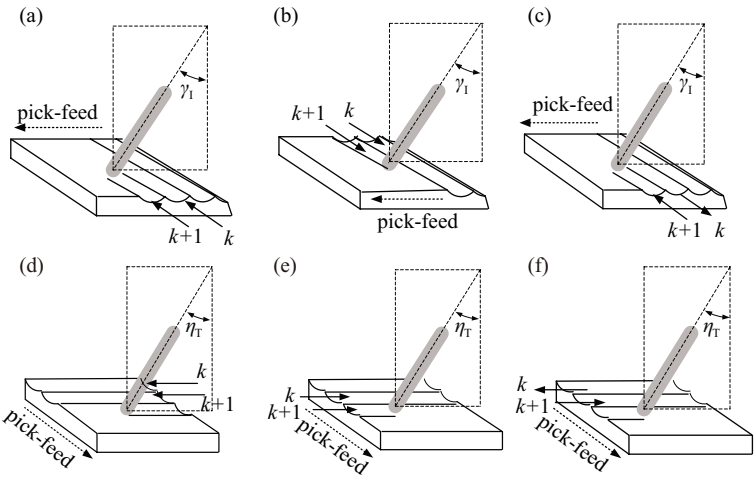

Figure 2.27. *Typical plane cutting modes: a) unidirectional up milling with inclined angle γ_I; b) unidirectional down milling with inclined angle γ_I; c) bidirectional milling with inclined angle γ_I; d) unidirectional up milling with inclined angle η_T; e) unidirectional down milling with inclined angle η_T; f) bidirectional milling with inclined angle η_T*

Complicated simulations of multi-axis ball end milling are addressed. Two cases of cutter-axis inclination are considered with $\gamma_I = 15^\circ$, $\eta_T = 10^\circ$ and $\gamma_I = 15^\circ$, $\eta_T = 0^\circ$. Figures 2.28(a–d) represent the simulated topographies in both milling modes. Correspondingly, Figures 2.28(e–h) represent machined surface micrographs obtained by a Nikon smz800 microscope. The main difference between Figures 2.28(a)–(d) is that the elliptical topographies are orientated differently depending upon the milling mode. In Figure 2.28(a), the ellipses incline right, whereas in Figure 2.28(b) the ellipses incline left and right alternatively. In Figure 2.28(c), the ellipses orient upright and in Figure 2.28(d) the ellipses orient horizontally and upright alternately. The same orientations can be found in the micrographs of Figure 2.28(e–h). Note that arrows in these figures denote the cutter feed direction.

Relevant roughness is listed in Table 2.5 for comparison. Although the surface topography shows a good level of accordance in certain cases, some

deviations do exist between the simulated roughness and the measured one. From the mechanistic point of view, it is known that the cutter will be pushed away in down milling and be pulled over in up milling. Here, the unidirectional milling mode shown in Figure 2.28 corresponds to the up milling while the bidirectional milling mode corresponds to an alternant effect of up milling and down milling. Hence, the difference between the measured roughness and the simulated roughness is relatively large in the bidirectional milling mode. Additionally, further investigations should be also made about the effect of the cutter deflection caused by cutting force upon the machined surface topography and roughness.

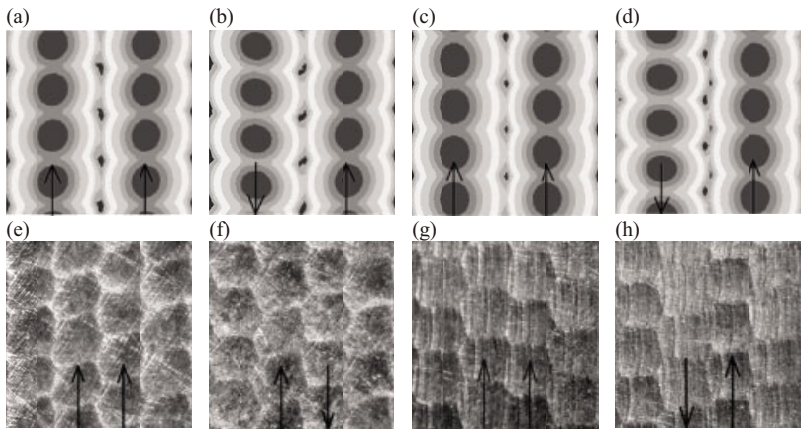

Figure 2.28. *Simulations and experiments of surface topographies: a) simulated unidirectional up milling ($\gamma_I = 15^\circ$, $\eta_T = 10^\circ$); b) simulated bidirectional milling ($\gamma_I = 15^\circ$, $\eta_T = 10^\circ$); c) simulated unidirectional up milling ($\gamma_I = 15^\circ$, $\eta_T = 0^\circ$); d) simulated bidirectional milling ($\gamma_I = 15^\circ$, $\eta_T = 0^\circ$); e) measured unidirectional up milling ($\gamma_I = 15^\circ$, $\eta_T = 10^\circ$); f) measured bidirectional milling ($\gamma_I = 15^\circ$, $\eta_T = 10^\circ$); g) measured unidirectional up milling ($\gamma_I = 15^\circ$, $\eta_T = 0^\circ$); h) measured bidirectional milling ($\gamma_I = 15^\circ$, $\eta_T = 0^\circ$)*

Feed mode	$\gamma_I(^\circ)$	$\eta_T(^\circ)$	Simulated $R_Z(\mu m)$	Experimental $R_Z(\mu m)$
Unidirectional up	15	10	8.006	7.907
Bidirectional	15	10	7.996	11.620
Unidirectional up	15	0	8.649	10.790
Bidirectional	15	0	7.777	9.036

Table 2.5. *Roughness comparison*

3

Dynamics of Milling Processes

Self-excited vibrations caused by regeneration of waviness, also known as regenerative chatter, result in unstable cutting processes, poor surface finish, reduced productivity and damage of machine tools and cutters. To ensure stable cutting, many strategies such as prediction of chatter stability in advance, installation of extra energy absorption devices and disruption of regenerative chatter have been proposed. Among these, the most time-saving method is to select chatter-free cutting parameters from the stability lobe diagram (SLD) based on the governing equation involving the frequency response function (FRF) of tool point. The prediction of milling stability lobe together with the method obtaining FRF will be detailed in this chapter.

3.1. Governing equation of the milling process

Self-excitation in the generation of chip thickness is the main cause of machine tool chatter vibrations. A wavy surface generated during the current cut period will be removed by the next cut period. As a result, a new wavy surface will be left owing to the structural vibration excited by cutting forces. Phase shift between two adjacent waves will lead to exponential growth of chip thickness, and thus regenerative chatter occurs. The fundamentals of the governing equation under this phenomenon will be explained in this section.

Milling Simulation: *Metal Milling Mechanics, Dynamics and Clamping Principles*,
First Edition. Weihong Zhang and Min Wan.

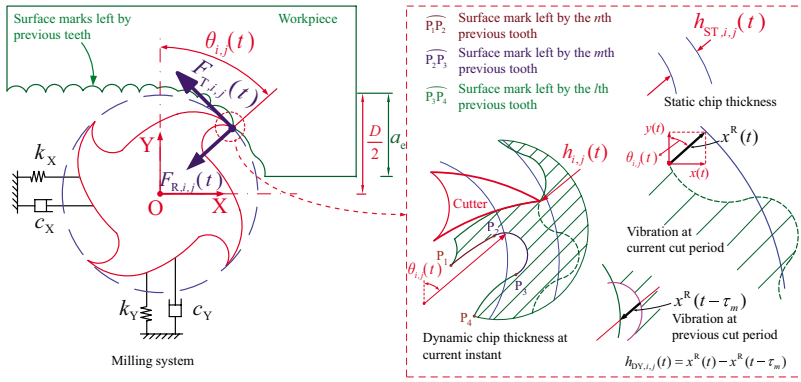

Figure 3.1. *Schematic mechanical model of a two degree of freedom (DOF) milling system (illustration for a 4-fluted cutter). For a color version of this figure, see www.iste.co.uk/zhang/milling.zip*

As shown in Figure 3.1, the cutting forces excite the structure in X and Y directions, causing lateral dynamic displacements $x(t)$ and $y(t)$, which then lead to an additional dynamic chip thickness to the static one. That is, chip thickness $h_{i,j}(t)$ physically consists of static, $h_{\mathrm{ST},i,j}(t)$, and dynamic, $h_{\mathrm{DY},i,j}(t)$, components.

$$h_{i,j}(t) = h_{\mathrm{ST},i,j}(t) + h_{\mathrm{DY},i,j}(t) \qquad [3.1]$$

with

$$\begin{aligned} h_{\mathrm{ST},i,j}(t) &= mf \sin\theta_{i,j}(t) + r_{i,j} - r_{i-m,j} \\ h_{\mathrm{DY},i,j}(t) &= x^{\mathrm{R}}(t) - x^{\mathrm{R}}(t-\tau_m) \\ &\leftarrow x^{\mathrm{R}}(t) = x(t)\sin\theta_{i,j}(t) + y(t)\cos\theta_{i,j}(t) \end{aligned} \qquad [3.2]$$

where t means time variable. τ_m is the time delay between the current cut location of the *j*th disk element of the *i*th flute and previously generated surface. It means that the current tooth at the present time t is to remove the surface waves that was generated at time $t - \tau_m$. Here, variable m in equation [3.2] means that the current cutting point is removing the surface mark left by the *m*th previous tooth. For a constant pitch cutter, the delay term τ_m in equation [3.2] is often assumed to be equal to the tooth passing period τ. That is, the

τ-delay differential system assumption is mostly adopted to model the real dynamic milling process. However, the occurrence of cutter runout will greatly affect the actual cutting radius of the concerned cutting point. As a result, the entry and exit angles related to different tooth will deviate from their nominal values.

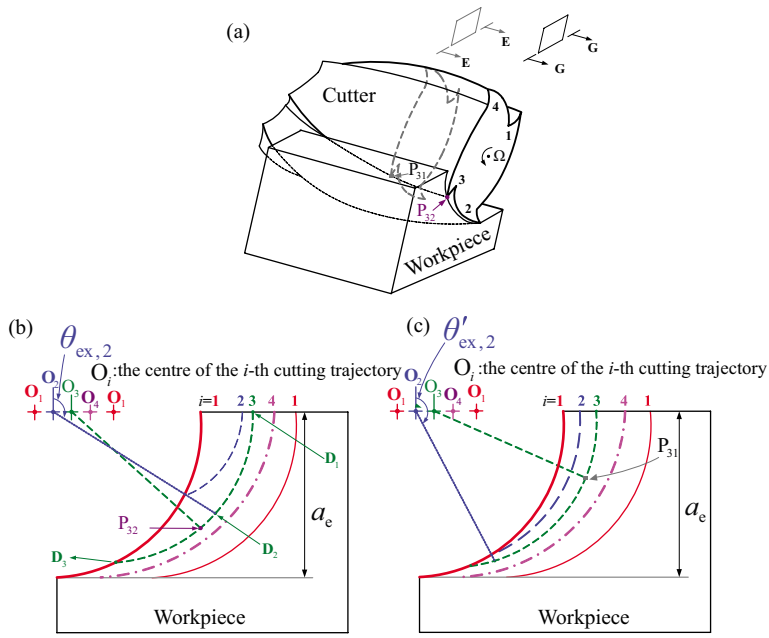

Figure 3.2. *Cutting trajectories for a four-fluted mill with cutter runout: a) the cutter-workpiece contact state at the concerned time t; b) for cross-section G-G; c) for cross-section E-E. For a color version of this figure, see www.iste.co.uk/zhang/milling.zip*

For an evenly pitched four-fluted cutter with cutter runout, Figures 3.2(b) and 3.2(c) illustrate the cutting trajectories of different cutting points related to two different cross-sections, i.e. G-G and E-E. From Figure 3.2(b) it can be seen that the value of exit angle corresponding to the second tooth is changed from π to $\theta'_{ex,2}$. Based on these influences produced by cutter runout, the following phenomena are found:

1) consider the same cutting point at different cutting instant. As shown in Figure 3.2(b), if P_{32} is in the D_1D_2 region of the third cutting trajectory, it will remove the surface left by the second tooth. Whereas, as time changes, it will

rotate from the D_1D_2 region to the D_2D_3 region. Correspondingly, it will then remove the surface generated by the first tooth. Here, P_{32} is the cutting point on the third tooth. This phenomenon means that even though the same cutting point is considered, at different cutting instant it may be to remove the surface generated by different tooth;

2) consider different cutting points at the same time. Let's use two different cutting points on the third cutting tooth at time *t* as an example, i.e. P_{31} and P_{32} as shown in Figure 3.2(a). From Figures 3.2(c) and 3.2(b) it can be obviously seen that P_{31} is to remove the surface generated by the second tooth whereas P_{32} will remove the surface left by the first tooth. This indicates that even though the same cutting instant is considered, different cutting points may be to remove the surface generated either by the first previous tooth or the *m*th ($m = 2, 3, ..., N$) previous tooth.

The above two features mean that there may be multiple delay terms in milling process when cutter runout occurs. Further analysis shows that any cutting point may be to remove the surface left either by the first previous tooth or the *m*th previous tooth ($m > 1$).

On the other hand, it should be noted that if the wavy surface and the current vibration between two subsequent teeth are in phase, the dynamic chip thickness $h_{\mathrm{DY},i,j}(t)$ will equal zero even though the tool is vibrating during material removal. This case corresponds to forced vibration or stable cutting. In contrast, if the wavy surface and the current vibration are not in phase, dynamic chip thickness $h_{\mathrm{DY},i,j}(t)$ will lead to self-excited vibrations and unstable cutting.

By substituting equation [3.1] into equations [1.8] and [1.14], one can obtain the total cutting forces as follows.

$$[F_{\mathrm{X},i,j}(t), F_{\mathrm{Y},i,j}(t)]^{\mathrm{T}} = \mathbf{F}_{\mathrm{ST},i,j}(t) + \mathbf{F}_{\mathrm{DY},i,j}(t) \qquad [3.3]$$

where $\mathbf{F}_{\mathrm{ST},i,j}$ is the cutting forces components related to the static chip thickness and defined as follows.

$$\begin{aligned}\mathbf{F}_{\mathrm{ST},i,j}(t) &= [F_{\mathrm{SX},i,j}(t), F_{\mathrm{SY},i,j}(t)]^{\mathrm{T}} \\ &= g(\theta_{i,j}(t))\mathbf{T}_{i,j}(t)[1:2, 1:2][K_{\mathrm{T}} z_{i,j} h_{\mathrm{ST},i,j}(t), K_{\mathrm{R}} z_{i,j} h_{\mathrm{ST},i,j}(t)]^{\mathrm{T}}\end{aligned} \qquad [3.4]$$

where $\mathbf{T}_{i,j}(*)$ is a transformation matrix defined as equation [1.75]. $\mathbf{F}_{\mathrm{DY},i,j}$ is the cutting forces induced by dynamic chip thickness and in the global directions it can be expressed as a function of tool vibrations as

$$\begin{aligned}\mathbf{F}_{\mathrm{DY},i,j}(t) &= \mathbf{T}_{i,j}(t)[1:2,1:2][\mathbf{H}_{m,i,j}(t)\mathbf{Q}(t) - \mathbf{H}_{m,i,j}(t)\mathbf{Q}(t-\tau_m)] \\ \mathbf{Q}(t) &= [x(t), y(t)]^{\mathrm{T}}\end{aligned} \quad [3.5]$$

with

$$\mathbf{H}_{m,i,j}(t) = g(\theta_{ij}(t))z_{i,j}\begin{bmatrix} K_{\mathrm{T}}\sin\theta_{i,j}(t) & K_{\mathrm{T}}\cos\theta_{i,j}(t) \\ K_{\mathrm{R}}\sin\theta_{i,j}(t) & K_{\mathrm{R}}\cos\theta_{i,j}(t)\end{bmatrix} \quad [3.6]$$

It should be noted that during the derivation procedure of equations [3.4] and [3.5], the cutter rotation angle φ occurring in equations [1.8] and [1.14] is directly replaced with t since φ is directly related to time t through the spindle rotation speed Ω.

The total dynamic cutting force vector ($\mathbf{F}(t)$) acting on the tool is evaluated by summing the contributions of all disk elements which remove the material:

$$\begin{aligned}&\mathbf{F}(t) = \mathbf{F}_{\mathrm{ST}}(t) + \mathbf{F}_{\mathrm{DY}}(t) \\ &\mathbf{F}_{\mathrm{ST}}(t) = \sum_{i,j}\mathbf{F}_{\mathrm{ST},i,j}(t) \\ &\mathbf{F}_{\mathrm{DY}}(t) = \sum_{i,j}\mathbf{F}_{\mathrm{DY},i,j}(t) = \sum_{m=1}^{N_{\mathrm{d}}}\mathbf{H}_m(t)\mathbf{Q}(t) - \sum_{m=1}^{N_{\mathrm{d}}}[\mathbf{H}_m(t)\mathbf{Q}(t-\tau_m)] \\ &\mathbf{H}_m(t) = \sum_{i,j}\{\mathbf{T}_{i,j}(t)[1:2,1:2]\mathbf{H}_{m,i,j}(t)\}\end{aligned} \quad [3.7]$$

where N_{d} means the total number of delay items. $\mathbf{F}_{\mathrm{DY}}(t)$ is the dynamic cutting force during milling expressed in equation [3.7]. The mechanical model of standard 2-DOF milling process is shown schematically in Figure 3.1, where the cutter is supposed to be flexible in comparison to the rigid workpiece. The lateral vibrations ($x(t)$, $y(t)$) of tool are modeled in the global X and Y directions as follows

$$\mathbf{M}\ddot{\mathbf{Q}}(t) + \mathbf{C}\dot{\mathbf{Q}}(t) + \mathbf{K}\mathbf{Q}(t) = \mathbf{F}_{\mathrm{DY}}(t) \quad [3.8]$$

where $\mathbf{M}$, $\mathbf{C}$ and $\mathbf{K}$ are the mass, damping and stiffness matrices. Note that the linearization of the system around stationary cutting, which is a periodic motion of the tool, will lead to a situation where the static component of the cutting force can be directly dropped from the right-hand side of the governing equation. The static chip thickness therefore does not contribute to the dynamic chip load regeneration mechanism. As a result, the static component $\mathbf{F}_{\mathrm{ST}}$ is not involved in equation [3.9].

$$\begin{aligned}\mathbf{M}\ddot{\mathbf{Q}}(t) + \mathbf{C}\dot{\mathbf{Q}}(t) + \mathbf{K}\mathbf{Q}(t) &= \mathbf{F}_{\mathrm{DY}}(t) \\ &= \sum_{m=1}^{N_{\mathrm{d}}} \mathbf{H}_m(t)\mathbf{Q}(t) - \sum_{m=1}^{N_{\mathrm{d}}} [\mathbf{H}_m(t)\mathbf{Q}(t-\tau_m)]\end{aligned} \quad [3.9]$$

The equation [3.9] is the basic governing equation used to study the chatter stability of milling process. In the following sections, emphasis will be placed on how to obtain the mode parameters and how to develop the stability analysis method.

3.2. Method for obtaining the frequency response function

The frequency response function (FRF) of the tool point is generally obtained by impact testing, which may be too costly and time-consuming in actual machining. Moreover, measurements of the FRFs are almost impractical for micro-machining tool. Hence, developments of general computing methods become a vital alternative for the determination of FRF of tool point. Receptance coupling substructure analysis (RCSA) allows the analytical assembly of spindle-holder substructure and the overhung part of tool substructure.

In this section, a systematic method is presented to predict the FRF of tool point. The tool-collet and holder-collet joint interfaces are considered as two distributed layers with varying stiffness. The tool is assumed to partly rest on the collet via a distributed damped-elastic tool-collet interface while the collet is assumed to rest on the resilient support provided by the spindle-holder assembly via a distributed damped-elastic holder-collet interface. Stiffness and damping properties of both joint interfaces are identified by minimizing the discrepancy between the measured and predicted FRFs of tool point. A computing procedure is proposed to eliminate repeated impact tests in obtaining the dynamics of the spindle-holder assembly of different sizes.

3.2.1. *Derivation of calculation formulations*

3.2.1.1. *Tool point dynamics analysis method*

Mathematically, the FRF of the tool point is defined as:

$$H(\omega) = \frac{Xe^{J\omega t}}{Fe^{J\omega t}} \qquad [3.10]$$

where $Xe^{J\omega t}$ is the dynamic displacement of the tool point under harmonic force $Fe^{J\omega t}$. t and ω denote time and angular frequency, respectively. It can be seen that the key issue related to the FRF is how to obtain the solution of $Xe^{J\omega t}$ under $Fe^{J\omega t}$. Based on Euler-Bernoulli beam theory, a procedure for solving $Xe^{J\omega t}$ is presented in this section. J is the unity of imaginary number.

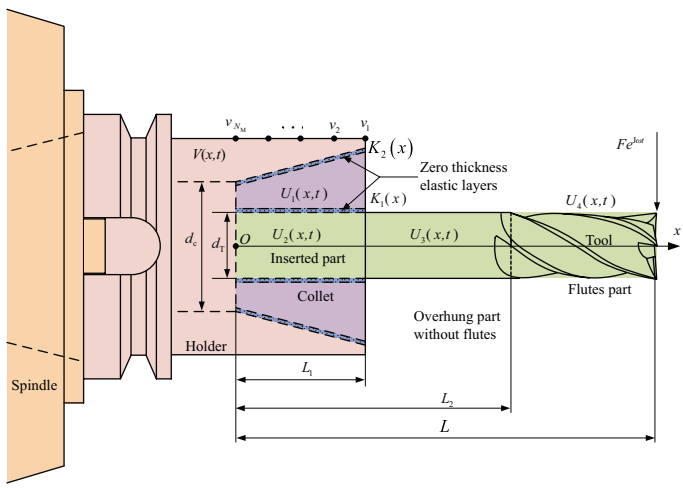

Figure 3.3. *The tool-spindle-holder assembly. For a color version of this figure, see www.iste.co.uk/zhang/milling.zip*

As shown in Figure 3.3, the tool-collet and holder-collet joint interfaces are modeled as two distributed joint interfaces. This is different from the existing one layer model [SCH 07, STA 64, AHM 07, AHM 10b]. Both joint interfaces are regarded as zero-thickness damped-elastic layers, whose contact rigidities are characterized by non-uniform stiffness coefficients $K_1(x)$ and $K_2(x)$, respectively. Here, x means the distance from the point

concerned to the end of the inserted part of the tool, as shown in Figure 3.3. The collet is modeled as a continuous beam with variable cross sections resting on a flexible support via the holder-collet joint interface. The tool is considered as a continuous step beam with three parts: inserted part of tool (IPT), tool overhung part without flutes (TOPWF) and flutes part of tool (FPT). The IPT rests on the collet via the tool-collet joint interface. Based on the Euler–Bernoulli beam theory, dynamics of the collet and the three parts of the tool are modeled as [AHM 07, RAO 11, LEI 11]:

$$\begin{aligned}
&\text{For collet}: \quad 0 \le x < L_1 : \\
&\frac{\partial^2}{\partial x^2}\left[E_1 I_1(x)\frac{\partial^2 U_1(x,t)}{\partial x^2}\right] + m_1(x)\frac{\partial^2 U_1(x,t)}{\partial t^2} \\
&= K_2(x)\left[V(x,t) - U_1(x,t)\right] - K_1(x)\left[U_1(x,t) - U_2(x,t)\right], \\
&\text{For IPT}: \quad 0 \le x < L_1 : \\
&E_2 I_2 \frac{\partial^4 U_2(x,t)}{\partial x^4} + m_2 \frac{\partial^2 U_2(x,t)}{\partial t^2} = K_1(x)\left[U_1(x,t) - U_2(x,t)\right], \\
&\text{For TOPWF}: \quad L_1 \le x < L_2 : \\
&E_2 I_3 \frac{\partial^4 U_3(x,t)}{\partial x^4} + m_3 \frac{\partial^2 U_3(x,t)}{\partial t^2} = 0, \\
&\text{For FPT}: \quad L_2 \le x \le L : E_2 I_4 \frac{\partial^4 U_4(x,t)}{\partial x^4} + m_4 \frac{\partial^2 U_4(x,t)}{\partial t^2} = 0.
\end{aligned} \qquad [3.11]$$

where L, $L - L_2$ and L_1 are the lengths of overall part, flutes and inserted part of the tool. E_1 and E_2 stand for the Young's moduli of the materials of the collet and the tool. $V(x,t)$ designates the lateral displacement of the holder at time t. $U_1(x,t)$, $U_2(x,t)$, $U_3(x,t)$ and $U_4(x,t)$ are the lateral displacements of the collet, IPT, TOPWF and FPT. $I_1(x)$, I_2, I_3 and I_4 are the area moments related to collet, IPT, TOPWF and FPT. $m_1(x)$, m_2, m_3 and m_4 are the mass per unit length corresponding to collet, IPT, TOPWF and FPT. $I_1(x)$ and $m_1(x)$ are functions of position x expressed as:

$$I_1(x) = \frac{\pi\left[(d_C + 2k_C x)^4 - {d_T}^4\right]}{64} \qquad [3.12]$$

$$m_1(x) = \frac{\pi\rho\left[(d_C + 2k_C x)^2 - {d_T}^2\right]}{4} \qquad [3.13]$$

where d_C and k_C are small diameter and slope of the outer profile of the collet. ρ is the material density of the collet. d_T is the diameter of the IPT. $K_1(x)$ and

$K_2(x)$, the stiffness coefficients of the tool-collet and holder-collet interfaces, can be approximated in polynomial form [AHM 07, EIS 94]:

$$\begin{aligned} K_1(x) &= (1 + \mathrm{J}\eta_{\mathrm{A}}) \sum_{q=0}^{Q} \kappa_{\mathrm{A},q} x^q \\ K_2(x) &= (1 + \mathrm{J}\eta_{\mathrm{B}}) \sum_{\hat{q}=0}^{\hat{Q}} \kappa_{\mathrm{B},\hat{q}} x^{\hat{q}} \end{aligned} \qquad [3.14]$$

where η_{A} and η_{B} are structural damping factors. $\kappa_{\mathrm{A},q}$ and $\kappa_{\mathrm{B},\hat{q}}$ are polynomial coefficients. q and $\hat{q}$ denote the degree of each term of both polynomials. Q and $\hat{Q}$ designate the degrees of both polynomials. Here, structural damping is used to take into account the displacement-dependent energy dissipation mechanism of the interface layers [AHM 07, AHM 10b, RAO 11]. To identify $K_1(x)$ and $K_2(x)$, an iterative procedure will be presented in section 3.3.

Based on the variable separation method, the solutions of equation [3.11] are expressed in the following form to separate the time and displacement.

$$\begin{aligned} U_k(x,t) &= W_k(x)\, e^{\mathrm{J}\omega t}, \qquad k = 1,2,3,4 \\ V(x,t) &= v(x)\, e^{\mathrm{J}\omega t} \end{aligned} \qquad [3.15]$$

where $W_k(x)\,(k = 1,2,3,4)$ and $v(x)$ are the complex shape functions due to the non-proportional damping mechanism of the system. Subsequently, if the extended holder is divided into N_{M} elements with identical axial length, $V(x,t)$ can be further expressed as a polynomial interpolation of the lateral displacements related to these elements.

$$\begin{aligned} V(x,t) &= v(x)\, e^{\mathrm{J}\omega t} = \left[p_1(x)\, v_1 + p_2(x)\, v_2 + \ldots + p_{N_{\mathrm{M}}}(x)\, v_{N_{\mathrm{M}}}\right] e^{\mathrm{J}\omega t} \\ &= \mathbf{p}^{\mathrm{T}} \mathbf{v} e^{\mathrm{J}\omega t} \end{aligned} \qquad [3.16]$$

with

$$\begin{aligned} \mathbf{p} &= \left[p_1(x), p_2(x), \ldots, p_{N_{\mathrm{M}}}(x)\right]^{\mathrm{T}} = \mathbf{P}\left[1, x, x^2 \ldots, x^{N_{\mathrm{M}}-1}\right]^{\mathrm{T}} \\ \mathbf{v} &= \left[v_1, v_2, \ldots, v_{N_{\mathrm{M}}}\right]^{\mathrm{T}} \end{aligned} \qquad [3.17]$$

in which $v_k\,(k=1,2,...,N_{\mathrm{M}})$ is the lateral displacement of the holder related to element k. $p_k\,(x)\,(k=1,2,...,N_{\mathrm{M}})$ is the Lagrange basis polynomials of degree $(N_{\mathrm{M}}-1)$. Matrix $\mathbf{P}$ is as follows.

$$\mathbf{P}=\begin{bmatrix} \bar{P}_{1,1} & \bar{P}_{1,2} & \bar{P}_{1,3} & \cdots & \bar{P}_{1,N_{\mathrm{M}}} \\ \bar{P}_{2,1} & \bar{P}_{2,2} & \bar{P}_{2,3} & \cdots & \bar{P}_{2,N_{\mathrm{M}}} \\ \bar{P}_{3,1} & \bar{P}_{3,2} & \bar{P}_{3,3} & \cdots & \bar{P}_{3,N_{\mathrm{M}}} \\ \vdots & \vdots & \vdots & \ddots & \vdots \\ \bar{P}_{N_{\mathrm{M}},1} & \bar{P}_{N_{\mathrm{M}},2} & \bar{P}_{N_{\mathrm{M}},3} & \cdots & \bar{P}_{N_{\mathrm{M}},N_{\mathrm{M}}} \end{bmatrix} \quad [3.18]$$

with

$$\begin{aligned}
&\bar{P}_{k_1,k_2}=\hat{P}_{k_1,k_2}/\prod_{k_3=1,k_3\neq k_1}^{N_{\mathrm{M}}}\left(x_{k_1}-x_{k_3}\right)\\
&\hat{P}_{k_1,N_{\mathrm{M}}}=1\\
&\hat{P}_{k_1,N_{\mathrm{M}}-1}=-\sum_{k_4=1,k_4\neq k_1}^{N_{\mathrm{M}}}x_{k_4}=\sum_{k_4=1,k_4\neq k_1}^{N_{\mathrm{M}}}T_{1,k_4}^{(k_1)}\\
&\hat{P}_{k_1,N_{\mathrm{M}}-k_5}=\sum_{k_4=1,k_4\neq k_1}^{N_{\mathrm{M}}-k_5+1}\left(-x_{k_4}\sum_{k_6=k_4+1,k_6\neq k_1}^{N_{\mathrm{M}}-k_5+2}T_{k_5-1,k_6}^{(k_1)}\right)\\
&\qquad=\sum_{k_4=1,k_4\neq k_1}^{N_{\mathrm{M}}-k_5+1}T_{k_5,k_4}^{(k_1)}\,(k_5=2,3,\ldots,N_{\mathrm{M}}-1)\\
&T_{k_5,k_4}^{(k_1)}=-x_{k_4}\sum_{k_6=k_4+1,k_6\neq k_1}^{N_{\mathrm{M}}-k_5+2}T_{k_5-1,k_6}^{(k_1)}
\end{aligned}$$

where x_k is the coordinate corresponding to v_k.

The substitution of equation [3.15] into equation [3.11] yields

$$\begin{aligned}
&\text{For collet}: \quad 0\le x<L_1:\\
&E_1 I_1(x)\frac{d^4W_1(x)}{dx^4}+E_1\frac{d^2I_1(x)}{dx^2}\frac{d^2W_1(x)}{dx^2}\\
&\quad+2E_1\frac{dI_1(x)}{dx}\frac{d^3W_1(x)}{dx^3}-m_1(x)\,\omega^2W_1(x)\\
&\quad=K_2(x)\left[v(x)-W_1(x)\right]-K_1(x)\left[W_1(x)-W_2(x)\right]
\end{aligned}$$

$$\begin{aligned}
&\text{For IPT}: \quad 0 \le x < L_1: \\
&E_2 I_2 \frac{d^4 W_2(x)}{dx^4} - m_2 \omega^2 W_2(x) = K_1(x)\left[W_1(x) - W_2(x)\right] \\
&\text{For TOPWF}: \quad L_1 \le x < L_2: \\
&E_2 I_3 \frac{d^4 W_3(x)}{dx^4} - m_3 \omega^2 W_3(x) = 0 \\
&\text{For FPT}: \quad L_2 \le x \le L: \\
&E_2 I_4 \frac{d^4 W_4(x)}{dx^4} - m_4 \omega^2 W_4(x) = 0
\end{aligned} \qquad [3.19]$$

Solutions of the above equations will be detailed below.

3.2.1.2. *Solutions of the dynamic equations*

According to the Weierstrass approximation theorem [RUD 76], continuous shape functions $W_1(x)$ and $W_2(x)$ in equation [3.15] can be approximated by the following polynomial functions

$$\begin{aligned}
W_2(x) &= \sum_{k=1}^{N_{\mathrm{K}}} a_k x^{k-1} = \mathbf{a}^{\mathrm{T}}\mathbf{x} \\
W_1(x) &= \sum_{k=1}^{N_{\mathrm{K}}} b_k x^{k-1} = \mathbf{b}^{\mathrm{T}}\mathbf{x}
\end{aligned} \qquad [3.20]$$

with $\mathbf{a} = \{a_1, a_2, ..., a_{N_{\mathrm{K}}}\}^{\mathrm{T}}$, $\mathbf{b} = \{b_1, b_2, ..., b_{N_{\mathrm{K}}}\}^{\mathrm{T}}$, and $\mathbf{x} = \left\{1, x, x^2, ..., x^{N_{\mathrm{K}}-1}\right\}^{\mathrm{T}}$. $k-1$ means the degree of each term of the polynomial. $N_{\mathrm{K}-1}$ designates the degree of the polynomial.

After substituting equations [3.12], [3.14], [3.16] and [3.20] into the first two equations of equation [3.19] and making the coefficients of polynomials on both sides of two equations equal, the recursive relation about $a_1, a_2, ..., a_{N_{\mathrm{K}}}$ can be expressed as:

$$a_k = \frac{(k-5)!}{E_2 I_2 (k-1)!}\left[\sum_{j_1=0}^{\min(Q,k-5)} \kappa_{\mathrm{A},j_1}\left(b_{k-4-j_1} - a_{k-4-j_1}\right) + m_2\omega^2 a_{k-4}\right]$$

with $k = 5, 6, ..., N_{\mathrm{K}}$.

While the recursive relation about $b_1, b_2, ..., b_{N_{\mathrm{K}}}$ can be expressed as:

1) b_5 corresponding to the coefficient of the constant term is

$$\frac{\pi E_1}{64}\frac{4!}{0!}\left({d_{\mathrm{C}}}^4 - {d_{\mathrm{T}}}^4\right)b_5 + \frac{\pi E_1 k_{\mathrm{C}}}{4}{d_{\mathrm{C}}}^3\frac{3!}{0!}b_4 + \frac{3\pi E_1 {k_{\mathrm{C}}}^2}{4}{d_{\mathrm{C}}}^2\frac{2!}{0!}b_3$$
$$-\frac{\pi\rho\omega^2}{4}{d_{\mathrm{C}}}^2 b_1 + \frac{\pi\rho\omega^2}{4}{d_{\mathrm{T}}}^2 b_1 = \kappa_{\mathrm{B},0}\left(w_1 - b_1\right) - \kappa_{\mathrm{A},0}\left(b_1 - a_1\right)$$

2) b_6 corresponding to the coefficient of the linear term $(k = 6)$ is

$$\frac{\pi E_1}{64}\frac{5!}{1!}\left({d_{\mathrm{C}}}^4 - {d_{\mathrm{T}}}^4\right)b_6 + \frac{\pi E_1}{64}\mathrm{C}_4^3{d_{\mathrm{C}}}^3(2k_{\mathrm{C}})^1\frac{4!}{0!}b_5$$
$$+\frac{\pi E_1 k_{\mathrm{C}}}{4}\mathrm{C}_3^2{d_{\mathrm{C}}}^2(2k_{\mathrm{C}})^1\frac{3!}{0!}b_4 + \frac{\pi E_1 k_{\mathrm{C}}}{4}\mathrm{C}_3^3{d_{\mathrm{C}}}^3(2k_{\mathrm{C}})^0\frac{4!}{1!}b_5$$
$$+\frac{3\pi E_1 {k_{\mathrm{C}}}^2}{4}\mathrm{C}_2^1{d_{\mathrm{C}}}^1(2k_{\mathrm{C}})^1\frac{2!}{0!}b_3 + \frac{3\pi E_1 {k_{\mathrm{C}}}^2}{4}\mathrm{C}_2^2{d_{\mathrm{C}}}^2(2k_{\mathrm{C}})^0\frac{3!}{1!}b_4$$
$$-\frac{\pi\rho\omega^2}{4}\mathrm{C}_2^1{d_{\mathrm{C}}}^1(2k_{\mathrm{C}})^1 b_1 - \frac{\pi\rho\omega^2}{4}\mathrm{C}_2^2{d_{\mathrm{C}}}^2(2k_{\mathrm{C}})^0 b_2\frac{\pi\rho\omega^2}{4}{d_{\mathrm{T}}}^2 b_2$$
$$= \sum_{i_5=\max(k-4-N_{\mathrm{M}},0)}^{\min\left(\hat{Q},k-5\right)}\kappa_{\mathrm{B},i_5}w_{k-4-i_5} - \sum_{i_6=0}^{\min\left(\hat{Q},k-5\right)}\kappa_{\mathrm{B},i_6}b_{k-4-i_6}$$
$$-\sum_{i_7=0}^{\min(Q,k-5)}\kappa_{\mathrm{A},i_7}\left(b_{k-4-i_7} - a_{k-4-i_7}\right)$$

3) b_7 corresponding to the coefficient of the quadratic term $(k = 7)$ is

$$\frac{\pi E_1}{64}\frac{6!}{2!}\left({d_{\mathrm{C}}}^4 - {d_{\mathrm{T}}}^4\right)b_7 + \frac{\pi E_1}{64}\mathrm{C}_4^2{d_{\mathrm{C}}}^2(2k_{\mathrm{C}})^2\frac{4!}{0!}b_5$$
$$+\frac{\pi E_1}{64}\mathrm{C}_4^3{d_{\mathrm{C}}}^3(2k_{\mathrm{C}})^1\frac{5!}{1!}b_6 + \frac{\pi E_1 k_{\mathrm{C}}}{4}\mathrm{C}_3^1{d_{\mathrm{C}}}^1(2k_{\mathrm{C}})^2\frac{3!}{0!}b_4$$
$$+\frac{\pi E_1 k_{\mathrm{C}}}{4}\mathrm{C}_3^2{d_{\mathrm{C}}}^2(2k_{\mathrm{C}})^1\frac{4!}{1!}b_5 + \frac{\pi E_1 k_{\mathrm{C}}}{4}\mathrm{C}_3^3{d_{\mathrm{C}}}^3(2k_{\mathrm{C}})^0\frac{5!}{2!}b_6$$

$$+\frac{3\pi E_1 {k_\mathrm{C}}^2}{4}\sum_{i_3=0}^{2}{\mathrm{C}_2^{i_3}}{d_\mathrm{C}}^{i_3}(2k_\mathrm{C})^{2-i_3}\frac{(k-5+i_3)!}{(k-7+i_3)!}b_{k-4+i_3}$$

$$-\frac{\pi\rho\omega^2}{4}\sum_{i_4=0}^{2}{\mathrm{C}_2^{i_4}}{d_\mathrm{C}}^{i_4}(2k_\mathrm{C})^{2-i_4}b_{k-6+i_4}+\frac{\pi\rho\omega^2}{4}{d_\mathrm{T}}^2 b_{k-4}$$

$$=\sum_{i_5=\max(k-4-N_\mathrm{M},0)}^{\min\left(\hat{Q},k-5\right)}\kappa_{\mathrm{B},i_5}w_{k-4-i_5}-\sum_{i_6=0}^{\min\left(\hat{Q},k-5\right)}\kappa_{\mathrm{B},i_6}b_{k-4-i_6}$$

$$-\sum_{i_7=0}^{\min(Q,k-5)}\kappa_{\mathrm{A},i_7}\left(b_{k-4-i_7}-a_{k-4-i_7}\right)$$

4) b_8 corresponding to the coefficient of the 3th-order term $(k=8)$ is

$$\frac{\pi E_1}{64}\frac{7!}{3!}\left({d_\mathrm{C}}^4-{d_\mathrm{T}}^4\right)b_8+\frac{\pi E_1}{64}\mathrm{C}_4^1{d_\mathrm{C}}^1(2k_\mathrm{C})^3\frac{4!}{0!}b_5$$

$$+\frac{\pi E_1}{64}\mathrm{C}_4^2{d_\mathrm{C}}^2(2k_\mathrm{C})^2\frac{5!}{1!}b_6+\frac{\pi E_1}{64}\mathrm{C}_4^3{d_\mathrm{C}}^3(2k_\mathrm{C})^1\frac{6!}{2!}b_7$$

$$+\frac{\pi E_1 k_\mathrm{C}}{4}\sum_{i_2=0}^{3}{\mathrm{C}_3^{i_2}}{d_\mathrm{C}}^{i_2}(2k_\mathrm{C})^{3-i_2}\frac{(k-5+i_2)!}{(k-8+i_2)!}b_{k-4+i_2}$$

$$+\frac{3\pi E_1 {k_\mathrm{C}}^2}{4}\sum_{i_3=0}^{2}{\mathrm{C}_2^{i_3}}{d_\mathrm{C}}^{i_3}(2k_\mathrm{C})^{2-i_3}\frac{(k-5+i_3)!}{(k-7+i_3)!}b_{k-4+i_3}$$

$$-\frac{\pi\rho\omega^2}{4}\sum_{i_4=0}^{2}{\mathrm{C}_2^{i_4}}{d_\mathrm{C}}^{i_4}(2k_\mathrm{C})^{2-i_4}b_{k-6+i_4}+\frac{\pi\rho\omega^2}{4}{d_\mathrm{T}}^2 b_{k-4}$$

$$=\sum_{i_5=\max(k-4-N_\mathrm{M},0)}^{\min\left(\hat{Q},k-5\right)}\kappa_{\mathrm{B},i_5}w_{k-4-i_5}-\sum_{i_6=0}^{\min\left(\hat{Q},k-5\right)}\kappa_{\mathrm{B},i_6}b_{k-4-i_6}$$

$$-\sum_{i_7=0}^{\min(Q,k-5)}\kappa_{\mathrm{A},i_7}\left(b_{k-4-i_7}-a_{k-4-i_7}\right)$$

5) b_k corresponding to the coefficient of the $(k-5)$th-order term $(k = 9, 10, ..., N_{\mathrm{K}})$ is

$$\begin{aligned}
&\frac{\pi E_1}{64}\frac{(k-1)!}{(k-5)!}\left({d_{\mathrm{C}}}^4 - {d_{\mathrm{T}}}^4\right) b_k \\
&+\frac{\pi E_1}{64}\sum_{i_1=0}^{3} \mathrm{C}_4^{i_1} {d_{\mathrm{C}}}^{i_1} (2k_{\mathrm{C}})^{4-i_1} \frac{(k-5+i_1)!}{(k-9+i_1)!} b_{k-4+i_1} \\
&+\frac{\pi E_1 k_{\mathrm{C}}}{4}\sum_{i_2=0}^{3} \mathrm{C}_3^{i_2} {d_{\mathrm{C}}}^{i_2} (2k_{\mathrm{C}})^{3-i_2} \frac{(k-5+i_2)!}{(k-8+i_2)!} b_{k-4+i_2} \\
&+\frac{3\pi E_1 {k_{\mathrm{C}}}^2}{4}\sum_{i_3=0}^{2} \mathrm{C}_2^{i_3} {d_{\mathrm{C}}}^{i_3} (2k_{\mathrm{C}})^{2-i_3} \frac{(k-5+i_3)!}{(k-7+i_3)!} b_{k-4+i_3} \\
&-\frac{\pi\rho\omega^2}{4}\sum_{i_4=0}^{2} \mathrm{C}_2^{i_4} {d_{\mathrm{C}}}^{i_4} (2k_{\mathrm{C}})^{2-i_4} b_{k-6+i_4} + \frac{\pi\rho\omega^2}{4} {d_{\mathrm{T}}}^2 b_{k-4} \\
&= \sum_{i_5=\max(k-4-N_{\mathrm{M}},0)}^{\min(\hat{Q},k-5)} \kappa_{\mathrm{B},i_5} w_{k-4-i_5} - \sum_{i_6=0}^{\min(\hat{Q},k-5)} \kappa_{\mathrm{B},i_6} b_{k-4-i_6} \\
&- \sum_{i_7=0}^{\min(Q,k-5)} \kappa_{\mathrm{A},i_7} \left(b_{k-4-i_7} - a_{k-4-i_7}\right)
\end{aligned}$$

where w_{k_*} is the element of vector $\mathbf{w}$, which equals $\mathbf{P}^{\mathrm{T}}\mathbf{v}$.

The above derivation yields the following relationship

$$\begin{aligned}
\mathbf{c} &= \left\{\mathbf{a}^{\mathrm{T}}, \mathbf{b}^{\mathrm{T}}\right\}^{\mathrm{T}} \\
&= \mathbf{T}_{\mathrm{v}}\mathbf{v} + \mathbf{T}_{\mathrm{c}}\{a_1, a_2, a_3, a_4, b_1, b_2, b_3, b_4\}^{\mathrm{T}} \\
&= \mathbf{T}_{\mathrm{v}}\mathbf{v} + \mathbf{T}_{\mathrm{c}}\hat{\mathbf{c}} \\
\hat{\mathbf{c}} &= \{a_1, a_2, a_3, a_4, b_1, b_2, b_3, b_4\}^{\mathrm{T}}
\end{aligned} \qquad [3.21]$$

where $\mathbf{T}_{\mathrm{v}}$ and $\mathbf{T}_{\mathrm{c}}$ are two matrices with sizes $2N_{\mathrm{K}} \times 2N_{\mathrm{M}}$ and $2N_{\mathrm{K}} \times 8$. Derivation procedure indicates that high-order polynomial coefficients a_k and $b_k\,(k = 5, ..., N_{\mathrm{K}})$ involved in equation [3.21] can be expressed by $\hat{\mathbf{c}}$ and $\mathbf{v}$. This means that only $a_1, a_2, a_3, a_4,\ b_1, b_2, b_3, b_4$ are needed to characterize equation [3.21]. $\mathbf{v}$ is the lateral displacement vector satisfying the following expression

$$\mathbf{v} = \mathbf{H}(\omega)\ \mathbf{F} \qquad [3.22]$$

where $\mathbf{H}(\omega)$ is the $N_{\mathrm{M}} \times N_{\mathrm{M}}$ displacement-to-force receptance matrix of the spindle-holder assembly. $\mathbf{F}$ is the discretization of the force applied on the holder, i.e. the counterforce of $K_2(x)\,[v(x) - W_1(x)]$ in equation [3.19], and can be formulated as follows

$$\mathbf{F} = (f_1, f_2, ..., f_{N_{\mathrm{M}}})^{\mathrm{T}} = \int_0^{L_1} \mathbf{p} K_2(x)\,[W_1(x) - v(x)]\,dx \qquad [3.23]$$

After substituting equation [3.23] into equation [3.22] and then replacing $v(x)$ with $\mathbf{p}^{\mathrm{T}}\mathbf{v}$, we have

$$\begin{aligned} \mathbf{v} &= (\mathbf{I}_{N_{\mathrm{M}} \times N_{\mathrm{M}}} + \mathbf{H}\mathbf{J}_{\mathrm{c}})^{-1}\mathbf{H} \int_0^{L_1} \mathbf{p} K_2(x)\, W_1(x)\, dx \\ &= (\mathbf{I}_{N_{\mathrm{M}} \times N_{\mathrm{M}}} + \mathbf{H}\mathbf{J}_{\mathrm{c}})^{-1}\mathbf{H}\mathbf{F}_0 \qquad [3.24] \\ \mathbf{J}_{\mathrm{c}} &= \int_0^{L_1} K_2(x)\, \mathbf{p}\mathbf{p}^{\mathrm{T}} dx \end{aligned}$$

where $\mathbf{I}_{N_{\mathrm{M}} \times N_{\mathrm{M}}}$ is the identity matrix. $\mathbf{F}_0$ is expressed as

$$\begin{aligned} \mathbf{F}_0 &= \int_0^{L_1} \mathbf{p} K_2(x)\, W_1(x)\, dx \\ &= \int_0^{L_1} \mathbf{p} K_2(x) \sum_{k=1}^{N_{\mathrm{K}}} b_k x^{k-1} dx = \sum_{k=1}^{N_{\mathrm{K}}} b_k \int_0^{L_1} \mathbf{p} K_2(x)\, x^{k-1} dx \end{aligned}$$

$$= \left[\int_0^{L_1} \mathbf{p} K_2(x)\, dx \ \int_0^{L_1} \mathbf{p} K_2(x)\, x dx \ \ldots \ \int_0^{L_1} \mathbf{p} K_2(x)\, x^{N_K-1} dx \right] \times \{b_1, b_2, ..., b_{N_K}\}^{\mathrm{T}} = \mathbf{M}\,\mathbf{b} = [\mathbf{O}, \mathbf{M}]\{\mathbf{a}^{\mathrm{T}}, \mathbf{b}^{\mathrm{T}}\}^{\mathrm{T}} = \tilde{\mathbf{M}}\mathbf{c} \quad [3.25]$$

in which $\tilde{\mathbf{M}} = [\mathbf{O}, \mathbf{M}]$. $\mathbf{M}$ is an $N_M \times N_K$ matrix, and $\mathbf{O}$ is an $N_M \times N_K$ zero matrix.

The combination of equations [3.21], [3.24] and [3.26] leads to

$$\mathbf{c} = \mathbf{S}\hat{\mathbf{c}} \quad [3.26]$$

with

$$\mathbf{S} = \left(\mathbf{I}_{2N_K \times 2N_K} - \mathbf{T}_v(\mathbf{I}_{N_M \times N_M} + \mathbf{H}\mathbf{J}_c)^{-1}\mathbf{H}\tilde{\mathbf{M}}\right)^{-1}\mathbf{T}_c \quad [3.27]$$

According to the theory of differential equations, the solutions of the last two equations of equation [3.19], i.e. shape functions $W_3(x)$ and $W_4(x)$, can be written in the following general form [RAO 11, LEI 11].

$$\begin{aligned} W_3(x) &= C_1 e^{i\alpha_3 x} + C_2 e^{-i\alpha_3 x} + C_3 e^{\alpha_3 x} + C_4 e^{-\alpha_3 x}, \quad L_1 \le x < L_2 \\ W_4(x) &= D_1 e^{i\beta_4 x} + D_2 e^{-i\beta_4 x} + D_3 e^{\beta_4 x} + D_4 e^{-\beta_4 x}, \quad L_2 \le x \le L \end{aligned} \quad [3.28]$$

with

$$\begin{aligned} \alpha_3^4 &= \frac{m_3\omega^2}{E_3 I_3} \\ \beta_4^4 &= \frac{m_4\omega^2}{E_4 I_4} \end{aligned} \quad [3.29]$$

The above derivations show that $W_k(x)$ $(k = 1, 2, 3, 4)$ can be expressed in terms of sixteen independent coefficients, whose determinations are presented below based on boundary and compatibility conditions.

Concerning the tool tip, related boundary conditions are a unit harmonic force and zero moment.

$$\begin{aligned} -E_4 I_4 \frac{d^3 W_4(L)}{dx^3} &= 1, \text{ a unit harmonic force} \\ E_4 I_4 \frac{d^2 W_4(L)}{dx^2} &= 0, \quad \text{zero moment} \end{aligned} \quad [3.30]$$

Boundary conditions at the other end of the tool are zero lateral force and zero moment.

$$\begin{aligned} E_2 I_2 \frac{d^3 W_2(0)}{dx^3} &= 0, \text{ zero lateral force} \\ E_2 I_2 \frac{d^2 W_2(0)}{dx^2} &= 0, \text{ zero moment} \end{aligned} \quad [3.31]$$

Regarding the connection section between IPT and TOPWF, the compatibility conditions correspond to the continuities of displacement, slope, moment and lateral force.

$$\begin{aligned} W_2(L_1) - W_3(L_1) &= 0, && \text{displacement continuity} \\ \frac{dW_2(L_1)}{dx} - \frac{dW_3(L_1)}{dx} &= 0, && \text{slope continuity} \\ E_2 I_2 \frac{d^2 W_2(L_1)}{dx^2} - E_3 I_3 \frac{d^2 W_3(L_1)}{dx^2} &= 0, && \text{moment continuity} \\ E_2 I_2 \frac{d^3 W_2(L_1)}{dx^3} - E_3 I_3 \frac{d^3 W_3(L_1)}{dx^3} &= 0, && \text{lateral force continuity} \end{aligned} \quad [3.32]$$

Similarly, compatibility conditions at the connection section of TOPWF and FPT are:

$$\begin{aligned} W_3(L_2) - W_4(L_2) &= 0, && \text{displacement continuity} \\ \frac{dW_3(L_2)}{dx} - \frac{dW_4(L_2)}{dx} &= 0, && \text{slope continuity} \\ E_3 I_3 \frac{d^2 W_3(L_2)}{dx^2} - E_4 I_4 \frac{d^2 W_4(L_2)}{dx^2} &= 0, && \text{moment continuity} \\ E_3 I_3 \frac{d^3 W_3(L_2)}{dx^3} - E_4 I_4 \frac{d^3 W_4(L_2)}{dx^3} &= 0, && \text{lateral force continuity} \end{aligned} \quad [3.33]$$

The boundary conditions on the left and right ends of the collet are zero lateral force and moment:

$$\begin{aligned}
&E_1 I_1(0)\frac{d^2W_1(0)}{dx^2}=0, && \text{zero moment on left end}\\
&\frac{d}{dx}\left[E_1 I_1(x)\frac{d^2W_1(x)}{dx^2}\right]_{x=0}=0, && \text{zero lateral force on left end}\\
&E_1 I_1(L_1)\frac{d^2W_1(L_1)}{dx^2}=0, && \text{zero moment on right end}\\
&\frac{d}{dx}\left[E_1 I_1(x)\frac{d^2W_1(x)}{dx^2}\right]_{x=L_1}=0, && \text{zero lateral force on right end}
\end{aligned} \qquad [3.34]$$

Equations [3.30] – [3.34] can be rewritten as:

$$\begin{aligned}
&\mathbf{Z}(\omega)\,\mathbf{d}=\{1,0,...,0\}^{\mathrm{T}}\\
&\mathbf{d}=\left\{D_1,D_2,D_3,D_4,C_1,C_2,C_3,C_4,\hat{\mathbf{c}}^{\mathrm{T}}\right\}^{\mathrm{T}}
\end{aligned} \qquad [3.35]$$

where $\mathbf{Z}(\omega)$ is a 16×16 full rank matrix closely related to matrix $\mathbf{S}$ and expressed as.

$$\mathbf{Z}=\begin{bmatrix}\mathbf{Z}_1 & \mathbf{Z}_2 & \mathbf{Z}_3\\ \mathbf{Z}_4 & \mathbf{Z}_5 & \mathbf{Z}_6\\ \mathbf{Z}_7 & \mathbf{Z}_8 & \mathbf{Z}_9\\ \mathbf{Z}_{10} & \mathbf{Z}_{11} & \mathbf{Z}_{12}\\ \mathbf{Z}_{13} & \mathbf{Z}_{14} & \mathbf{Z}_{15}\end{bmatrix},$$

where $\mathbf{Z}_2$, $\mathbf{Z}_4$ and $\mathbf{Z}_5$ are three 2×4 zero matrices. $\mathbf{Z}_3$ is a 2×8 zero matrix. $\mathbf{Z}_{12}$ is a 4×8 zero matrix. $\mathbf{Z}_7$, $\mathbf{Z}_{13}$ and $\mathbf{Z}_{14}$ are three 4×4 zero matrices.

$$\mathbf{Z}_1=\begin{bmatrix}E_4I_4\mathrm{J}\beta_4^3\mathrm{e}^{\mathrm{J}\beta_4L} & -E_4I_4\mathrm{J}\beta_4^3\mathrm{e}^{-\mathrm{J}\beta_4L} & -E_4I_4\beta_4^3\mathrm{e}^{\beta_4L} & E_4I_4\beta_4^3\mathrm{e}^{-\beta_4L}\\ -\beta_4^2\mathrm{e}^{\mathrm{J}\beta_4L} & -\beta_4^2\mathrm{e}^{-\mathrm{J}\beta_4L} & \beta_4^2\mathrm{e}^{\beta_4L} & \beta_4^2\mathrm{e}^{-\beta_4L}\end{bmatrix}$$

$\mathbf{Z}_6$ is a 2×8 matrix whose elements are

$$Z_{k_1k_2}=\begin{cases}S_{4,k_2} & k_1=1,k_2=1,2,...,8\\ S_{3,k_2} & k_1=2,k_2=1,2,...,8\end{cases}.$$

$$\mathbf{Z}_8 = \begin{bmatrix} -\mathrm{e}^{\mathrm{J}\alpha_3 L_1} & -\mathrm{e}^{-\mathrm{J}\alpha_3 L_1} & -\mathrm{e}^{\alpha_3 L_1} & -\mathrm{e}^{-\alpha_3 L_1} \\ -\mathrm{J}\alpha_3 \mathrm{e}^{\mathrm{J}\alpha_3 L_1} & \mathrm{J}\alpha_3 \mathrm{e}^{-\mathrm{J}\alpha_3 L_1} & -\alpha_3 \mathrm{e}^{\alpha_3 L_1} & \alpha_3 \mathrm{e}^{-\alpha_3 L_1} \\ E_3 I_3 \alpha_3^2 \mathrm{e}^{\mathrm{J}\alpha_3 L_1} & E_3 I_3 \alpha_3^2 \mathrm{e}^{-\mathrm{J}\alpha_3 L_1} & -E_3 I_3 \alpha_3^2 \mathrm{e}^{\alpha_3 L_1} & -E_3 I_3 \alpha_3^2 \mathrm{e}^{-\alpha_3 L_1} \\ E_3 I_3 \mathrm{J}\alpha_3^3 \mathrm{e}^{\mathrm{J}\alpha_3 L_1} & -E_3 I_3 \mathrm{J}\alpha_3^3 \mathrm{e}^{-\mathrm{J}\alpha_3 L_1} & -E_3 I_3 \alpha_3^3 \mathrm{e}^{\alpha_3 L_1} & E_3 I_3 \alpha_3^3 \mathrm{e}^{-\alpha_3 L_1} \end{bmatrix}$$

$\mathbf{Z}_9$ is a 4×8 matrix whose elements are

$$Z_{k_1 k_2} = \begin{cases} \sum_{k=1}^{K} L_1^{k-1} S_{k,k_2} & k_1 = 1, k_2 = 1, 2, ..., 8 \\ \sum_{k=2}^{K} (k-1) L_1^{k-2} S_{k,k_2} & k_1 = 2, k_2 = 1, 2, ..., 8 \\ E_2 I_2 \sum_{k=3}^{K} \frac{(k-1)!}{(k-3)!} L_1^{k-3} S_{k,k_2} & k_1 = 3, k_2 = 1, 2, ..., 8 \\ E_2 I_2 \sum_{k=4}^{K} \frac{(k-1)!}{(k-4)!} L_1^{k-4} S_{k,k_2} & k_1 = 4, k_2 = 1, 2, ..., 8 \end{cases}$$

$$\mathbf{Z}_{10} = \begin{bmatrix} -\mathrm{e}^{\mathrm{J}\beta_4 L_2} & -\mathrm{e}^{-\mathrm{J}\beta_4 L_2} & -\mathrm{e}^{\beta_4 L_2} & -\mathrm{e}^{-\beta_4 L_2} \\ -\mathrm{J}\beta_4 \mathrm{e}^{\mathrm{J}\beta_4 L_2} & \mathrm{J}\beta_4 \mathrm{e}^{-\mathrm{J}\beta_4 L_2} & -\beta_4 \mathrm{e}^{\beta_4 L_2} & \beta_4 \mathrm{e}^{-\beta_4 L_2} \\ E_4 I_4 \beta_4^2 \mathrm{e}^{\mathrm{J}\beta_4 L_2} & E_4 I_4 \beta_4^2 \mathrm{e}^{-\mathrm{J}\beta_4 L_2} & -E_4 I_4 \beta_4^2 \mathrm{e}^{\beta_4 L_2} & -E_4 I_4 \beta_4^2 \mathrm{e}^{-\beta_4 L_2} \\ E_4 I_4 \mathrm{J}\beta_4^3 \mathrm{e}^{\mathrm{J}\beta_4 L_2} & -E_4 I_4 \mathrm{J}\beta_4^3 \mathrm{e}^{-\mathrm{J}\beta_4 L_2} & -E_4 I_4 \beta_4^3 \mathrm{e}^{\beta_4 L_2} & E_4 I_4 \beta_4^3 \mathrm{e}^{-\beta_4 L_2} \end{bmatrix}$$

$$\mathbf{Z}_{11} = \begin{bmatrix} \mathrm{e}^{\mathrm{J}\alpha_3 L_2} & \mathrm{e}^{-\mathrm{J}\alpha_3 L_2} & \mathrm{e}^{\alpha_3 L_2} & \mathrm{e}^{-\alpha_3 L_2} \\ \mathrm{J}\alpha_3 \mathrm{e}^{\mathrm{J}\alpha_3 L_2} & -\mathrm{J}\alpha_3 \mathrm{e}^{-\mathrm{J}\alpha_3 L_2} & \alpha_3 \mathrm{e}^{\alpha_3 L_2} & -\alpha_3 \mathrm{e}^{-\alpha_3 L_2} \\ -E_3 I_3 \alpha_3^2 \mathrm{e}^{\mathrm{J}\alpha_3 L_2} & -E_3 I_3 \alpha_3^2 \mathrm{e}^{-\mathrm{J}\alpha_3 L_2} & E_3 I_3 \alpha_3^2 \mathrm{e}^{\alpha_3 L_2} & E_3 I_3 \alpha_3^2 \mathrm{e}^{-\alpha_3 L_2} \\ -E_3 I_3 \mathrm{J}\alpha_3^3 \mathrm{e}^{\mathrm{J}\alpha_3 L_2} & E_3 I_3 \mathrm{J}\alpha_3^3 \mathrm{e}^{-\mathrm{J}\alpha_3 L_2} & E_3 I_3 \alpha_3^3 \mathrm{e}^{\alpha_3 L_2} & -E_3 I_3 \alpha_3^3 \mathrm{e}^{-\alpha_3 L_2} \end{bmatrix}$$

$\mathbf{Z}_{15}$ is a 4×8 matrix whose elements are

$$Z_{k_1 k_2} = \begin{cases} S_{N_\mathrm{K}+3,k_2} & k_1 = 1, k_2 = 1, 2, ..., 8 \\ 6 I_1(0) S_{N_\mathrm{K}+4,k_2} + 2 I_1'(0) S_{N_\mathrm{K}+3,k_2} & k_1 = 2, k_2 = 1, 2, ..., 8 \\ \sum_{k=3}^{N_\mathrm{K}} \frac{(k-1)!}{(k-3)!} L_1^{k-3} S_{N_\mathrm{K}+k,k_2} & k_1 = 3, k_2 = 1, 2, ..., 8 \\ I_1(L_1) \sum_{k=4}^{N_\mathrm{K}} \frac{(k-1)!}{(k-4)!} L_1^{k-4} S_{N_\mathrm{K}+k,k_2} & \\ + I_1'(L_1) \sum_{k=3}^{K} \frac{(k-1)!}{(k-3)!} L_1^{k-3} S_{N_\mathrm{K}+k,k_2} & k_1 = 4, k_2 = 1, 2, ..., 8 \end{cases}$$

Note that $\mathbf{S}_{k_1,k_2}$ in the above equations denote elements of matrix $\mathbf{S}$ defined in equation [3.27].

Note that the first element of the right-hand side vector equaling one corresponds to the first equation of equation [3.30], which is non-homogenous among the boundary and compatibility conditions. If the receptance of the spindle-holder assembly $\mathbf{H}(\omega)$ is given in equation [3.27], the sixteen unknown coefficients can be immediately obtained by solving equation [3.35]. Subsequently, the tool point receptance $H_{\mathrm{T}}(\omega)$ given in equation [3.10] can be calculated using the determined D_1, D_2, D_3 and D_4.

$$H_{\mathrm{T}}(\omega) = \frac{W_4(L)\, e^{\mathrm{J}\omega t}}{e^{\mathrm{J}\omega t}} = D_1 e^{\mathrm{J}\beta_4 L} + D_2 e^{-\mathrm{J}\beta_4 L} + D_3 e^{\beta_4 L} + D_4 e^{-\beta_4 L} \qquad [3.36]$$

3.2.2. *Identification of model parameters*

3.2.2.1. *Calculation of spindle-holder assembly receptance*

As stated above, the receptance matrix of spindle-holder assembly $\mathbf{H}(\omega)$ is the precondition for solving equation [3.35]. A literature review shows that it was generally determined by experimental methods [AHM 07]. The inconvenience of this kind of methods lies in the fact that once the holder changes its size, impact testing has to be re-carried out. In this section, a computing method is presented to determine $\mathbf{H}(\omega)$ based on RCSA [SCH 05, SCH 09, SCH 00, EWI 00].

As illustrated in Figure 3.4, the spindle-holder assembly is first partitioned into two rigidly connected components, i.e. spindle-holder base (Component I) and extended holder (Component II). The latter is divided into M identical elements with the nodes numbered in a sequence that begins with 1 from the free end of the holder, as shown in Figure 3.4. The procedure for determining $H_{k_1 k_2}(\omega)$ is taken as an example to illustrate how to obtain an arbitrary element of $\mathbf{H}(\omega)$. Mathematically, $H_{k_1 k_2}(\omega)$ is defined as

$$H_{k_1 k_2} = Y_{k_1} / F_{k_2} \qquad [3.37]$$

where Y_{k_1} means the lateral displacement of assembly related to node k_1 under the lateral force F_{k_2} applied to node k_2, and is calculated according to the following RCSA procedure.

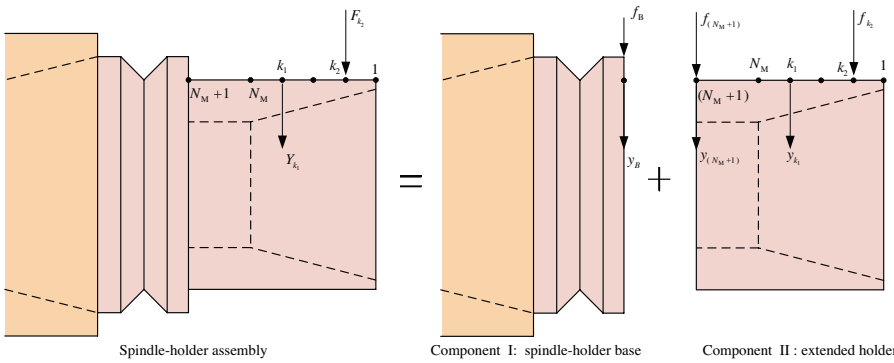

Figure 3.4. *Spindle-holder assembly and components*

For Components I and II, corresponding lateral displacements y_{B} and $y_{(N_{\mathrm{M}}+1)}$ at the partition section of both components are expressed as:

$$\begin{aligned} y_{\mathrm{B}} &= h_{\mathrm{BB}} f_{\mathrm{B}}, && \text{component I} \\ y_{(N_{\mathrm{M}}+1)} &= h_{(N_{\mathrm{M}}+1)(N_{\mathrm{M}}+1)} f_{(N_{\mathrm{M}}+1)} + h_{(N_{\mathrm{M}}+1)k_2} f_{k_2}, && \text{component II} \end{aligned} \quad [3.38]$$

where h_{BB} and f_{B} denote the receptance and the lateral force of Component I at this partition section, respectively. $h_{k_1k_2}$ is the receptance at node k_1 under the lateral force f_{k_2} applied to node k_2. Similarly, the lateral displacement y_{k_1} of node k_1 under the lateral force f_{k_2} and $f_{(N_{\mathrm{M}}+1)}$ can be written as

$$y_{k_1} = h_{k_1k_2} f_{k_2} + h_{k_1(N_{\mathrm{M}}+1)} f_{(N_{\mathrm{M}}+1)} \quad [3.39]$$

According to the equilibrium and compatibility conditions, the lateral forces and displacements at the partition section of both components satisfy

$$f_{(N_{\mathrm{M}}+1)} + f_{\mathrm{B}} = 0, \quad f_{k_2} = F_{k_2}, \quad y_{(N_{\mathrm{M}}+1)} = y_{\mathrm{B}} \quad [3.40]$$

Since the component and assembly coordinates are coincident, the following relation holds

$$y_{k_1} = Y_{k_1} \quad [3.41]$$

Note that upper case variables are used to designate assembly terms, and lower case variables to identify component terms.

The combination of equations [3.38]–[3.41] gives

$$Y_{k_1} = \left[h_{k_1k_2} - h_{k_1(N_\mathrm{M}+1)}\left(h_\mathrm{BB} + h_{(N_\mathrm{M}+1)(N_\mathrm{M}+1)}\right)^{-1} h_{(N_\mathrm{M}+1)k_2}\right] F_{k_2} \quad [3.42]$$

Finally, the substitution of equation [3.42] into equation [3.37] leads to

$$\begin{aligned} H_{k_1k_2} &= \frac{Y_{k_1}}{F_{k_2}} = \frac{y_{k_1}}{F_{k_2}} \\ &= \frac{\left[h_{k_1k_2} - h_{k_1(N_\mathrm{M}+1)}\left(h_\mathrm{BB} + h_{(N_\mathrm{M}+1)(N_\mathrm{M}+1)}\right)^{-1} h_{(N_\mathrm{M}+1)k_2}\right] F_{k_2}}{F_{k_2}} \\ &= h_{k_1k_2} - h_{k_1(N_\mathrm{M}+1)}\left(h_\mathrm{BB} + h_{(N_\mathrm{M}+1)(N_\mathrm{M}+1)}\right)^{-1} h_{(N_\mathrm{M}+1)k_2} \end{aligned} \quad [3.43]$$

Notice that only lateral displacements (y_{k_1}, Y_{k_1}) and shear forces (f_{k_2}, F_{k_2}) are taken into consideration in the above derivation. Furthermore, as stated in [SCH 09, PAR 03], both rotations $(\theta_{k_1}, \Theta_{k_1})$ and moments (m_{k_2}, M_{k_2}) have obvious effects on $H_{k_1k_2}$. Thus the influences from both factors should be considered in obtaining $H_{k_1k_2}$. Minor modification should be carried out in equation [3.43]. Concretely, displacement-to-force receptances $(h_{k_1k_2}, H_{k_1k_2})$ in equation [3.43] are replaced by receptance matrices $(\mathbf{R}_{ij}, \mathbf{G}_{ij})$ which contain displacement-to-force $(h_{k_1k_2}, H_{k_1k_2})$, displacement-to-moment $(l_{k_1k_2}, L_{k_1k_2})$, rotation-to-force $(n_{k_1k_2}, N_{k_1k_2})$, and rotation-to-moment $(p_{k_1k_2}, P_{k_1k_2})$ receptances.

$$\mathbf{G}_{k_1k_2} = \mathbf{R}_{k_1k_2} - \mathbf{R}_{i(N_\mathrm{M}+1)}\left(\mathbf{R}_\mathrm{BB} + \mathbf{R}_{(N_\mathrm{M}+1)(N_\mathrm{M}+1)}\right)^{-1} \mathbf{R}_{(N_\mathrm{M}+1)k_2} \quad [3.44]$$

with $\mathbf{R}_\mathrm{BB} = \begin{bmatrix} h_\mathrm{BB} & l_\mathrm{BB} \\ n_\mathrm{BB} & p_\mathrm{BB} \end{bmatrix}$, $\mathbf{R}_{k_1k_2} = \begin{bmatrix} h_{k_1k_2} & l_{k_1k_2} \\ n_{k_1k_2} & p_{k_1k_2} \end{bmatrix}$, $\mathbf{G}_{k_1k_2} = \begin{bmatrix} H_{k_1k_2} & L_{k_1k_2} \\ N_{k_1k_2} & P_{k_1k_2} \end{bmatrix}$, $l_{k_1k_2} = y_{k_1}/m_{k_1}$, $n_{k_1k_2} = \theta_{k_1}/f_{k_2}$,$p_{k_1k_2} = \theta_{k_1}/m_{k_2}$. Notice that

$L_{k_1k_2} = Y_{k_1}/M_{k_2}$, $N_{k_1k_2} = \Theta_{k_1}/F_{k_2}$ and $P_{k_1k_2} = \Theta_{k_1}/M_{k_2}$. $\mathbf{R}_{k_1k_2}$, $\mathbf{R}_{k_1(N_\mathrm{M}+1)}$, $\mathbf{R}_{(N_\mathrm{M}+1)k_2}$ and $\mathbf{R}_{(N_\mathrm{M}+1)(N_\mathrm{M}+1)}$ are calculated by the RCSA proposed in [INS 02]. The receptance matrix $\mathbf{R}_{\mathrm{BB}}$ of the spindle-holder base (Component I) can be obtained by the inverse receptance coupling substructure analysis (IRCSA) method [SCH 05, ALB 13]. The final $H_{k_1k_2}(\omega)$ is taken as the first element of matrix $\mathbf{G}_{k_1k_2}$.

Figure 3.5 presents a total computing routine for the calculation of tool point receptance, as well as the identification of the properties of joint interfaces.

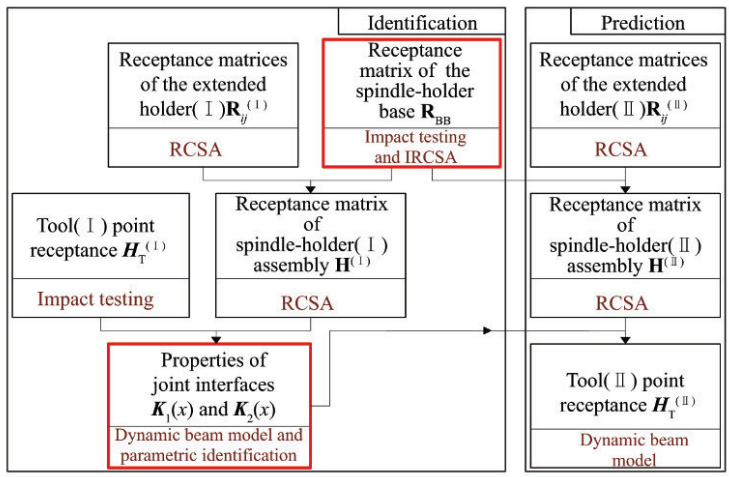

Figure 3.5. *Total computing routine of tool point receptance*

3.2.2.2. *Identification of stiffness and damping coefficients of joint interfaces*

The stiffness and damping properties of the tool-collet and holder-collet joint interfaces are identified by minimizing the discrepancy between the predicted FRF and that measured from a sample tool.

$$\min_{\kappa_{\mathrm{A},q},\eta_{\mathrm{A}},\kappa_{\mathrm{B},\hat{q}},\eta_{\mathrm{B}}} \left\| \log \left| H_{\mathrm{T}}^{\mathrm{M}} - H_{\mathrm{T}}^{\mathrm{P}} \right| \right\| \qquad [3.45]$$

where $H_{\mathrm{T}}^{\mathrm{M}}$ is the tool point FRF measured by impact testing. $H_{\mathrm{T}}^{\mathrm{P}}$ is the tool FRF predicted by using the calculation procedure described in

section 3.2.1.1. It should be noted that only the first-order polynomial forms of equation [3.14] are used to characterize the stiffness coefficients and damping of the joint interfaces, since high order polynomial forms cannot obviously improve the accuracy but drastically increase computing time. The identification procedure is shown in Figure 3.6.

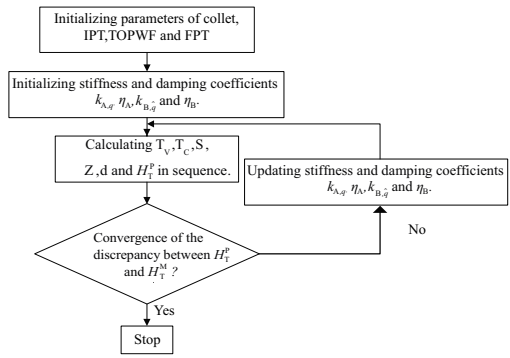

Figure 3.6. *Identification procedure for properties of joint interfaces*

3.2.2.3. *Experimental identification of spindle-holder assembly receptances*

The receptance matrix of the spindle-holder base $\mathbf{R}_{BB}$ is obtained experimentally on machining center. The spindle-holder system given in Figure 3.7(a) is illustrated for the identification of the FRF of the spindle-holder base. It should be noted that since the spindle-holder base is rigidly connected with the extended holder, a direct measurement of $\mathbf{R}_{BB}$ by exciting the base with impact testing will be greatly influenced by the additional mass of the extended holder. In other words, it is generally difficult to directly measure $\mathbf{R}_{BB}$. Hence, the indirect approach given in [SCH 05] is adopted to extract the FRF of the spindle-holder base. Three positions of the extended holder, shown in Figure 3.7(a), are first adopted to measure the corresponding direct and cross FRFs, and then the finite difference method and IRCSA method are adopted to calculate the receptance matrix of spindle-holder base $\mathbf{R}_{BB}$. Figure 3.7(b) illustrates a set of results obtained from these experiments.

With the receptance matrix of the spindle-holder base obtained above, the receptances of any spindle-holder assembly with different extended holder geometries can be predicted by using the method described in section 3.2.2.1.

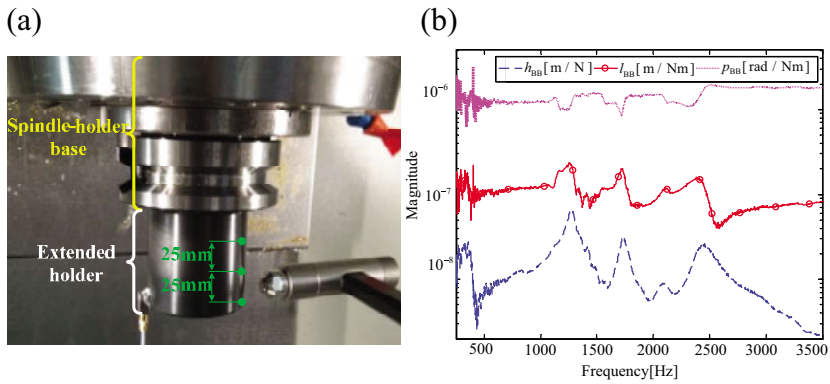

Figure 3.7. *Extraction of receptance matrix of spindle-holder base: a) experimental set-up for extraction of spindle-holder base receptance matrix; b) elements of receptance matrix of spindle-holder base* $\mathbf{R}_{BB}$. *For a color version of this figure, see www.iste.co.uk/zhang/milling.zip*

3.3. Prediction of stability lobe

3.3.1. *Improved semi-discretization method*

The vibration vector $\mathbf{Q}(t)$ in equation [3.9] can be described by the modal displacements as

$$\begin{aligned}\mathbf{Q}(t) &= \mathbf{U}\mathbf{q}(t)\\ \mathbf{q}(t) &= [q_1(t), q_2(t), ..., q_{N_{\mathrm{mo}}}(t)]^{\mathrm{T}}\end{aligned} \qquad [3.46]$$

where N_{mo} is the number of the dominant modes. $\mathbf{U}$ and $\mathbf{q}(t)$ are the mass normalized mode shape and the modal coordinates, respectively. After substituting equation [3.46] into equation [3.9], the delayed differential equation can be expressed in the modal space as

$$\begin{aligned}\ddot{\mathbf{q}}(t) + 2\boldsymbol{\xi}\boldsymbol{\omega}\dot{\boldsymbol{q}}(t) + \boldsymbol{\omega}^2\mathbf{q}(t) &= \mathbf{U}^{\mathrm{T}}\mathbf{H}(t)\mathbf{U}\mathbf{q}(t)\\ &\quad - \sum_{m=1}^{N_{\mathrm{d}}}[\mathbf{U}^{\mathrm{T}}\mathbf{H}_m(t)\mathbf{U}\mathbf{q}(t-\tau_m)]\end{aligned} \qquad [3.47]$$

with

$$\mathbf{H}(t) = \sum_{m=1}^{N_\mathrm{d}} \mathbf{H}_m(t) \qquad [3.48]$$

where $\boldsymbol{\xi}$ and $\boldsymbol{\omega}$ are the diagonal damping ratio and natural frequency matrices with the size $N_\mathrm{mo} \times N_\mathrm{mo}$, respectively.

Equation [3.47] is a typical second-order nonlinear damping system with multiple delays. The roots of such a mathematical problem may be obtained by the method in [STE 89]. It is difficult to directly determine the stability of this system. Fortunately, by using Cauchy transformation, equation [3.47] can be rewritten as a set of first-order differential equations:

$$\dot{\boldsymbol{\Theta}}(t) = \mathbf{A}(t)\boldsymbol{\Theta}(t) + \sum_{m=1}^{N_\mathrm{d}} \mathbf{B}_m(t)\boldsymbol{\Theta}(t-\tau_m) \qquad [3.49]$$

with

$$\begin{aligned}
\boldsymbol{\Theta}(t) &= [\mathbf{q}(t)^\mathrm{T}, \dot{\mathbf{q}}(t)^\mathrm{T}]^\mathrm{T} \\
\mathbf{A}(t) &= \begin{bmatrix} \mathbf{O}_{N_\mathrm{mo}\times N_\mathrm{mo}} & \mathbf{I}_{N_\mathrm{mo}\times N_\mathrm{mo}} \\ -\boldsymbol{\omega}^2 + \mathbf{U}^\mathrm{T}\mathbf{H}(t)\mathbf{U} & -2\boldsymbol{\xi}\boldsymbol{\omega} \end{bmatrix} \\
\mathbf{B}_m(t) &= \begin{bmatrix} \mathbf{O}_{N_\mathrm{mo}\times N_\mathrm{mo}} & \mathbf{O}_{N_\mathrm{mo}\times N_\mathrm{mo}} \\ -\mathbf{U}^\mathrm{T}\mathbf{H}_m(t)\mathbf{U} & \mathbf{O}_{N_\mathrm{mo}\times N_\mathrm{mo}} \end{bmatrix}
\end{aligned} \qquad [3.50]$$

where $\mathbf{O}_{*\times *}$ and $\mathbf{I}_{*\times *}$ are zero and identity matrices, respectively.

Obviously, the nonlinear problem has been transformed into a linear problem. Now, the problem is how to determine the stability of this linear damping system. If N_d=1, equation [3.49] is degenerated into a single delay problem, which has been solved by Insperger *et al.* [INS 04]. However, the existing method is not suitable for systems in which the delay number is more than one. In the present section, an improved version of the semi-discretization method is proposed for time periodic systems with multiple delays.

Equation [3.49] can be discretized in the time domain by dividing the spindle period T into ς number of equal time intervals with the length $\Delta t = T/\varsigma$. If Δt is small enough, the following linear ordinary differential equation can be used to approximate equation [3.49] at discrete time interval $[a\Delta t, (a+1)\Delta t]$

$$\mathbf{\Theta}_{a+1} = \mathbf{A}_a\mathbf{\Theta}_a + \sum_{m=1}^{N_\mathrm{d}} \left(w_{m,1}\mathbf{B}_{m,a}\mathbf{\Theta}_{a-v_m+1} + w_{m,2}\mathbf{B}_{m,a}\mathbf{\Theta}_{a-v_m}\right) \qquad [3.51]$$

with

$$\begin{aligned} &\mathbf{\Theta}_a = \mathbf{\Theta}(a\Delta t) \\ &w_{m,1} = w_{m,2} = \tfrac{1}{2} \end{aligned} \qquad [3.52]$$

where $\mathbf{A}_a$=(1/Δt) $\int_{a\Delta t}^{(a+1)\Delta t} \mathbf{A}(t)dt$ and $\mathbf{B}_{m,a}$=(1/Δt) $\int_{a\Delta t}^{(a+1)\Delta t} \mathbf{B}_m(t)dt$, and v_m is the number of intervals covering the delay item τ_m. By using the solution of equation [3.51] and applying the continuity conditions at the two ends of the interval, the following linear map can be obtained to bridge the solutions at the two consecutive time intervals:

$$\begin{aligned} \mathbf{V}_{a+1} &= \mathbf{\Phi}_a\mathbf{V}_a \ \leftarrow \mathbf{V}_a \\ &= [\mathbf{\Theta}_a{}^{\mathrm{T}}, \mathbf{\Theta}_{a-1}{}^{\mathrm{T}}, ..., \mathbf{\Theta}_{a-v_1}{}^{\mathrm{T}}, ...\mathbf{\Theta}_{a-v_2}{}^{\mathrm{T}}, ...\mathbf{\Theta}_{a-v_{N_\mathrm{d}}}{}^{\mathrm{T}}]^{\mathrm{T}} \end{aligned} \qquad [3.53]$$

where $\mathbf{\Phi}_a$ is the state matrix related to equation [3.51] and can be evaluated as

$$\mathbf{\Phi}_a = \begin{bmatrix} \mathbf{P}_a & 0\,0\cdots 0 & w_{1,1}\mathbf{V}_{1,a} & w_{1,2}\mathbf{V}_{1,a} & \cdots 0 & w_{2,1}\mathbf{V}_{2,a} & w_{2,2}\mathbf{V}_{2,a} & \cdots 0 & w_{N_d,1}\mathbf{V}_{N_d,a} & w_{N_d,2}\mathbf{V}_{N_d,a} \\ \mathbf{I} & 0\,0\cdots 0 & 0 & 0 & \cdots 0 & 0 & 0 & \cdots 0 & 0 & 0 \\ 0 & \mathbf{I}\,0\cdots 0 & 0 & 0 & \cdots 0 & 0 & 0 & \cdots 0 & 0 & 0 \\ \vdots & \vdots\ \vdots\ \vdots\ \vdots & \vdots & \vdots & \vdots\ \vdots & \vdots & \vdots & \ddots & \vdots & \vdots \\ 0 & 0\,0\cdots 0 & 0 & 0 & 0\ 0 & 0 & 0 & \cdots \mathbf{I} & 0 & 0 \\ 0 & 0\,0\cdots 0 & 0 & 0 & 0\ 0 & 0 & 0 & \cdots 0 & \mathbf{I} & 0 \end{bmatrix} \qquad [3.54]$$

The process is periodic at spindle period $T = \varsigma\Delta t$, i.e. $\mathbf{\Phi}_a$ equals $\mathbf{\Phi}_{a+\varsigma}$. Thus, Floquet theory can be used to project $\mathbf{V}_a$ to $\mathbf{V}_{a+\varsigma}$ through the following transition matrix:

$$\mathbf{\Psi} = \mathbf{\Phi}_{a+\varsigma-1}\mathbf{\Phi}_{a+\varsigma-2}\cdots\mathbf{\Phi}_{a+1}\mathbf{\Phi}_a \qquad [3.55]$$

whose eigenvalues are applied to evaluate the stability of the system. If all the eigenvalues of $\mathbf{\Psi}$ at each spindle speed and axial depth of cut are less than unity, the system is asymptotically stable. Otherwise, if any one of the eigenvalues is outside the unit circle, the process is unstable. The critical stability occurs when the eigenvalues lie on the unit circle. By repeating the eigenvalue evaluation at the interested range of spindle speeds and axial depths of cut, the stability lobes can be constructed. Note that when the system is dominated by one mode ($N_{\mathrm{mo}} = 1$), the dimension of the transition matrix is reduced.

The typical characteristics of the proposed method can be listed as follows; multiple delays are considered. The influence of every possible delay on the Floquet transition matrix is separately reflected in equation [3.54]. This constitutes an important mathematical basis for studying the practical milling process that may have two or more delays due to cutter runout or un-pitch space angles. However, only one delay is involved in [ALT 92, INS 04, ALT 00, KOE 67], where the least period of the system is assumed to be the tooth passing period τ of constant pitch cutter, regardless of the runout's effect. Besides, although the above model is derived for a two-DOF milling system, a similar analysis can be performed for any *n*-DOF delay system only by changing the dimensions of $\mathbf{V}_a$ and $\mathbf{\Psi}$, as long as their basic mathematical problems are the same.

Experiments will now be described to verify the algorithm.

Cutting tests are performed on a vertical CNC milling machine to cut aluminum alloy 7050. A three-fluted end mill with a diameter of 16mm and a helix angle of 30° is used. Four down milling tests are conducted. The cutting conditions are listed in Table 3.1. By employing the method described in [WAN 09a], Test 1 and Test 2 are combined to calibrate the cutting force coefficients and the runout parameters. The average values from both tests are used for stability prediction in the present work. Table 3.2 shows the values of the modal parameters and the cutting force coefficients. In the following stability results, only the first mode is considered in the proposed simulation method, as it is significantly more flexible than the second one. The stability lobes are predicted for the following cutting conditions: $f = 0.0273$ mm/tooth and $a_{\mathrm{e}} = 5$ mm. As described in the above section, there may be at most three delays for this cutter, i.e. $N_{\mathrm{d}} = 3$. For every cutting instant, the

delay corresponding to every disk element can be determined using the method in [KLI 83].

Test No.	Radial depth of cut a_e(mm)	Axial depth of cut a_p(mm)	Feed per tooth f(mm/tooth)	Spindle speed(rpm)
1	8	2	0.05	2000
2	8	2	0.05	2000
3	5	13.2	0.0273	4500
4	5	13.2	0.0273	5500

Table 3.1. *Cutting conditions*

Parameter type			Parameter items		
Modal parameters	Direction	Mode	Natural frequency (Hz)	Modal effective mass (kg)	Damping ratios (-)
	X	1	898.22	1.576	0.040041
		2	1135.3	44.259	0.00535
	Y	1	852.51	0.852	0.036768
		2	1185.1	22.589	0.00777
Cutting force coefficients and cutter runout prameters	K_T (MPa)	K_R (MPa)	ρ (μm)	λ ($^\circ$)	
	1209.355	501.095	7.2	65.09	

Table 3.2. *Cutting parameters of the milling system*

To see the effect of runout on stability lobes, both the actual runout parameters (i.e. $\rho = 7.2\ \mu\mathrm{m}$ and $\lambda = 65.09^\circ$) and the zero runout parameters (i.e. $\rho = 0\ \mu\mathrm{m}$ and $\lambda = 0^\circ$) are taken into account in the proposed method. The simulation results are shown in Figure 3.8. The stability boundaries predicted by the method developed by Altintas [ALT 00] are also plotted in Figure 3.8 for comparison. As can be seen from Figure 3.8, when the runout parameters are zero, the proposed method and the method of Altintas are close to one another. However, once the actual runout parameters are considered, obvious deviations occur among the three charts.

Firstly, let us consider the stability chart predicted by Altintas's method and the one predicted by the proposed method under the zero-runout assumption. Both lobes indicate that the milling system would be unstable at a spindle speed of 5500 rpm, axial depth of $a_p = 13.2$ mm, radial depth of $a_e = 5$ mm and the feed per tooth of 0.0273 mm/tooth (i.e. the cutting

condition of Test 4). However, the cutting test results given in the right column of Figure 3.8 show that the milling process is stable under the above cutting conditions. The reason is that the cutter runout may have a relatively great influence on the stability lobes. On the other hand, the stability lobes, in which the actual runout parameters are considered, indicate that the cutting condition of Test 4 would be stable, which agrees well with the milling test results. The stability lobes obtained from different methods and different conditions indicate that the cutting condition of Test 3 would lead to unstable milling, which is verified by the cutting test results, as shown in Figure 3.8. The Fast Fourier Transformation of F_Y shows the severity of chatter vibrations which produce large amplitude forces and spectrum at a chatter frequency of 821.4 Hz. It is worth noting that the spectrum Sp_p ($p = 1, 2, ..., 5$) in Figure 3.8 is the harmonics force produced by the cutter runout. For details about this issue, one can refer to [LIA 94, WAN 09a].

3.3.2. *Lowest envelope method*

3.3.2.1. *Proof of the lowest envelope method*

Firstly, the modal parameters listed in Table 3.3, which are taken from [ALT 13], are selected to carry out a numerical study by using the improved SDM described in section 3.3.1. Based on the four pairs of dominant modes listed in Table 3.3, simulations are performed by the following steps.

1) predict the stability lobe by only using the *k*th mode;

2) predict the stability lobe by including all modes in computation;

3) plot the results obtained from the above steps in the same figure.

Final results are shown in Figure 3.9. It can be found that the lowest envelope of the stability lobes associated with each single mode is very close to the stability lobe directly predicted from multiple modes. This means that the stability lobe of a system with multiple modes may be approximately obtained by taking the lowest envelope of stability lobes corresponding to all single modes other than directly using the multiple modes. Without the loss of generality, a theoretical proof will be made to confirm that taking the lowest envelope can be used as a basic principle for the construction of stability lobes in the following. It should be mentioned that since SDM is a time domain solution performed from a numerical point of view, it is very difficult

to directly conduct the theoretical proof in the semi-discrete time domain. Fortunately, expressing milling dynamics problem in the frequency domain is a powerful analytical means, which makes it possible to conduct theoretical analysis. For this reason, frequency domain analysis, i.e. the ZOA method reported in [ALT 12], is employed to carry out the following theoretical proof.

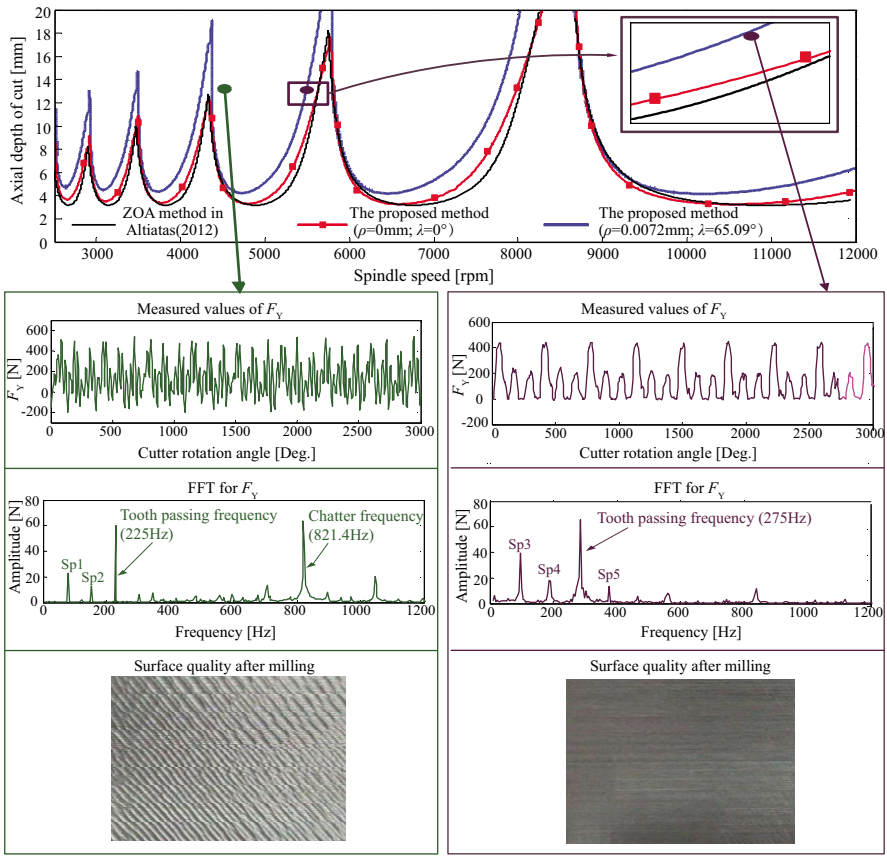

Figure 3.8. *Stability lobes, forces and surface quality obtained by experiments and simulations for constant pitch cutter with runout. For a color version of this figure, see www.iste.co.uk/zhang/milling.zip*

	Modal Direction	Mode No. k	Natural Frequency $\omega_{s,k}$(Hz)	Damping Ratio $\xi_{s,k}(10^{-2})$	Modal Mass $m_{s,k}$(Kg)
Modal parameters	X	1	624	5.2	5.3344
	X	2	871	3.3	5.3756
	X	3	2311	2.2	0.4126
	X	4	3052	2.9	0.3943
	Y	1	692	4.2	4.0201
	Y	2	862	5.2	4.0621
	Y	3	2289	1.9	0.3819
	Y	4	3050	2.7	0.4084
Cutting parameters		K_{T} (MPa) 713	K_{R}(MPa) 50.4		

Table 3.3. *Cutting parameters of the milling system in [ALT 13]*

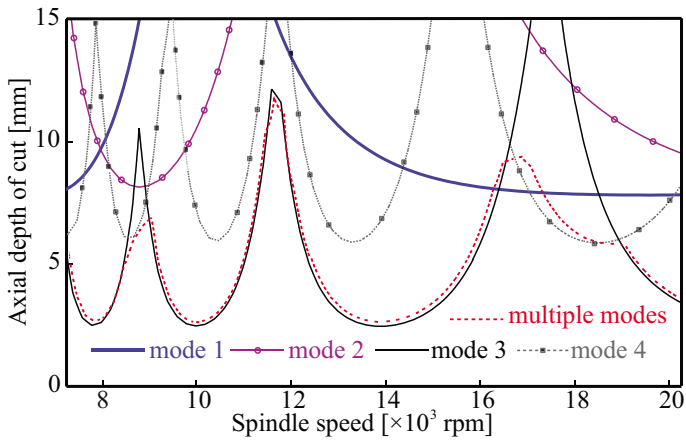

Figure 3.9. *Simulated stability lobes using the improved SDM. "Mode k (k = 1, 2, 3, 4)" means that the result is obtained by only using the kth dominant mode in computation, while "multiple modes" corresponds to the stability lobe that is calculated by directly substituting all modes into SDM. For a color version of this figure, see www.iste.co.uk/zhang/milling.zip*

According to [ALT 12], the critical axial depth of cut $a_{\mathrm{p,\,lim}}$ for the chatter stability limit can be determined by

$$a_{\mathrm{p,\,lim}} = -\frac{2\pi\Lambda_{\mathrm{R}}}{NK_{\mathrm{T}}}(1+\kappa_{\mathrm{D}}{}^2)$$
$$\kappa_{\mathrm{D}} = \Lambda_{\mathrm{I}}/\Lambda_{\mathrm{R}} \qquad [3.56]$$

where Λ_R and Λ_I are the real and imaginary parts of the eigenvalue of the following characteristic equation. K_T is the tangential cutting force coefficient.

$$a_0\Lambda^2 + a_1\Lambda + 1 = 0 \qquad [3.57]$$

with

$$\begin{aligned} a_0 &= \upsilon\varphi_{XX}(J\omega_c)\varphi_{YY}(J\omega_c) \\ a_1 &= \alpha_{XX}\varphi_{XX}(J\omega_c) + \alpha_{YY}\varphi_{YY}(J\omega_c) \end{aligned}$$

$$\begin{aligned} \varphi_{ss}(J\omega_c) &= \sum_{k=1}^{N_{mo}} \varphi_{ss,k}(J\omega_c) \\ &= \sum_{k=1}^{N_{mo}} \frac{1}{m_{s,k}(J\omega_c)^2 + 2\xi_{s,k}\omega_{s,k}m_{s,k}(J\omega_c) + \omega_{s,k}^2 m_{s,k}} \end{aligned} \qquad [3.58]$$

with

$$\begin{aligned} &\upsilon = \alpha_{XX}\alpha_{YY} - \alpha_{XY}\alpha_{YX} \\ &s = \text{X or Y} \end{aligned} \qquad [3.59]$$

in which α_{XX}, α_{YY}, α_{XY} and α_{YX} are the average directional factors which depended on the radial depth of cut bounded by entry (θ_{en}) and exit (θ_{ex}) angles, as reported in [ALT 12]. J is the imaginary unit of complex number. $\varphi_{ss,k}(J\omega_c)$ is the transfer function of mode k ($k = 1, 2, ..., N_{mo}$), with $\xi_{s,k}$ and $\omega_{s,k}$ being the damping ratio and natural frequency in direction s (s = X or Y).

The solution Λ of equation [3.57] can also be written as

$$\Lambda = \frac{-1}{2a_0}\left(a_1 \pm \sqrt{a_1^2 - 4a_0}\right) \qquad [3.60]$$

Substituting equation [3.58] into equation [3.60] and rearranging it gives

$$\Lambda = \frac{-\chi_1 \mp \chi_2}{2\upsilon\varphi_{XX}(J\omega_c)\varphi_{YY}(J\omega_c)} \qquad [3.61]$$

with

$$\chi_1 = \alpha_{XX}\varphi_{XX}(J\omega_c) + \alpha_{YY}\varphi_{YY}(J\omega_c)$$
$$\chi_2 = \sqrt{(\alpha_{XX}\varphi_{XX}(J\omega_c) + \alpha_{YY}\varphi_{YY}(J\omega_c))^2 - 4\upsilon\varphi_{XX}(J\omega_c)\varphi_{YY}(J\omega_c)} \quad [3.62]$$

Since the milling tool-spindle assembly is nearly a symmetric system, the measured dynamic receptances of the tool point in X and Y directions are always close to each other, as observed by a number of previous researchers [MAN 05, GRA 05, ZHA 01b, CIF 10, LI 14]. Thus, by assuming $\varphi_{XX}(J\omega_c) = \varphi_{YY}(J\omega_c)$, equation [3.61] can be rewritten as

$$\Lambda = \frac{\chi}{\varphi_{XX}(J\omega_c)} \quad [3.63]$$

with

$$\chi = -\frac{\alpha_{XX} + \alpha_{YY} \pm \sqrt{\alpha_{XX}^2 + \alpha_{YY}^2 + 2\alpha_{XX}\alpha_{YY} - 4\upsilon}}{2\upsilon} \quad [3.64]$$

Obviously, Λ directly varies with respect to $\varphi_{XX}(J\omega_c)$ as χ in equation [3.63] is a certain real number. Actually, $\varphi_{XX}(J\omega_c)$ can be rearranged as follows.

$$\begin{aligned}\varphi_{XX}(J\omega_c) &= \sum_{k=1}^{N_{mo}} \frac{1}{-m_{X,k}\omega_c^2 + 2\xi_{X,k}\omega_{X,k}m_{X,k}\omega_c J + m_{X,k}\omega_{X,k}^2} \\ &= \sum_{k=1}^{N_{mo}} \frac{m_{X,k}(\omega_{X,k}^2 - \omega_c^2) - 2\xi_{X,k}\omega_{X,k}m_{X,k}\omega_c J}{m_{X,k}^2(\omega_{X,k}^2 - \omega_c^2)^2 + 4\xi_{X,k}^2\omega_{X,k}^2 m_{X,k}^2\omega_c^2} \\ &= \sum_{k=1}^{N_{mo}} \frac{m_{X,k}(\omega_{X,k}^2 - \omega_c^2) - 2\xi_{X,k}\omega_{X,k}m_{X,k}\omega_c J}{m_{X,k}^2(\omega_{X,k}^4 + \omega_c^4) - 2\omega_{X,k}^2 m_{X,k}^2\omega_c^2 + 4\xi_{X,k}^2\omega_{X,k}^2 m_{X,k}^2\omega_c^2}\end{aligned} \quad [3.65]$$

Generally, $\xi_{X,k}$ is a pure fractional number smaller than 0.1 in most metal structures as reported in [ALT 12, ZHA 01b, ALT 13, LI 14, BRA 05]. Based

on this fact, the following derivation can be achieved.

$$\begin{aligned} & \xi_{\mathrm{X},k} < 0.1 \\ \Rightarrow\ & \xi_{\mathrm{X},k}^2 < 0.01 \\ \Rightarrow\ & \xi_{\mathrm{X},k}^2 < 0.04 = 0.02 \times 2 \ll 2 \\ \Rightarrow\ & \xi_{\mathrm{X},k}^2 \omega_{\mathrm{X},k}^2 m_{\mathrm{X},k}^2 \omega_{\mathrm{c}}^2 < 0.02 \times 2\omega_{\mathrm{X},k}^2 m_{\mathrm{X},k}^2 \omega_{\mathrm{c}}^2 \ll 2\omega_{\mathrm{X},k}^2 m_{\mathrm{X},k}^2 \omega_{\mathrm{c}}^2 \end{aligned} \quad [3.66]$$

Equation [3.66] means that $4\xi_{\mathrm{X},k}^2 \omega_{\mathrm{X},k}^2 m_{\mathrm{X},k}^2 \omega_{\mathrm{c}}^2$ is a small quantity that is less than 2/100 of $2\omega_{\mathrm{X},k}^2 m_{\mathrm{X},k}^2 \omega_{\mathrm{c}}^2$. Thus, it can be dropped from the denominator of equation [3.65]. It is noted that, as verified in section 3.3.2, dropping out this term does not greatly affect the prediction accuracy. That is,

$$\begin{aligned} & m_{\mathrm{X},k}^2 (\omega_{\mathrm{X},k}^2 - \omega_{\mathrm{c}}^2)^2 + 4\xi_{\mathrm{X},k}^2 \omega_{\mathrm{X},k}^2 m_{\mathrm{X},k}^2 \omega_{\mathrm{c}}^2 \\ & = m_{\mathrm{X},k}^2 (\omega_{\mathrm{X},k}^4 + \omega_{\mathrm{c}}^4) - 2m_{\mathrm{X},k}^2 \omega_{\mathrm{X},k}^2 \omega_{\mathrm{c}}^2 + 4\xi_{\mathrm{X},k}^2 \omega_{\mathrm{X},k}^2 m_{\mathrm{X},k}^2 \omega_{\mathrm{c}}^2 \\ & \approx m_{\mathrm{X},k}^2 (\omega_{\mathrm{X},k}^4 + \omega_{\mathrm{c}}^4) - 2m_{\mathrm{X},k}^2 \omega_{\mathrm{X},k}^2 \omega_{\mathrm{c}}^2 \\ & = m_{\mathrm{X},k}^2 (\omega_{\mathrm{X},k}^2 - \omega_{\mathrm{c}}^2)^2 \end{aligned} \quad [3.67]$$

As a result, equation [3.65] can be rewritten as

$$\varphi_{\mathrm{XX}}(\mathrm{J}\omega_{\mathrm{c}}) \approx \sum_{k=1}^{N_{\mathrm{mo}}} \frac{m_{\mathrm{X},k}(\omega_{\mathrm{X},k}^2 - \omega_{\mathrm{c}}^2) - 2\xi_{\mathrm{X},k}\omega_{\mathrm{X},k} m_{\mathrm{X},k}\omega_{\mathrm{c}}\mathrm{J}}{m_{\mathrm{X},k}^2 (\omega_{\mathrm{X},k}^2 - \omega_{\mathrm{c}}^2)^2} \quad [3.68]$$

It is important to note that the critical depth of cut $a_{\mathrm{p,lim}}$ is solved by substituting a chatter frequency ω_{c} around a dominant mode $\omega_{\mathrm{X},k}$ into equations [3.63] and [3.56] . This means that $a_{\mathrm{p,lim}}$ corresponds to a frequency ω_{c} that is very close to one of $\omega_{\mathrm{X},1}$, $\omega_{\mathrm{X},2}$,...,$\omega_{\mathrm{X},N_{\mathrm{mo}}}$. If $\omega_{\mathrm{c}} = (1 + \mu_{\mathrm{D}})\omega_{s,k}$ ($|\mu_{\mathrm{D}}| < 0.1$) and the preconditions discussed in section 3.3.2.2 are satisfied, the following relationship holds

$$\begin{aligned} & \frac{m_{\mathrm{X},k}(\omega_{\mathrm{X},k}^2 - \omega_{\mathrm{c}}^2) - 2\xi_{\mathrm{X},k}\omega_{\mathrm{X},k} m_{\mathrm{X},k}\omega_{\mathrm{c}}\mathrm{J}}{m_{\mathrm{X},k}^2 (\omega_{\mathrm{X},k}^2 - \omega_{\mathrm{c}}^2)^2} \\ \gg & \sum_{\varsigma=1,\ \varsigma\neq k}^{N_{\mathrm{mo}}} \frac{m_{\mathrm{X},\varsigma}(\omega_{\mathrm{X},\varsigma}^2 - \omega_{\mathrm{c}}^2) - 2\xi_{\mathrm{X},\varsigma}\omega_{\mathrm{X},\varsigma} m_{\mathrm{X},\varsigma}\omega_{\mathrm{c}}\mathrm{J}}{m_{\mathrm{X},\varsigma}^2 (\omega_{\mathrm{X},\varsigma}^2 - \omega_{\mathrm{c}}^2)^2} \end{aligned} \quad [3.69]$$

In light of equations [3.69], [3.68] can be approximated as

$$\varphi_{\mathrm{XX}}(\mathrm{J}\omega_{\mathrm{c}}) = \frac{m_{\mathrm{X},k}(\omega_{\mathrm{X},k}^2 - \omega_{\mathrm{c}}^2) - 2\xi_{\mathrm{X},k}\omega_{\mathrm{X},k}m_{\mathrm{X},k}\omega_{\mathrm{c}}\mathrm{J}}{m_{\mathrm{X},k}^2(\omega_{\mathrm{X},k}^2 - \omega_{\mathrm{c}}^2)^2} \quad [3.70]$$

Substituting equation [3.70] into equation [3.63] gives

$$\begin{aligned}\Lambda = \frac{\chi}{\varphi_{\mathrm{XX}}(\mathrm{J}\omega_{\mathrm{c}})} &= \chi\frac{m_{\mathrm{X},k}^2(\omega_{\mathrm{X},k}^2 - \omega_{\mathrm{c}}^2)^2}{m_{\mathrm{X},k}(\omega_{\mathrm{X},k}^2 - \omega_{\mathrm{c}}^2) - 2\xi_{\mathrm{X},k}\omega_{\mathrm{X},k}m_{\mathrm{X},k}\omega_{\mathrm{c}}\mathrm{J}} \\ &= \chi m_{\mathrm{X},k}^2(\omega_{\mathrm{X},k}^2 - \omega_{\mathrm{c}}^2)^2\frac{m_{\mathrm{X},k}(\omega_{\mathrm{X},k}^2 - \omega_{\mathrm{c}}^2) + 2\xi_{\mathrm{X},k}\omega_{\mathrm{X},k}m_{\mathrm{X},k}\omega_{\mathrm{c}}\mathrm{J}}{m_{\mathrm{X},k}^2(\omega_{\mathrm{X},k}^2 - \omega_{\mathrm{c}}^2)^2 + 4\xi_{\mathrm{X},k}^2\omega_{\mathrm{X},k}^2m_{\mathrm{X},k}^2\omega_{\mathrm{c}}^2}\end{aligned} \quad [3.71]$$

Combining equation [3.71] with equation [3.67] yields

$$\Lambda \approx \chi[m_{\mathrm{X},k}(\omega_{\mathrm{X},k}^2 - \omega_{\mathrm{c}}^2) + 2\xi_{\mathrm{X},k}\omega_{\mathrm{X},k}m_{\mathrm{X},k}\omega_{\mathrm{c}}\mathrm{J}] = \frac{\chi}{\varphi_{\mathrm{XX},k}(\mathrm{J}\omega_{\mathrm{c}})} \quad [3.72]$$

Evidently, in the case of multiple modes, the solutions of equation [3.57] associated with the selected chatter frequency ω_{c} are approximate to the solutions related to the dominant mode around which ω_{c} is selected. This implies that the final $a_{\mathrm{p,lim}}$ is taken as the minimum of all candidate values, which are calculated based on the solutions of equation [3.57] through scanning the chatter frequencies around all dominant modes evident on the transfer functions. This concludes that the solution of the stability lobe can be alternatively treated as a single mode problem instead of a multiple modes problem, according to the following procedure:

– predict the stability lobe under the *k*th dominant mode as a single mode problem;

- select chatter frequencies around this mode, and solve the corresponding eigenvalues from equation [3.60],

- calculate the critical depth of cut from equation [3.56],

- calculate the spindle speed for each stability lobe based on the method given in [ALT 12],

- construct the stability lobe related to this mode;

– repeat the above procedure for all modes;

– select the lowest envelope of the stability lobes associated with all dominant modes as the ultimate stability lobe.

In other words, the above scheme proves that the lowest envelope of a group of stability lobes, which are calculated by separately considering different dominant modes composing the overall dynamic compliance, can be used to predict the stability lobes of milling systems with multiple dominant modes. For convenience, this procedure is called the lowest envelope method (LEM). Note that although LEM is proved in the frequency domain, it cannot be treated as a frequency domain solution. It is just a general principle that can be used to explain the construction mechanism of stability lobes under multiple modes, and it can be performed by combination with either frequency domain methods or time domain solutions.

It should also be noted that the frequency domain solution can predict the stability lobe much more efficiently than the time domain method. At this point, there is no obvious advantage of computational efficiency by combining LEM with a frequency domain method such as the ZOA method. The frequency domain method is not a panacea. It will fail in prediction if there exist simultaneous multiple modes and instantaneous process parameters such as cutter runout-induced multiple delays. In this case, one must resort to other means such as a time domain method, e.g. the semi-discretization method (SDM). To this end, as demonstrated below, LEM is of great significance to save prediction time and memory usage when combined with the improved SDM.

Simulations were performed on a 3.30 GHz Intel(R) Xeon(R) CPU computer for the same milling case as in Figure 3.9. Spindle speed increased with an interval of 500 rpm and the axial depth of cut increased with a step of 0.5 mm. Three cases of the number of time intervals with $w = 40$, 80 and 120 were considered in simulations. Results show that the time cost related to multiple modes is higher than that of LEM, which is the time summation associated with all single modes. Especially, the time difference between the two methods becomes very large, along with the increase of w. For example, in the case of $w = 120$, the time cost of LEM is only 9 percent of the time spent executing multiple modes codes. Besides, the memory usage of LEM is

greatly lower than that related to multiple modes, and the difference between both increases with w.

3.3.2.2. *Premise of the lowest envelope method*

This section aims at explaining the precondition of LEM from the theoretical point of view. First, a two-mode symmetric system with the transfer function defined in equation [3.73] is selected for illustration. Since $\varphi_{XX}(J\omega_c)$ is assumed to be equal to $\varphi_{YY}(J\omega_c)$ in section 3.3.2.1, only the X direction is used for explanation:

$$\varphi_{XX}(J\omega_c) = \varphi_{XX,R} + \varphi_{XX,I} \times J \qquad [3.73]$$

with

$$\begin{aligned}\varphi_{XX,R}(J\omega_c) &= \frac{1}{m_{X,1}(\omega_{X,1}^2 - \omega_c^2)} + \frac{1}{m_{X,2}(\omega_{X,2}^2 - \omega_c^2)} \\ \varphi_{XX,I}(J\omega_c) &= -\frac{2\xi_{X,1}\omega_{X,1}\omega_c}{m_{X,1}(\omega_{X,1}^2 - \omega_c^2)^2} - \frac{2\xi_{X,2}\omega_{X,2}\omega_c}{m_{X,2}(\omega_{X,2}^2 - \omega_c^2)^2}\end{aligned} \qquad [3.74]$$

where $\varphi_{XX,R}(J\omega_c)$ and $\varphi_{XX,I}(J\omega_c)$ are the real and imaginary parts of $\varphi_{XX}(J\omega_c)$. For convenience, $\omega_{X,2}$ is assumed as

$$\omega_{X,2} = \eta_D \omega_{X,1} \quad \leftarrow \quad \eta_D > 1 \qquad [3.75]$$

If chatter frequency ω_c is generally selected in the vicinity of the first dominant frequency $\omega_{X,1}$, ω_c can be expressed as

$$\omega_c = (1 + \mu_D)\omega_{X,1} \quad \leftarrow \quad |\mu_D| < 0.1 \qquad [3.76]$$

Substitution of equations [3.75] and [3.76] into equation [3.74] gives

$$\varphi_{XX,R}(J\omega_c) = \frac{1}{\omega_{X,1}^2}\left[\frac{1}{m_{X,1}(-2\mu_D - {\mu_D}^2)} + \frac{1}{m_{X,2}({\eta_D}^2 - (1+\mu_D)^2)}\right] \qquad [3.77]$$

$$\varphi_{\mathrm{XX,I}}(\mathrm{J}\omega_{\mathrm{c}}) = \frac{2(1+\mu_{\mathrm{D}})}{{\omega_{\mathrm{X},1}}^2} \times \left[\frac{\xi_{\mathrm{X},1}}{m_{\mathrm{X},1}{\mu_{\mathrm{D}}}^2(\mu_{\mathrm{D}}+2)^2} + \frac{\xi_{\mathrm{X},2}}{m_{\mathrm{X},2}\left[{\eta_{\mathrm{D}}}^2-(1+\mu_{\mathrm{D}})^2\right]^2} \right] \quad [3.78]$$

Based on equations [3.77] and [3.78], the following relative errors are defined.

$$\delta_{\mathrm{R}} = \frac{m_{\mathrm{X},1}(-2\mu_{\mathrm{D}}-{\mu_{\mathrm{D}}}^2)}{m_{\mathrm{X},2}[{\eta_{\mathrm{D}}}^2-(1+\mu_{\mathrm{D}})^2]} \quad [3.79]$$

$$\delta_{\mathrm{I}} = \frac{\eta_{\mathrm{D}}\xi_{\mathrm{X},2}m_{\mathrm{X},1}{\mu_{\mathrm{D}}}^2(2+\mu_{\mathrm{D}})^2}{\xi_{\mathrm{X},1}m_{\mathrm{X},2}[{\eta_{\mathrm{D}}}^2-(1+\mu_{\mathrm{D}})^2]^2} \quad [3.80]$$

Actually, as long as

$$|\delta_{\mathrm{R}}| \leq \epsilon_{\mathrm{E}} \quad [3.81]$$

$$|\delta_{\mathrm{I}}| \leq \epsilon_{\mathrm{E}} \quad [3.82]$$

the second items of equations [3.77] and [3.78] could be considered removable. Here, ϵ_{E} is a given small tolerance.

Substitution of equation [3.79] into [3.81] gives

$$\eta_{\mathrm{D}} \geq \eta_{\delta} \quad [3.83]$$

with

$$\eta_{\delta} = \sqrt{\frac{m_{\mathrm{X},1}\,|-2\mu_{\mathrm{D}}-{\mu_{\mathrm{D}}}^2|}{m_{\mathrm{X},2}E} + (1+\mu_{\mathrm{D}})^2} \quad [3.84]$$

If equations [3.83] and [3.82] hold, it means that equation [3.68] could be approximated by equation [3.70]. That is, the stability of the system with multiple modes can be predicted by the proposed LEM. It should be mentioned that for a milling system with multiple modes, equations [3.83] and [3.82] need to be repeatedly checked for all mode pairs that are arbitrarily paired among all dominant modes.

It is also important to note that the actual chatter frequency changes over cutting conditions, as shown in Figure 3.8. As a result, μ_{D} is not a constant. For example, with respect to mode 4, μ_{D} is in [-0.022, +0.018]. Here, Figure 3.10 is the chatter frequency versus natural frequency related to the example given in section 3.3.2. To comprehensively consider the varying process information, equations [3.83] and [3.82] are checked according to the following steps:

1) calculate the chatter frequency of the system with multiple modes by using the frequency method given in [ALT 12];

2) estimate the value of μ_{D} related to each mode by taking the ratio of average chatter frequency to the natural frequency, and select the maximum of μ_{D} associated with all modes as the final value of μ_{D};

3) substitute the value of μ_{D} obtained above into equation [3.84] to calculate η_{δ};

4) calculate η_{D} for each pair of modes group using equation [3.75], and select the minimum of η related to all pairs as the final value of η_{D};

5) check whether equation [3.83] is satisfied based on the final values of η_{D} and η_{δ} obtained above. If equation [3.83] is not satisfied, it confirms that LEM cannot be used in this case; otherwise, go to step 6;

6) check whether equation [3.82] is satisfied based on the final value of η_{D} obtained from the step (4). If it is, this confirms that LEM is effective to predict the stability.

Table 3.4 checks the preconditions of LEM for the milling system shown in Table 3.3. It can be found that that both equations [3.83] and [3.82] are satisfied. Hence, as indicated in Figure 3.9, the stability of the system can be predicted by LEM.

Example No.	Value of μ_D related to each mode	Final value of μ_D	Final value of η_D	η_δ	Is equation [3.83] satisfied?	Is equation [3.82] satisfied?
Example 1: milling system in section 3.3.2.1	For mode 1: 0.0152 For mode 2: no chatter frequency For mode 3: 0.0019 For mode 4: 0.0049	0.0152	1.327	1.284	Yes	Yes

Table 3.4. *Checking the preconditions of LEM (ϵ_E is artificially set to be 0.05)*

3.3.3. *Time-domain simulation method*

From equations [3.1] to [3.3] it can be clearly found that the calculation of total cutting forces relies on both $h_{i,j}(t)$, K_T and K_R. $h_{i,j}(t)$ can be calculated by equation [3.1]. K_T and K_R should have enough calibration accuracy to accurately predict the cutting forces. Generally, the constant cutting force coefficient [ALT 00] and the instantaneous cutting force coefficient [YUN 01, WAN 07a, AZE 04, WAN 07b, WAN 09a, WAN 10a] are two typical concepts used for cutting force modeling. The former combines the shearing effect and the rubbing effect into a single constant coefficient for each cutting force component, whereas the latter often treats the coefficients as a nonlinear function of the instantaneous uncut chip thickness.

In fact, most existing stability lobe prediction methods were conducted under the assumption of constant cutting force coefficients. However, the influence of the instantaneous cutting force coefficients on the stability lobes of a milling system is still under research. Recently, Ahmadi and Ismail [AHM 10a] used the instantaneous cutting force model to detect the chatter phenomenon in flank milling of curved surfaces on a 5-axis machine. However, the distribution of stability lobes was not explored for instantaneous cutting force coefficients. Although Dombovari *et al*. [DOM 10] adopted a nonlinear function of the chip thickness to express cutting force coefficients, predicted stability lobes are limited to use constant cutting force coefficients averaged over a spindle period. In the following presentation, based on three cutting force models, the time-domain simulation method will be described to solve

the deflection of the milling system; and then stability lobe predictions will be studied:

– *cutting force model 1*: the cutting force coefficients given in equation [1.57] are used;

– *cutting force model 2*: the cutting force coefficients given in equation [1.73] are used;

– *cutting force model 3*: constant cutting force coefficients are used [WAN 09a].

A time-domain simulation method is described to solve the vibration deflection time history of the cutter motion. It incorporates the instantaneous cutting force coefficients, the instantaneous variation of the entry and exit angles and the influences of multiple delays together. Details will be presented below.

Theoretically, equation [3.8] is a typical second-order delay differential equation (DDE) in terms of $\mathbf{Q}(t)$. It cannot be integrated in any analytical way due to its high nonlinearity. A possible approach is to resort to the implicit Runge-Kutta method [SHA 01] aiming at solving general first-order problems of the following form

$$\dot{\mathbf{z}}(t) = \mathbf{fun}(\chi(t), \chi(t-\tau_1), \chi(t-\tau_2), ..., \chi(t-\tau_{N_\mathrm{k}})) \qquad [3.85]$$

where τ_k (k=1,2,...,N_k) is a constant delay with $\min(\tau_1, \tau_2, ..., \tau_{N_\mathrm{k}}) > 0$ and independent of time t. N_k is the total number of delay items. χ stands for the unknown system variable vector of the delay equation concerned.

Considering the multiple delays induced by cutter runout of mills with regular pitches, equation [3.8] can be rewritten in the following compact form

$$\dot{\mathbf{z}}(t) = \mathbf{v}[\mathbf{z}(t), \mathbf{z}(t-\tau), \mathbf{z}(t-2\tau), ..., \mathbf{z}(t-N_\mathrm{d}\tau)] \qquad [3.86]$$

where

$$\mathbf{z}(t) = \left[x(t),\ y(t),\ \dot{x}(t),\ \dot{y}(t)\right]^\mathrm{T} \qquad [3.87]$$

$$\mathbf{v} = \begin{bmatrix} \dot{x}(t) \\ \dot{y}(t) \\ \frac{1}{m_{\mathrm{X}}} F_{\mathrm{X}}(t) - 2\xi_{\mathrm{X}}\omega_{\mathrm{X}}\dot{x}(t) - \omega_{\mathrm{X}}^2 x(t) \\ \frac{1}{m_{\mathrm{Y}}} F_{\mathrm{Y}}(t) - 2\xi_{\mathrm{Y}}\omega_{\mathrm{Y}}\dot{y}(t) - \omega_{\mathrm{Y}}^2 y(t) \end{bmatrix} \quad [3.88]$$

Note that $F_{\mathrm{X}}(t)$ and $F_{\mathrm{Y}}(t)$ depend on $\mathbf{z}(t - k\tau)$ (k=0, 1, 2,...,N_{d}), and K_{T} and K_{R}. Obviously, equation [3.86] is a typical application case of equation [3.85] to solve $x(t - k\tau)$ and $y(t - k\tau)$ (k=0, 1, 2, ..., N_{d}). Three remarks should be considered before solving equation [3.86]:

Determination of the initial values of $\mathbf{z}(0)$ *and* $F_s(0)$ *(*s=*X, Y)*

Since the cutter is stationary at the initial cutting instant with zero deflections and velocities, $\mathbf{z}(0)$ can be predetermined as

$$\mathbf{z}(0) = [0,\ 0,\ 0,\ 0]^{\mathrm{T}} \quad [3.89]$$

Under this condition, the dynamic chip thickness $h_{\mathrm{DY},i,j}(0)$ can be directly dropped from equation [3.1] at t=0. $F_{\mathrm{X}}(0)$ and $F_{\mathrm{Y}}(0)$ can be calculated with equation [3.3] by replacing $h_{i,j}(0)$ with $h_{\mathrm{ST},i,j}(0)$.

Determination of the instantaneous values of $\theta_{en}(t)$ *and* $\theta_{ex}(t)$

Both angles involved in $F_{\mathrm{X}}(t)$ and $F_{\mathrm{Y}}(t)$ denote the instantaneous engagement state between the cutter and the workpiece. It is well known that large vibrations will directly lead to loss of the contact. This implies that $\theta_{\mathrm{en}}(t)$ and $\theta_{\mathrm{ex}}(t)$ are also influenced by the current vibration deflection $\mathbf{Q}(t)$.

Now, down milling will be taken as an example to illustrate the influence of $\mathbf{Q}(t)$ on $\theta_{\mathrm{en}}(t)$ and $\theta_{\mathrm{ex}}(t)$. If $y(t)$ is larger than the nominal radial depth of cut a_{e}, the cutter will be completely in air cut. In this case, one can set $\theta_{\mathrm{en}}(t) = \theta_{\mathrm{ex}}(t)$. If $y(t) < a_{\mathrm{e}}$, the entry angle will be changed according to the following pattern.

$$\theta_{\mathrm{en}}(t) = \arccos\left(\frac{2a_{\mathrm{e}}(t) - D}{D}\right) = \arccos\left(\frac{2a_{\mathrm{e}} - 2y(t) - D}{D}\right) \quad [3.90]$$

where $a_{\mathrm{e}}(t)$ is the instantaneous radial depth of cut corresponding to time t. Similarly, the engagement variation in up milling can be simulated as above:

Determination of the instantaneous values of cutting force coefficient K_q *(*q=*T, R)*

From equations [1.57] and [1.73] it can be seen that K_q relates to $h_{i,j}(t)$, which is associated with the vibration deflections $x(t - k\tau)$ and $y(t - k\tau)$ (k=0, 1, 2, ...,N_{d}), as indicated in equation [3.2]. Thus, at each considered time t, one should use equations [3.1] and [3.2] to update $h_{i,j}(t)$, and then use equation [1.57] or equation [1.73] to update K_q.

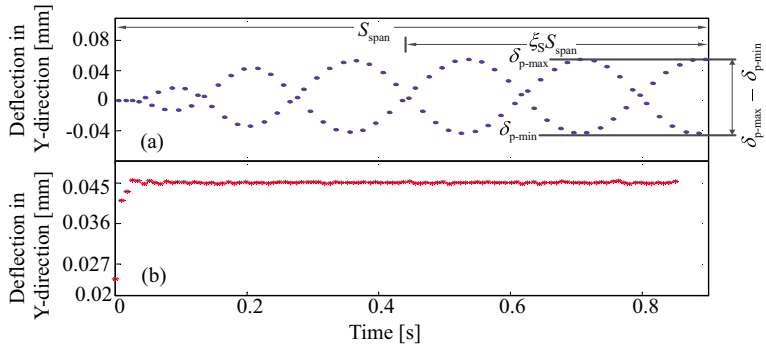

Figure 3.10. *1/revolution sampled time history of vibration deflection signals. For a color version of this figure, see www.iste.co.uk/zhang/milling.zip*

With the above points and the schemes in [SHA 01], the vibration deflections over time t can be successfully obtained from equation [3.86]. Subsequently, a sequence of points can be obtained by a 1/revolution sampling method from the obtained vibration deflection time history. Figure 3.10 illustrates two typical cases of the 1/revolution sampled time history for the periodical second-order nonlinear oscillator of equation [3.8]. Poincaré section theory shows that if the system is stable, the 1/revolution sampled values will reach a fixed point in the last few periods, as shown in Figure 3.10(b). Whereas once the system becomes unstable, the 1/revolution sampled values will be in the status of decentralization, as shown in Figure 3.10(a). An in-depth analysis indicates that the stable milling case will satisfy the following criterion;

$$\sigma = \frac{\delta_{\mathrm{p-max}} - \delta_{\mathrm{p-min}}}{\max\{\left|\delta_{\mathrm{p-max}}\right|, \left|\delta_{\mathrm{p-min}}\right|\}} < \epsilon_{\mathrm{S}} \qquad [3.91]$$

in which $\delta_{\mathrm{p-max}}$ and $\delta_{\mathrm{p-min}}$ are the maximum and the minimum values of the 1/revolution sampled deflections in the range of $\xi_{\mathrm{S}}\, S_{\mathrm{span}}$, as shown in Figure 3.10(a). ξ_{S} is the scale factor. ϵ_{S} is the tolerance used to ensure stable milling.

With the criterion equation [3.91], the stability lobe could be theoretically plotted by sweeping the axial depth of cut and spindle speed to check the system stability. Obviously, this sweeping procedure may lead to a relatively large simulation time because every possible case should be checked.

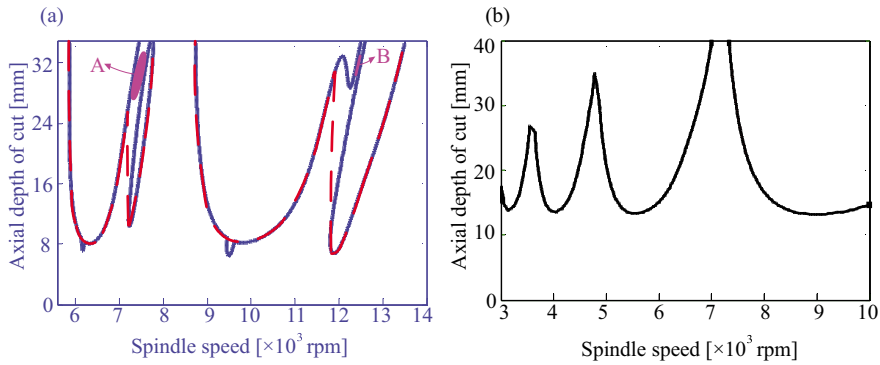

Figure 3.11. *Schematic charts of stability lobes: a) small radial immersion; b) large radial immersion. For a color version of this figure, see www.iste.co.uk/zhang/milling.zip*

A review of the literature indicates that the stability lobe generally has the distribution as in Figure 3.11, from which it can be clearly seen that:

– for large radial immersion, the axial depth of cut is a single-valued function of spindle speed, as shown in Figure 3.11 (b);

– for small radial immersion, island-like or byland-like lobes may arise due to period-doubling bifurcations [PAT 08, ZAT 06, WAN 10b], as shown in Figure 3.11(a). These phenomena directly lead to the presence of some narrow chatter-free regions, such as the regions A and B indicated in Figure 3.11(a). Theoretically, the axial depth of cut in these regions can be considered for chatter-free milling design. However, due to the disturbance effect of noise factors, chatter may still occur if the cutting parameters are selected from these narrow regions. In industry practice, the acceptable chatter free cutting

parameters are often ensured by the lobe's outer contour (see the dashed lines shown in Figure 3.11(a)), which is also a single-valued function of spindle speed.

The above two comments imply that the axial depth of cut can be assumed to be the single-valued function of spindle speed for the stability lobes in industry application, no matter what radial immersion is concerned. Keeping this in mind, one can use the dichotomy method to constitute the stability lobe based on equation [3.91] according to the following steps:

1) Set the values of a_{e}, f and S_{span}. Suppose that the effective cutting length of the cutter is $a_{\mathrm{p}}^{\max}$;

2) Set l=0 and $S^{(l)}$=S_{In}; S_{In} is the initial spindle speed used for simulation;

3) Set k=0 and attribute $a_{\mathrm{p}}^{\max}$ to $a_{\mathrm{p}}{}^{(k)}$. Set $a_{\mathrm{p,L}} = 0$ and $a_{\mathrm{p,U}} = a_{\mathrm{p}}^{\max}$. $a_{\mathrm{p,L}}$ and $a_{\mathrm{p,U}}$ are the lower and upper bounds used to designate dichotomy interval;

4) Set t=0 and substitute $a_{\mathrm{e}}(0)$ into equation [3.90] to calculate $\theta_{\mathrm{en}}(0)$ and $\theta_{\mathrm{ex}}(0)$. Calculate $h_{\mathrm{ST},i,j}(0)$ with equation [3.2] and set $h_{i,j}(0) = h_{\mathrm{ST},i,j}(0)$. Note that $a_{\mathrm{e}}(0) = a_{\mathrm{e}}$;

5) Set $\mathbf{z}(0)$ by equation [3.89];

6) Determine the instantaneous cutting force coefficient K_q using equation [1.57] or [1.73], or directly using the constant coefficient K_q;

7) Based on $\theta_{\mathrm{en}}(t)$ and $\theta_{\mathrm{ex}}(t)$, calculate $F_{\mathrm{X}}(t)$ and $F_{\mathrm{Y}}(t)$ with equation [3.7];

8) Substitute $\mathbf{z}(t)$ and $F_s(t)$ (s=X, Y) into equation [3.86] and then solve $x(t)$ and $y(t)$ using the schemes in [SHA 01];

9) Set $t = t + \Delta t$ and update the entry angle $\theta_{\mathrm{en}}(t)$ or exit angle $\theta_{\mathrm{ex}}(t)$ based on $x(t)$ and $y(t)$. For example, equation [3.90] can be used to update the entry angle in case of down milling. Δt is the time increment;

10) Use $x(t - k\tau)$ and $y(t - k\tau)$ (k=0, 1, 2, ..., N_{d}) to calculate $h_{i,j}(t)$ with equations [3.1] and [3.2];

11) Update $\mathbf{z}(t)$ using equation [3.87];

12) Repeat steps (6)–(11) until t reaches S_{span};

13) Check the stability status using equation [3.91]. The sub-steps are as follows:

i) if the system is stable at $a_{\mathrm{p}}^{(k)} = a_{\mathrm{p}}^{\max}$, $a_{\mathrm{p}}^{\max}$ is assumed to be the limit of the axial depth of cut that can ensure stable milling for $S^{(l)}$. Set *l*=*l*+1, $S^{(l)}$=$S^{(l-1)} + \Delta S$ and go to step (3). ΔS is spindle speed increment;

ii) if the system is stable at $a_{\mathrm{p}}^{(k)} < a_{\mathrm{p}}^{\max}$,

- if $\left| a_{\mathrm{p}}^{(k)} - a_{\mathrm{p}}^{(k-1)} \right| < \epsilon_{\mathrm{p}}$, $a_{\mathrm{p}}^{(k)}$ is assumed to be the limit of the axial depth of cut that can ensure stable milling for $S^{(l)}$. Set *l*=*l*+1, $S^{(l)}$=$S^{(l-1)} + \Delta S$ and go to step (3). ϵ_{p} is the tolerance used to check the convergence.

- otherwise, set *k*=*k*+1, $a_{\mathrm{p}}^{(k)} = (a_{\mathrm{p,L}} + a_{\mathrm{p,U}})/2$ and $a_{\mathrm{p,L}} = a_{\mathrm{p}}{}^{(k-1)}$, and then go to step (4).

iii) in the case of unstable milling, set *k*=*k*+1, $a_{\mathrm{p}}^{(k+1)} = (a_{\mathrm{p,L}} + a_{\mathrm{p,U}})/2$ and $a_{\mathrm{p,U}} = a_{\mathrm{p}}^{(k-1)}$. And then go to step (4).

14) Repeat steps (2)–(13) until all concerned spindle speeds are simulated;

15) Plot the stability lobes using the results obtained above.

It is worth noting that in the above simulation procedure, $x(t - k\tau)$ and $y(t - k\tau)$ (*k*= 1, 2, ..., N_{d}) are artificially assumed to be zero when t is less than the cutter cutting period. Superscripts (k) and (l) in the above procedure represent the iteration steps.

Verifications of the proposed methods will be described as follows.

Direction	Mode	Natural frequency (Hz)	Modal mass(kg)	Damping ratios (-)
X	1	739.03	1.357	0.058995
Y	1	708.54	1.725	0.051897
	2	1183.2	3.62	0.034145

Table 3.5. *Modal parameters*

To investigate the effectiveness of the method described above, a series of experimental tests are performed on a vertical CNC milling machine. A three-fluted carbide end mill with a diameter of 16 mm and a helix angle of 30° is employed to cut aluminum alloy AL7050.

Test No.	Radial depth of cut a_e(mm)	Axial depth of cut a_p(mm)	Feed per tooth f(mm/tooth)	Spindle speed S(rpm)
1	8	2	0.1	2000
2	4	24.5	0.1	6000
3	4	24.5	0.1	7000

Table 3.6. *Cutting conditions*

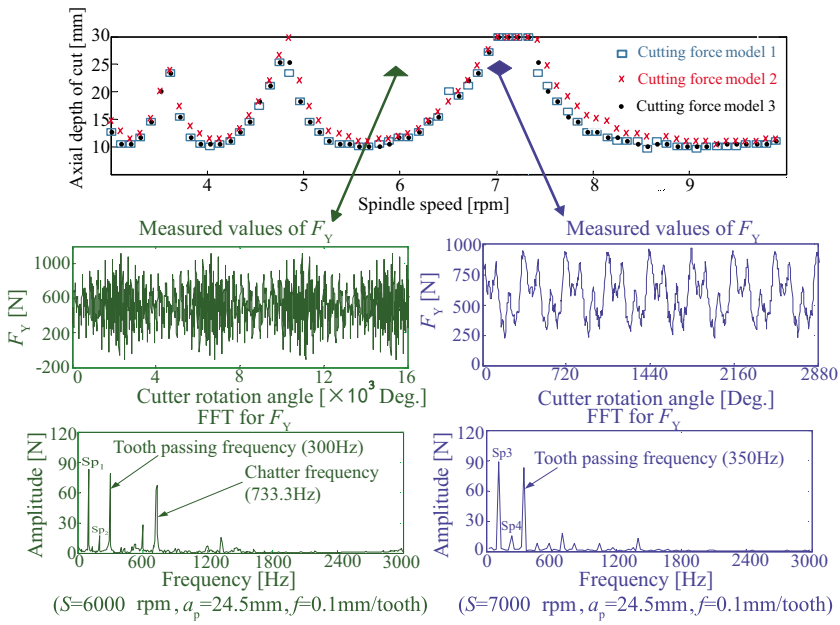

Figure 3.12. *Predicted stability lobes and measured cutting forces for a_e=4mm and f=0.1mm/tooth: the cutting force coefficients calibrated from Test 2 are used in simulation. For a color version of this figure, see www.iste.co.uk/zhang/milling.zip*

In Figure 3.12, the predicted stability lobes are shown for the following conditions: $a_e = 4$ mm and $f = 0.1$ mm/tooth. Modal parameters used in simulation are listed in Table 3.5. Figure 3.12 shows the stability lobes generated using the proposed method for the three cutting force models, whose cutting force coefficients are only calibrated from Test 1 in Table 3.6. Obviously, a good agreement exists between the predicted results.

Two cutting tests, i.e. Tests 2 and 3 in Table 3.6, are carried out at the axial depth of cut $a_{\mathrm{p}} = 24.5$ mm, $a_{\mathrm{e}} = 4$ mm and $f = 0.1$ mm/tooth. One is at a spindle speed of 6000 rpm, where unstable cutting occurs. From the measured cutting forces and their Fourier spectrum shown in Figure 3.12, it can be seen that chatter vibrations are severe and evident at 6000 rpm. The chatter occurs at frequency 733.3 Hz, close to the frequency of the first mode of the machine-tool system. When the spindle speed is increased to 7000 rpm, the chatter vibrations disappear. Note that the spectrum $\mathrm{Sp}_k(k = 1, 2, 3, 4)$ in Figure 3.12 stands for the harmonic force due to the cutter runout. Detailed explanations of this issue can be found in [WAN 09a, WAN 10b]. The above two tests mean that the proposed methods are valid to plan chatter-free processes.

4

Mathematical Modeling of the Workpiece-Fixture System

In general, fixtures mechanical devices used to assist machining, assembly, inspection, welding, and other manufacturing operations. The function of fixtures is to locate and ensure the desired positions and orientations of workpieces during the manufacturing process. In traditional and modern manufacturing systems, how to plan the workpiece holding is the basic issue of the machining operation to be confronted for the fixture design. In this chapter, a series of models and methods about configuring the fixture locating scheme and clamping strategies are given and well discussed.

4.1. Criteria of locating scheme correctness

4.1.1. *The DOFs constraining principle*

As shown in Figure 4.1, the workpiece coordinate system $X^wY^wZ^w$ attached rigidly to the workpiece can be movable whereas the global coordinate system XYZ is fixed. Without loss of generality, we denote $\mathbf{r}_w^* = [x_w^*, y_w^*, z_w^*]^T$, $\boldsymbol{\theta}_w^* = [\alpha_w^*, \beta_w^*, \gamma_w^*]^T$, $\mathbf{v}_w = [\delta x_w^*, \delta y_w^*, \delta z_w^*]^T$ and $\boldsymbol{\omega}_w = [\delta\alpha_w^*, \delta\beta_w^*, \delta\gamma_w^*]^T$ as the position, orientation, linear and angular velocities of $X^wY^wZ^w$ related to XYZ, respectively. In addition, $\mathbf{r}_P = [x_P, y_P, z_P]^T$ and $\mathbf{r}_P^w = [x_P^w, y_P^w, z_P^w]^T$ are used to represent the coordinates of an arbitrary point P in XYZ and $X^wY^wZ^w$, respectively. If

Milling Simulation: *Metal Milling Mechanics, Dynamics and Clamping Principles*,
First Edition. Weihong Zhang and Min Wan.

$X^wY^wZ^w$ is assumed to coincide with XYZ, then the velocity of point P can be expressed as

$$\mathbf{v}_P = \mathbf{v}_w + \boldsymbol{\omega}_w \times \mathbf{r}_P \quad [4.1]$$

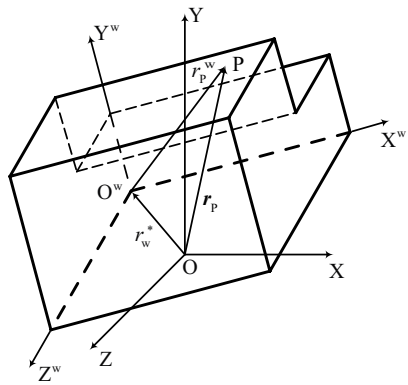

Figure 4.1. *The motion status of the workpiece*

In order to study the relationship between the constrained degrees of freedom (DOFs) of the workpiece and its machining dimensions, equation [4.1] is rewritten in differentiation form:

$$\begin{bmatrix} \delta x_P \\ \delta y_P \\ \delta z_P \end{bmatrix} = \begin{bmatrix} \delta x_w^* + \delta\beta_w^* z_P - \delta\gamma_w^* y_P \\ \delta y_w^* + \delta\gamma_w^* x_P - \delta\alpha_w^* z_P \\ \delta z_w^* + \delta\alpha_w^* y_P - \delta\beta_w^* x_P \end{bmatrix} \quad [4.2]$$

or

$$\delta\mathbf{r}_P = \mathbf{E}\delta\mathbf{q}_w^* \quad [4.3]$$

with

$$\delta\mathbf{q}_w^* = \left[\mathbf{v}_w^T, \omega_w^T\right]^T = \left[\delta x_w^*, \delta y_w^*, \delta z_w^*, \delta\alpha_w^*, \delta\beta_w^*, \delta\gamma_w^*\right]^T \quad [4.4]$$

where $\delta\mathbf{q}_{\mathrm{w}}^{*}$ represents the desired DOF vector of the workpiece to be constrained correspondingly. $\mathbf{E}$ is the position matrix of point P. It is important to note that $\delta\mathbf{r}_{\mathrm{P}}$ is the machining-dimension vector of the workpiece in its perturbation form.

$$\mathbf{E} = \left[\mathbf{E}_1^{\mathrm{T}}, \mathbf{E}_2^{\mathrm{T}}, \mathbf{E}_3^{\mathrm{T}}\right]^{\mathrm{T}}, \mathbf{E}_i = \left[\mathbf{e}_i^{\mathrm{T}}, -(\mathbf{e}_i \times \mathbf{r}_{\mathrm{P}})^{\mathrm{T}}\right] \quad [4.5]$$

with $\mathbf{e}_1 = [1,0,0]^{\mathrm{T}}$, $\mathbf{e}_2 = [0,1,0]^{\mathrm{T}}$ and $\mathbf{e}_3 = [0,0,1]^{\mathrm{T}}$.

Obviously, the achievement of the considered machining dimensions relies on the constrained DOFs in $\delta\mathbf{q}_{\mathrm{w}}^{*}$. For example, if the machining dimension is aligned in the X direction,

$$\delta x_{\mathrm{P}} = \delta x_{\mathrm{w}}^{*} + \delta\beta_{\mathrm{w}}^{*} z_{\mathrm{P}} - \delta\gamma_{\mathrm{w}}^{*} y_{\mathrm{P}} = 0 \quad [4.6]$$

Because y_{P} and z_{P} can take arbitrary values, equation [4.6] is valid if and only if

$$\delta x_{\mathrm{w}}^{*} = \delta\beta_{\mathrm{w}}^{*} = \delta\gamma_{\mathrm{w}}^{*} = 0 \quad [4.7]$$

In other words, only when three DOFs ($\delta x_{\mathrm{w}}^{*}$,$\delta\beta_{\mathrm{w}}^{*}$,$\delta\gamma_{\mathrm{w}}^{*}$) are constrained, the machining operation is correct. Similarly, if machining dimensions are required simultaneously in the X and Y directions, the following conditions have to hold,

$$\begin{cases} \delta x_{\mathrm{P}} = \delta x_{\mathrm{w}}^{*} + \delta\beta_{\mathrm{w}}^{*} z_{\mathrm{P}} - \delta\gamma_{\mathrm{w}}^{*} y_{\mathrm{P}} = 0 \\ \delta y_{\mathrm{P}} = \delta y_{\mathrm{w}}^{*} + \delta\gamma_{\mathrm{w}}^{*} x_{\mathrm{P}} - \delta\alpha_{\mathrm{w}}^{*} z_{\mathrm{P}} = 0 \end{cases} \quad [4.8]$$

The constrained DOFs are then

$$\delta x_{\mathrm{w}}^{*} = \delta y_{\mathrm{w}}^{*} = \delta\alpha_{\mathrm{w}}^{*} = \delta\beta_{\mathrm{w}}^{*} = \delta\gamma_{\mathrm{w}}^{*} = 0 \quad [4.9]$$

Meanwhile, if the machining dimensions ought to be guaranteed in all three directions, we have

$$\begin{cases} \delta x_{\mathrm{P}} = \delta x_{\mathrm{w}}^{*} + \delta\beta_{\mathrm{w}}^{*} z_{\mathrm{P}} - \delta\gamma_{\mathrm{w}}^{*} y_{\mathrm{P}} = 0 \\ \delta y_{\mathrm{P}} = \delta y_{\mathrm{w}}^{*} + \delta\gamma_{\mathrm{w}}^{*} x_{\mathrm{P}} - \delta\alpha_{\mathrm{w}}^{*} z_{\mathrm{P}} = 0 \\ \delta z_{\mathrm{P}} = \delta z_{\mathrm{w}}^{*} + \delta\alpha_{\mathrm{w}}^{*} y_{\mathrm{P}} - \delta\beta_{\mathrm{w}}^{*} x_{\mathrm{P}} = 0 \end{cases} \quad [4.10]$$

It follows that

$$\delta x_{\mathrm{w}}^{*} = \delta y_{\mathrm{w}}^{*} = \delta z_{\mathrm{w}}^{*} = \delta \alpha_{\mathrm{w}}^{*} = \delta \beta_{\mathrm{w}}^{*} = \delta \gamma_{\mathrm{w}}^{*} = 0 \qquad [4.11]$$

Therefore, the machining dimensions in three directions can be achieved only when six DOFs are all constrained. To make the discussion easier, all the above constrained DOFs derived from machining dimensions are referred to as theoretical constrained DOFs that are essentially the required constraints. A summary is given in Figure 4.2 to show the relationship between the machining dimensions and the theoretical constrained DOFs.

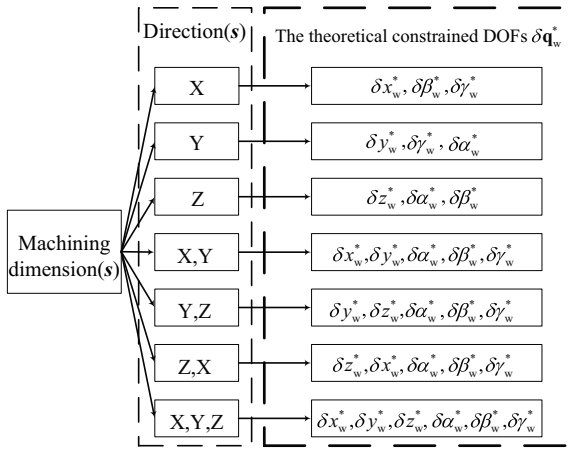

Figure 4.2. *The relationship diagram between the machining dimensions and the theoretical constrained DOFs*

4.1.2. *The locating scheme*

In fact, locating schemes depend upon locator number and positions. The aim of designing a workable locating scheme consists of constraining first of all the undesired DOFs of the workpiece. As shown in Figure 4.3, to obtain the machining surface with specified dimensions a and b, a variety of locating schemes can be designed to locate a block workpiece. The workpiece is theoretically fixed in all directions by locating schemes 1 and 2. However, it can move in the Z direction if constrained by locating scheme 3 and 4. With locating schemes 5 and 6, the workpiece can translate in both X and Z

directions and rotate about the Y axis so that the machining dimension a cannot be guaranteed by both locating schemes because the DOFs of the workpiece cannot be properly constrained. Here, it is necessary to note that the difference between "partial location" and "under location" is that partial location can correctly constrain DOFs of the workpiece whereas under location cannot.

Therefore, during the fixture design of a locating scheme, it is very important to ensure the validity of the locator number and positions. In order to model the locating scheme mathematically, following assumptions are used throughout this chapter.

– workpiece and locators are rigid bodies;

– only point contacts exist between each locator and workpiece;

– the contact surface of the workpiece is piecewise differentiable.

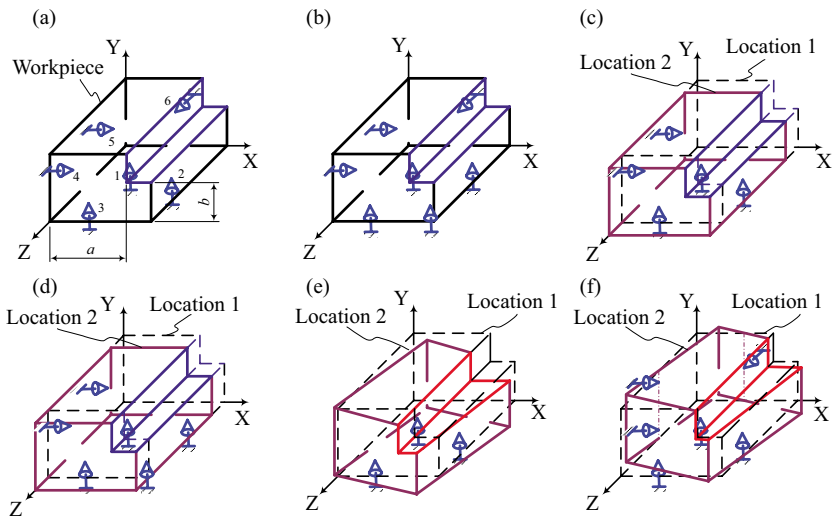

Figure 4.3. *Effect of the locator number and positions: a) locating scheme 1: deterministic location; b) locating scheme 2: complete over location; c) locating scheme 3: partial location; d) locating scheme 4: partial over location; e) locating scheme 5: under location; f) locating scheme 6: under over location. For a color version of this figure, see www.iste.co.uk/zhang/milling.zip*

As illustrated in Figure 4.4, the contact surface of the workpiece is supposed to be

$$f^{\mathrm{w}}\left(\mathbf{r}^{\mathrm{w}}\right) = f^{\mathrm{w}}\left(x^{\mathrm{w}}, y^{\mathrm{w}}, z^{\mathrm{w}}\right) = 0 \qquad [4.12]$$

in which $\mathbf{r}^{\mathrm{w}} = [x^{\mathrm{w}}, y^{\mathrm{w}}, z^{\mathrm{w}}]^{\mathrm{T}}$ designates the coordinate vector of an arbitrary point on the workpiece with respect to $\mathrm{X^wY^wZ^w}$.

Therefore, the coordinate vector $\mathbf{r}$ in XYZ can be expressed as

$$\mathbf{r} = \mathbf{T}\left(\boldsymbol{\theta}_{\mathrm{w}}\right) \cdot \mathbf{r}^{\mathrm{w}} + \mathbf{r}_{\mathrm{w}} \qquad [4.13]$$

where

$$\mathbf{T}\left(\boldsymbol{\theta}_{\mathrm{w}}\right) = \begin{bmatrix} \mathrm{c}\beta_{\mathrm{w}}\mathrm{c}\gamma_{\mathrm{w}} & -\mathrm{c}\alpha_{\mathrm{w}}\mathrm{s}\gamma_{\mathrm{w}} + \mathrm{s}\alpha_{\mathrm{w}}\mathrm{s}\beta_{\mathrm{w}}\mathrm{c}\gamma_{\mathrm{w}} & \mathrm{s}\alpha_{\mathrm{w}}\mathrm{s}\gamma_{\mathrm{w}} + \mathrm{c}\alpha_{\mathrm{w}}\mathrm{s}\beta_{\mathrm{w}}\mathrm{c}\gamma_{\mathrm{w}} \\ \mathrm{c}\beta_{\mathrm{w}}\mathrm{s}\gamma_{\mathrm{w}} & \mathrm{c}\alpha_{\mathrm{w}}\mathrm{c}\gamma_{\mathrm{w}} + \mathrm{s}\alpha_{\mathrm{w}}\mathrm{s}\beta_{\mathrm{w}}\mathrm{s}\gamma_{\mathrm{w}} & -\mathrm{s}\alpha_{\mathrm{w}}\mathrm{c}\gamma_{\mathrm{w}} + \mathrm{c}\alpha_{\mathrm{w}}\mathrm{s}\beta_{\mathrm{w}}\mathrm{s}\gamma_{\mathrm{w}} \\ -\mathrm{s}\beta_{\mathrm{w}} & \mathrm{s}\alpha_{\mathrm{w}}\mathrm{c}\beta_{\mathrm{w}} & \mathrm{c}\alpha_{\mathrm{w}}\mathrm{c}\beta_{\mathrm{w}} \end{bmatrix} \qquad [4.14]$$

is an orthogonal rotation matrix with c = cos and s = sin.

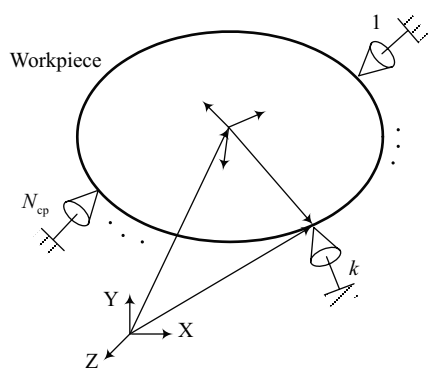

Figure 4.4. *Illustration of the locating scheme to the workpiece*

By inserting equation [4.13] into equation [4.12], the latter will be expressed in XYZ as follows

$$f^{\mathrm{w}}\left[\mathbf{T}(\boldsymbol{\theta}_{\mathrm{w}})^{\mathrm{T}} \cdot (\mathbf{r} - \mathbf{r}_{\mathrm{w}})\right] = 0 \qquad [4.15]$$

By assigning $\mathbf{q}_{\mathrm{w}} = \left[\mathbf{r}_{\mathrm{w}}^{\mathrm{T}}, \boldsymbol{\theta}_{\mathrm{w}}^{\mathrm{T}}\right]^{\mathrm{T}} = [x_{\mathrm{w}}, y_{\mathrm{w}}, z_{\mathrm{w}}, \alpha_{\mathrm{w}}, \beta_{\mathrm{w}}, \gamma_{\mathrm{w}}]^{\mathrm{T}}$, one has

$$f^{\mathrm{w}}(\mathbf{q}_{\mathrm{w}}) = f^{\mathrm{w}}\left[\mathbf{T}(\boldsymbol{\theta}_{\mathrm{w}})^{\mathrm{T}}(\mathbf{r} - \mathbf{r}_{\mathrm{w}})\right] = 0 \qquad [4.16]$$

Let $\mathbf{r}_k = [x_k, y_k, z_k]^{\mathrm{T}} (1 \leq k \leq N_{\mathrm{cp}})$ be the coordinate vector of the kth contact point, then the following relation holds

$$\mathbf{r}_k = \mathbf{T}(\boldsymbol{\theta}_{\mathrm{w}}) \cdot \mathbf{r}_k^{\mathrm{w}} + \mathbf{r}_{\mathrm{w}} \qquad [4.17]$$

where N_{cp} is the total number of contact points or locators. Thus, the following equations have to hold simultaneously provided that locators $\mathbf{r}_k (1 \leq k \leq N_{\mathrm{cp}})$ remain in contact with the workpiece surface.

$$f^{\mathrm{w}}(\mathbf{q}_{\mathrm{w}}, \mathbf{r}_k) = 0, \quad 1 \leq k \leq N_{\mathrm{cp}} \qquad [4.18]$$

Physically, such a system describes the workpiece position $\mathbf{q}_{\mathrm{w}}$ constrained by the locating scheme of N_{cp} locators. Let $\mathbf{q}_{\mathrm{w}}^*$ denote the desired workpiece position associated with the machining dimensions, $\mathbf{q}_{\mathrm{w}} = \mathbf{q}_{\mathrm{w}}^*$ is then a solution of the above set of homogeneous linear system only when the locator number and position are correctly configured.

In contrast to the definition of $\delta\mathbf{q}_{\mathrm{w}}^*$, denote $\delta\mathbf{q}_{\mathrm{w}}$ to be the workpiece position variation near the desired position $\mathbf{q}_{\mathrm{w}}^*$. No matter what the variation of $\delta\mathbf{q}_{\mathrm{w}}$ is, N_{cp} contact points must be theoretically kept in touch with the workpiece surface. Otherwise, the practical locating operation becomes meaningless. So, equation [4.18] can be further written as

$$f^{\mathrm{w}}(\mathbf{q}_{\mathrm{w}}, \mathbf{r}_k) = f^{\mathrm{w}}(\mathbf{q}_{\mathrm{w}}^* + \delta\mathbf{q}_{\mathrm{w}}, \mathbf{r}_k) = 0, 1 \leq k \leq N_{\mathrm{cp}} \qquad [4.19]$$

With the Taylor expansion at $\mathbf{q}_{\mathrm{w}}^*$ and neglecting higher order terms, it then follows that

$$f^{\mathrm{w}}(\mathbf{q}_{\mathrm{w}}^* + \delta\mathbf{q}_{\mathrm{w}}, \mathbf{r}_k) = f^{\mathrm{w}}(\mathbf{q}_{\mathrm{w}}^*, \mathbf{r}_k) + \mathbf{G}_k^{\mathrm{T}}\delta\mathbf{q}_{\mathrm{w}} = 0, 1 \leq k \leq N_{\mathrm{cp}} \qquad [4.20]$$

where $\mathbf{G}_k$ is the gradient vector.

The comparison between equations [4.18] and [4.20] shows that the workpiece remains in contact with N_{cp} locators at $\mathbf{q}_{\mathrm{w}} = \mathbf{q}_{\mathrm{w}}^{*} + \delta\mathbf{q}_{\mathrm{w}}$ if and only if

$$\mathbf{J}_{\mathrm{Jac},k}\delta\mathbf{q}_{\mathrm{w}} = \mathbf{0}, 1 \le k \le N_{\mathrm{cp}} \qquad [4.21]$$

with $\mathbf{J}_{\mathrm{Jac},k} = \mathbf{G}_{k}^{\mathrm{T}}$. If the $\mathrm{X^wY^wZ^w}$ is assumed to be identically oriented with the XYZ, we have

$$\begin{aligned}\mathbf{J}_{\mathrm{Jac},k} = \Big[&- n_{kx}^{\mathrm{w}},\ -n_{ky}^{\mathrm{w}},\ -n_{kz}^{\mathrm{w}},\ n_{kz}^{\mathrm{w}}y_{k}^{\mathrm{w}} - n_{ky}^{\mathrm{w}}z_{k}^{\mathrm{w}},\\ &n_{kx}^{\mathrm{w}}z_{k}^{\mathrm{w}} - n_{kz}^{\mathrm{w}}x_{k}^{\mathrm{w}}, n_{ky}^{\mathrm{w}}x_{k}^{\mathrm{w}} - n_{kx}^{\mathrm{w}}y_{k}^{\mathrm{w}}\Big]\end{aligned} \qquad [4.22]$$

with the normal vector of the workpiece surface at the *k*th contact point $\mathbf{n}_{k}^{\mathrm{w}} = \left[n_{kx}^{\mathrm{w}}, n_{ky}^{\mathrm{w}}, n_{kz}^{\mathrm{w}}\right]^{\mathrm{T}} = \left[\frac{\partial f^{\mathrm{w}}}{\partial x_{k}^{\mathrm{w}}}, \frac{\partial f^{\mathrm{w}}}{\partial y_{k}^{\mathrm{w}}}, \frac{\partial f^{\mathrm{w}}}{\partial z_{k}^{\mathrm{w}}}\right]^{\mathrm{T}}$.

The compact expression of equation [4.21] can be rewritten in matrix form

$$\mathbf{J}_{\mathrm{Jac}}\delta\mathbf{q}_{\mathrm{w}} = \mathbf{0} \qquad [4.23]$$

with the Jacobian matrix $\mathbf{J}_{\mathrm{Jac}} = [\mathbf{J}^{\mathrm{T}}{}_{\mathrm{Jac},1}, \mathbf{J}^{\mathrm{T}}{}_{\mathrm{Jac},2}, ..., \mathbf{J}^{\mathrm{T}}{}_{\mathrm{Jac},N_{\mathrm{cp}}}]^{\mathrm{T}}$.

In equation [4.23], all zero terms of $\delta\mathbf{q}_{\mathrm{w}}$ are the so-called practical constrained DOFs of the workpiece depending upon the locator number N_{cp} and positions.

4.1.3. *Judgment criteria of locating scheme correctness*

Here, let operator num( ) denote the allowable number of DOFs. Scalar m denotes the number of unconstrained allowable DOFs in num( ) that do not satisfy equation [4.23]. Consequently, num( )-*m* is the number of DOFs belonging to the practical constrained DOFs. Recall that N_{cp} refers to the locator number. Some judgment criteria can be derived below to verify the locating scheme correctness.

– *Case 1*: if $N_{\mathrm{cp}} < 6$, then the locating scheme is:

- partial location when $\mathrm{rank}\,(\mathbf{J}_{\mathrm{Jac}}) = N_{\mathrm{cp}}$ and $\mathrm{rank}\,(\mathbf{J}_{\mathrm{Jac}}) + \mathrm{num}\,(\delta\mathbf{q}_{\mathrm{w}}^{*}) - m = 6$; as illustrated in Figure 4.3(c);

- under location when $\text{rank}\,(\mathbf{J}_{\text{Jac}}) = N_{\text{cp}}$ and $\text{rank}\,(\mathbf{J}_{\text{Jac}}) + \text{num}\,(\delta\mathbf{q}_{\text{w}}^{*}) - m < 6$; as illustrated in Figure 4.3(e);

- partial over location when $\text{rank}\,(\mathbf{J}_{\text{Jac}}) < N_{\text{cp}}$ and $\text{rank}\,(\mathbf{J}_{\text{Jac}}) + \text{num}\,(\delta\mathbf{q}_{\text{w}}^{*}) - m = 6$;

- under over location when $\text{rank}\,(\mathbf{J}_{\text{Jac}}) < N_{\text{cp}}$ and $\text{rank}\,(\mathbf{J}_{\text{Jac}}) + \text{num}\,(\delta\mathbf{q}_{\text{w}}^{*}) - m < 6$.

– *Case 2*: if $N_{\text{cp}} = 6$, then the locating scheme is:

- complete location when $\text{rank}\,(\mathbf{J}_{\text{Jac}}) = 6$, as shown in Figure 4.3(a);

- partial over location when $\text{rank}\,(\mathbf{J}_{\text{Jac}}) < 6$ and $\text{rank}\,(\mathbf{J}_{\text{Jac}}) + \text{num}\,(\delta\mathbf{q}_{\text{w}}^{*}) - m = 6$, as shown in Figure 4.3(d);

- under over location when $\text{rank}\,(\mathbf{J}_{\text{Jac}}) < 6$ and $\text{rank}\,(\mathbf{J}_{\text{Jac}}) + \text{num}\,(\delta\mathbf{q}_{\text{w}}^{*}) - m < 6$, as shown in Figure 4.3(f).

– *Case 3*: if $N_{\text{cp}} > 6$, then the locating scheme is:

- complete over location when $\text{rank}\,(\mathbf{J}_{\text{Jac}}) = 6$, as shown in Figure 4.3(b);

- partial over location when $\text{rank}\,(\mathbf{J}_{\text{Jac}}) < 6$ and $\text{rank}\,(\mathbf{J}_{\text{Jac}}) + \text{num}\,(\delta\mathbf{q}_{\text{w}}^{*}) - m = 6$;

- under over location when $\text{rank}\,(\mathbf{J}_{\text{Jac}}) < 6$ and $\text{rank}\,(\mathbf{J}_{\text{Jac}}) + \text{num}\,(\delta\mathbf{q}_{\text{w}}^{*}) - m < 6$.

Finally, flowcharts are given in Figure 4.5 to summarize judgment criteria for different locating schemes.

4.1.4. *Analysis of locating scheme incorrectness*

Generally speaking, a workable locating scheme is able to constrain the undesired DOFs of the workpiece. The fixture designer must determine the layout of the certain number of locators so as to locate the workpiece in the desired position. In fact, a variety of locating schemes will be obtained by changing the number and layout of locators, as shown in Figure 4.3. Based on the three cases discussed in the above section, we can judge the correctness of the locating scheme. However, it is more important to figure out incorrect

locating schemes. To do this, an additional three cases are given to analyze the number and layout of locators.

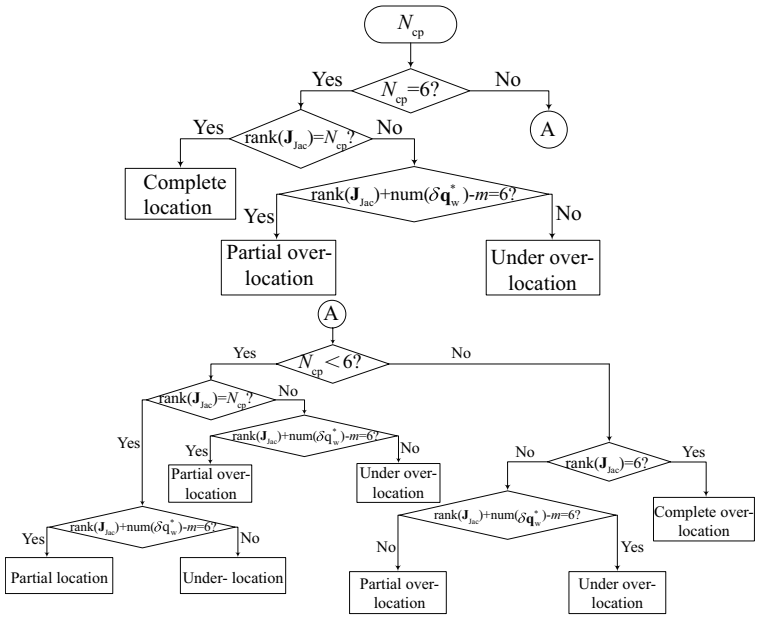

Figure 4.5. *Flowchart verifying different locating schemes*

– *Case 4*: if $N_{\mathrm{cp}} < 6$, then:

- when $N_{\mathrm{cp}} < 6 - \mathrm{num}\,(\delta\mathbf{q}_{\mathrm{w}}^*)$ and $\mathrm{rank}\,(\mathbf{J}_{\mathrm{Jac}}) = N_{\mathrm{cp}}$ and $\mathrm{rank}\,(\mathbf{J}_{\mathrm{Jac}}) + \mathrm{num}\,(\delta\mathbf{q}_{\mathrm{w}}^*) - m < 6$, the locator number N_{cp} is insufficient;

- when $N_{\mathrm{cp}} > 6 - \mathrm{num}\,(\delta\mathbf{q}_{\mathrm{w}}^*)$ and $\mathrm{rank}\,(\mathbf{J}_{\mathrm{Jac}}) = N_{\mathrm{cp}}$ and $\mathrm{rank}\,(\mathbf{J}_{\mathrm{Jac}}) + \mathrm{num}\,(\delta\mathbf{q}_{\mathrm{w}}^*) - m < 6$, the locator number N_{cp} is excessive;

- when $\mathrm{rank}\,(\mathbf{J}_{\mathrm{Jac}}) < N_{\mathrm{cp}}$ and $\mathrm{rank}\,(\mathbf{J}_{\mathrm{Jac}}) + \mathrm{num}\,(\delta\mathbf{q}_{\mathrm{w}}^*) - m = 6$, the locator number is also excessive;

- when $N_{\mathrm{cp}} < 6 - \mathrm{num}\,(\delta\mathbf{q}_{\mathrm{w}}^*)$ and $\mathrm{rank}\,(\mathbf{J}_{\mathrm{Jac}}) < N_{\mathrm{cp}}$ and $\mathrm{rank}\,(\mathbf{J}_{\mathrm{Jac}}) + \mathrm{num}\,(\delta\mathbf{q}_{\mathrm{w}}^*) - m < 6$, not only the locator layout is improper, but also the locator number is excessive;

- when $N_{\mathrm{cp}} = 6 - \mathrm{num}\,(\delta\mathbf{q}_{\mathrm{w}}^*)$ and $\mathrm{rank}\,(\mathbf{J}_{\mathrm{Jac}}) < N_{\mathrm{cp}}$ and $\mathrm{rank}\,(\mathbf{J}_{\mathrm{Jac}}) + \mathrm{num}\,(\delta\mathbf{q}_{\mathrm{w}}^*) - m < 6$, the locator layout is improper;

- when $N_{\mathrm{cp}} > 6 - \mathrm{num}\,(\delta\mathbf{q}_{\mathrm{w}}^{*})$ and $\mathrm{rank}\,(\mathbf{J}_{\mathrm{Jac}}) < N_{\mathrm{cp}}$ and $\mathrm{rank}\,(\mathbf{J}_{\mathrm{Jac}}) + \mathrm{num}\,(\delta\mathbf{q}_{\mathrm{w}}^{*}) - m < 6$, not only the locator layout is improper, but also the locator number is insufficient.

– *Case 5*: if $N_{\mathrm{cp}} = 6$, then:

- when $\mathrm{rank}\,(\mathbf{J}_{\mathrm{Jac}}) < N_{\mathrm{cp}}$ and $\mathrm{rank}\,(\mathbf{J}_{\mathrm{Jac}}) + \mathrm{num}\,(\delta\mathbf{q}_{\mathrm{w}}^{*}) - m = 6$, the locator number is excessive;

- when $N_{\mathrm{cp}} = 6 - \mathrm{num}\,(\delta\mathbf{q}_{\mathrm{w}}^{*})$ and $\mathrm{rank}\,(\mathbf{J}_{\mathrm{Jac}}) < N_{\mathrm{cp}}$ and $\mathrm{rank}\,(\mathbf{J}_{\mathrm{Jac}}) + \mathrm{num}\,(\delta\mathbf{q}_{\mathrm{w}}^{*}) - m < 6$, the locator layout is improper;

- when $N_{\mathrm{cp}} > 6 - \mathrm{num}\,(\delta\mathbf{q}_{\mathrm{w}}^{*})$ and $\mathrm{rank}\,(\mathbf{J}_{\mathrm{Jac}}) < N_{\mathrm{cp}}$ and $\mathrm{rank}\,(\mathbf{J}_{\mathrm{Jac}}) + \mathrm{num}\,(\delta\mathbf{q}_{\mathrm{w}}^{*}) - m < 6$, not only the locator layout is bad, but also the locator number is excessive.

– *Case 6*: if $N_{\mathrm{cp}} > 6$, then:

- when $\mathrm{rank}\,(\mathbf{J}_{\mathrm{Jac}}) = 6$, the locator number is usually excessive;

- when $\mathrm{rank}\,(\mathbf{J}_{\mathrm{Jac}}) < 6$ and $\mathrm{rank}\,(\mathbf{J}_{\mathrm{Jac}}) + \mathrm{num}\,(\delta\mathbf{q}_{\mathrm{w}}^{*}) - m = 6$, the locator number is excessive;

- when $\mathrm{rank}\,(\mathbf{J}_{\mathrm{Jac}}) < 6$ and $\mathrm{rank}\,(\mathbf{J}_{\mathrm{Jac}}) + \mathrm{num}\,(\delta\mathbf{q}_{\mathrm{w}}^{*}) - m < 6$, not only is the locator layout wrong, but the locator number is also excessive.

It is worth noting that although the application of a great number of locators and supports can increase the workpiece stiffness, the addition of a locator into a fixture may increase the workpiece set-up time, fixture capital cost and weight, and reduces cutting tool access to the workpiece. Therefore, when the locator layout is correctly made, the minimum locator number required is $6 - \mathrm{num}\,(\delta\mathbf{q}_{\mathrm{w}}^{*})$.

4.2. Analysis of locating scheme correctness

4.2.1. *Localization source errors*

To establish a general fixture model describing the relationship between the workpiece position error and the localization source errors, we must analyze a variety of localization source errors in detail. As shown in Figure 4.6(a), if the localization source error exists due to the setup errors of

the locators, the tool-setting point will deviate from its nominal position and then the position of the contact point with respect to the tool-setting point can vary. The workpiece will move along with the movement of the contact points. Here, note that {GCS} and {WCS} denote the global coordinate system and the workpiece coordinate system, respectively. As shown in Figure 4.6(b), if another localization source error associated with the manufacturing default of the locator appears, positions of contact points and workpiece will vary. The third localization source error as shown in Figure 4.6(c), is concerned with the manufacturing error of the workpiece. Its presence will change not only the position of contact point with respect to locating point, but also lead to the translation and rotation of the workpiece.

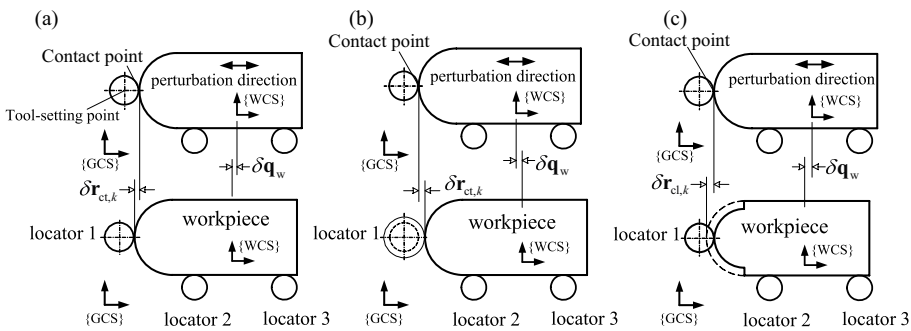

Figure 4.6. *The locating scheme consists of locators: a) illustration of the setup error; b) illustration of the manufacturing default of locator; c) illustration of the manufacturing default of workpiece.*

Based on the above analysis of effects of localization source errors on the workpiece position, the qualitative relationship among the localization source errors due to workpiece surface and fixture setup errors, the position variation of locating points with respect to tool-setting as well as the workpiece position error can be schematically figured out in Figure 4.7.

4.2.2. *Fixture modeling*

To investigate the quantitative relationship between the localization source error and the workpiece position error, a fixture model will be established for the study.

As is known, a workpiece is theoretically desired to be well kept in the specified position after it is located in a fixture. However, position variations of the locating points with respect to tool-setting points induced by the localization source errors will lead to the movement of the workpiece.

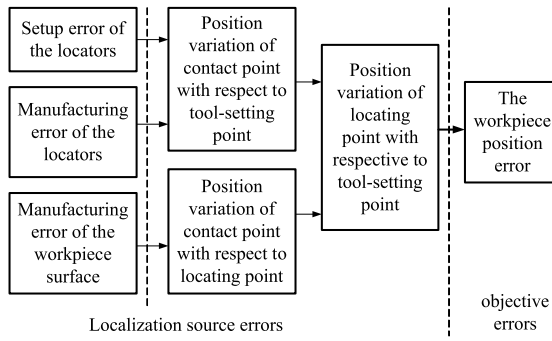

Figure 4.7. *Relationship between source error and objective error*

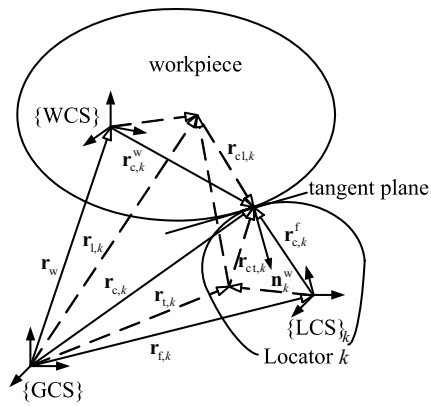

Figure 4.8. *Fixture locating scheme*

As shown in Figure 4.8, the locating scheme consists of N_{cp} ($k = 1, 2, ..., N_{\mathrm{cp}}$) locators. Suppose that the workpiece is a rigid body with a surface represented by a piecewise differentiable function in {WCS}.

$$f^{\mathrm{W}}(\mathbf{r}^{\mathrm{W}}) = f^{\mathrm{W}}(x^{\mathrm{W}}, y^{\mathrm{W}}, z^{\mathrm{W}}) = 0 \qquad [4.24]$$

where $\mathbf{r}^{\mathrm{w}} = [x^{\mathrm{w}}, y^{\mathrm{w}}, z^{\mathrm{w}}]^{\mathrm{T}}$ is the coordinate vector of any point on the workpiece with respect to {WCS}. Then, at the kth contact point of the workpiece surface, the equation of tangent plane related to {WCS} is as follows

$$\varphi_k^{\mathrm{w}}(\mathbf{r}^{\mathrm{w}}) = \mathbf{n}_k^{\mathrm{wT}}(\mathbf{r}^{\mathrm{w}} - \mathbf{r}_{\mathrm{c},k}^{\mathrm{w}}) = 0 \qquad [4.25]$$

where $\mathbf{n}_k^{\mathrm{w}}$ is the unit normal vector of the workpiece surface at the kth contact point whose coordinate vector is $\mathbf{r}_{\mathrm{c},k}^{\mathrm{w}} = \left[x_{\mathrm{c},k}^{\mathrm{w}},\ y_{\mathrm{c},k}^{\mathrm{w}},\ z_{\mathrm{c},k}^{\mathrm{w}}\right]^{\mathrm{T}}$ in {WCS}.

If the orientation and position of the workpiece are known, the workpiece point $\mathbf{r}^{\mathrm{w}}$ can be mapped from {WCS} to {GCS} by the following

$$\mathbf{r} = \mathrm{T}(\boldsymbol{\theta}_{\mathrm{w}})\mathbf{r}^{\mathrm{w}} + \mathbf{r}_{\mathrm{w}} \qquad [4.26]$$

where

$$\mathrm{T}(\boldsymbol{\theta}_{\mathrm{w}}) = \begin{bmatrix} c\beta_{\mathrm{w}}c\gamma_{\mathrm{w}} & -c\alpha_{\mathrm{w}}s\gamma_{\mathrm{w}} + s\alpha_{\mathrm{w}}s\beta_{\mathrm{w}}c\gamma_{\mathrm{w}} & s\alpha_{\mathrm{w}}s\gamma_{\mathrm{w}} + c\alpha_{\mathrm{w}}s\beta_{\mathrm{w}}c\gamma_{\mathrm{w}} \\ c\beta_{\mathrm{w}}s\gamma_{\mathrm{w}} & c\alpha_{\mathrm{w}}c\gamma_{\mathrm{w}} + s\alpha_{\mathrm{w}}s\beta_{\mathrm{w}}s\gamma_{\mathrm{w}} & -s\alpha_{\mathrm{w}}c\gamma_{\mathrm{w}} + c\alpha_{\mathrm{w}}s\beta_{\mathrm{w}}s\gamma_{\mathrm{w}} \\ -s\beta_{\mathrm{w}} & s\alpha_{\mathrm{w}}c\beta_{\mathrm{w}} & c\alpha_{\mathrm{w}}c\beta_{\mathrm{w}} \end{bmatrix}$$

is an orthogonal rotation matrix with $c = \cos$ and $s = \sin$. $\mathbf{r}_{\mathrm{w}} = [x_{\mathrm{w}}, y_{\mathrm{w}}, z_{\mathrm{w}}]^{\mathrm{T}}$ denotes the position of the origin of {WCS} in {GCS}. $\boldsymbol{\theta}_{\mathrm{w}} = [\alpha_{\mathrm{w}}, \beta_{\mathrm{w}}, \gamma_{\mathrm{w}}]^{\mathrm{T}}$ is the orientation of {WCS} with respect to {GCS}.

By substituting equation [4.26] into equation [4.25], the equation of tangent plane can be rewritten as

$$\varphi_k(\mathbf{q}_{\mathrm{w}}, \mathbf{r}) = \mathbf{n}_k^{\mathrm{wT}}\mathrm{T}(\boldsymbol{\theta}_{\mathrm{w}})^{\mathrm{T}}(\mathbf{r} - \mathbf{r}_{\mathrm{w}}) - \mathbf{n}_k^{\mathrm{wT}}\mathbf{r}_{\mathrm{c},k}^{\mathrm{w}} = 0, 1 \le k \le N_{\mathrm{cp}} \qquad [4.27]$$

where the vector $\mathbf{q}_{\mathrm{w}} = [\mathbf{r}_{\mathrm{w}}, \boldsymbol{\theta}_{\mathrm{w}}]^{\mathrm{T}} = [x_{\mathrm{w}}, y_{\mathrm{w}}, z_{\mathrm{w}}, \alpha_{\mathrm{w}}, \beta_{\mathrm{w}}, \gamma_{\mathrm{w}}]^{\mathrm{T}}$ represents six DOFs of the workpiece.

Likewise, at the kth contact point of the locator surface, we can obtain the equation of the tangent plane related to $\{\mathrm{LCS}\}_k$

$$\phi_k^{\mathrm{f}}(\mathbf{r}^{\mathrm{f}}) = \mathrm{T}(\boldsymbol{\theta}_{\mathrm{w}}^{\mathrm{f},k})\mathbf{n}_k^{\mathrm{wT}}(\mathbf{r}^{\mathrm{f}} - \mathbf{r}_{\mathrm{c},k}^{\mathrm{f}}) = 0 \qquad [4.28]$$

where $\mathbf{r}_{c,k}^{f} = \left[x_{c,k}^{f},\ y_{c,k}^{f},\ z_{c,k}^{f}\right]^{T}$ is the coordinate vector of the kth contact point represented in the kth locator coordinate system $\{LCS\}_k$, $T(\boldsymbol{\theta}_{w}^{f,k})$ is a transformation matrix from $\{WCS\}$ to $\{LCS\}_k$.

It is well known that any point $\mathbf{r}^{f}$ defined in $\{LCS\}_k$ can be mapped to $\{GCS\}$ following

$$\mathbf{r} = T(\boldsymbol{\theta}_{f,k})\mathbf{r}^{f} + \mathbf{r}_{f,k} \qquad [4.29]$$

where

$$T(\boldsymbol{\theta}_{f,k}) = \begin{bmatrix} c\beta_{f,k}c\gamma_{f,k} & -c\alpha_{f,k}s\gamma_{f,k} + s\alpha_{f,k}s\beta_{f,k}c\gamma_{f,k} & s\alpha_{f,k}s\gamma_{f,k} + c\alpha_{f,k}s\beta_{f,k}c\gamma_{f,k} \\ c\beta_{f,k}s\gamma_{f,k} & c\alpha_{f,k}c\gamma_{f,k} + s\alpha_{f,k}s\beta_{f,k}s\gamma_{f,k} & -s\alpha_{f,k}c\gamma_{f,k} + c\alpha_{f,k}s\beta_{f,k}s\gamma_{f,k} \\ -s\beta_{f,k} & s\alpha_{f,k}c\beta_{f,k} & c\alpha_{f,k}c\beta_{f,k} \end{bmatrix}$$

is an orthogonal rotation matrix. $\mathbf{r}_{f,k} = [x_{f,k}, y_{f,k}, z_{f,k}]^{T}$ and $\boldsymbol{\theta}_{f,k} = [\alpha_{f,k}, \beta_{f,k}, \gamma_{f,k}]^{T}$ denote the position and orientation of $\{LCS\}_k$ with respect to $\{GCS\}$, respectively.

By substituting equation [4.29] into equation [4.28], the plane tangent to the kth locator element can be described by the following equation

$$\phi_k(\mathbf{q}_{f,k}, \mathbf{r}) = T(\boldsymbol{\theta}_{w}^{f,k})\mathbf{n}_{k}^{wT}T(\boldsymbol{\theta}_{f,k})^{T}(\mathbf{r} - \mathbf{r}_{f,k}) - T(\boldsymbol{\theta}_{w}^{f,k})\mathbf{n}_{k}^{wT}\mathbf{r}_{c,k}^{f} = 0, \quad 1 \le k \le N_{cp} \qquad [4.30]$$

where the vector $\mathbf{q}_{f,k} = [\mathbf{r}_{f,k}^{T}, \boldsymbol{\theta}_{f,k}^{T}]^{T} = [x_{f,k}, y_{f,k}, z_{f,k}, \alpha_{f,k}, \beta_{f,k}, \gamma_{f,k}]^{T}$ represents position and orientation of the kth locator element.

Thus, the contact between the workpiece and locator k holds at the kth point if and only if $\varphi_k(\mathbf{q}_w, \mathbf{r}_{l,k} + \mathbf{r}_{cl,k})$ and $\phi_k(\mathbf{q}_{f,k}, \mathbf{r}_{t,k} + \mathbf{r}_{ct,k})$ are identical, i.e.

$$\varphi_k(\mathbf{q}_w, \mathbf{r}_{l,k} + \mathbf{r}_{cl,k}) - \phi_k(\mathbf{q}_{f,k}, \mathbf{r}_{t,k} + \mathbf{r}_{ct,k}) = 0 \qquad [4.31]$$

where,

$$\mathbf{r}_{cl,k} = \mathbf{r}_{c,k} - \mathbf{r}_{l,k} \qquad [4.32]$$

$$\mathbf{r}_{\mathrm{ct},k} = \mathbf{r}_{\mathrm{c},k} - \mathbf{r}_{\mathrm{t},k} \quad [4.33]$$

In order to study the relationship among the workpiece position error and the surface errors of workpiece and locators, equation [4.31] is differentiated with respect to $\mathbf{q}_{\mathrm{w}}$, $\mathbf{r}_{\mathrm{cl},k}$ and $\mathbf{r}_{\mathrm{ct},k}$ such that

$$\frac{\partial \varphi_k}{\partial \mathbf{q}_{\mathrm{w}}}\delta\mathbf{q}_{\mathrm{w}} + \frac{\partial \varphi_k}{\partial \mathbf{r}_{\mathrm{cl},k}}\delta\mathbf{r}_{\mathrm{cl},k} = \frac{\partial \phi_k}{\partial \mathbf{r}_{\mathrm{ct},k}}\delta\mathbf{r}_{\mathrm{ct},k}, 1 \le k \le N_{\mathrm{cp}} \quad [4.34]$$

or in a compact form

$$\mathbf{J}_{\mathrm{Jac},k}\delta\mathbf{q}_{\mathrm{w}} + \mathbf{n}_k^{\mathrm{wT}}\mathrm{T}(\boldsymbol{\theta}_{\mathrm{w}})^{\mathrm{T}}\delta\mathbf{r}_{\mathrm{cl},k} = \mathbf{T}(\boldsymbol{\theta}_{\mathrm{w}}^{\mathrm{f},k})\mathbf{n}_k^{\mathrm{wT}}\mathrm{T}(\boldsymbol{\theta}_{\mathrm{f},k})^{\mathrm{T}}\delta\mathbf{r}_{\mathrm{ct},k} \quad [4.35]$$

with the Jacobian matrix being

$$\begin{aligned}\mathbf{J}_{\mathrm{Jac},k} = [&-n_{kx}^{\mathrm{w}},\ -n_{ky}^{\mathrm{w}},\ -n_{kz}^{\mathrm{w}},\ n_{kz}^{\mathrm{w}}y_{\mathrm{c},k}^{\mathrm{w}} - n_{ky}^{\mathrm{w}}z_{\mathrm{c},k}^{\mathrm{w}},\\ &n_{kx}^{\mathrm{w}}z_{\mathrm{c},k}^{\mathrm{w}} - n_{kz}^{\mathrm{w}}x_{\mathrm{c},k}^{\mathrm{w}},\ n_{ky}^{\mathrm{w}}x_{\mathrm{c},k}^{\mathrm{w}} - n_{kx}^{\mathrm{w}}y_{\mathrm{c},k}^{\mathrm{w}}]\end{aligned} \quad [4.36]$$

where $\delta\mathbf{q}_{\mathrm{w}}$ represents the practical position errors of the workpiece. $\delta\mathbf{r}_{\mathrm{ct},k}$ and $\delta\mathbf{r}_{\mathrm{cl},k}$ represent the position variations of the contact point with respect to the tool-setting point and locating point, respectively.

Without the loss of generality, we can always assume that {WCS} and $\{\mathrm{LCS}\}_k$ are identically oriented with {GCS}. Then $\mathrm{T}(\boldsymbol{\theta}_{\mathrm{w}})$, $\mathrm{T}(\boldsymbol{\theta}_{\mathrm{f},k})$ and $\mathrm{T}(\boldsymbol{\theta}_{\mathrm{w}}^{\mathrm{f},k})$ will be unit matrices of $\mathrm{I}_{3\times3}$. In this case, the matrix form of equation [4.35] can be rearranged by representing $\delta\mathbf{q}_{\mathrm{w}}$ as a function of $\delta\mathbf{r}_{\mathrm{lt}}$

$$\begin{aligned}\mathbf{J}_{\mathrm{Jac},k}\delta\mathbf{q}_{\mathrm{w}} &= -(\mathbf{n}_k^{\mathrm{wT}}\mathrm{T}(\boldsymbol{\theta}_{\mathrm{w}})^{\mathrm{T}}\delta\mathbf{r}_{\mathrm{cl},k} - \mathrm{T}(\boldsymbol{\theta}_{\mathrm{w}}^{\mathrm{f},k})\mathbf{n}_k^{\mathrm{wT}}\mathrm{T}(\boldsymbol{\theta}_{\mathrm{f},k})^{\mathrm{T}}\delta\mathbf{r}_{\mathrm{ct},k})\\ &= -\mathbf{n}_k^{\mathrm{wT}}(\delta\mathbf{r}_{\mathrm{cl},k} - \delta\mathbf{r}_{\mathrm{ct},k})\\ &= -\mathbf{n}_k^{\mathrm{wT}}\delta\mathbf{r}_{\mathrm{lt},k}\end{aligned} \quad [4.37]$$

Equation [4.37] can be rewritten in matrix form

$$\mathbf{J}_{\mathrm{Jac}}\delta\mathbf{q}_{\mathrm{w}} = -\mathrm{N}^{\mathrm{T}}\delta\mathbf{r}_{\mathrm{lt}} \quad [4.38]$$

with $\mathbf{J}_{\text{Jac}} = [\mathbf{J}_{\text{Jac},1}^{\text{T}}, \mathbf{J}_{\text{Jac},2}^{\text{T}}, \cdots, \mathbf{J}_{\text{Jac},N_{\text{cp}}}^{\text{T}}]^{\text{T}}$, $\delta\mathbf{r}_{\text{lt}} = [\delta\mathbf{r}_{\text{lt},1}^{\text{T}}, \delta\mathbf{r}_{\text{lt},2}^{\text{T}}, \cdots, \delta\mathbf{r}_{\text{lt},N_{\text{cp}}}^{\text{T}}]^{\text{T}}$, $\text{N} = diag(\mathbf{n}_1^{\text{w}}, \mathbf{n}_2^{\text{w}}, \cdots, \mathbf{n}_{N_{\text{cp}}}^{\text{w}})$.

Generally, $\delta\mathbf{q}_{\text{w}}$ can be decomposed into two parts according to equation [4.38] (see [LAN 85])

$$\begin{aligned}\delta\mathbf{q}_{\text{w}} &= \delta\mathbf{q}_{\text{w}}^{s} + \delta\mathbf{q}_{\text{w}}^{h} \\ &= -\mathbf{J}_{\text{Jac}}{}^{+}\text{N}^{\text{T}}\delta\mathbf{r}_{\text{lt}} + \left(\text{I}_{6\times 6} - \mathbf{J}_{\text{Jac}}{}^{+}\mathbf{J}_{\text{Jac}}\right)\boldsymbol{\lambda}_{\text{Con}}\end{aligned} \qquad [4.39]$$

with $\delta\mathbf{q}_{\text{w}}^{s} = -\mathbf{J}_{\text{Jac}}{}^{+}\text{N}^{\text{T}}\delta\mathbf{r}_{\text{lt}}$, $\delta\mathbf{q}_{\text{w}}^{h} = (\text{I}_{3\times 3} - \mathbf{J}_{\text{Jac}}{}^{+}\mathbf{J}_{\text{Jac}})\boldsymbol{\lambda}_{\text{Con}}$, $\mathbf{J}_{\text{Jac}}{}^{+} \in \mathbb{R}^{6\times k}$ is a Moore–Penrose inverse matrix of $\mathbf{J}_{\text{Jac}}$, and $\boldsymbol{\lambda}_{\text{Con}} \in \mathbb{R}^{6\times 1}$ is an arbitrary constant vector.

In the above equation, the first term $\delta\mathbf{q}_{\text{w}}^{s}$ results from the position variation $\delta\mathbf{r}_{\text{lt}}$ of the locating point to the tool-setting, and the second term $\delta\mathbf{q}_{\text{w}}^{h}$ is induced by the free DOFs of the workpiece, which are not constrained by locators.

To have a good understanding, Figures 4.9(a) and (b) show a 2-D workpiece constrained by two locators represented by triangles. In both cases, the workpiece is obviously free to either translate along X direction or rotate about point O. This means that a non-zero $\boldsymbol{\lambda}_{\text{Con}}$ exists. On the contrary, the workpiece is determinately constrained in case of Figure 4.9(c) so that the second item $\delta\mathbf{q}_{\text{w}}^{h}$ will vanish.

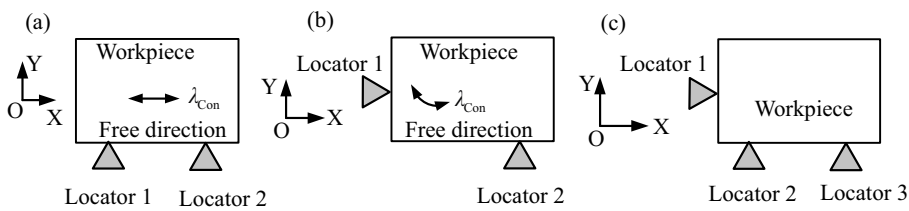

Figure 4.9. *Locating scheme: a) translation along X direction; b) rotation about point O; c) deterministic constraint*

4.2.3. *Locating scheme correctness*

4.2.3.1. *Locating principle*

In principle, design of a locating scheme consists of some basic steps including the determination of number, layout and dimensions of locators. In fact, a variety of locating schemes will be obtained by changing the number and layout of locators as shown in Figure 4.9. The aim of designing a workable locating scheme consists of first constraining all the undesired DOFs of the workpiece. Now let us consider the effect of $\delta\mathbf{q}_{\mathrm{w}}^{h}$ in equation [4.39] upon the variation of the workpiece position. According to equation [4.39], we can write

$$\mathbf{J}_{\mathrm{Jac}}\delta\mathbf{q}_{\mathrm{w}}^{h} = 0 \qquad [4.40]$$

Suppose $\delta\mathbf{q}_{\mathrm{w}}^{*} = [\delta x, \delta y, \delta z, \delta\alpha, \delta\beta, \delta\gamma]^{\mathrm{T}}$ defines the allowable variation of the workpiece position. There could be certain DOFs required to be constrained, for instance δx, then $\delta x = 0$. Otherwise, a non-zero arbitrary constant may be attributed to δx.

In practical applications, $\delta\mathbf{q}_{\mathrm{w}}^{*}$ is the allowable displacement vector determined in advance based on the machining requirements of the workpiece. Comparatively, $\delta\mathbf{q}_{\mathrm{w}}^{h}$ calculated by equation [4.40] corresponds to the real displacement of the workpiece after the locating setup. Now, assume $\mathrm{S}(\delta\mathbf{q}_{\mathrm{w}}^{h})$ and $\mathrm{S}(\delta\mathbf{q}_{\mathrm{w}}^{*})$ be the sets of constrained DOFs in $\delta\mathbf{q}_{\mathrm{w}}^{h}$ and $\delta\mathbf{q}_{\mathrm{w}}^{*}$, respectively, relation to $\mathrm{S}(\delta\mathbf{q}_{\mathrm{w}}^{h}) \supseteq \mathrm{S}(\delta\mathbf{q}_{\mathrm{w}}^{*})$ signifies that really constrained DOFs in $\delta\mathbf{q}_{\mathrm{w}}^{h}$ are equal or more than the desired ones involved in $\delta\mathbf{q}_{\mathrm{w}}^{*}$. Hence, the relationship between $\delta\mathbf{q}_{\mathrm{w}}^{*}$ and $\delta\mathbf{q}_{\mathrm{w}}^{h}$ determines the correctness of the locating scheme. From this point of view, six corollaries can be used to verify the correctness of the locating scheme mathematically dominated by equation [4.40].

COROLLARY 4.1.–

If $\mathrm{rank}\,(\mathbf{J}_{\mathrm{Jac}}) = N_{\mathrm{cp}} = 6$, then this is a sufficient and necessary condition for the complete location.

COROLLARY 4.2.–

If rank $(\mathbf{J}_{\text{Jac}}) = N_{\text{cp}} < 6$, i.e. matrix $\mathbf{J}_{\text{Jac}}$ is row full rank, then this is:

– a necessary condition for the partial location and under-location as well;

– a sufficient and necessary condition of the partial location only when $\text{S}(\delta\mathbf{q}_{\text{w}}^{h}) \supseteq \text{S}(\delta\mathbf{q}_{\text{w}}^{*})$;

– a sufficient and necessary condition for the under-location only when $\text{S}(\delta\mathbf{q}_{\text{w}}^{h}) \subset \text{S}(\delta\mathbf{q}_{\text{w}}^{*})$.

COROLLARY 4.3.–

If rank $(\mathbf{J}_{\text{Jac}}) < N_{\text{cp}}$, then this is:

– a sufficient and necessary condition for the over-location;

– a necessary condition for the under over-location.

COROLLARY 4.4.–

If $N_{\text{cp}} > 6$ and rank $(\mathbf{J}_{\text{Jac}}) = 6$, i.e. matrix $\mathbf{J}_{\text{Jac}}$ is column full rank, then this is:

– a sufficient necessary condition for the complete over-location;

– a sufficient condition for the over-location.

COROLLARY 4.5.–

If rank $(\mathbf{J}_{\text{Jac}}) < N_{\text{cp}}$, rank $(\mathbf{J}_{\text{Jac}}) < 6$ and $\text{S}(\delta\mathbf{q}_{\text{w}}^{h}) \supseteq \text{S}(\delta\mathbf{q}_{\text{w}}^{*})$, then this is:

– a sufficient necessary condition for the partial over-location;

– a sufficient condition for the over-location.

COROLLARY 4.6.–

If rank $(\mathbf{J}_{\text{Jac}}) < N_{\text{cp}}$ and $\text{S}(\delta\mathbf{q}_{\text{w}}^{h}) \subset \text{S}(\delta\mathbf{q}_{\text{w}}^{*})$, then this is a sufficient and necessary condition for the under over-location.

Finally, a flowchart is given in Figure 4.10 to summarize six corollaries for the verification of different locating schemes.

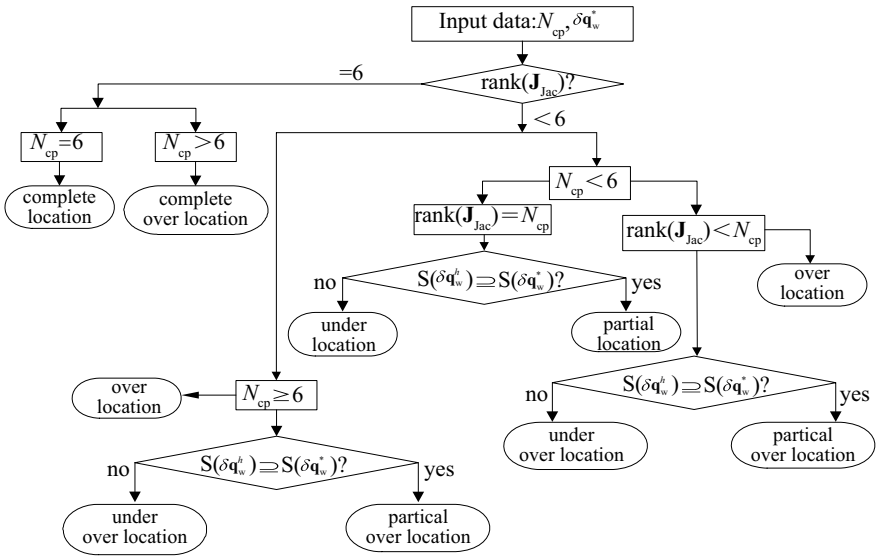

Figure 4.10. *Flowchart verifying different locating schemes*

4.2.3.2. *Robust design model of locating scheme*

After verifying the correctness of a locating scheme by means of the locating principle equation [4.40] and six corollaries, it is further required to design the optimal layout and dimensions of locators. As mentioned before, even if the locating scheme is sound, the position of the workpiece may still be perturbed due to the localization source errors $\delta\mathbf{r}_{lt}$, as shown in Figure 4.11. So, the first term in equation [4.39] consists of

$$\delta\mathbf{q}_w^s = -\mathbf{J}_{Jac}{}^{+}\mathbf{N}^{T}\delta\mathbf{r}_{lt} \qquad [4.41]$$

which relates the position error of the workpiece $\delta\mathbf{q}_w^s$ to the localization source errors $\delta\mathbf{r}_{lt}$.

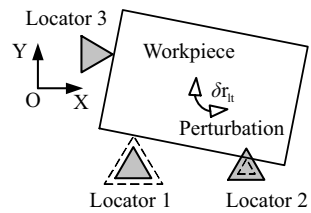

Figure 4.11. *The position variation of the workpiece*

Due to lots of non-deterministic factors such as manufacturing errors, measurement errors, assembly errors and mechanical wear will contribute to $\delta \mathbf{r}_{\mathrm{lt}}$, the latter is characteristic of randomicity. Consequently, $\delta \mathbf{q}_{\mathrm{w}}^{s}$ is also a stochastic variable. In this study, suppose that $\delta \mathbf{q}_{\mathrm{w}}^{s}$ obeys a normal distribution as shown in Figure 4.12. Theoretical and mean values of $\delta \mathbf{q}_{\mathrm{w}}^{s}$ are $\delta \hat{\mathbf{q}}_{\mathrm{w}}^{s} = 0$ and $\delta \bar{\mathbf{q}}_{\mathrm{w}}^{s} = 0$, respectively.

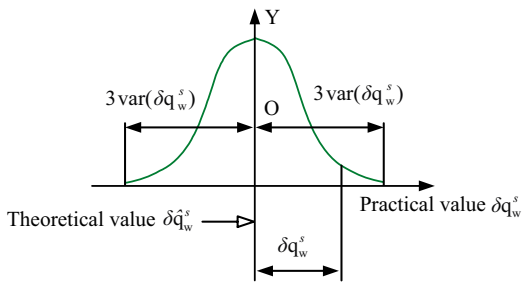

Figure 4.12. *A normal distribution of* $\delta \mathbf{q}_{w}^{s}$

Robust design aims at minimizing the fluctuation of $\delta \mathbf{q}_{\mathrm{w}}^{s}$. Therefore, according to the quality loss function $L(\delta \mathbf{r}_{\mathrm{lt}})$ of the nominal-is-best characteristic, we adopt its mean value $E\{L(\delta \mathbf{r}_{\mathrm{lt}})\}$ as the rule function ν in robust design, namely

$$\begin{aligned} \nu(\delta \mathbf{r}_{\mathrm{lt}}) &= E\{L(\delta \mathbf{r}_{\mathrm{lt}})\} = E\{(\delta \mathbf{q}_{\mathrm{w}}^{s} - \delta \hat{\mathbf{q}}_{\mathrm{w}}^{s})^2\} = E\{(\delta \mathbf{q}_{\mathrm{w}}^{s} - \delta \bar{\mathbf{q}}_{\mathrm{w}}^{s})^2\} \\ &= \mathrm{var}(\delta \mathbf{q}_{\mathrm{w}}^{s}) \end{aligned} \quad [4.42]$$

Note that $\mathrm{var}(\cdot)$ means variance. Hence, the optimum design model of fixture locating scheme corresponds to

$$\begin{aligned} &\text{find} \quad \mathbf{r}_{\mathrm{lt}} = [\mathbf{r}_{\mathrm{lt},1}^{\mathrm{T}}, \mathbf{r}_{\mathrm{lt},2}^{\mathrm{T}}, \cdots, \mathbf{r}_{\mathrm{lt},N_{\mathrm{cp}}}^{\mathrm{T}}]^{\mathrm{T}} \\ &\min \quad \mathrm{var}(\delta \mathbf{q}_{\mathrm{w}}^{s}) \\ &\text{s.t.} \\ &\qquad G(\mathbf{r}_{\mathrm{lt}}) \leq 0 \\ &\qquad H(\mathbf{r}_{\mathrm{lt}}) \leq 0 \end{aligned} \tag{4.43}$$

where $G(\mathbf{r}_{\mathrm{lt}}) \leq 0$ is a geometric constraint condition including feasible layout regions of locators and effective regions of assembling. $H(\mathbf{r}_{\mathrm{lt}}) \leq 0$ is a performance constraint condition to control the workpiece position error $\delta \mathbf{q}_{\mathrm{w}}^{s}$ within the allowable tolerance.

As $\delta \mathbf{r}_{\mathrm{lt}}$ and $\delta \mathbf{q}_{\mathrm{w}}^{s}$ are stochastic variables, their maximum values $ES(\mathbf{r}_{\mathrm{lt}})$ and $ES(\mathbf{q}_{\mathrm{w}}^{s})$ are also stochastic variables. Thus, equation [4.43] can be rewritten as

$$\begin{aligned} &\text{find} \quad \mathbf{r}_{\mathrm{lt}} = [\mathbf{r}_{lt1}^{\mathrm{T}}, \mathbf{r}_{lt2}^{\mathrm{T}}, \cdots, \mathbf{r}_{ltk}^{\mathrm{T}}]^{\mathrm{T}} \\ &\min \quad \mathrm{var}(ES(\mathbf{q}_{\mathrm{w}}^{s})) \\ &\text{s.t.} \\ &\qquad G(ES(\mathbf{r}_{\mathrm{lt}})) \leq 0 \\ &\qquad H(ES(\mathbf{r}_{\mathrm{lt}})) \leq 0 \end{aligned} \tag{4.44}$$

where, $ES(\mathbf{r}_{\mathrm{lt}})$ and $ES(\mathbf{q}_{\mathrm{w}}^{s})$ are referred to as upper deviations of $\mathbf{r}_{\mathrm{lt}}$ and $\mathbf{q}_{\mathrm{w}}^{s}$, respectively.

4.3. Analysis of workpiece stability

4.3.1. *Modeling of workpiece stability*

Two locating schemes are shown in Figure 4.13 with three locators at the bottom of a prismatic workpiece. During the locating operation, suppose that

the workpiece is only subject to its gravity force whose center is denoted by point G. As G is beyond the crosshatched region formed by three locators in Figure 4.13(a), the workpiece will upset and detach from locator L2 so that it is unstable and cannot occupy an accurate position. On the contrary, if the gravity center G is within the crosshatched region as shown in Figure 4.13(b), the workpiece may be in equilibrium to hold the stability. Based on the qualitative analysis, we can understand that a stable workpiece should satisfy both static equilibrium equations and friction constraints in all fixturing steps.

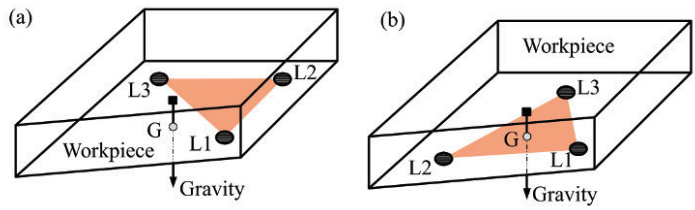

Figure 4.13. *Locating scheme with 3 locators: a) gravity center outside the crosshatched region; b) gravity center inside the crosshatched region*

4.3.1.1. *Workpiece static equilibrium constraints*

Suppose that a workpiece-fixture system consists of a workpiece, m locators and n clamps. Denote $\mathbf{W}_e = [W_{e1}, W_{e2}, W_{e3}, W_{e4}, W_{e5}, W_{e6}]^{\mathrm{T}} \in \mathbb{R}^{6\times 1}$ the external wrench including only cutting force $\mathbf{W}_m$ and the workpiece weight $\mathbf{W}_g$; $\mathbf{n}_k \in \mathbb{R}^{3\times 1}$, $\mathbf{t}1_k \in \mathbb{R}^{3\times 1}$ and $\mathbf{t}2_k \in \mathbb{R}^{3\times 1}$ the unit inner normal vector and two orthogonal unit tangential vectors of the workpiece at contact point $\mathbf{r}_k \in \mathbb{R}^{3\times 1}$ of the kth fixture element, respectively. Contacts between the workpiece and fixture elements are considered as frictional contacts.

As shown in Figure 4.14, for the kth fixture element, $\mathbf{f}_k(t) = \mathbf{f}_{\mathbf{n}k} + \mathbf{f}_{\mathbf{t}1k} + \mathbf{f}_{\mathbf{t}2k} \in \mathbb{R}^{3\times 1}$ denotes the kth contact force resultant expressed in the global coordinate system {GCS} with $\mathbf{f}_{\mathbf{n}k}$, $\mathbf{f}_{\mathbf{t}1k}$ and $\mathbf{f}_{\mathbf{t}2k}$

being the three components of $\mathbf{f}_k$ along $\mathbf{n}_k = [n_{kx}, n_{ky}, n_{kz}]^{\mathrm{T}}$, $\mathbf{t}1_k = [t1_{kx}, t1_{ky}, t1_{kz}]^{\mathrm{T}}$ and $\mathbf{t}2_k = [t2_{kx}, t2_{ky}, t2_{kz}]^{\mathrm{T}}$, respectively. Hence,

$$\begin{cases} \mathbf{f}_{\mathbf{n}k} = f^{\mathrm{c}}_{\mathbf{n}k}\mathbf{n}_k \\ \mathbf{f}_{\mathbf{t}1k} = f^{\mathrm{c}}_{\mathbf{t}1k}\mathbf{t}1_k \\ \mathbf{f}_{\mathbf{t}2k} = f^{\mathrm{c}}_{\mathbf{t}2k}\mathbf{t}2_k \end{cases}, 1 \le k \le m+n \qquad [4.45]$$

where $\mathbf{f}^{\mathrm{c}}_k = [f^{\mathrm{c}}_{\mathbf{n}k}, f^{\mathrm{c}}_{\mathbf{t}1k}, f^{\mathrm{c}}_{\mathbf{t}2k}]^{\mathrm{T}}$ is the kth contact force vector in the local contact coordinate system $\{\mathrm{CCS}\}_k$.

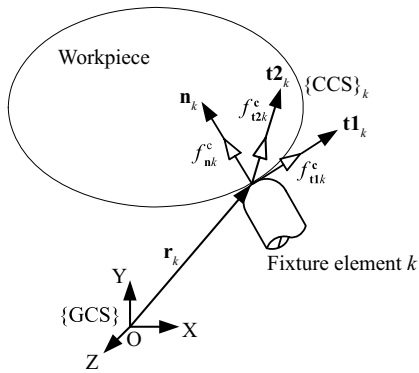

Figure 4.14. *Fixturing scheme of the workpiece*

When the machining forces and moments vary with respect to time, the reaction forces and frictions at all fixture elements will correspondingly change with respect to the machining time. Nevertheless, the workpiece-fixture system must be in static equilibrium for a stable fixture configuration to be realized over the machining time. At any instant, the equilibrium equation system of the workpiece-fixture system is obtained as

$$\sum_k \begin{bmatrix} \mathbf{f}^{\mathrm{c}}_k(t) \\ \mathbf{r}_k(t) \times \mathbf{f}^{\mathrm{c}}_k(t) \end{bmatrix} + \mathbf{W}_e(t) = 0 \qquad [4.46]$$

with t being the instantaneous machining time.

The substitution of equation [4.45] into equation [4.46] results in

$$\sum_k \mathbf{G}_k \mathbf{f}_k^c + \mathbf{W}_e(t) = 0 \qquad [4.47]$$

where

$$\mathbf{G}_k = [\mathbf{G}_{\mathbf{n}k}, \mathbf{G}_{\mathbf{t}1k}, \mathbf{G}_{\mathbf{t}2k}] = \begin{bmatrix} \mathbf{n}_k & \mathbf{t}1_k & \mathbf{t}2_k \\ \mathbf{r}_k \times \mathbf{n}_k & \mathbf{r}_k \times \mathbf{t}1_k & \mathbf{r}_k \times \mathbf{t}2_k \end{bmatrix} \in \mathbb{R}^{6\times 3} \qquad [4.48]$$

is a layout matrix of the kth fixture element.

4.3.1.2. *Modeling of the clamping sequence*

The workpiece stability is related directly to the clamping sequence. In general, a workpiece may require multiple clamping steps to keep the workholding before machining. All these clamping steps will form a clamping sequence in accordance with loading histories of gravity, clamping and machining forces. Figure 4.15 illustrates the fixturing scheme of a workpiece with multiple clamps that can be decomposed into a sequence of steps. As shown in Figure 4.16, each step has its own contact points and external forces.

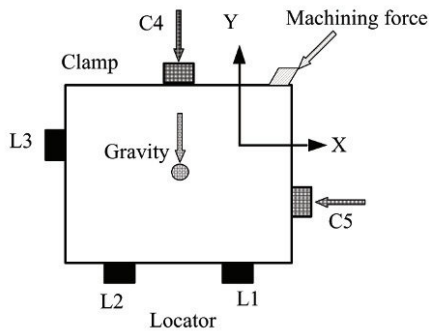

Figure 4.15. *Fixturing scheme with multiple clamps*

Before studying, it is important to outline the basic difference between a locator and a clamp. A locator only acts as a passive element to support clamping and external forces. At the contact point with the workpiece, both

the normal pressure and tangential friction force exist. A clamp is, however, an active element that cannot generate frictional forces by itself. The frictional force related to the current clamp may produce only when a new clamp is then applied in the next step.

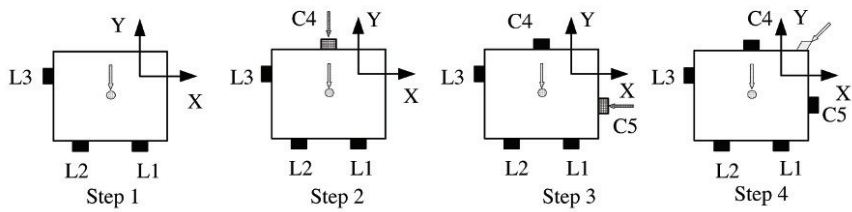

Figure 4.16. *Clamping sequence*

Now consider the problem illustrated in Figure 4.16. In step 1, suppose the workpiece is mounted with $m = 3$ locators. The gravity force serves as the external loading, i.e.$\mathbf{W}_e = \mathbf{W}_g$ that will be balanced by the normal and frictional forces related to locators. Then, the static equilibrium equation of the workpiece is given as

$$\mathbf{G}_{\text{lc0}}\mathbf{f}^{\text{c}}_{\text{lc0}} = -\mathbf{W}_g \qquad [4.49]$$

with

$$\mathbf{G}_{\text{lc0}} = [\mathbf{G}_1, \mathbf{G}_2, \cdots, \mathbf{G}_m] \in \mathbb{R}^{6\times 3\,m} \qquad [4.50]$$

$$\begin{aligned}\mathbf{f}^{\text{c}}_{\text{lc0}} &= [(\mathbf{f}^{\text{c}}_1)^{\text{T}}, \cdots, (\mathbf{f}^{\text{c}}_m)^{\text{T}}]^{\text{T}} \\ &= [f^{\text{c}}_{\mathbf{n}1}, f^{\text{c}}_{\mathbf{t}11}, f^{\text{c}}_{\mathbf{t}21}, \cdots, f^{\text{c}}_{\mathbf{n}m}, f^{\text{c}}_{\mathbf{t}1m}, f^{\text{c}}_{\mathbf{t}2m}]^{\text{T}} \\ &\in \mathbb{R}^{3m\times 1}\end{aligned} \qquad [4.51]$$

In step 2, clamp C4 is applied. The set of external forces is enlarged with the addition of a normal clamping force $f^{\text{c}}_{\mathbf{n}(m+1)}$ related to C4. So, the static equilibrium equation of the workpiece becomes

$$\mathbf{G}_{\text{lc1}}\mathbf{f}^{\text{c}}_{\text{lc1}} = -\mathbf{W}_g \qquad [4.52]$$

with

$$\mathbf{G}_{\mathrm{lc}1} = [\mathbf{G}_1, \mathbf{G}_2, \cdots, \mathbf{G}_m, |\mathbf{G}_{(m+1)}] \in \mathbb{R}^{6\times 3\ (m+1)} \tag{4.53}$$

$$\begin{aligned}\mathbf{f}^{\mathrm{c}}_{\mathrm{lc}1} &= [(\mathbf{f}^{\mathrm{c}}_1)^{\mathrm{T}}, \cdots, (\mathbf{f}^{\mathrm{c}}_m)^{\mathrm{T}}, |(\mathbf{f}^{\mathrm{c}}_{(m+1)})^{\mathrm{T}}]^{\mathrm{T}} \\ &= [f^{\mathrm{c}}_{\mathbf{n}1}, f^{\mathrm{c}}_{\mathbf{t}11}, f^{\mathrm{c}}_{\mathbf{t}21}, \cdots, |f^{\mathrm{c}}_{\mathbf{n}(m+1)}, 0, 0]^{\mathrm{T}} \\ &\in \mathbb{R}^{3(m+1)\times 1}\end{aligned} \tag{4.54}$$

In step 3, clamp C4 that was an active element becomes now a passive locator element with the generation of tangential forces at the contact point of C4. In addition, a normal clamping force $f^{\mathrm{c}}_{\mathbf{n}(m+2)}$ associated with clamp C5 will be exerted so that the static equilibrium equation of the workpiece becomes

$$\mathbf{G}_{\mathrm{lc}2}\mathbf{f}^{\mathrm{c}}_{\mathrm{lc}2} = -\mathbf{W}_g \tag{4.55}$$

with

$$\mathbf{G}_{\mathrm{lc}1} = [\mathbf{G}_1, \mathbf{G}_2, \cdots, \mathbf{G}_m, \mathbf{G}_{(m+1)}, |\mathbf{G}_{(m+2)}] \in \mathbb{R}^{6\times 3(m+2)} \tag{4.56}$$

$$\begin{aligned}\mathbf{f}^{\mathrm{c}}_{\mathrm{lc}2} &= [(\mathbf{f}^{\mathrm{c}}_1)^{\mathrm{T}}, \cdots, (\mathbf{f}^{\mathrm{c}}_{m+1})^{\mathrm{T}}, |(\mathbf{f}^{\mathrm{c}}_{m+2})^{\mathrm{T}}]^{\mathrm{T}} \\ &= [f^{\mathrm{c}}_{\mathbf{n}1}, f^{\mathrm{c}}_{\mathbf{t}11}, f^{\mathrm{c}}_{\mathbf{t}21}, \cdots, f^{\mathrm{c}}_{\mathbf{n}(m+2)}, 0, 0]^{\mathrm{T}} \\ &\in \mathbb{R}^{3(m+2)\times 1}\end{aligned} \tag{4.57}$$

By analogy, the static equilibrium equation in step *j* is generally stated as

$$\mathbf{G}_{\mathrm{lc}j}\mathbf{f}^{\mathrm{c}}_{\mathrm{lc}j} = -\mathbf{W}_e \tag{4.58}$$

with

$$\mathbf{W}_e = \begin{cases} \mathbf{W}_g, & 0 \le j \le n \\ \mathbf{W}_g + \mathbf{W}_m, & j = n+1 \end{cases} \tag{4.59}$$

$$\mathbf{G}_{\mathrm{lc}j} = [\mathbf{G}_1, \mathbf{G}_2, \cdots, \mathbf{G}_m, \mathbf{G}_{(m+1)}, \cdots, |\mathbf{G}_{(m+j)}] \in \mathbb{R}^{6\times 3\ (m+j)} \quad [4.60]$$

$$\begin{aligned}\mathbf{f}^{\mathrm{c}}_{\mathrm{lc}j} &= [(\mathbf{f}^{\mathrm{c}}_1)^{\mathrm{T}}, \cdots, (\mathbf{f}^{\mathrm{c}}_m)^{\mathrm{T}}, (\mathbf{f}^{\mathrm{c}}_{(m+1)})^{\mathrm{T}}, \cdots, |(\mathbf{f}^{\mathrm{c}}_{(m+j)})^{\mathrm{T}}]^{\mathrm{T}} \\ &= [f^{\mathrm{c}}_{\mathbf{n}1}, f^{\mathrm{c}}_{\mathbf{t}11}, f^{\mathrm{c}}_{\mathbf{t}21}, \cdots, |f^{\mathrm{c}}_{\mathbf{n}(m+j)}, 0, 0]^{\mathrm{T}} \\ &\in \mathbb{R}^{3(m+j)\times 1}\end{aligned} \quad [4.61]$$

4.3.1.3. *Friction cone constraints*

To prevent the workpiece detachment from the fixture elements in the fixturing process, the normal forces at any contact point between the workpiece and fixture element must be in compression such that

$$f^{\mathrm{c}}_{\mathbf{n}k} \geq 0 \quad [4.62]$$

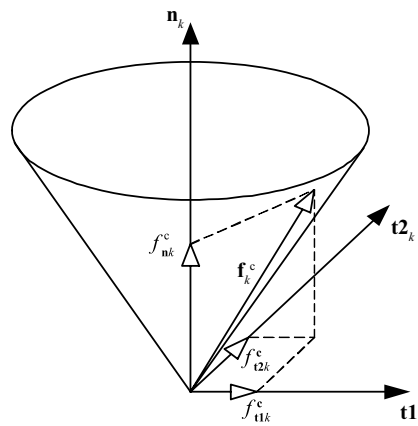

Figure 4.17. *Friction cone*

Furthermore, the resultant of normal and frictional forces at any contact point must also lie within the friction cone to prevent the workpiece from slipping. In view of Coulomb's friction law shown in Figure 4.17, it follows

$$(f^{\mathrm{c}}_{\mathbf{t}1k})^2 + (f^{\mathrm{c}}_{\mathbf{t}2k})^2 \leq (\mu_k f^{\mathrm{c}}_{\mathbf{n}k})^2 \quad [4.63]$$

where μ_k is the friction coefficient between the workpiece and the kth fixture element.

4.3.1.4. *Modeling of workpiece stability*

In the fixture design, stability analysis is actually concerned with the evaluation of the workpiece static equilibrium and friction constraints under given fixturing conditions and machining forces [WAN 01]. Thus, in clamping sequence $j+1$, the necessary and sufficient conditions for a workpiece to be stable are obtained as

$$\begin{aligned} & \mathbf{G}_{\mathrm{lc}j}\,\mathbf{f}^{\mathrm{c}}_{\mathrm{lc}j} = -\mathbf{W}_g \\ \text{s.t.} \quad & \\ & f^{\mathrm{c}}_{\mathbf{n}k} \geq 0 \\ & (f^{\mathrm{c}}_{\mathbf{t}1k})^2 + (f^{\mathrm{c}}_{\mathbf{t}2k})^2 \leq (\mu_k f^{\mathrm{c}}_{\mathbf{n}k})^2 \end{aligned} \qquad [4.64]$$

where $1 \leq k \leq m+j$.

In the particular case of neglecting friction forces, the workpiece stability model can be simplified as

$$\begin{aligned} & \mathbf{G}_{\mathrm{lc}j}\,\mathbf{f}^{\mathrm{c}}_{\mathrm{lc}j} = -\mathbf{W}_g \\ \text{s.t.} \quad & \\ & f^{\mathrm{c}}_{\mathbf{n}k} \geq 0 \end{aligned} \qquad [4.65]$$

If equations [4.64] or [4.65] are satisfied, the workpiece is said to be stable. In other words, this implies that at least a solution to equations [4.64] or [4.65] exists. From the mechanistic viewpoint, the workpiece stability can be classified as locating, clamping and machining stability in detail. Such a classification is as follows:

– if equation [4.64] has solutions for $j = 0$, the workpiece is of locating stability;

– if equation [4.64] has solutions for $1 \leq j \leq n$, the workpiece is of clamping stability;

– if equation [4.64] has solutions for $j = n+1$ and $\mathbf{W}_e = \mathbf{W}_g + \mathbf{W}_m$, the workpiece is of machining stability.

To do this, almost all existing methods were focused on predicting directly contact forces satisfying equations [4.64]or [4.65]. Whether the solution is feasible or not, a complete computing procedure has to be carried out. To circumvent this inconvenience, we propose below an indirect approach that transforms the original problem into an equivalent linear programming one.

4.3.2. *Solution techniques to the model of workpiece stability*

4.3.2.1. *Linear programming techniques*

In the study of form closure grasps, linear programming techniques were used by Asada and Kitagawa [ASA 89] to solve kinematic equations. These techniques are extended here to analyze force closure and force feasibility. Firstly, consider below a set of linear equations with $r \geq s$ and $b_k \geq 0$ $(1 \leq k \leq s)$.

$$\begin{cases} a_{11}x_1 + a_{12}x_2 + \cdots a_{1r}x_r = b_1 \\ a_{21}x_1 + a_{22}x_2 + \cdots a_{2r}x_r = b_2 \\ \qquad \cdots\cdots \\ a_{s1}x_1 + a_{s2}x_2 + \cdots a_{sr}x_r = b_s \end{cases} \qquad [4.66]$$

s.t.

$$x_1, x_2, \cdots, x_r \geq 0 \qquad [4.67]$$

Mathematically, the solution existence of equations [4.66] and [4.67] can be examined equivalently by solving the following linear programming problem;

$$\max \quad w = c_1x_1 + c_2x_2 + \cdots + c_rx_r \qquad [4.68]$$

$$\begin{cases} a_{11}x_1 + a_{12}x_2 + \cdots a_{1r}x_r \leq b_1 \\ a_{21}x_1 + a_{22}x_2 + \cdots a_{2r}x_r \leq b_2 \\ \quad \cdots\cdots \\ a_{s1}x_1 + a_{s2}x_2 + \cdots a_{sr}x_r \leq b_s \\ x_1, x_2, \cdots, x_r \geq 0 \end{cases} \quad [4.69]$$

where,

$$c_j = \sum_{k=1}^{s} a_{kj} \quad [4.70]$$

It is important to note that equalities in equation [4.66] are all relaxed into inequalities in equation [4.69]. Theoretically, it proves that a solution satisfying equations [4.66] and [4.67] exists if and only if

$$\max(w) = \sum_{k=1}^{s} b_k \quad [4.71]$$

4.3.2.2. *Workpiece stability without friction*

With the above idea in mind, the verification of the workpiece stability without friction is equivalent to the investigation of the solution existence of equation [4.65].

Based on equation [4.48], [4.65] is thus developed as

$$\begin{cases} n_{1x}f^{\mathrm{c}}_{\mathbf{n}1} + n_{2x}f^{\mathrm{c}}_{\mathbf{n}2} + \cdots + n_{(m+j)_x}f^{\mathrm{c}}_{\mathbf{n}(m+j)} = -W_{e1} \\ n_{1y}f^{\mathrm{c}}_{\mathbf{n}1} + n_{2y}f^{\mathrm{c}}_{\mathbf{n}2} + \cdots + n_{(m+j)_y}f^{\mathrm{c}}_{\mathbf{n}(m+j)} = -W_{e2} \\ n_{1z}f^{\mathrm{c}}_{\mathbf{n}1} + n_{2z}f^{\mathrm{c}}_{\mathbf{n}2} + \cdots + n_{(m+j)_z}f^{\mathrm{c}}_{\mathbf{n}(m+j)} = -W_{e3} \\ (n_{1z}y_1 - n_{1y}z_1)f^{\mathrm{c}}_{\mathbf{n}1} + \cdots + (n_{(m+j)_z}y_{(m+j)} \\ \qquad -n_{(m+j)_y}z_{(m+j)})f^{\mathrm{c}}_{\mathbf{n}(m+j)} = -W_{e4} \\ (n_{1x}z_1 - n_{1z}x_1)f^{\mathrm{c}}_{\mathbf{n}1} + \cdots + (n_{(m+j)x}z_{(m+j)} \\ \qquad -n_{(m+j)z}x_{(m+j)})f^{\mathrm{c}}_{\mathbf{n}(m+j)} = -W_{e5} \\ (n_{1y}x_1 - n_{1x}y_1)f^{\mathrm{c}}_{\mathbf{n}1} + \cdots + (n_{(m+j)y}x_{(m+j)} \\ \qquad -n_{(m+j)x}y_{(m+j)})f^{\mathrm{c}}_{\mathbf{n}(m+j)} = -W_{e6} \end{cases} \quad [4.72]$$

s.t.

$$f^{\mathrm{c}}_{\mathbf{n}k} \geq 0, 1 \leq k \leq m+j \tag{4.73}$$

with $-W_{ek} \geq 0$ $(1 \leq k \leq 6)$. Denote now a sign function of $-W_{ek}$

$$\mathrm{sign}(-W_{ek}) = \begin{cases} 1, & -W_{ek} \geq 0 \\ -1, & -W_{ek} < 0 \end{cases} \tag{4.74}$$

If two members of equation [4.72] are multiplied simultaneously by $\mathrm{sign}(-W_{ek})$, then equations [4.72] and [4.73] can be transformed as

$$\begin{cases} \mathrm{sign}(-W_{e1})(n_{1x}f^{\mathrm{c}}_{\mathbf{n}1} + n_{2x}f^{\mathrm{c}}_{\mathbf{n}2} + \cdots + n_{(m+j)_x}f^{\mathrm{c}}_{\mathbf{n}(m+j)}) \\ \qquad = (-W_{e1})\mathrm{sign}(-W_{e1}) \\ \mathrm{sign}(-W_{e2})(n_{1y}f^{\mathrm{c}}_{\mathbf{n}1} + n_{2y}f^{\mathrm{c}}_{\mathbf{n}2} + \cdots + n_{(m+j)_y}f^{\mathrm{c}}_{\mathbf{n}(m+j)}) \\ \qquad = (-W_{e2})\mathrm{sign}(-W_{e2}) \\ \mathrm{sign}(-W_{e3})(n_{1z}f^{\mathrm{c}}_{\mathbf{n}1} + n_{2z}f^{\mathrm{c}}_{\mathbf{n}2} + \cdots + n_{(m+j)_z}f^{\mathrm{c}}_{\mathbf{n}(m+j)}) \\ \qquad = (-W_{e3})\mathrm{sign}(-W_{e3}) \\ \mathrm{sign}(-W_{e4})((n_{1z}y_1 - n_{1y}z_1)f^{\mathrm{c}}_{\mathbf{n}1} + \cdots + (n_{(m+j)_z}y_{(m+j)} - \\ \qquad n_{(m+j)_y}z_{(m+j)})f^{\mathrm{c}}_{\mathbf{n}(m+j)}) = (-W_{e4})\mathrm{sign}(-W_{e4}) \\ \mathrm{sign}(-W_{e5})((n_{1x}z_1 - n_{1z}x_1)f^{\mathrm{c}}_{\mathbf{n}1} + \cdots + (n_{(m+j)x}z_{(m+j)} - \\ \qquad n_{(m+j)z}x_{(m+j)})f^{\mathrm{c}}_{\mathbf{n}(m+j)}) = (-W_{e5})\mathrm{sign}(-W_{e5}) \\ \mathrm{sign}(-W_{e6})((n_{1y}x_1 - n_{1x}y_1)f^{\mathrm{c}}_{\mathbf{n}1} + \cdots + (n_{(m+j)y}x_{(m+j)} - \\ \qquad n_{(m+j)x}y_{(m+j)})f^{\mathrm{c}}_{\mathbf{n}(m+j)}) = (-W_{e6})\mathrm{sign}(-W_{e6}) \end{cases} \tag{4.75}$$

$$f^{\mathrm{c}}_{\mathbf{n}k} \geq 0, 1 \leq k \leq m+j \tag{4.76}$$

Now, a comparison between equations [4.75] and [4.76] and equations [4.66] and [4.67] shows that both systems have the same form. Therefore, the following linear programming can be solved:

$$\max \quad w = c_1 f^{\mathrm{c}}_{\mathbf{n}1} + c_2 f^{\mathrm{c}}_{\mathbf{n}2} + \cdots + c_{(m+j)} f^{\mathrm{c}}_{\mathbf{n}(m+j)} \tag{4.77}$$

$$\begin{cases} \text{sign}(-W_{e1})(n_{1x}f^{\text{c}}_{\mathbf{n}1} + n_{2x}f^{\text{c}}_{\mathbf{n}2} + \cdots + n_{(m+j)_x}f^{\text{c}}_{\mathbf{n}(m+j)}) \\ \qquad\qquad \leq (-W_{e1})\text{sign}(-W_{e1}) \\ \text{sign}(-W_{e2})(n_{1y}f^{\text{c}}_{\mathbf{n}1} + n_{2y}f^{\text{c}}_{\mathbf{n}2} + \cdots + n_{(m+j)_y}f^{\text{c}}_{\mathbf{n}(m+j)}) \\ \qquad\qquad \leq (-W_{e2})\text{sign}(-W_{e2}) \\ \text{sign}(-W_{e3})(n_{1z}f^{\text{c}}_{\mathbf{n}1} + n_{2z}f^{\text{c}}_{\mathbf{n}2} + \cdots + n_{(m+j)_z}f^{\text{c}}_{\mathbf{n}(m+j)}) \\ \qquad\qquad \leq (-W_{e3})\text{sign}(-W_{e3}) \\ \text{sign}(-W_{e4})((n_{1z}y_1 - n_{1y}z_1)f^{\text{c}}_{\mathbf{n}1} + \cdots + (n_{(m+j)_z}y_{(m+j)} - \\ \qquad\qquad n_{(m+j)_y}z_{(m+j)})f^{\text{c}}_{\mathbf{n}(m+j)}) \leq (-W_{e4})\text{sign}(-W_{e4}) \\ \text{sign}(-W_{e5})((n_{1x}z_1 - n_{1z}x_1)f^{\text{c}}_{\mathbf{n}1} + \cdots + (n_{(m+j)x}z_{(m+j)} - \\ \qquad\qquad n_{(m+j)z}x_{(m+j)})f^{\text{c}}_{\mathbf{n}(m+j)}) \leq (-W_{e5})\text{sign}(-W_{e5}) \\ \text{sign}(-W_{e6})((n_{1y}x_1 - n_{1x}y_1)f^{\text{c}}_{\mathbf{n}1} + \cdots + (n_{(m+j)y}x_{(m+j)} - \\ \qquad\qquad n_{(m+j)x}y_{(m+j)})f^{\text{c}}_{\mathbf{n}(m+j)}) \leq (-W_{e6})\text{sign}(-W_{e6}) \\ f^{\text{c}}_{\mathbf{n}1}, f^{\text{c}}_{\mathbf{n}2}, \cdots, f^{\text{c}}_{\mathbf{n}(m+j)} \geq 0 \end{cases} \quad [4.78]$$

where,

$$\begin{aligned} c_k &= \text{sign}(-W_{e1})n_{kx} + \text{sign}(-W_{e2})n_{ky} + \text{sign}(-W_{e3})n_{kz} \\ &+ \text{sign}(-W_{e4})(n_{kz}y_{ck} - n_{ky}z_{ck}) + \text{sign}(-W_{e5})(n_{kx}z_{ck} - n_{kz}x_{ck}) \\ &+ \text{sign}(-W_{e6})(n_{ky}x_{ck} - n_{kx}y_{ck}), 1 \leq k \leq m+j \end{aligned} \quad [4.79]$$

It now turns out that the workpiece is of stability provided that the following criterion holds

$$\max(w) = \sum_{k=1}^{6}(-W_{ek})\text{sign}(-W_{ek}) \quad [4.80]$$

Alternatively, if the clamping force is specified in advance with $f^{\text{c}}_{\mathbf{n}(m+j)} = \iota_j$, the above system can be applied to check its feasibility. If the workpiece holds the stability for any ι_j varying in the interval $[0, +\infty)$, the workpiece is said to be in strong stability. Otherwise, the workpiece is in weak stability if ι_j is limited in a finite interval.

4.3.2.3. *Workpiece stability with friction*

As equation [4.63] is quadratic in terms of contact forces, and both $f^{c}_{\mathbf{t}1k}$ and $f^{c}_{\mathbf{t}2k}$ may take positive or negative values, equation [4.64] cannot be solved directly by using equations [4.68] and [4.69]. To circumvent this difficulty, equation [4.62] will be approximately linearized and tangential forces will be substituted with non-negative variables.

Linear approximation of friction cone [DEM 94]

As shown in Figure 4.18(a), the friction cone is approximated by a polyhedron whose approximation accuracy can be improved with the increase of the plane number. Figure 4.18(b) is a projection of $4N_{\mathrm{pk}}$ (N_{pk} is a natural number) sided polyhedral cone in plane $f^{c}_{\mathbf{t}1k} - f^{c}_{\mathbf{t}2k}$, with α_s being an inclination angle of the line perpendicular to side s. Thus,

$$\alpha_s = \frac{\pi}{4} + \frac{\pi}{2k}(s-1), 1 \le s \le 4N_{\mathrm{pk}},\ 0 \le \alpha_s \le 2\pi \qquad [4.81]$$

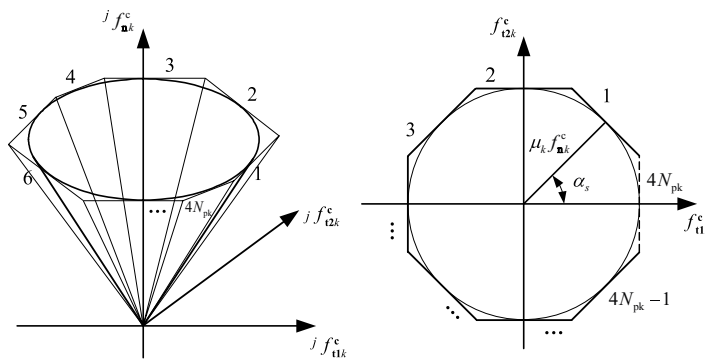

Figure 4.18. *Linearized friction cone: a) tangent polyhedral cone; b) projection in plane* $f^{c}_{\mathbf{t}1k} - f^{c}_{\mathbf{t}2k}$

So, any plane of a $4N_{\mathrm{pk}}$-sided polygon can be described by the equation

$$\mu_k f^{c}_{\mathbf{n}k} + f^{c}_{\mathbf{t}1k}\cos\alpha_s - f^{c}_{\mathbf{t}2k}\sin\alpha_s = 0 \qquad [4.82]$$

Consequently, the friction cone constraint is approximated as:

$$\mu_k f^{c}_{\mathbf{n}k} + f^{c}_{\mathbf{t}1k}\cos\alpha_s - f^{c}_{\mathbf{t}2k}\sin\alpha_s \ge 0, 1 \le s \le 4N_{\mathrm{pk}},\ 1 \le k \le m+j \qquad [4.83]$$

or,

$$\mathbf{C}_{4N_{\mathrm{pk}}k}\mathbf{f}^{\mathrm{c}}_{\mathrm{lc}\,k} \geq 0, 1 \leq k \leq m+j \qquad [4.84]$$

with the polyhedron matrix being,

$$\mathbf{C}_{4N_{\mathrm{pk}}k} = \begin{bmatrix} \mu_k & \cos\alpha_1 & -\sin\alpha_1 \\ \mu_k & \cos\alpha_2 & -\sin\alpha_2 \\ \cdots & \cdots & \cdots \\ \mu_k & \cos\alpha_{4N_{\mathrm{pk}}} & -\sin\alpha_{4N_{\mathrm{pk}}} \end{bmatrix} \in \mathbb{R}^{4N_{\mathrm{pk}}\times 3} \qquad [4.85]$$

Non-negative variable transformation

As done conventionally in linear programming, tangential force components of $f^{\mathrm{c}}_{\mathbf{t}1k}$ and $f^{\mathrm{c}}_{\mathbf{t}2k}$ will be represented as a difference between two non-negative variables with

$$\begin{cases} f^{\mathrm{c}}_{\mathbf{t}1k} = u1_k - v1_k \\ f^{\mathrm{c}}_{\mathbf{t}2k} = u2_k - v2_k \end{cases} \qquad [4.86]$$

where $1 \leq k \leq m+j$; $u1_k, v1_k, u2_k, v2_k \geq 0$

Verification of workpiece stability with friction

Based on the above approximation and transformation, equation [4.64] may be converted into the following standard form

$$\begin{aligned} &\mathbf{G'}_{\mathrm{lc}j}\,\mathbf{f'}^{\mathrm{c}}_{\mathrm{lc}j} = -\mathbf{W}_e \\ &\text{s.t.} \\ &\mathbf{f'}^{\mathrm{c}}_{\mathrm{lc}j} \geq 0 \\ &\mathbf{C'}_{4N_{\mathrm{pk}}}\mathbf{f'}^{\mathrm{c}}_{\mathrm{lc}j} \geq 0 \end{aligned} \qquad [4.87]$$

where

$$\mathbf{G'}_{\mathrm{lc}j} = \begin{bmatrix} \mathbf{n}_1 & \mathbf{t}1_1 & -\mathbf{t}1_1 & \mathbf{t}2_1 & -\mathbf{t}2_1 & \cdots & \mathbf{n}_{m+j} \\ \mathbf{r}_1 \times \mathbf{n}_1 & \mathbf{r}_1 \times \mathbf{t}1_1 & -\mathbf{r}_1 \times \mathbf{t}1_1 & \mathbf{r}_1 \times \mathbf{t}2_1 & -\mathbf{r}_1 \times \mathbf{t}2_1 & \cdots & \mathbf{r}_{m+j} \times \mathbf{n}_{m+j} \end{bmatrix}$$
$$\begin{bmatrix} \mathbf{t}1_{m+j} & -\mathbf{t}1_{m+j} & \mathbf{t}2_{m+j} & -\mathbf{t}2_{m+j} \\ \mathbf{r}_{m+j} \times \mathbf{t}1_{m+j} & -\mathbf{r}_{m+j} \times \mathbf{t}1_{m+j} & \mathbf{r}_{m+j} \times \mathbf{t}2_{m+j} & -\mathbf{r}_{m+j} \times \mathbf{t}2_{m+j} \end{bmatrix}$$
$$\in \mathbb{R}^{6\times 5(m+j)} \qquad [4.88]$$

$$\mathbf{f'}^{\mathrm{c}}_{\mathrm{lc}j} = [f^{\mathrm{c}}_{\mathbf{n}1}, u1_1, v1_1, u2_1, v2_1, \cdots, f^{\mathrm{c}}_{\mathbf{n}(m+j)}, u1_{(m+j)}, v1_{(m+j)}, u2_{(m+j)}, v2_{(m+j)}]^{\mathrm{T}} \in \mathbb{R}^{5(m+j)\times 1} \qquad [4.89]$$

$$\mathbf{C'}_{4N_{\mathrm{pk}}} = \begin{bmatrix} \mathbf{C'}_{4N_{\mathrm{pk}}1} & & & \\ & \mathbf{C'}_{4N_{\mathrm{pk}}2} & & \\ & & \ddots & \\ & & & \mathbf{C'}_{4N_{\mathrm{pk}}(m+j)} \end{bmatrix} \qquad [4.90]$$
$$\in \mathbb{R}^{4N_{\mathrm{pk}}(m+j)\times 5(m+j)}$$

$$\mathbf{C'}_{4N_{\mathrm{pk}}p} = \begin{bmatrix} \mu_k & \cos\alpha_1 & -\cos\alpha_1 & -\sin\alpha_1 & \sin\alpha_1 \\ \mu_k & \cos\alpha_2 & -\cos\alpha_2 & -\sin\alpha_2 & \sin\alpha_2 \\ \cdots & \cdots & \cdots & \cdots & \cdots \\ \mu_k & \cos\alpha_{4N_{\mathrm{pk}}} & -\cos\alpha_{4N_{\mathrm{pk}}} & -\sin\alpha_{4N_{\mathrm{pk}}} & \sin\alpha_{4N_{\mathrm{pk}}} \end{bmatrix} \qquad [4.91]$$
$$\in \mathbb{R}^{4N_{\mathrm{pk}}\times 5}$$

Therefore, the workpiece stability with friction can be verified by solving the following linear programming problem with the same criterion.

$$\begin{aligned} \max \quad & w = c_1 f^{\mathrm{c}}_{\mathbf{n}1} + c_2 u1_1 + c_3 v1_1 + c_4 u2_1 + c_5 v2_1 + \cdots \\ & + c_{[5(m+j)-4]} f^{\mathrm{c}}_{\mathbf{n}(m+j)} + c_{[5(m+j)-3]} u1_{(m+j)} + \\ & c_{[5(m+j)-2]} v1_{(m+j)} + c_{[5(m+j)-1]} u2_{(m+j)} + c_{5(m+j)} v2_{(m+j)} \end{aligned} \qquad [4.92]$$

s.t.

$$\begin{aligned}&\mathrm{diag}(\mathrm{sign}(-\mathbf{W}_e))\mathbf{G'}_{\mathrm{lc}j}\mathbf{f'}^{\mathrm{c}}_{\mathrm{lc}j} \le \mathrm{diag}(\mathrm{sign}(-\mathbf{W}_e))(-\mathbf{W}_e)\\ &\mathbf{f'}^{\mathrm{c}}_{\mathrm{lc}j} \ge 0\\ &C'_{4N_{\mathrm{pk}}}\mathbf{f'}^{\mathrm{c}}_{\mathrm{lc}j} \ge 0\end{aligned} \quad [4.93]$$

$$\begin{aligned}c_{(5k-4)} &= \mathrm{sign}(-W_{e1})n_{kx} + \mathrm{sign}(-W_{e2})n_{ky} + \mathrm{sign}(-W_{e3})n_{kz} +\\ &\quad \mathrm{sign}(-W_{e4})(n_{kz}y_k - n_{ky}z_k) + \mathrm{sign}(-W_{e5})(n_{kx}z_k - n_{kz}x_k)\\ &\quad +\mathrm{sign}(-W_{e6})(n_{ky}x_k - n_{kx}y_k)\\ c_{(5k-3)} &= \mathrm{sign}(-W_{e1})t1_{kx} + \mathrm{sign}(-W_{e2})t1_{ky} + \mathrm{sign}(-W_{e3})t1_{kz}\\ &\quad +\mathrm{sign}(-W_{e4})(t1_{kz}y_k - t1_{ky}z_k) + \mathrm{sign}(-W_{e5})(t1_{kx}z_k - t1_{kz}x_k)\\ &\quad +\mathrm{sign}(-W_{e6})(t1_{ky}x_k - t1_{kx}y_k)\\ c_{(5k-2)} &= -c_{(5k-3)}\\ c_{(5k-1)} &= \mathrm{sign}(-W_{e1})t2_{kx} + \mathrm{sign}(-W_{e2})t2_{ky}\\ &\quad +\mathrm{sign}(-W_{e3})t2_{kz} + \mathrm{sign}(-W_{e4})(t2_{kz}y_k - t2_{ky}z_k)\\ &\quad +\mathrm{sign}(-W_{e5})(t2_{kx}z_k - t2_{kz}x_k) + \mathrm{sign}(-W_{e6})(t2_{ky}x_k - t2_{kx}y_k)\\ c_{5k} &= -c_{(5k-1)}\\ &\quad 1 \le k \le m + j\end{aligned} \quad [4.94]$$

4.4. Modeling of the workpiece-fixture geometric default and compliance

4.4.1. *Source error analysis*

4.4.1.1. *Source errors due to workpiece-fixture geometric default*

A workpiece-fixture system is illustrated in Figure 4.19. The workholding aims to guarantee the finished workpiece feature during the machining operation. For example, dimension h shown in Figure 4.19 is the machining requirement of the current machining step with respect to the processing datum plane AA′ (the upper plane of the workpiece). Note that $\{\mathrm{CCS}\}_k$ denotes the contact coordinate system consisting of the normal unit vector $\mathbf{n}_k$ and two orthogonal tangential unit vectors $\boldsymbol{\tau}_k$ and $\boldsymbol{\eta}_k$ at the kth contact point, respectively.

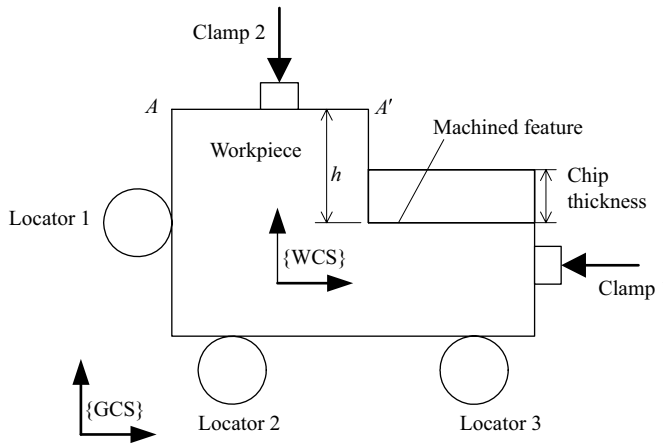

Figure 4.19. *Illustration of the workpiece-fixture system*

As shown in Figure 4.20(a), source errors relative to geometric defaults correspond to the setup errors and manufacturing errors of locators and the workpiece. These errors will finally cause the translation and rotation of the workpiece, i.e. the so-called workpiece position error (WPE). δh will be the workpiece machining error (WME) whose value varies along the machined feature. Moreover, the inconsistent datum error (IDE) is another kind of source error. As shown in Figure 4.20(c), if the processing datum plane for machined feature h is not identical with the locating datum plane (the lower plane) and if the manufacturing default of the processing datum plane, being equal to $H_{\max} - H_{\min}$, exists with respect to the locating datum plane, the IDE will occur for dimension h and equals also $H_{\max} - H_{\min}$.

4.4.1.2. *Source errors due to workpiece-fixture compliance*

It is well known that clamps are used to exert clamping forces to press the workpiece against locators. However, insufficient clamping forces cannot prevent the workpiece from slipping or detaching from locators whereas excessive clamping forces may cause strongly the workpiece deformations and overall workpiece motions. Therefore, besides gravity and machining forces, clamping forces have a significant impact on the machining quality.

Mathematically, gravity, machining forces, clamping forces and corresponding moments may be described by a resultant wrench vector.

Under their solicitations, three kinds of deformations will occur, i.e. the locator deformation, the contact deformation and the workpiece deformation as illustrated in Figure 4.21(a-c).

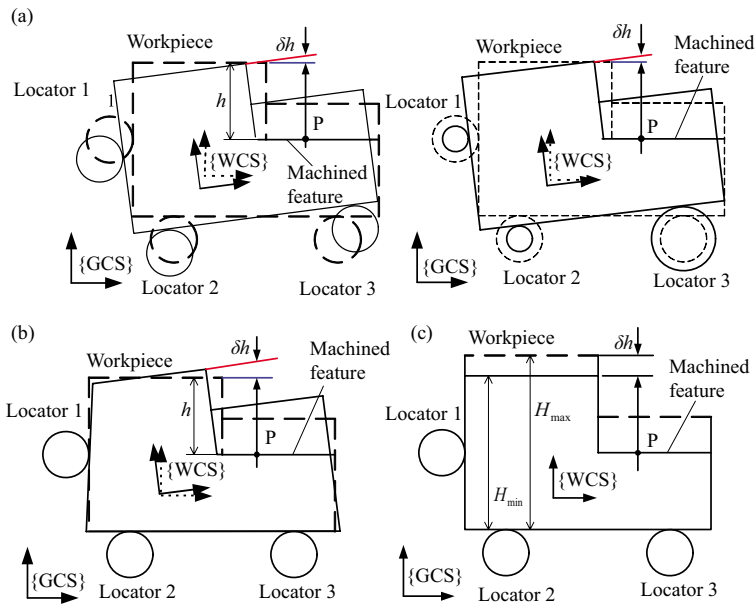

Figure 4.20. *Source errors due to geometric default: a) illustration of the setup-error and manufacturing-error of locator; b) illustration of the manufacturing default of workpiece locating plane; c) illustration of the IDE*

Contact stiffness

Contact deformations between the workpiece and the fixels can be characterized by a locally elastic model based on the classical Hertz contact theory [JOH 85]. Denote $E_{\mathrm{w},k}$ and $E_{\mathrm{f},k,}$ as the Young's moduli of the workpiece and fixture, respectively, at the *k*th contact point. $\nu_{\mathrm{w},k}$ and $\nu_{\mathrm{f},k}$ are Possion ratios. $G_{\mathrm{w},k}$ and $G_{\mathrm{f},k}$ are the shear moduli of two contact bodies. $R'_{\mathrm{w},k}$, $R''_{\mathrm{w},k}$ and $R'_{\mathrm{f},k}$, $R''_{\mathrm{f},k}$ are the principal radii of the workpiece and the *k*th fixel at the *k*th contact point, respectively. Then the equivalent radius reads

$$R_k^* = \sqrt{R_{ak} R_{bk}} \qquad [4.95]$$

where

$$
\begin{aligned}
R_{ak} &= \frac{1}{(A_k + B_k) - (B_k - A_k)} \\
R_{bk} &= \frac{1}{(A_k + B_k) + (B_k - A_k)} \\
A_k + B_k &= \frac{1}{2}\left(\frac{1}{R'_{\mathrm{w},k}} + \frac{1}{R''_{\mathrm{w},k}} + \frac{1}{R'_{\mathrm{f},k}} + \frac{1}{R''_{\mathrm{f},k}}\right) \\
B_k - A_k &= \frac{1}{2}[BA_1 + BA_2]^{\frac{1}{2}} \\
BA_1 &= \left(\frac{1}{R'_{\mathrm{w},k}} - \frac{1}{R''_{\mathrm{w},k}}\right)^2 + \left(\frac{1}{R'_{\mathrm{f},k}} - \frac{1}{R''_{\mathrm{f},k}}\right)^2 \\
BA_2 &= 2\left(\frac{1}{R'_{\mathrm{w},k}} - \frac{1}{R''_{\mathrm{w},k}}\right)\left(\frac{1}{R'_{\mathrm{f},k}} - \frac{1}{R''_{\mathrm{f},k}}\right)\cos 2\theta_k
\end{aligned}
\qquad [4.96]
$$

where θ_k is the angle between planes containing $R'_{\mathrm{w},k}$ and $R'_{\mathrm{f},k}$ or $R''_{\mathrm{w},k}$ and $R''_{\mathrm{f},k}$.

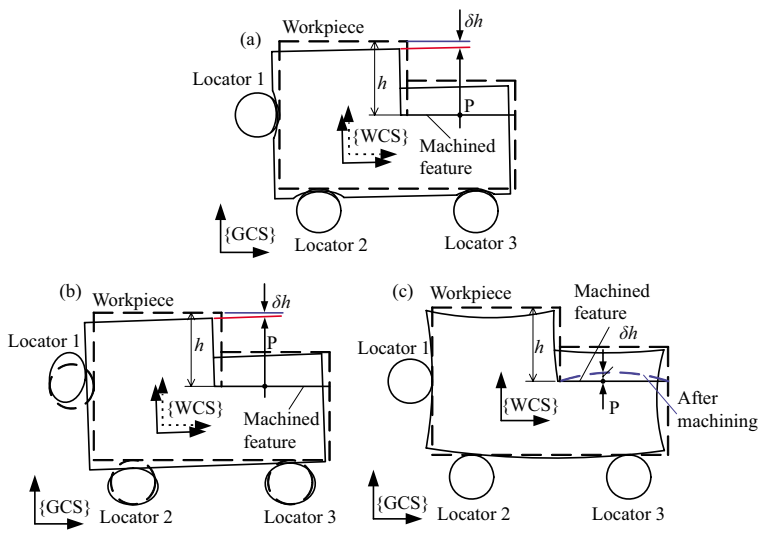

Figure 4.21. *Source errors due to workpiece-fixture compliance: a) illustration of the contact deformation; b) illustration of the locator deformation; c) illustration of the workpiece deformation.*

An elliptical contact area forms when the 3D workpiece is in contact with the kth fixel. So major and minor radii of contact ellipse can be written as

$$\begin{aligned} a_k &= \left(\frac{R_{ak}}{R_{bk}}\right)^{\frac{1}{3}} c_k \\ b_k &= \left(\frac{R_{bk}}{R_{ak}}\right)^{\frac{1}{3}} c_k \\ c_k &= \left(\frac{3R_k^* f_{k\mathbf{n}}^{\mathrm{c}}}{4E_k^*}\right)^{\frac{1}{3}} \alpha_k \end{aligned} \qquad [4.97]$$

Thus, the contact deformation in $\{\mathrm{CCS}\}_k$ at the kth contact point can be achieved as

$$\begin{aligned} \Delta_{\mathrm{c},k,\mathbf{n}}^{\mathrm{c}} &= \left(\frac{9 f_{k\mathbf{n}}^{\mathrm{c}}}{16 E_k^{*2} R_k^*}\right)^{\frac{1}{3}} \frac{\alpha_k}{\beta_k^2} \\ \Delta_{\mathrm{c},k,\boldsymbol{\tau}}^{\mathrm{c}} &= \frac{f_{k\boldsymbol{\tau}}^{\mathrm{c}}}{8 a_k G_k^*} \gamma_k \\ \Delta_{\mathrm{c},k,\boldsymbol{\eta}}^{\mathrm{c}} &= \frac{f_{k\boldsymbol{\eta}}^{\mathrm{c}}}{8 a_k G_k^*} \lambda_k \end{aligned} \qquad [4.98]$$

Equation [4.98] is differentiated with respect to the deformations, $\Delta_{\mathrm{c},k,\mathbf{n}}^{\mathrm{c}}$, $\Delta_{\mathrm{c},k,\boldsymbol{\tau}}^{\mathrm{c}}$, $\Delta_{\mathrm{c},k,\boldsymbol{\eta}}^{\mathrm{c}}$, and the corresponding loads, $f_{k\mathbf{n}}^{\mathrm{c}}$, $f_{k\boldsymbol{\tau}}^{\mathrm{c}}$, $f_{k\boldsymbol{\eta}}^{\mathrm{c}}$, such that the contact stiffness can be obtained as

$$\begin{aligned} K_{\mathrm{c},k,\mathbf{n}}^{\mathrm{c}} &= \frac{\left(6 R_k^* E_k^{*2} f_{k\mathbf{n}}^{\mathrm{c}}\right)^{\frac{1}{3}}}{\alpha_k \beta_k} \\ K_{\mathrm{c},k,\boldsymbol{\tau}}^{\mathrm{c}} &= \frac{8 a_k G_k^*}{\gamma_k} \\ K_{\mathrm{c},k,\boldsymbol{\eta}}^{\mathrm{c}} &= \frac{8 a_k G_k^*}{\lambda_k} \end{aligned} \qquad [4.99]$$

where, E_k^*,G_k^* and ν_k^* are the equivalent Young's modulus, shear modulus and Poisson ratio which can be formulated as

$$\begin{aligned}\frac{1}{E_k^*} &= \frac{1-\nu_{\mathrm{w},k}^2}{E_{\mathrm{w},k}} + \frac{1-\nu_{\mathrm{f},k}^2}{E_{\mathrm{f},k}} \\ \frac{1}{G_k^*} &= \frac{2-\nu_{\mathrm{w},k}}{G_{\mathrm{w},k}} + \frac{2-\nu_{\mathrm{f},k}}{G_{\mathrm{f},k}} \\ \frac{1}{\nu_k^*} &= \frac{1}{2\nu_{\mathrm{w},k}} + \frac{1}{2\nu_{\mathrm{f},k}}\end{aligned} \qquad [4.100]$$

and, α_k,β_k,γ_k andλ_k are the correction factors whose expressions are as follows:

$$\begin{aligned}\alpha_k &\approx 1 - \left[\left(\frac{R_{ak}}{R_{bk}}\right)^{0.0602} - 1\right]^{1.456} \\ \beta_k &\approx 1 - \left[\left(\frac{R_{ak}}{R_{bk}}\right)^{0.0684} - 1\right]^{1.531} \\ \gamma_k &\approx 1 + (1.4 - 0.8\nu_k^*)\log\left(\frac{a_k}{b_k}\right) \\ \lambda_k &\approx 1 + (1.4 + 0.8\nu_k^*)\log\left(\frac{a_k}{b_k}\right)\end{aligned} \qquad [4.101]$$

Specially, if $R'_{\mathrm{w},k}$,$R''_{\mathrm{w},k}$ and $R'_{\mathrm{f},k}$,$R''_{\mathrm{f},k}$ tend to be infinite and the kth fixel has high elastic modulus and cylindrical cross-section, the contact stiffness can be simplified as

$$\begin{aligned}K_{\mathrm{c},k,\mathbf{n}}^{\mathrm{c}} &= \frac{2E_{\mathrm{w},k}r_{\mathrm{f},k}}{1-\nu_{\mathrm{w},k}^2} \\ K_{\mathrm{c},k,\tau}^{\mathrm{c}} &= K_{\mathrm{c},k,\eta}^{\mathrm{c}} = \frac{8G_{\mathrm{w},k}r_{\mathrm{f},k}}{2-\nu_{\mathrm{w},k}}\end{aligned} \qquad [4.102]$$

where $r_{\mathrm{f},k}$ is the radius of the fixel at the kth contact point.

Locator stiffness:

Fixture elements may be modeled as cantilevered beam elements with a cylindrical cross-section of radius $r_{\mathrm{f},k}$ and length $l_{\mathrm{f},k}$. Thus, the stiffness of fixel k in $\{\mathrm{CCS}\}_k$ is written as

$$K^{\mathrm{c}}_{\mathrm{f},k,\mathbf{n}} = \frac{\pi E_{\mathrm{f},k} r^2_{\mathrm{f},k}}{l_{\mathrm{f},k}}$$
$$K^{\mathrm{c}}_{\mathrm{f},k,\tau} = K^{\mathrm{c}}_{\mathrm{f},k,\eta} = \frac{3\pi G_{\mathrm{f},k} r^2_{\mathrm{f},k}}{4 l_{\mathrm{f},k}} \qquad [4.103]$$

Local stiffness:

Considering the contact stiffness and locator stiffness presented above, we can write the overall local stiffness terms in each direction at the kth contact point as follows

$$\frac{1}{K^{\mathrm{c}}_{k\mathbf{n}}} = \frac{1}{K^{\mathrm{c}}_{\mathrm{c},k,\mathbf{n}}} + \frac{1}{K^{\mathrm{c}}_{\mathrm{f},k,\mathbf{n}}}$$
$$\frac{1}{K^{\mathrm{c}}_{k\tau}} = \frac{1}{K^{\mathrm{c}}_{\mathrm{c},k,\tau}} + \frac{1}{K^{\mathrm{c}}_{\mathrm{f},k,\tau}} \qquad [4.104]$$
$$\frac{1}{K^{\mathrm{c}}_{k\eta}} = \frac{1}{K^{\mathrm{c}}_{\mathrm{c},k,\eta}} + \frac{1}{K^{\mathrm{c}}_{\mathrm{f},k,\eta}}$$

4.4.2. *Workpiece position error*

4.4.2.1. *Workpiece position error relative to geometric default [QIN 06b]*

From section 4.4.1.1, we know that only setup-error and manufacturing error can cause WPE (I) corresponding to the rigid motion of the workpiece. In this section, a generic mathematical formulation is derived to describe their relationship.

As shown in Figure 4.22, the workpiece-fixture system consists of m locators and n clamps. $\mathbf{r}_{\mathrm{c},k} = [x_{\mathrm{c},k}, y_{\mathrm{c},k}, z_{\mathrm{c},k}]^{\mathrm{T}}$ is the coordinate vector of the kth contact point measured in $\{\mathrm{GCS}\}$. $\mathbf{n}_k$, $\boldsymbol{\tau}_k$ and $\boldsymbol{\eta}_k$ denote the unit inner

normal vector and two orthogonal unit tangential vectors of the workpiece at the contact point $\mathbf{r}_{c,k}$, respectively. $\{\text{LCS}\}_k$ is the locator coordinate system. When, $\{\text{WCS}\}$ and $\{\text{LCS}\}_k$ are assumed to be identically oriented with $\{\text{GCS}\}$. The WPE (I) measured in $\{\text{GCS}\}$ reads

$$\mathbf{J}_{\text{Jac}}\delta\mathbf{q}_{\text{w}}^{[\text{I}]} = -\mathbf{N}^{\text{T}}\delta\mathbf{r}_c \qquad [4.105]$$

where $\delta\mathbf{q}_{\text{w}}^{[\text{I}]} = \left[\delta\mathbf{r}_{\text{w}}^{\text{T}}, \delta\theta_{\text{w}}^{\text{T}}\right]^{\text{T}} = \left[\delta x_{\text{w}}, \delta y_{\text{w}}, \delta z_{\text{w}}, \delta\alpha_{\text{w}}, \delta\beta_{\text{w}}, \delta\gamma_{\text{w}}\right]^{\text{T}}$ is the measure of WPE (I). $\mathbf{J}_{\text{Jac}} = \left[\mathbf{J}_{\text{Jac},1}^{\text{T}}, \mathbf{J}_{\text{Jac},2}^{\text{T}}, \ldots, \mathbf{J}_{\text{Jac},m}^{\text{T}}\right]^{\text{T}}$ and $\mathbf{N} = \text{diag}\left(\mathbf{n}_1^{\text{w}}, \mathbf{n}_2^{\text{w}}, \ldots, \mathbf{n}_m^{\text{w}}\right)$ are the Jacobian matrix and the normal vector matrix with

$$\begin{aligned}\mathbf{J}_{\text{Jac},k} = [&-n_{kx}^{\text{w}},\ -n_{ky}^{\text{w}},\ -n_{kz}^{\text{w}},\ n_{kz}^{\text{w}}y_{\text{c},k}^{\text{w}} - n_{ky}^{\text{w}}z_{\text{c},k}^{\text{w}},\\ &n_{kx}^{\text{w}}z_{\text{c},k}^{\text{w}} - n_{kz}^{\text{w}}x_{\text{c},k}^{\text{w}},\ n_{ky}^{\text{w}}x_{\text{c},k}^{\text{w}} - n_{kx}^{\text{w}}y_{\text{c},k}^{\text{w}}]\end{aligned} \qquad [4.106]$$

and $\mathbf{n}_k^{\text{w}} = \left[n_{kx}^{\text{w}}, n_{ky}^{\text{w}}, n_{kz}^{\text{w}}\right]^{\text{T}}$ at the kth contact point, respectively. $\delta\mathbf{r}_c$ is the resultant error vector consisting of setup-error and manufacturing error of locators as well as manufacturing error of workpiece. It worth mentioning that the significance of $\delta\mathbf{r}_c$ is the position variation of the locating datum with respect to the tool-setting datum whose detailed discussion can be found in [QIN 06b].

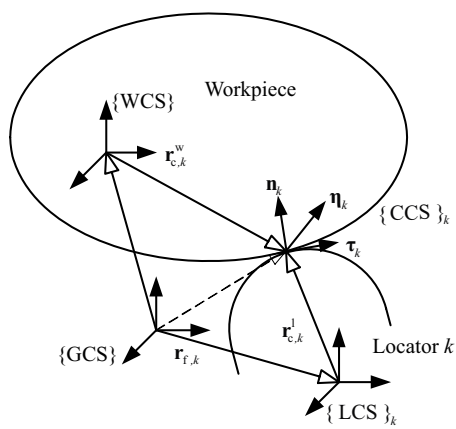

Figure 4.22. *Workpiece-fixture system*

Generally, if the locating scheme is sound, the workpiece position error $\delta\mathbf{q}_{\mathrm{w}}^{[\mathrm{I}]}$ can be solved as

$$\delta\mathbf{q}_{\mathrm{w}}^{[\mathrm{I}]} = -\mathbf{J}_{\mathrm{Jac}}{}^{+}\mathbf{N}^{\mathrm{T}}\delta\mathbf{r}_{c} \qquad [4.107]$$

with $\mathbf{J}_{\mathrm{Jac}}{}^{+}$ being a Moore-Penrose inverse matrix of $\mathbf{J}_{\mathrm{Jac}}$.

4.4.2.2. *Workpiece position error relative to local deformation [QIN 05]*

As stated above, the WPE (II) is due to local deformation. Without loss of generality, we can always assume that {WCS} is identically oriented with {GCS}. It can be therefore demonstrated that the WPE (II), denoted by $\delta\mathbf{q}_{\mathrm{w}}^{[\mathrm{II}]} = \left[\delta\mathbf{r}_{\mathrm{w}}^{\mathrm{T}}, \delta\boldsymbol{\theta}_{\mathrm{w}}^{\mathrm{T}}\right]^{\mathrm{T}}$, and the local deformation vector of all locators, denoted by $\Delta_{l}^{\mathrm{c}} = \left[\left(\Delta_{1}^{\mathrm{c}}\right)^{\mathrm{T}}, ..., \left(\Delta_{m}^{\mathrm{c}}\right)^{\mathrm{T}}\right]^{\mathrm{T}}$, have the following relationship

$$\mathbf{E}\delta\mathbf{q}_{\mathrm{w}}^{[\mathrm{II}]} = \mathbf{T}\left(\boldsymbol{\theta}\right)\Delta_{l}^{\mathrm{c}} \qquad [4.108]$$

where, $\mathbf{E} = \left[\mathbf{E}_{1}^{\mathrm{T}}, ..., \mathbf{E}_{m}^{\mathrm{T}}\right]^{\mathrm{T}}$ and $\mathbf{T}\left(\Theta\right) = \mathrm{diag}\left(\mathbf{T}\left(\boldsymbol{\theta}_{1}\right), ..., \mathbf{T}\left(\boldsymbol{\theta}_{m}\right)\right)$ are the location matrix of locators and the system transformation matrix, respectively.

$$\mathbf{E}_{k} = \begin{bmatrix} 1 & 0 & 0 & 0 & z_{\mathrm{c},k}^{\mathrm{w}} & -y_{\mathrm{c},k}^{\mathrm{w}} \\ 0 & 1 & 0 & -z_{\mathrm{c},k}^{\mathrm{w}} & 0 & x_{\mathrm{c},k}^{\mathrm{w}} \\ 0 & 0 & 1 & y_{\mathrm{c},k}^{\mathrm{w}} & -x_{\mathrm{c},k}^{\mathrm{w}} & 0 \end{bmatrix} \qquad [4.109]$$

and

$$\mathbf{T}\left(\boldsymbol{\theta}_{k}\right) = \left[\mathbf{n}_{k}, \boldsymbol{\tau}_{k}, \boldsymbol{\eta}_{k}\right] \qquad [4.110]$$

According to Hooke's law, $\Delta_{l}^{\mathrm{c}} = \left(\mathbf{K}_{l}^{\mathrm{c}}\right)^{-1}\mathbf{f}_{l}^{\mathrm{c}}$.

Here, $\mathbf{K}_{l}^{\mathrm{c}} = \mathrm{diag}\left(\mathbf{K}_{1}^{\mathrm{c}}, ..., \mathbf{K}_{m}^{\mathrm{c}}\right) = \mathrm{diag}\left(K_{1\mathbf{n}}^{\mathrm{c}}, K_{1\tau}^{\mathrm{c}}, K_{1\eta}^{\mathrm{c}}, ..., K_{m\mathbf{n}}^{\mathrm{c}}, K_{m\tau}^{\mathrm{c}}, K_{m\eta}^{\mathrm{c}}\right)$ is the local stiffness matrix. $\mathbf{f}_{l}^{\mathrm{c}} = \left[\left(\mathbf{f}_{1}^{\mathrm{c}}\right)^{\mathrm{T}}, \cdots, \left(\mathbf{f}_{m}^{\mathrm{c}}\right)^{\mathrm{T}}\right]^{\mathrm{T}} = [f_{1\mathbf{n}}^{\mathrm{c}}, f_{1\tau}^{\mathrm{c}}, f_{1\eta}^{\mathrm{c}}, \cdots, f_{m\mathbf{n}}^{\mathrm{c}}, f_{m\tau}^{\mathrm{c}}, f_{m\eta}^{\mathrm{c}}]^{\mathrm{T}}$ is the contact force vector. If the located

workpiece is deterministically in an equilibrium state, the following equation will hold:

$$\delta \mathbf{q}_{\mathrm{w}}^{[\mathrm{II}]} = \mathbf{E}^{+}\mathbf{T}\left(\boldsymbol{\theta}\right)\left(\mathbf{K}_{l}^{\mathrm{c}}\right)^{-1}\mathbf{f}_{l}^{\mathrm{c}} \qquad [4.111]$$

where $\mathbf{E}^{+}$ is a Moore–Penrose inverse matrix of $\mathbf{E}$.

Note that $\delta \mathbf{r}_{c}$ in equation [4.107] is known whereas $\mathbf{f}_{l}^{\mathrm{c}}$ in equation [4.111] is unknown. Therefore, contact forces $\mathbf{f}_{l}^{\mathrm{c}}$ must be determined firstly. To this end, we can apply the principle of the total complementary energy stating that for all statically admissible forces satisfying equilibrium, the actual state of forces (the one corresponding to kinematically compatible displacements) leads to an extreme value for the total complementary energy Π^{*}[PIL 94]. The latter has the form of

$$\Pi^{*} = U^{*} - W^{*} \qquad [4.112]$$

For a workpiece-fixture model as described in equation [4.111], as the workpiece is assumed to be rigid and contacts between the workpiece and the fixture elements are considered as frictional point-wise contacts with friction coefficient μ_{k}, the complementary strain energy is only concerned with deformable fixels

$$U^{*} = \frac{1}{2}(\mathbf{f}_{l}^{\mathrm{c}})^{\mathrm{T}}(\mathbf{K}_{l}^{\mathrm{c}})^{-1}\mathbf{f}_{l}^{\mathrm{c}} \qquad [4.113]$$

In our case, as the prescribed displacement vector δ_{l}^{c} is zero, the related potential W^{*} is also zero with

$$W^{*} = (\mathbf{f}_{l}^{\mathrm{c}})^{\mathrm{T}}\delta_{l}^{\mathrm{c}} = 0 \qquad [4.114]$$

Consequently, $\mathbf{f}_l^{\mathrm{c}}$ can be obtained by finding the extreme value of the following problem:

$$\begin{aligned}
&\text{find } \mathbf{f}_l^{\mathrm{c}}\\
&\min \ \frac{1}{2}(\mathbf{f}_l^{\mathrm{c}})^{\mathrm{T}}(\mathbf{K}_l^{\mathrm{c}})^{-1}\mathbf{f}_l^{\mathrm{c}}\\
&\text{s.t.}\\
&\quad (\text{static equilibrium constraints})\ \mathbf{G}_l\mathbf{f}_l^{\mathrm{c}} = -\mathbf{W}_e - \mathbf{G}_a\mathbf{f}_a^{\mathrm{c}}\\
&\quad (\text{contact condition})\ \mathbf{N}^{\mathrm{T}}\mathbf{T}(\boldsymbol{\theta})\,\mathbf{f}_l^{\mathrm{c}} \geq \mathbf{0}\\
&\quad (\text{friction cone constraints})\ \mathbf{H}\mathbf{f}_l^{\mathrm{c}} \geq \mathbf{0}
\end{aligned} \qquad [4.115]$$

where $\mathbf{W}_e$ is the wrench vector consisting of gravity, machining forces and their corresponding moments.

$$\mathbf{G}_l = \begin{bmatrix} \mathbf{n}_1 & \cdots & \mathbf{n}_m \\ \mathbf{r}_{c1} \times \mathbf{n}_1 & \cdots & \mathbf{r}_{cm} \times \mathbf{n}_m \end{bmatrix} \qquad [4.116]$$

$$\mathbf{G}_a = \begin{bmatrix} \mathbf{n}_{m+1} & \cdots & \mathbf{n}_{m+n} \\ \mathbf{r}_{c(m+1)} \times \mathbf{n}_{m+1} & \cdots & \mathbf{r}_{c(m+n)} \times \mathbf{n}_{m+n} \end{bmatrix} \qquad [4.117]$$

are the locator configuration matrix and the clamp configuration matrix, respectively.

$$\begin{aligned}
\mathbf{f}_a^{\mathrm{c}} &= \left[\left(\mathbf{f}_{m+1}^{\mathrm{c}}\right)^{\mathrm{T}}, \cdots, \left(\mathbf{f}_{m+n}^{\mathrm{c}}\right)^{\mathrm{T}}\right]^{\mathrm{T}}\\
&= \left[f_{(m+1)\mathbf{n}}^{\mathrm{c}}, 0, 0, \cdots, f_{(m+n)\mathbf{n}}^{\mathrm{c}}, 0, 0\right]^{\mathrm{T}}
\end{aligned} \qquad [4.118]$$

is the active clamping force vector.

$$\mathbf{H} = \mathrm{diag}\left(\mathbf{H}_{4N_{\mathrm{cp}}1}, ..., \mathbf{H}_{4N_{\mathrm{cp}}m}\right) \qquad [4.119]$$

is the overall matrix describing the linear approximation of the friction cone. The latter consists of m sub-matrices with:

$$\mathbf{H}_{4N_{\mathrm{cp}_k}} = \begin{bmatrix} \mu_k & -\cos\alpha_1 & -\sin\alpha_1 \\ \cdots & \cdots & \cdots \\ \mu_k & -\cos\alpha_s & -\sin\alpha_2 \\ \cdots & \cdots & \cdots \\ \mu_k & -\cos\alpha_{4N_{\mathrm{cp}}} & -\sin\alpha_{4N_{\mathrm{cp}}} \end{bmatrix}, \ (k = 1, \cdots, m) \qquad [4.120]$$

with the inclined angle

$$\alpha_s = \frac{\pi}{4} + \frac{\pi}{2\mathrm{k}}(s-1), 1 \leq s \leq 4N_{\mathrm{cp}} \qquad [4.121]$$

4.4.3. *Machining error analysis*

The machining error refers to the deviation of the actual dimension from the theoretical one. Due to the existence of WPE, IDE and workpiece elastic deformation (WED) of the workpiece-fixture system, the machining error is unavoidable and should be controlled within an allowable variation range, i.e. dimensional tolerance. Machining errors include linear and angular dimension errors fundamentally as those are generated by the relative position/motion of the cutting-tool with respect to the processing datum. As the motion path of the cutting-tool is assumed to be planned for the machining operation, the evaluation of machining errors can be equivalently transformed into the evaluation of the variation of processing datum with respect to the $\{\mathrm{GCS}\}$ if the workpiece is considered to be rigid, as shown in Figure 4.20(a, c) and Figure 4.21(a, b). In this section a systematic modeling is presented to show how source errors influence the machining error.

4.4.3.1. *Machining error relative to geometric default*

As shown in Figure 4.23, $\mathbf{r}_{\mathrm{P}} = [x_{\mathrm{P}}, y_{\mathrm{P}}, z_{\mathrm{P}}]^{\mathrm{T}}$ and $\mathbf{r}_{\mathrm{P}}^{\mathrm{w}} = [x_{\mathrm{P}}^{\mathrm{w}}, y_{\mathrm{P}}^{\mathrm{w}}, z_{\mathrm{P}}^{\mathrm{w}}]^{\mathrm{T}}$ are the coordinate vectors of the processing datum point P in $\{\mathrm{GCS}\}$ and $\{\mathrm{WCS}\}$, respectively. Therefore the relationship between $\mathbf{r}_{\mathrm{P}}^{\mathrm{w}}$ and $\mathbf{r}_{\mathrm{P}}$ can be described as

$$\mathbf{r}_{\mathrm{P}} = \mathbf{T}(\boldsymbol{\theta}_{\mathrm{w}})\mathbf{r}_{\mathrm{P}}^{\mathrm{w}} + \mathbf{r}_{\mathrm{w}} \qquad [4.122]$$

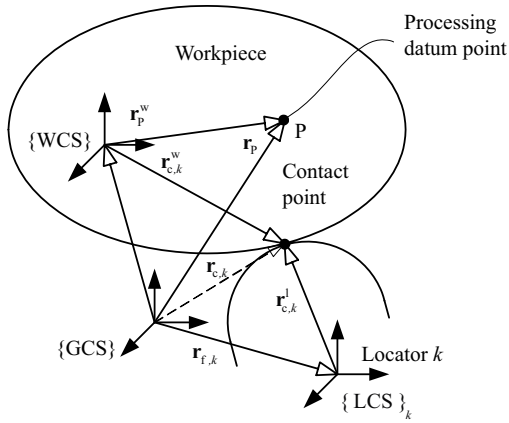

Figure 4.23. *Machining error relative to geometric default*

Note that the system transformation matrix, $\mathbf{T}(\boldsymbol{\theta}_{\mathrm{W}})$, will be a unit matrix if $\{\mathrm{WCS}\}$ has the same orientation with $\{\mathrm{GCS}\}$. In this case, it is easily demonstrated that the machining error relative to the geometric default can be evaluated by differentiating equation [4.122].

$$\delta\mathbf{r}_{\mathrm{P}}^{[\mathrm{I}]} = \mathbf{E}_{\mathrm{P}}\delta\mathbf{q}_{\mathrm{W}}^{[\mathrm{I}]} + \delta\mathbf{r}_{\mathrm{P}}^{w[\mathrm{I}]} \qquad [4.123]$$

with

$$\mathbf{E}_{\mathrm{P}} = \begin{bmatrix} 1 & 0 & 0 & 0 & z_{\mathrm{P}}^{\mathrm{W}} & -y_{\mathrm{P}}^{\mathrm{W}} \\ 0 & 1 & 0 & -z_{\mathrm{P}}^{\mathrm{W}} & 0 & x_{\mathrm{P}}^{\mathrm{W}} \\ 0 & 0 & 1 & y_{\mathrm{P}}^{\mathrm{W}} & -x_{\mathrm{P}}^{\mathrm{W}} & 0 \end{bmatrix} \qquad [4.124]$$

where $\delta\mathbf{r}_{\mathrm{P}}^{[\mathrm{I}]}$ is the machining error of the linear dimension. $\delta\mathbf{q}_{\mathrm{W}}^{[\mathrm{I}]}$ is the WPE (I) due to the workpiece-fixture geometric default and is derived from equation [4.107]. $\delta\mathbf{r}_{\mathrm{P}}^{w[\mathrm{I}]}$ refers to IDE of point P.

In fact, equation [4.123] is the velocity composition law of a kinematic particle. The physical meanings of $\delta\mathbf{r}_{\mathrm{P}}^{[\mathrm{I}]}$, $\delta\mathbf{r}_{\mathrm{P}}^{w[\mathrm{I}]}$ and $\mathbf{E}_{\mathrm{P}}\delta\mathbf{q}_{\mathrm{W}}^{[\mathrm{I}]}$ are the absolute velocity, the relative velocity and the transportation velocity of point P, respectively. In order to have a good understanding, we denote $\mathbf{v}_a^{[\mathrm{I}]} = \delta\mathbf{r}_{\mathrm{P}}^{[\mathrm{I}]}$,

$\mathbf{v}_r^{[\mathrm{I}]} = \delta\mathbf{r}_{\mathrm{P}}^{w[\mathrm{I}]}$ and $\mathbf{v}_t^{[\mathrm{I}]} = \mathbf{E}_{\mathrm{P}}\delta\mathbf{q}_{\mathrm{w}}^{[\mathrm{I}]} = \mathbf{v}_{\mathrm{w}}^{[\mathrm{I}]} + \omega_{\mathrm{w}}^{[\mathrm{I}]} \times \mathbf{r}_{\mathrm{P}}^{\mathrm{w}}$. In the last expression, $\mathbf{v}_{\mathrm{w}}^{[\mathrm{I}]} = [\delta x_{\mathrm{w}}, \delta y_{\mathrm{w}}, \delta z_{\mathrm{w}}]^{\mathrm{T}}$ and $\omega_{\mathrm{w}}^{[\mathrm{I}]} = [\delta\alpha_{\mathrm{w}}, \delta\beta_{\mathrm{w}}, \delta\gamma_{\mathrm{w}}]^{\mathrm{T}}$ denote the linear velocity and angular velocity of the origin of$\{\mathrm{WCS}\}$, respectively.

It is worth noting that the machining error model of the linear dimension described by equation [4.123] can be extended to evaluate the machining error of the angular dimension.

In Figure 4.24, suppose that line $\overline{\mathrm{P_1P_2}}$ denotes the processing datum of an angular dimension. Similarly, linear velocities, $\mathbf{v}_{r1}^{[\mathrm{I}]}$ and $\mathbf{v}_{r2}^{[\mathrm{I}]}$, at point $\mathrm{P_1}$ and $\mathrm{P_2}$ can be obtained following equation [4.123]

$$\mathbf{v}_{r1}^{[\mathrm{I}]} = \delta\mathbf{r}_{P1}^{[\mathrm{I}]} = \mathbf{E}_{P1}\delta\mathbf{q}_{\mathrm{w}}^{[\mathrm{I}]} + \delta\mathbf{r}_{P1}^{w[\mathrm{I}]} \qquad [4.125]$$

$$\mathbf{v}_{r2}^{[\mathrm{I}]} = \delta\mathbf{r}_{P2}^{[\mathrm{I}]} = \mathbf{E}_{P2}\delta\mathbf{q}_{\mathrm{w}}^{[\mathrm{I}]} + \delta\mathbf{r}_{P2}^{w[\mathrm{I}]} \qquad [4.126]$$

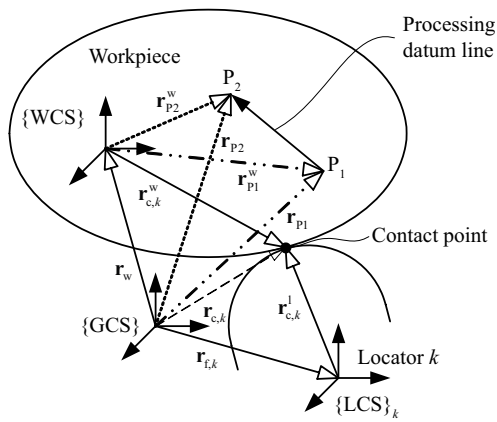

Figure 4.24. *Machining error of angular dimension*

Then, the linear velocity $\mathbf{v}_{12}^{[\mathrm{I}]}$ of the datum line $\overline{\mathrm{P_1P_2}}$ can be defined according to the theoretical mechanics [CHE 89]

$$\mathbf{v}_{12}^{[\mathrm{I}]} = \mathbf{v}_{r1}^{[\mathrm{I}]} - \mathbf{v}_{r2}^{[\mathrm{I}]} \qquad [4.127]$$

Then, the relationship between the linear velocity $\mathbf{v}_{12}^{[\mathrm{I}]}$ and the angular velocity of the reference line $\overline{\mathrm{P}_1\mathrm{P}_2}$ is given as

$$\boldsymbol{\omega}_{12}^{[\mathrm{I}]} \times \mathbf{r}_{12} = \mathbf{v}_{12}^{[\mathrm{I}]} \quad [4.128]$$

with $\mathbf{r}_{12} = \mathbf{r}_{\mathrm{P}1} - \mathbf{r}_{\mathrm{P}2}$.

So the angular velocity of line $\overline{\mathrm{P}_1\mathrm{P}_2}$ is obtained as

$$\boldsymbol{\omega}_{12}^{[\mathrm{I}]} = \mathbf{v}_{12}^{[\mathrm{I}]} \times \frac{\mathbf{r}_{12}}{\|\mathbf{r}_{12}\|^2} = -\frac{1}{\|\mathbf{r}_{12}\|^2}\mathbf{r}_{12} \times \mathbf{v}_{12}^{[\mathrm{I}]} \quad [4.129]$$

Combing equation [4.123] with equation [4.129], the locating error of the angular dimension with respect to the datum line can be determined by

$$\delta\boldsymbol{\theta}_{12}^{[\mathrm{I}]} = -\frac{1}{\|\mathbf{r}_{12}\|^2}\left[\left(\Omega_{\mathrm{P}1}^{\mathrm{w}} - \Omega_{\mathrm{P}2}^{\mathrm{w}}\right), \left(\Omega_{\mathrm{P}2}^{\mathrm{w}} - \Omega_{\mathrm{P}1}^{\mathrm{w}}\right)\right]\begin{bmatrix}\delta\mathbf{r}_{\mathrm{P}1}\\ \delta\mathbf{r}_{\mathrm{P}2}\end{bmatrix} \quad [4.130]$$

where

$$\Omega_k^{\mathrm{w}} = \begin{bmatrix} 0 & -z_k^{\mathrm{w}} & y_k^{\mathrm{w}} \\ z_k^{\mathrm{w}} & 0 & -x_k^{\mathrm{w}} \\ -y_k^{\mathrm{w}} & x_k^{\mathrm{w}} & 0 \end{bmatrix}, k = \mathrm{P}_1, \mathrm{P}_2 \quad [4.131]$$

4.4.3.2. *Machining error relative to workpiece-fixture compliance*

Similarly to equation [4.123], the machining error $\delta\mathbf{r}_{\mathrm{P}}^{[\mathrm{II}]}$ resulting from the workpiece-fixture deformations can be derived as

$$\delta\mathbf{r}_{\mathrm{P}}^{[\mathrm{II}]} = \mathbf{E}_{\mathrm{P}}\delta\mathbf{q}_{\mathrm{w}}^{[\mathrm{II}]} + \delta\mathbf{r}_{\mathrm{P}}^{\mathrm{w}[\mathrm{II}]} \quad [4.132]$$

where $\delta\mathbf{r}_{\mathrm{P}}^{\mathrm{w}[\mathrm{II}]}$ is the workpiece deformation of the processing datum point P mentioned qualitatively in Figure 4.21(a). It is worth noting that $\delta\mathbf{r}_{\mathrm{P}}^{\mathrm{w}[\mathrm{II}]}$ can be computed as the nodal displacement based on the commercial finite element software. Conversely to equation [4.115], we will solve the mathematical

programming problem defined by the complementary strain energy of the workpiece

$$\begin{aligned}
&\text{find} \quad \mathbf{f}_{\mathrm{w}} \\
&\min \quad \frac{1}{2}(\mathbf{f}_{\mathrm{w}})^{\mathrm{T}}(\mathbf{K}_{\mathrm{w}})^{-1}\mathbf{f}_{\mathrm{w}} \\
&\text{s.t.} \\
&\quad (\text{Static equilibrium constraints}) \ \mathbf{G}_l\mathbf{f}_l^{\mathrm{c}} = -\mathbf{W}_e - \mathbf{G}_a\mathbf{f}_a^{\mathrm{c}} \\
&\quad (\text{Contact condition}) \ \mathbf{N}^{\mathrm{T}}\mathbf{T}\left(\boldsymbol{\theta}\right)\mathbf{f}_l^{\mathrm{c}} \geq \mathbf{0} \\
&\quad (\text{Friction cone constraints}) \ \mathbf{H}\mathbf{f}_l^{\mathrm{c}} \geq \mathbf{0}
\end{aligned} \qquad [4.133]$$

where, $\mathbf{K}_{\mathrm{w}}$ is the workpiece stiffness matrix. $\mathbf{f}_{\mathrm{w}}$ is the external load vector including the gravity $\mathbf{f}_g$, the machining force $\mathbf{f}_m$, the clamping force $\mathbf{f}_a^{\mathrm{c}}$ and corresponding contact force $\mathbf{f}_l = \mathbf{T}\left(\boldsymbol{\theta}\right)\mathbf{f}_l^{\mathrm{c}}$ at locators.

When contact forces $\mathbf{f}_l$ are computed at all locators by commercial FEM software, the workpiece deformation can be simultaneously derived as

$$\mathbf{U}_{\mathrm{w}} = (\mathbf{K}_{\mathrm{w}})^{-1}\mathbf{f}_{\mathrm{w}} \qquad [4.134]$$

Similarly, equation [4.132] can also be interpreted as the velocity composition law of the kinematic particle. $\mathbf{v}_a^{[\mathrm{II}]} = \delta\mathbf{r}_{\mathrm{P}}^{[\mathrm{II}]}$ means the absolute velocity, $\mathbf{v}_r^{[\mathrm{II}]} = \delta\mathbf{r}_{\mathrm{P}}^{\mathrm{w}[\mathrm{II}]}$ is the relative velocity, and $\mathbf{v}_t^{[\mathrm{II}]} = \mathbf{E}_{\mathrm{P}}\delta\mathbf{q}_{\mathrm{w}}^{[\mathrm{II}]} = \mathbf{v}_{\mathrm{w}}^{[\mathrm{II}]} + \boldsymbol{\omega}_{\mathrm{w}}^{[\mathrm{II}]} \times \mathbf{r}_{\mathrm{P}}^{\mathrm{w}}$ corresponds to the transportation velocity with $\mathbf{v}_{\mathrm{w}}^{[\mathrm{II}]} = [\delta x_{\mathrm{w}}, \delta y_{\mathrm{w}}, \delta z_{\mathrm{w}}]^{\mathrm{T}}$ and $\boldsymbol{\omega}_{\mathrm{w}}^{[\mathrm{II}]} = [\delta\alpha_{\mathrm{w}}, \delta\beta_{\mathrm{w}}, \delta\gamma_{\mathrm{w}}]^{\mathrm{T}}$ of the linear velocity and angular velocity of the origin of $\{\mathrm{WCS}\}$.

4.4.3.3. *Overall machining error*

In the previous sections, we focused our efforts on modeling the machining error relative to geometric defaults and deformations of the workpiece-fixture system independently. Now we will evaluate the overall machining error resulting from all source errors in the workpiece-fixture system.

As a resultant velocity can be expressed as a vectorial combination of all components, the overall machining error of a datum point on the workpiece in $\{GCS\}$ can be obtained by combining equations [4.123] and [4.132]

$$\delta \mathbf{r}_P = \mathbf{E}_P \delta \mathbf{q}_w + \delta \mathbf{r}_P^w \qquad [4.135]$$

with

$$\delta \mathbf{q}_w = \delta \mathbf{q}_w^{[I]} + \delta \mathbf{q}_w^{[II]}, \delta \mathbf{r}_P^w = \delta \mathbf{r}_P^{w[I]} + \delta \mathbf{r}_P^{w[II]} \qquad [4.136]$$

A flowchart is given in Figure 4.25 to summarize the whole procedure for the computation of the overall machining error. From an engineering application point of view, some simplifications can be made to improve the computation efficiency [DEM 01, RON 99]. If the workpiece is characteristic of strong stiffness, the geometric variation and local deformation will dominate the machining error such that

$$\delta \mathbf{q}_w = \delta \mathbf{q}_w^{[I]} + \delta \mathbf{q}_w^{[II]}, \delta \mathbf{r}_P^w = \delta \mathbf{r}_P^{w[I]} \qquad [4.137]$$

In the extreme case, the source error relative to local contact deformations may be further negligible such that equation [4.137] becomes

$$\delta \mathbf{q}_w = \delta \mathbf{q}_w^{[I]}, \delta \mathbf{r}_P^w = \delta \mathbf{r}_P^{w[I]} \qquad [4.138]$$

Alternatively, if the workpiece material is substantially softer than the fixture elements, the elastic deformation of the workpiece may be dominant. equation [4.136] can be thus simplified as

$$\delta \mathbf{q}_w = \delta \mathbf{q}_w^{[I]}, \delta \mathbf{r}_P^w = \delta \mathbf{r}_P^{w[I]} + \delta \mathbf{r}_P^{w[II]} \qquad [4.139]$$

Likewise, in the extreme case when the source error relative to geometric defaults is negligible, equation [4.139] becomes

$$\delta \mathbf{r}_P^w = \delta \mathbf{r}_P^{w[II]} \qquad [4.140]$$

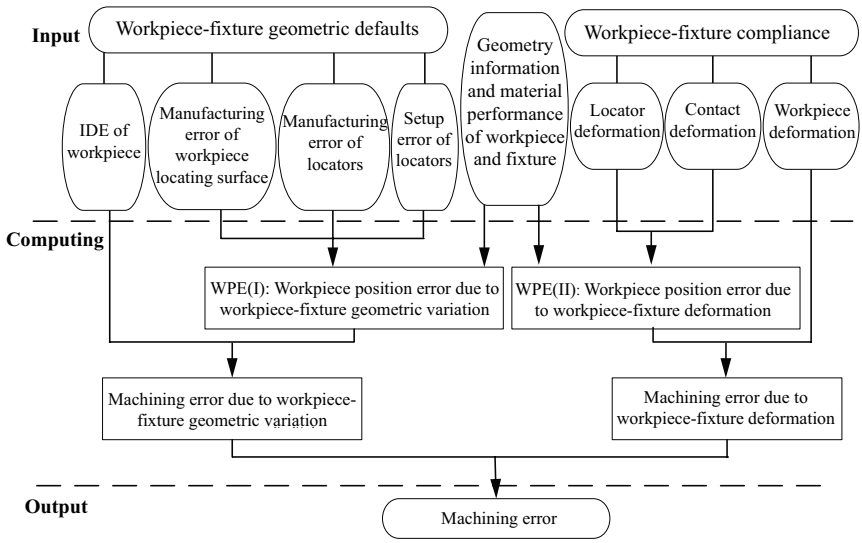

Figure 4.25. *Computing procedure of the overall machining error*

4.5. Optimal design of the fixture clamping sequence

4.5.1. *Effect of clamping sequence on high-stiffness workpiece*

If a workpiece is of high-stiffness, the local deformation will be the main factors influencing the workpiece quality [DEM 01]. On the contrary, if the workpiece material is substantially softer than the fixture elements, the elastic deformation of the workpiece may be dominant. Therefore the effects of the clamping sequence on the workpiece quality can be analyzed following the workpiece stiffness.

4.5.1.1. *Description of multiple fixture elements*

When multiple clamps are set up one by one onto the workpiece with known force magnitudes, directions and placements [COG 92], the clamping sequence will influence the redistribution of resultant contact forces generated between the workpiece and fixture elements (fixels). As shown in Table 4.1, the clamping sequence can be decomposed into basic clamping steps and each step possesses its own passive and active elements with corresponding passive and active forces. From the above description, locators and clamps will act as passive and active elements, respectively. However, an active

clamp applied in the present step will serve as a passive element in the next step when a new clamp is applied. This is because tangential frictions will occur. Physically, clamping forces are frequently controlled by a hydraulic or pneumatic actuator. A summary of elements and forces in each clamping step is shown in Table 4.1.

Clamping step	Simplified diagram	Passive element	Active element	Active contact forces		Passive contact forces	
				Applied	Pre-load	Resultant	Incremental
1	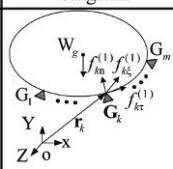	G_1 G_2 $\cdots$ G_m	-	$\mathbf{W}_g$	-	$\mathbf{f}_{P1}^{(1)}$ $\mathbf{f}_{P2}^{(1)}$ $\cdots$ $\mathbf{f}_{Pm}^{(1)}$	-
2	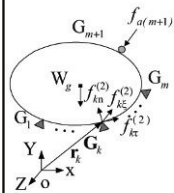	G_1 G_2 $\cdots$ G_m	G_{m+1}	$\mathbf{f}_{a(m+1)}$	$\mathbf{W}_g$	$\mathbf{f}_{P1}^{(1)}$ $\mathbf{f}_{P2}^{(1)}$ $\cdots$ $\mathbf{f}_{Pm}^{(1)}$	$\mathbf{f}_{P1}^{(2)} - \mathbf{f}_{P1}^{(1)}$ $\mathbf{f}_{P2}^{(2)} - \mathbf{f}_{P2}^{(1)}$ $\cdots$ $\mathbf{f}_{Pm}^{(2)} - \mathbf{f}_{Pm}^{(1)}$
$\cdots$	$\cdots$	$\cdots$	$\cdots$	$\cdots$	$\cdots$	$\cdots$	$\cdots$
j+1	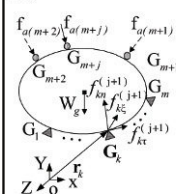	G_1 G_2 $\cdots$ G_{m+j-1}	G_{m+j}	$\mathbf{f}_{a(m+j)}$	$\mathbf{W}_g$ $\mathbf{f}_{a(m+1)}$ $\cdots$ $\mathbf{f}_{a(m+j-1)}$	$\mathbf{f}_{P1}^{(j+1)}$ $\mathbf{f}_{P2}^{(j+1)}$ $\cdots$ $\mathbf{f}_{P(m+j-1)}^{(j+1)}$	$\mathbf{f}_{P1}^{(j+1)} - \mathbf{f}_{P1}^{(j)}$ $\mathbf{f}_{P2}^{(j+1)} - \mathbf{f}_{P2}^{(j)}$ $\cdots$ $\mathbf{r}_{f1} - \mathbf{r}_{f2}$ $\mathbf{f}_{P(m+j-1)}^{(j+1)}$
$\cdots$	$\cdots$	$\cdots$	$\cdots$	$\cdots$	$\cdots$	$\cdots$	$\cdots$
n+2	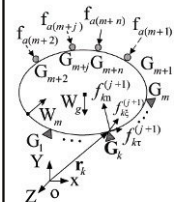	G_1 G_2 $\cdots$ G_{m+n}	-	$\mathbf{W}_m$	$\mathbf{W}_g$ $\mathbf{f}_{a(m+1)}$ $\cdots$ $\mathbf{f}_{a(m+n)}$	$\mathbf{f}_{P1}^{(n+2)}$ $\mathbf{f}_{P2}^{(n+2)}$ $\cdots$ $\mathbf{f}_{P(m+n)}^{(n+2)}$	$\mathbf{f}_{P1}^{(n+2)} - \mathbf{f}_{P1}^{(n+1)}$ $\mathbf{f}_{P2}^{(n+2)} - \mathbf{f}_{P2}^{(n+1)}$ $\cdots$ $\mathbf{r}_{f3} - \mathbf{r}_{f4}$ $\mathbf{f}_{P(m+n)}^{(n+2)}$
Nomenclature: $\mathbf{r}_{f1} = \mathbf{f}_{P(m+j-2)}^{(j+1)}$; $\mathbf{r}_{f2} = \mathbf{f}_{P(m+j-2)}^{(j)}$; $\mathbf{r}_{f3} = \mathbf{f}_{P(m+n-1)}^{(n+2)}$; $\mathbf{r}_{f4} = \mathbf{f}_{P(m+n-1)}^{(n+1)}$							

Table 4.1. *Passive and active elements and contact forces in clamping steps*

4.5.1.2. *Mathematical modeling of clamping sequence*

In section 4.5.1.1, the clamping sequence is qualitatively illustrated. Now, let us study the clamping sequence and related contact forces quantitatively. In

each clamping step, contact forces must satisfy static equilibrium equations of the workpiece.

– *Step 1*: given the set of passive fixels characterized by layout matrices $G_1, G_2, \ldots, G_m$, only $\mathbf{W}_g$ is applied as the external gravity force vector onto the workpiece as listed in Table 4.1. Then, the static equilibrium system of equations of the workpiece is dominated by

$$\mathbf{G}_{\mathrm{P}}^{(1)}\mathbf{f}_{\mathrm{P}}^{(1)} = -\mathbf{W}_g \qquad [4.141]$$

where the configuration matrix and the resultant contact force vector of total passive elements in step 1 are

$$\mathbf{G}_{\mathrm{P}}^{(1)} = [\mathrm{G}_1, \mathrm{G}_2, \cdots, \mathrm{G}_m] \qquad [4.142]$$

$$\begin{aligned}\mathbf{f}_{\mathrm{P}}^{(1)} &= [\mathbf{f}_{\mathrm{P1}}^{(1)\mathrm{T}}, \mathbf{f}_{\mathrm{P2}}^{(1)\mathrm{T}}, \cdots, \mathbf{f}_{\mathrm{P}m}^{(1)\mathrm{T}}]^{\mathrm{T}} \\ &= [f_{1\mathbf{n}}^{(1)}, f_{1\boldsymbol{\tau}}^{(1)}, f_{1\boldsymbol{\xi}}^{(1)}, \cdots, f_{m\mathbf{n}}^{(1)}, f_{m\boldsymbol{\tau}}^{(1)}, f_{m\boldsymbol{\xi}}^{(1)}]^{\mathrm{T}}\end{aligned} \qquad [4.143]$$

– *Step 2*: the first clamp numbered *m*+1 is now set up as an active element with a prescribed clamping force $\mathbf{f}_{a\,(m+1)}$ applied to the workpiece whereas previous locators $(k = 1,\ 2,\ \ldots, m)$ are passive elements. Therefore, the current static equilibrium equation system can be obtained as

$$\mathbf{G}_{\mathrm{P}}^{(2)}\mathbf{f}_{\mathrm{P}}^{(2)} = -\mathbf{W}_g - \mathrm{G}_{m+1}\mathbf{f}_{a(m+1)} \qquad [4.144]$$

where the configuration matrix of passive elements, $\mathbf{G}_{\mathrm{P}}^{(2)}$, is identical to $\mathbf{G}_{\mathrm{P}}^{(1)}$ and the resultant contact force vector of all passive elements in step 2 is

$$\begin{aligned}\mathbf{f}_{\mathrm{P}}^{(2)} &= [\mathbf{f}_{\mathrm{P1}}^{(2)\mathrm{T}}, \mathbf{f}_{\mathrm{P2}}^{(2)\mathrm{T}}, \cdots, \mathbf{f}_{\mathrm{P}m}^{(2)\mathrm{T}}]^{\mathrm{T}} \\ &= [f_{1\mathbf{n}}^{(2)}, f_{1\boldsymbol{\tau}}^{(2)}, f_{1\boldsymbol{\xi}}^{(2)}, \cdots, f_{m\mathbf{n}}^{(2)}, f_{m\boldsymbol{\tau}}^{(2)}, f_{m\boldsymbol{\xi}}^{(2)}]^{\mathrm{T}}\end{aligned} \qquad [4.145]$$

– *Step 3*: suppose that the second active clamp numbered *m*+2 is put in use to the workpiece with a known clamping force of $\mathbf{f}_{a\,(m+2)}$. Note that clamp *m*+1 used in step 2 now becomes a passive element with the presence of frictional forces. Therefore, the current static equilibrium equation system of the workpiece can be written as

$$\mathbf{G}_{\mathrm{P}}^{(3)}\mathbf{f}_{\mathrm{P}}^{(3)} = -\mathbf{W}_g - \mathrm{G}_{m+2}\mathbf{f}_{a(m+2)} \qquad [4.146]$$

where the configuration matrix of passive elements, $\mathbf{G}_{\mathrm{P}}^{(3)}$, is an extension of $\mathbf{G}_{\mathrm{P}}^{(2)}$ with

$$\mathbf{G}_{\mathrm{P}}^{(3)} = [\mathbf{G}_{\mathrm{P}}^{(2)}, \mathrm{G}_{m+1}] \tag{4.147}$$

and the resultant contact force vector of total passive elements in Step 3 is

$$\begin{aligned}\mathbf{f}_{\mathrm{P}}^{(3)} &= [\mathbf{f}_{\mathrm{P1}}^{(3)\mathrm{T}}, \mathbf{f}_{\mathrm{P2}}^{(3)\mathrm{T}}, \cdots, \mathbf{f}_{\mathrm{P}(m+1)}^{(3)\mathrm{T}}]^{\mathrm{T}} \\ &= [f_{1\mathbf{n}}^{(3)}, f_{1\boldsymbol{\tau}}^{(3)}, f_{1\boldsymbol{\xi}}^{(3)}, \cdots, f_{m\mathbf{n}}^{(3)}, f_{m\boldsymbol{\tau}}^{(3)}, f_{m\boldsymbol{\xi}}^{(3)}, f_{(m+1)\mathbf{n}}^{(3)}, f_{(m+1)\boldsymbol{\tau}}^{(3)}, f_{(m+1)\boldsymbol{\xi}}^{(3)}]^{\mathrm{T}} \\ &= [f_{1\mathbf{n}}^{(3)}, f_{1\boldsymbol{\tau}}^{(3)}, f_{1\boldsymbol{\xi}}^{(3)}, \cdots, f_{m\mathbf{n}}^{(3)}, f_{m\boldsymbol{\tau}}^{(3)}, f_{m\boldsymbol{\xi}}^{(3)}, f_{(m+1)\mathbf{n}}, f_{(m+1)\boldsymbol{\tau}}^{(3)}, f_{(m+1)\boldsymbol{\xi}}^{(3)}]^{\mathrm{T}}\end{aligned} \tag{4.148}$$

– Through analogy, the static equilibrium equation in Step j is generally stated as

$$\mathbf{G}_{\mathrm{P}}^{(j)}\mathbf{f}_{\mathrm{P}}^{(j)} = -\mathbf{W}_e - \mathrm{G}_{m+j-1}\mathbf{f}_{a(m+j-1)} \tag{4.149}$$

where G_k $(k = 1, \ldots, m+n)$ and $\mathbf{f}_{aj}$ $(j = 1, \ldots, n)$ are the layout matrix and active contact force vector at the kth fixture element.

$$\mathbf{W}_e = \begin{cases} \mathbf{W}_g, & 2 \le j \le n+1 \\ \mathbf{W}_g + \mathbf{W}_m, & j = n+2 \end{cases} \tag{4.150}$$

is the external load vector applied to the workpiece in step j.

4.5.1.3. *Determination of contact forces in the clamping sequence*

For a 3D workpiece clamped in step j, as its fixture generally consists of $m \ge 6$ locators and $n = j - 1$ clamps, there exist $3(m + j - 2)$ unknown components of contact forces to be determined in equation [4.149], which is indeterminate from the equilibrium viewpoint. True force components of $\mathbf{f}_{\mathrm{P}}^{(j)}$ will be evaluated based on the principle of minimum total complementary energy for $(m + j - 2)$ passive fixture elements.

As shown in Table 4.1, $\mathbf{f}_{\mathrm{P}}^{(j-1)}$ and $\mathbf{f}_{\mathrm{P}}^{(j)}$ denote resultant contact forces of dimensions $3(m + j - 3) \times 1$ and $3(m + j - 2) \times 1$ in step j-1 and step j,

respectively. By introducing a new notation for resultant contact forces $\mathbf{f}_{\mathrm{P}}^{(j-1)}$ in step *j*-1,

$$\mathbf{f'}_{\mathrm{P}}^{(j-1)} = \begin{cases} \mathbf{0}_{3m\times 1},\ j=1 \\ [\mathbf{f}_{\mathrm{P}}^{(j-1)T}, \mathbf{z}_3^{\mathrm{T}}]^{\mathrm{T}},\ 2\le j\le n+2 \end{cases} \quad [4.151]$$

with

$$\mathbf{z}_3 = [0,0,0]^{\mathrm{T}} \quad [4.152]$$

$\mathbf{f}_{\mathrm{P}}^{(j)} - \mathbf{f'}_{\mathrm{P}}^{(j-1)}$ represents then the force increment of dimension $3(m+j-2)\times 1$ generated in step *j*.

Contact forces $\mathbf{f}_{\mathrm{P}}^{(j)}$ can be determined by means of the principle of the total complementary energy. The latter states that among all statically admissible stress/forces satisfying equilibrium, the actual state of stress/forces (the one corresponding to kinematically compatible displacements) leads to an extreme value for the total complementary energy Π [PIL 94, HUR 02] with

$$\Pi = U^* - W^* \quad [4.153]$$

Since the workpiece is assumed to be rigid, our workpiece-fixture model is only concerned with deformable fixels whose complementary strain energy associated with the force increment from step $j-1$ to step j is expressed as

$$U^* = \frac{1}{2}(\mathbf{f}_{\mathrm{P}}^{(j)} - \mathbf{f'}_{\mathrm{P}}^{(j-1)})^{\mathrm{T}}(\mathbf{K}_{\mathrm{P}}^{(j)})^{-1}(\mathbf{f}_{\mathrm{P}}^{(j)} - \mathbf{f'}_{\mathrm{P}}^{(j-1)}) \quad [4.154]$$

Note that the above expression is approximate if the stiffness matrix varies with respect to the contact forces.

Moreover, the potential of prescribed displacements, W^*, equals zero as prescribed displacements, $\overline{\delta\mathbf{d}}_{\mathrm{P}}^{(j)}$, are equal to zero in our case

$$W^* = (\mathbf{f}_{\mathrm{P}}^{(j)} - \mathbf{f'}_{\mathrm{P}}^{(j-1)})^{\mathrm{T}}\overline{\delta\mathbf{d}}_{\mathrm{P}}^{(j)} = 0 \quad [4.155]$$

Therefore, the contact force vector of $\mathbf{f}_{\mathrm{P}}^{(j)}$ in step j can be obtained by finding the extreme value of the following nonlinear programming problem

$$\min \quad \frac{1}{2}(\mathbf{f}_{\mathrm{P}}^{(j)} - \mathbf{f'}_{\mathrm{P}}^{(j-1)})^{\mathrm{T}}(\mathbf{K}_{\mathrm{P}}^{(j)})^{-1}(\mathbf{f}_{\mathrm{P}}^{(j)} - \mathbf{f'}_{\mathrm{P}}^{(j-1)})$$

s.t.

$$\begin{aligned}
&\mathbf{G}_{\mathrm{P}}^{(j)}\mathbf{f}_{\mathrm{P}}^{(j)} = -\mathbf{W}_e - \mathrm{G}_{m+j-1}\mathbf{f}_{a(m+j-1)} \\
&\mathbf{N}_{\mathrm{P}}^{(j)T}\mathbf{T}(\boldsymbol{\theta}_c^{(j)})\mathbf{f}_{\mathrm{P}}^{(j)} \geq 0 \\
&\mathbf{C}_{4k}^{(j)}\mathbf{f}_{\mathrm{P}}^{(j)} \geq 0 \\
&\mathbf{T}_z^{(j)}\mathbf{f}_{\mathrm{P}}^{(j)} = \mathbf{f}_a^{(j)}
\end{aligned} \qquad [4.156]$$

Here, the first set of constraints refers to equilibrium that must be verified to be statically admissible $\mathbf{f}_{\mathrm{P}}^{(j)}$. The second and third sets refer to unilateral and friction constraints required to ensure the attachment and no slipping between the workpiece and the fixels. The last constraint set refers to the known clamping forces exerted by hydraulic clamps. Below are details of related terms:

$$\begin{aligned}
&\mathbf{K}_{\mathrm{P}}^{(j)} = \mathrm{diag}(K_{p1}^{(j)}, K_{p2}^{(j)}, \cdots, K_{p(m+j-2)}^{(j)}) \\
&\mathbf{K}_{\mathrm{P}k}^{(j)} = \mathrm{diag}(K_{k\mathbf{n}}^{(j)}, K_{k\boldsymbol{\tau}}^{(j)}, K_{k\boldsymbol{\xi}}^{(j)}) \\
&\mathbf{N}_{\mathrm{P}}^{(j)} = \mathrm{diag}(\mathbf{n}_1, \mathbf{n}_2, \cdots, \mathbf{n}_{(m+j-2)}) \\
&\mathbf{T}(\boldsymbol{\theta}_c^{(j)}) = \mathrm{diag}(\mathbf{T}(\boldsymbol{\theta}_{c1}), \mathbf{T}(\boldsymbol{\theta}_{c2}), \cdots, \mathbf{T}(\boldsymbol{\theta}_{c(m+j-2)})) \\
&\mathbf{T}(\boldsymbol{\theta}_{ck}) = [\mathbf{n}_k, \boldsymbol{\tau}_k, \boldsymbol{\xi}_k] \\
&\mathbf{C}_{4l}^{(j)} = \mathrm{diag}(C_{4l1}, C_{4l2}, \cdots, C_{4l(m+j-2)}) \\
&\mathbf{T}_z^{(j)} = \mathrm{diag}(\underbrace{Z_3, \cdots, Z_3}_{m}, \underbrace{U_3, \cdots, U_3}_{j-2}) \\
&\mathbf{Z}_3 = \mathrm{diag}(0, 0, 0) \\
&\mathbf{U}_3 = \mathrm{diag}(1, 0, 0) \\
&\mathbf{f}_a^{(j)} = [\underbrace{\mathrm{z}_3^{\mathrm{T}}, \cdots, \mathrm{z}_3^{\mathrm{T}}}_{m}, \mathbf{f}_{a(m+1)}^{\mathrm{T}}, \mathbf{f}_{a(m+2)}^{\mathrm{T}}, \cdots, \mathbf{f}_{a(m+j-2)}^{\mathrm{T}}]^{\mathrm{T}}
\end{aligned} \qquad [4.157]$$

4.5.2. *Effect of clamping sequence on low-stiffness workpiece*

In this case, deformations of fixels are considered to be relatively negligible with respect to those of the workpiece. Compared to equation [4.156], the mathematical programming problem will be formulated as

$$\begin{aligned}
&\min \quad \frac{1}{2}(\mathbf{f}_{\mathrm{w}}^{(j)} - \mathbf{f'}_{\mathrm{w}}^{(j-1)})^{\mathrm{T}}(\mathbf{K}_{\mathrm{w}})^{-1}(\mathbf{f}_{\mathrm{w}}^{(j)} - \mathbf{f'}_{\mathrm{w}}^{(j-1)}) \\
&\text{s.t.} \\
&\quad \mathbf{G}_{\mathrm{P}}^{(j)}\mathbf{f}_{\mathrm{P}}^{(j)} = -\mathbf{W}_e - \mathrm{G}_{m+j-1}\mathbf{f}_{a(m+j-1)} \\
&\quad \mathbf{N}_{\mathrm{P}}^{(j)T}\mathbf{T}(\boldsymbol{\theta}_{\mathrm{c}}^{(j)})\mathbf{f}_{\mathrm{P}}^{(j)} \geq 0 \\
&\quad \mathbf{C}_{4l}^{(j)}\mathbf{f}_{\mathrm{P}}^{(j)} \geq 0 \\
&\quad \mathbf{T}_z^{(j)}\mathbf{f}_{\mathrm{P}}^{(j)} = \mathbf{f}_a^{(j)}
\end{aligned} \qquad [4.158]$$

where $\mathbf{K}_{\mathrm{w}}$ denotes the workpiece stiffness matrix of $3r \times 3r$ (r is the nodal number). $\mathbf{f}_{\mathrm{w}}^{(j)}$ denotes the external load vector of $3r \times 1$ consisting of the gravity force $\mathbf{f}_g$, the machining forces $\mathbf{f}_m$ and corresponding contact forces $\mathbf{f}_{\mathrm{P}}^{(j)}$ at locators, including frictions between the workpiece and fixture elements.

From equation [4.158], it is known that contact forces $\mathbf{f}_{\mathrm{P}}^{(j)}$ in step j depend on contact forces $\mathbf{f}_{\mathrm{P}}^{(j-1)}$ in step $j-1$. Therefore, $\mathbf{f}_{\mathrm{P}}^{(j-1)}$ must be equivalently applied to the workpiece in way of initial stresses for the evaluation of $\mathbf{f}_{\mathrm{P}}^{(j)}$ with the commercial FEM software. In the meantime, the increment of displacement vector $\delta\mathbf{d}_{\mathrm{w}}^{(j)}$ can be obtained for the evaluation of total displacement vector.

$$\boldsymbol{\delta}_{\mathrm{w}}^{(j)} = \boldsymbol{\delta}_{\mathrm{w}}^{(j-1)} + \delta\mathbf{d}_{\mathrm{w}}^{(j)} \qquad [4.159]$$

where $\boldsymbol{\delta}_{\mathrm{w}}^{(j-1)}$ and $\boldsymbol{\delta}_{\mathrm{w}}^{(j)}$ are the workpiece deformations in step *j*-1 and step *j*, respectively.

4.5.3. *Optimization of clamping sequence*

Due to the effect of clamping sequence on the workpiece machining accuracy, it is necessary to model the clamping sequence and then find the optimal one to ensure the machining accuracy.

4.5.3.1. *Optimization of clamping sequence for high-stiffness workpiece*

Local deformation analysis of the workpiece-fixture system

Without the loss of generality, consider the local deformation of the workpiece-fixture system in step *j*. The matrix form of the solution can be expressed as follows at all contact points

$$\Delta \mathbf{d}_{\mathrm{P}}^{(j)} = \left(\mathbf{K}_{\mathrm{P}}^{(j)}\right)^{-1} \mathbf{f}_{\mathrm{P}}^{(j)} \tag{4.160}$$

where

$$\Delta \mathbf{d}_{\mathrm{P}}^{(j)} = \left[\Delta \mathbf{d}_{\mathrm{P1}}^{(j)\mathrm{T}}, \Delta \mathbf{d}_{\mathrm{P2}}^{(j)\mathrm{T}}, \cdots, \Delta \mathbf{d}_{\mathrm{P}(m+j-2)}^{(j)\mathrm{T}}\right]^{\mathrm{T}} \tag{4.161}$$

Deviation of the position and orientation of the workpiece

Consider a workpiece as shown in Figure 4.26. $\mathbf{r}_{\mathrm{w}}^{(j)}$ and $\boldsymbol{\theta}_{\mathrm{w}}^{(j)}$ represent the position and orientation of the workpiece with respect to {GCS} in step *j*, respectively. $\mathbf{r}_k^{\mathrm{w}} = [x_k^{\mathrm{w}}, y_k^{\mathrm{w}}, z_k^{\mathrm{w}}]^{\mathrm{T}}$ is the position of the *k*th contact point in the {WCS}. When {WCS} is assumed to be aligned with {GCS}, the variation of the position and rotation of the workpiece, $\Delta \mathbf{q}_{\mathrm{w}}^{(j)}$, produced by the local deformation, $\Delta \mathbf{d}_{\mathrm{P}}^{(j)}$, of passive elements obeys

$$\mathbf{E}_{\mathrm{P}}^{(j)T} \Delta \mathbf{q}_{\mathrm{w}}^{(j)} = \mathbf{T}(\boldsymbol{\theta}_{\mathrm{c}}^{(j)}) \Delta \mathbf{d}_{\mathrm{P}}^{(j)} \tag{4.162}$$

with

$$\begin{aligned} \Delta \mathbf{q}_{\mathrm{w}}^{(j)} &= \left[\Delta \mathbf{r}_{\mathrm{w}}^{(j)\mathrm{T}}, \Delta \boldsymbol{\theta}_{\mathrm{w}}^{(j)\mathrm{T}}\right]^{\mathrm{T}} \\ &= \left[\Delta x_{\mathrm{w}}^{(j)}, \Delta y_{\mathrm{w}}^{(j)}, \Delta z_{\mathrm{w}}^{(j)}, \Delta \alpha_{\mathrm{w}}^{(j)}, \Delta \beta_{\mathrm{w}}^{(j)}, \Delta \gamma_{\mathrm{w}}^{(j)}\right]^{\mathrm{T}} \end{aligned} \tag{4.163}$$

$$\mathbf{E}_{\mathrm{P}}^{(j)} = [E_{\mathrm{P1}}^{(j)}, E_{\mathrm{P2}}^{(j)}, \cdots, E_{\mathrm{P}(m+j-2)}^{(j)}] \quad [4.164]$$

$$\mathbf{E}_{\mathrm{P}k}^{(j)} = \begin{bmatrix} 1 & 0 & 0 \\ 0 & 1 & 0 \\ 0 & 0 & 1 \\ 0 & z_k^{\mathrm{w}} & -y_k^{\mathrm{w}} \\ -z_k^{\mathrm{w}} & 0 & x_k^{\mathrm{w}} \\ y_k^{\mathrm{w}} & -x_k^{\mathrm{w}} & 0 \end{bmatrix} \quad [4.165]$$

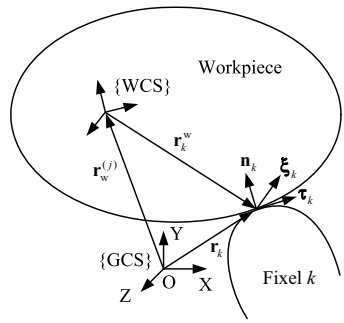

Figure 4.26. *Coordinate system of a workpiece-fixture system*

Optimization of clamping sequence

According to equation [4.162], given a clamping sequence, the location accuracy of the workpiece in step j can be calculated. However, it is possible to specify different clamping sequences for the same fixture consisting of m locators and n clamps and each sequence may give rise to a variant location accuracy of the workpiece. Thus, the optimal clamping sequence corresponds to the solution minimizing the deviation of location accuracy in the final step $n + 2$.

$$\begin{aligned} &\min \quad \Delta = \sqrt{\Delta\mathbf{q}_{\mathrm{w}}^{(n+2)\mathrm{T}} \Delta\mathbf{q}_{\mathrm{w}}^{(n+2)}} \\ &\text{s.t.} \\ &\qquad \mathbf{E}_{\mathrm{P}}^{(n+2)\mathrm{T}} \Delta\mathbf{q}_{\mathrm{w}}^{(n+2)} = \mathbf{T}(\boldsymbol{\theta}_c^{(n+2)}) \Delta\mathbf{d}_{\mathrm{P}}^{(n+2)} \\ &\qquad \Delta\mathbf{d}_{\mathrm{P}}^{(n+2)} = (\mathbf{K}_{\mathrm{P}}^{(n+2)})^{-1} \mathbf{f}_{\mathrm{P}}^{(n+2)} \end{aligned} \quad [4.166]$$

Note that the objective function Δ is a function of the clamping sequence.

4.5.3.2. *Optimization of clamping sequence for low-stiffness workpiece*

Similarly, the optimal clamping sequence for a low-stiffness workpiece can be achieved by minimizing the maximum module of nodal deflection of the workpiece in the final step. Based on equation [4.159], the following model can be used to this end.

$$\begin{aligned} \min \quad \Delta &= \max_{l} \sqrt{(\left\| \boldsymbol{\delta}_{\mathrm{w}l}^{(n+2)} \right\|)} \\ &= \max_{l} (\sqrt{(\delta x_{\mathrm{w}l}^{(n+2)})^2 + (\delta y_{\mathrm{w}l}^{(n+2)})^2 + (\delta z_{\mathrm{w}l}^{(n+2)})^2}) \end{aligned} \quad [4.167]$$

s.t.

$$\boldsymbol{\delta}_{\mathrm{w}l}^{(n+2)} = \sum_{j=1}^{n+2} \delta \mathbf{d}_{\mathrm{w}l}^{(j)}, \quad (1 \leq l \leq r)$$

Bibliography

[AHM 07] AHMADI K., AHMADIAN H., "Modeling machine tool dynamics using a distributed parameter tool-holder joint interface", *International Journal of Machine Tools and Manufacture*, vol. 47, nos. 12–13, pp. 1916–1928, 2007.

[AHM 10a] AHMADI K., ISMAIL F., "Machining chatter in flank-milling", *International Journal of Machine Tools and Manufacture*, vol. 50, no. 1, pp. 75–85, 2010.

[AHM 10b] AHMADIAN H., NOURMOHAMMADI M., "Tool point dynamics prediction by a three-component model utilizing distributed joint interfaces", *International Journal of Machine Tools and Manufacture*, vol. 50, no. 11, pp. 998–1005, 2010.

[AKS 98] AKSHAY J., KAPOOR S.G., DEVOR R.E. *et al.*, "A model-based approach for radial run-out estimation in the facemilling process", *Transactions of NAMRC/SME*, pp. 261–266, 1998.

[ALB 60] ALBRECHT P., "New developments in the theory of metal-cutting process, Part I: the ploughing process in metal cutting", *Journal of Engineering for Industry – Transactions of the ASME*, vol. 82, no. 4, pp. 348–357, 1960.

[ALB 61] ALBRECHT P., "New developments in the theory of the metal-cutting process, Part II: the theory of chip formation", *Journal of Engineering for Industry – Transactions of the ASME*, vol. 83, pp. 557–568, 1961.

[ALB 13] ALBERTELLI P., GOLETTI M., MONNO M., "A new receptance coupling substructure analysis methodology to improve chatter free cutting conditions prediction", *International Journal of Machine Tools and Manufacture*, vol. 72, pp. 16–24, 2013.

[ALT 91] ALTINTAS Y., SPENCE A., TLUSTY J., "End-milling force algorithms for CAD systems", *CIRP Annals-Manufacturing Technology*, vol. 40, no. 1, pp. 31–34, 1991.

[ALT 92] ALTINTAS Y., CHAN P., "In-process detection and suppression of chatter in milling", *International Journal of Machine Tools and Manufacture*, vol. 32, no. 3, pp. 329–347, 1992.

[ALT 95] ALTINTAS Y., BUDAK E., "Analytical prediction of stability lobes in milling", *CIRP Annals – Manufacturing Technology*, vol. 44, no. 1, pp. 357–362, 1995.

Milling Simulation: *Metal Milling Mechanics, Dynamics and Clamping Principles*,
First Edition. Weihong Zhang and Min Wan.

[ALT 99a] ALTINTAS Y., ENGIN S., BUDAK E., "Analytical stability prediction and design of variable pitch cutters", *Journal of Manufacturing Science and Engineering – Transactions of the ASME*, vol. 121, no. 2, pp. 173–178, 1999.

[ALT 99b] ALTINTAS Y., SHAMOTO E., LEE P. *et al.*, "Analytical prediction of stability lobes in ball end-milling", *Journal of Manufacturing Science and Engineering – Transactions of the ASME*, vol. 121, no. 4, pp. 586–592, 1999.

[ALT 00] ALTINTAS Y., *Manufacturing Automation*, Cambridge University Press, 2000.

[ALT 08] ALTINTAS Y., STEPAN G., MERDOL D. *et al.*, "Chatter stability of milling in frequency and discrete time domain", *CIRP Journal of Manufacturing Science and Technology*, vol. 1, pp. 35–44, 2008.

[ALT 12] ALTINTAS Y., *Manufacturing Automation, 2nd edition*, Cambridge University Press, 2012.

[ALT 13] ALTINTAS Y., KILIC Z.M., "Generalized dynamic model of cutting operations", *CIRP Annals – Manufacturing Technology*, vol. 62, no. 1, pp. 47–50, 2013.

[ANT 03] ANTONIADIS A., SAVAKIS C., BILALIS N. *et al.*, "Prediction of surface topomorphy and roughness in ball end milling", *The International Journal of Advanced Manufacturing Technology*, vol. 21, no. 12, pp. 965–971, 2003.

[ARA 08] ARAS E., Cutter-workpiece engagement identification in multi-axis milling, PhD thesis, University of British Columbia, 2008.

[ARA 11] ARAS E., FENG H.Y., "Vector model-based workpiece update in multi-axis milling by moving surface of revolution", *International Journal of Advanced Manufacturing Technology*, vol. 52, nos. 9–12, pp. 913–927, 2011.

[ARM 85] ARMAREGO E.J.A., WHITFIELD R.C., "Computer-based modeling of popular machining operations for forces and power prediction", *CIRP Annals – Manufacturing Technology*, vol. 34, no. 1, pp. 65–69, 1985.

[ARM 89] ARMAREGO E.J.A., DESPANDE N.P., "Computerized predictive cutting model for cutting forces in end-milling including eccentricity effects", *CIRP Annals – Manufacturing Technology*, vol. 38, no. 1, pp. 45–49, 1989.

[ASA 89] ASADA H., KITAGAWA M., "Kinematic analysis and planning for form closure grasps by robotic hands', *Robotics and Computer Integrated Manufacturing*, vol. 5, no. 4, pp. 293–299, 1989.

[AZE 04] AZEEM A., FENG H.Y., WANG L.H., "Simplified and efficient calibration of a mechanistic cutting force model for ball end milling", *International Journal of Machine Tools and Manufacture*, vol. 44, nos. 2–3, pp. 291–298, 2004.

[BAY 03] BAYLY P.V., HALLEY J.E., MANN B.P. *et al.*, "Stability of interrupted cutting by temporal finite element analysis", *Journal of Manufacturing Science and Engineering – Transactions of the ASME*, vol. 125, no. 2, pp. 220–225, 2003.

[BOH 02] BOHEZ E.L.J., "Compensation for systematic errors in 5-axis NC machining", *Computer-Aided Design*, vol. 34, no. 5, pp. 391–403, 2002.

[BOU 03] BOUZAKIS K.D., AICHOUH P., EFSTATHIOU K., "Determination of the chip geometry, cutting force and roughness in free form surfaces finishing milling with ball end tools", *International Journal of Machine Tools and Manufacture*, vol. 43, no. 5, pp. 499–514, 2003.

[BRA 05] BRAVO U., ALTUZARRA O., LACALLE L.N.L.D. *et al.*, "Stability limits of milling considering the flexibility of the workpiece and the machine", *International Journal of Machine Tools and Manufacture*, vol. 45, no. 15, pp. 1669–1680, 2005.

[BUD 92] BUDAK E., ALTINTAS Y., "Flexible milling force model for improved surface error predictions", *Proceedings of Engineering System Design and Analysis*, *Transactions of the ASME*, vol. 47, no. 1, pp. 89–94, 1992.

[BUD 94] BUDAK E., ALTINTAS Y., "Peripheral milling conditions for improved dimensional accuracy", *International Journal of Machine Tools and Manufacture*, vol. 34, no. 7, pp. 907–918, 1994.

[BUD 95] BUDAK E., ALTINTAS Y., "Modeling and avoidance of static form errors in peripheral milling of plates", *International Journal of Machine Tools and Manufacture*, vol. 35, no. 3, pp. 459–476, 1995.

[BUD 96] BUDAK E., ALTINTAS Y., ARMAREGO E.J.A., "Prediction of milling force coefficients from orthogonal cutting data", *Journal of Manufacturing Science and Engineering – Transactions of the ASME*, vol. 118, no. 2, pp. 216–224, 1996.

[BUD 98a] BUDAK E., ALTINTAS Y., "Analytical prediction of chatter stability in milling, Part I: General formulation", *Journal of Dynamic System, Measurements, and Control – Transactions of the ASME*, vol. 120, no. 1, pp. 22–30, 1998.

[BUD 98b] BUDAK E., ALTINTAS Y., "Analytical prediction of chatter stability in milling, Part II: Application of general formulation to common milling systems", *Journal of Dynamic System, Measurements, and Control – Transactions of the ASME*, vol. 120, no. 1, pp. 31–36, 1998.

[BUD 03a] BUDAK E., "An analytical design method for milling cutters with nonconstant pitch to increase stability, Part I: Theory", *Journal of Manufacturing Science and Engineering – Transactions of the ASME*, vol. 125, no. 1, pp. 29–34, 2003.

[BUD 03b] BUDAK E., "An analytical design method for milling cutters with nonconstant pitch to increase stability, Part II: Application", *Journal of Manufacturing Science and Engineering – Transactions of the ASME*, vol. 125, no. 1, pp. 35–38, 2003.

[CAM 03] CAMPOMANES M.L., ALTINTAS Y., "An improved time domain simulation for dynamic milling at small radial immersions", *Journal of Manufacturing Science and Engineering – Transactions of the ASME*, vol. 125, no. 3, pp. 416–422, 2003.

[CHE 89] CHETAEV N.G., *Theoretical Mechanics*, Springer, 1989.

[CHE 97] CHENG P.J., TSAY J.T., LIN S.C., "A study on instantaneous cutting force coefficients in face-milling", *International Journal of Machine Tools and Manufacture*, vol. 37, no. 10, pp. 1393–1408, 1997.

[CHO 97] CHOI B.K., KIM D.H., JERARD R.B., "C-space approach to tool path generation for die and mould machining", *Computer-Aided Design*, vol. 29, no. 9, pp. 657–669, 1997.

[CHO 03] CHO M.W., SEO T.I., KWON H.D., "Integrated error compensation method using OMM system for profile-milling operation", *Journal of Materials Processing Technology*, vol. 136, nos. 1–3, pp. 88–99, 2003.

[CIF 10] CIFUENTES E.D., GARCIA H.P., VILLASENOR M.G. *et al.*, "Dynamic analysis of runout correction in milling", *International Journal of Machine Tools and Manufacture*, vol. 50, no. 8, pp. 709–717, 2010.

[COG 92] COGUN C., "The importance of the application sequence of clamping forces on workpiece accuracy", *Journal of Engineering for Industry – Transactions of the ASME*, vol. 114, no. 4, pp. 539–543, 1992.

[DAN 10] DANG J.W., ZHANG W.H., YANG Y. *et al.*, "Cutting force modeling for flat end milling including bottom-edge cutting effect", *International Journal of Machine Tools and Manufacture*, vol. 50, no. 11, pp. 986–997, 2010.

[DEM 94] DEMETER E.C., "Restraint analysis of fixtures which rely on surface contact", *Journal of Engineering for Industry – Transactions of the ASME*, vol. 116, no. 2, pp. 207–215, 1994.

[DEM 01] DEMETER E.C., XIE W., CHOUDHURI S. *et al.*, "A model to predict minimum required clamp pre-loads in light of fixture-workpiece compliance", *International Journal of Machine Tools and Manufacture*, vol. 41, no. 7, pp. 1031–1054, 2001.

[DEP 06] DEPINCE P., HASCOET J.Y., "Active integration of tool deflection effects in end milling, Part 2: Compensation of tool deflection", *International Journal of Machine Tools and Manufacture*, vol. 46, no. 9, pp. 945–956, 2006.

[DES 09] DESAI K.A., AGARWAL P.K., RAO P.V.M., "Process geometry modeling with cutter runout for milling of curved surfaces", *International Journal of Machine Tools and Manufacture*, vol. 49, nos. 12–13, pp. 1015–1028, 2009.

[DOM 10] DOMBOVARI Z., ALTINTAS Y., STEPAN G., "The effect of serration on mechanics and stability of milling cutters", *International Journal of Machine Tools and Manufacture*, vol. 50, no. 6, pp. 511–520, 2010.

[EHM 94] EHMANN K.F., HONG M.S., "A generalized model of the surface generation process in metal cutting", *CIRP Annals – Manufacturing Technology*, vol. 43, no. 1, pp. 483–486, 1994.

[EIS 94] EISENBERGER M., "Vibration frequencies for beams on variable one- and two-parameter elastic foundations", *Journal of Sound and Vibration*, vol. 176, no. 5, pp. 577–584, 1994.

[ELB 94] ELBESTAWI M.A., ISMAIL F., YUEN K.M., "Surface topography characterization in finish-milling, *International Journal of Machine Tools and Manufacture*, vol. 34, no. 2, pp. 245–255, 1994.

[ELM 98] EL MOUNAYRI H., SPENCE A.D., ELBESTAWI M.A., "Milling process simulation – A generic solid modeller based paradigm", *Journal of Manufacturing Science and Engineering – Transactions of the ASME*, vol. 120, no. 2, pp. 213–221, 1998.

[END 90] ENDRES W.J., SUTHERLAND J.W., DEVOR R.E. *et al.*, "A dyanamic model of the cutting force system in turning process", *Proceedings of the ASME Symposium on Monitoring and Control for Manufacturing Processes*, pp. 193–212, 1990.

[END 95] ENDRES W.J., DEVOR R.E. *et al.*, "A dual-mechanism approach to the prediction of machining forces, Part 1: Model development", *Journal of Engineering for Industry – Transactions of the ASME*, vol. 117, no. 4, pp. 526–533, 1995.

[ENG 01] ENGIN S., ALTINTAS Y., "Mechanics and dynamics of general milling cutters-Part I: helical end-mills", *International Journal of Machine Tools and Manufacture*, vol. 41, no. 15, pp. 2195–2212, 2001.

[ERD 06] ERDIM H., LAZOGLU I., OZTURK B., "Feedrate scheduling strategies for free-form surfaces", *International Journal of Machine Tools and Manufacture*, vol. 46, nos. 7–8, pp. 747–757, 2006.

[EWI 00] EWINS D.J., *Model Testing: Theory, Practice and Application*, Research Studies Press LTD, Hertfordshire, 2nd edition, 2000.

[FEN 94a] FENG H.Y., MENQ C.H., "The prediction of the cutting forces in the ball end milling process – I. Model formulation and model building procedure", *International Journal of Machine Tools and Manufacture*, vol. 34, no. 5, pp. 697–710, 1994.

[FEN 94b] FENG H.Y., MENQ C.H., "The prediction of the cutting forces in the ball end milling process – II. Cut geometry analysis and model verification", *International Journal of Machine Tools and Manufacture*, vol. 34, no. 5, pp. 711–719, 1994.

[FER 08a] FERRY W., YIP-HOI D., "Cutter-workpiece engagement calculations by parallel slicing for five-axis flank milling of jet engine impellers", *Journal of Manufacturing Science and Engineering – Transactions of the ASME*, vol. 130, no. 5, pp. 051011, 2008.

[FER 08b] FERRY W., ALTINTAS Y., "Virtual five-axis flank milling of jet engine impellers-Part I: mechanics of five-axis flank-milling", *Journal of Manufacturing Science and Engineering – Transactions of the ASME*, vol. 130, p. 011005, 2008.

[FUS 03] FUSSELL B.K., JERARD R.B., HEMMETT J.G., "Modeling of cutting geometry and forces for 5-axis sculptured surface machining", *Computer-Aided Design*, vol. 35, no. 4, pp. 333–346, 2003.

[GAO 06] GAO T., ZHANG W.H., QIU K.P. *et al.*, "Numerical simulation of machined surface topography and roughness in milling process", *Journal of Manufacturing Science and Engineering – Transactions of the ASME*, vol. 128, no. 1, pp. 96–103, 2006.

[GON 09] GONG H., WANG N., "Analytical calculation of the envelope surface for generic milling tools directly from CL-data based on the moving frame method", *Computer-Aided Design*, vol. 41, no. 11, pp. 848–855, 2009.

[GON 10] GONZALO O., BERISTAIN J., JAUREGI H. *et al.*, "A method for the identification of the specific force coefficients for mechanistic milling simulation", *International Journal of Machine Tools and Manufacture*, vol. 50, no. 9, pp. 765–774, 2010.

[GRA 04] GRADISEK J., KALVERAM M., WEINERT K., "Mechanistic identification of specific force coefficients for a general end-mill", *International Journal of Machine Tools and Manufacture*, vol. 44, no. 4, pp. 401–414, 2004.

[GRA 05] GRADISEK J., KALVERAM M., INSPERGER T. *et al.*, "On the stability prediction for milling", *International Journal of Machine Tools and Manufacture*, vol. 45, pp. 769–781, 2005.

[GUO 01] GUO H.X., LUO Y.X., HE Z.M., "The robustness and optimal design of the positioning scheme of fixture", *Machinery Manufacturing Engineer*, vol. 4, pp. 34–35, 2001.

[HOF 91] HOFFMAN E.G., *Jig and Fixture Design*, Delmar Publishers, Albany, New York, 1991.

[HUR 02] HURTADO J.F., MELKOTE S.N., "Modeling and analysis of the effect of fixture-workpiece conformability on static stability", *Journal of Manufacturing Science and Engineering – Transactions of the ASME*, vol. 124, no. 2, pp. 234–241, 2002.

[IMA 98] IMANI B.M., SADEGHI M.H., ELBESTAWI M.A., "An improved process simulation system for ball end milling of sculptured surfaces", *International Journal of Machine Tools and Manufacture*, vol. 38, no. 9, pp. 1089–1107, 1998.

[IMA 01] IMANI B.M., ELBESTAWI M.A., "Geometric simulation of ball end milling operations", *Journal of Manufacturing Science and Engineering – Transactions of the ASME*, vol. 123, no. 2, pp. 177–184, 2001.

[INS 02] INSPERGER T., STEPAN G., "Semi-discretization method for delayed systems", *International Journal for Numerical Methods in Engineering*, vol. 55, no. 5, pp. 503–518, 2002.

[INS 04] INSPERGER T., STEPAN G., "Updated semi-discretization method for periodic delay-differential equations with discrete delay", *International Journal for Numerical Methods in Engineering*, vol. 61, no. 1, pp. 117–141, 2004.

[INS 07] INSPERGER T., STEPAN G., TURI J., "State-dependent delay in regenerative turning processes", *Nonlinear Dynamics*, vol. 47, nos. 1–3, pp. 275–283, 2007.

[INS 08a] INSPERGER T., BARTON D.A.W., STEPAN G., "Criticality of Hopf bifurcation in state-dependent delay model of turning processes", *International Journal of Non-Linear Mechanics*, vol. 43, no. 2, pp. 140–149, 2008.

[INS 08b] INSPERGER T., MANN B.P., SURMANN T. *et al.*, "On the chatter frequencies of milling process with runout", *International Journal of Machine Tools and Manufacture*, vol. 48, no. 10, pp. 1081–1089, 2008.

[ISM 93] ISMAIL F., ELBESTAWI M.A., DU R. *et al.*, "Generation of milled surfaces including tool dynamics and wear", *Journal of Engineering for Industry – Transactions of the ASME*, vol. 115, no. 3, pp. 245–252, 1993.

[JOH 85] JOHNSON K.L., *Contact Mechanics*, Cambridge University Press, 1985.

[JUN 05a] JUNG T.S., MING Y.Y., LEE K.J., "A new approach to analyzing machined surface by ball end milling, Part I: Formulation of characteristic lines of cut remainder", *The International Journal of Advanced Manufacturing Technology*, vol. 25, nos. 9–10, pp. 833–840, 2005.

[JUN 05b] JUNG T.S., MING Y.Y., LEE K.J., "A new approach to analyzing machined surface by ball end milling, Part II: Roughness prediction and experimental verification", *The International Journal of Advanced Manufacturing Technology*, vol. 25, nos. 9–10, pp. 841–849, 2005.

[KAR 10] KARUNAKARAN K.P., SHRINGI R., RAMAMURTHI D. *et al.*, "Octree-based NC simulation system for optimization of feed rate in milling using instantaneous force model", *International Journal of Advanced Manufacturing Technology*, vol. 46, no. 5, pp. 465–490, 2010.

[KIM 06] KIM Y.H., KO S.L., "Improvement of cutting simulation using the octree method", *International Journal of Advanced Manufacturing Technology*, vol. 28, nos. 11-12, pp. 1152–1160, 2006.

[KLI 82a] KLINE W.A., DEVOR R.E., LINDBERG J.R., "The prediction of cutting forces in end milling with application to cornering cuts", *International Journal of Machine Tool Design and Research*, vol. 22, no. 1, pp. 7–22, 1982.

[KLI 82b] KLINE W.A., DEVOR R.E., SHAREEF I.A., "The prediction of surface accuracy in end milling", *Journal of Engineering for Industry – Transactions of the ASME*, vol. 104, no. 3, pp. 272–278, 1982.

[KLI 83] KLINE W.A., DEVOR R.E., "The effect of runout on cutting geometry and forces in end-milling", *International Journal of Machine Tool Design and Research*, vol. 23, nos. 2–3, pp. 123–140, 1983.

[KO 02] KO J.H., YUN W.S., CHO D.W., EHMANN K.F., "Development of a virtual machining system – Part I: approximation of the size effect for cutting force prediction", *International Journal of Machine Tools and Manufacture*, vol. 42, no. 15, pp. 1595–1605, 2002.

[KO 05] KO J.H., CHO D.W., "3D ball end milling force model using instantaneous cutting force coefficients", *Journal of Manufacturing Science and Engineering – Transactions of the ASME*, vol. 127, no. 1, pp. 1–12, 2005.

[KOE 61] KOENIGSBERGER F., SABBERWAL A.J.P., "An investigation into the cutting force pulsations during milling operations", *International Journal of Machine Tool Design and Research*, vol. 1, nos. 1–2, pp. 15–33, 1961.

[KOE 67] KOENIGSBERGER F., TLUSTY J., *Machine Tool Structure – Vol I: Stability Against Chatter*, Pergamon press, 1967.

[KOL 86] KOLMANOVSKII V.B., NOSOV V.R., *Stability of Functional Differential Equations*, Academic Press, London, 1986.

[KOP 90] KOPS L., VO D.T., "Determination of the equivalent diameter of an end mill based on its compliance", *CIRP Annals – Manufacturing Technology*, vol. 39, no. 1, pp. 93–96, 1990.

[LAG 98] LAGARIAS J.C., REEDS J.A., WRIGHT M.H. *et al.*, "Convergence properties of the Nelder-Mead simplex method in low dimensions", *SIAM Journal of Optimization*, vol. 9, no. 1, pp. 112–147, 1998.

[LAK 88] LAKSHMIKANTHAM V., TRIGIANTE D., *Theory of Difference Equation, Numerical Methods and Applications*, Academic Press, London, 1988.

[LAN 85] LANCASTER P., TISMENETSKY M., *The Theory of Matrices, 2nd edition*, Academic Press Inc, 1985.

[LAN 03] LANDON Y., SEGONDS S., MOUSSEIGNE M. *et al.*, "Correction of milling tool paths by tool positioning defect compensation", *Proceedings of the Institution of Mechanical Engineers, Part B: Journal of Engineering Manufacture*, vol. 217, no. 8, pp. 1063–1073, 2003.

[LAR 03] LARUE A., ANSELMETTI B., "Deviation of a machined surface in flank milling", *International Journal of Machine Tools and Manufacture*, vol. 43, no. 2, pp. 129–138, 2003.

[LAW 99] LAW K.M.Y., GEDDAM A., OSTAFIEV V.A., "A process design approach to error compensation in the end milling of pockets", *Journal of Materials Processing Technology*, vol. 90, pp. 238–244, 1999.

[LAW 03] LAW K.M.Y., GEDDAM A., "Error compensation in the end milling of pockets: A methodology", *Journal of Materials Processing Technology*, vol. 139, nos. 1–3, pp. 21–27, 2003.

[LAZ 03] LAZOGLU I., "Sculpture surface machining: a generalized model of ball end milling force system", *International Journal of Machine Tools and Manufacture*, vol. 43, no. 5, pp. 453–462, 2003.

[LAZ 11] LAZOGLU I., BOZ Y., ERDIM H., "Five-axis milling mechanics for complex free form surfaces", *CIRP Annals - Manufacturing Technology*, vol. 60, no. 1, pp. 117–120, 2011.

[LEI 11] LEISSA A.W., QATU M.S., *Vibration of Continuous Systems*, McGraw Hill Professional, 2011.

[LI 01] LI M.B., CHENG Y., ZHANG B.P. *et al.*, "Web-based distributed design method of fixture scheme", *China Mechanical Engineering*, vol. 12, no. 9, pp. 1011–1014, 2001.

[LI 02] LI S.J., LIU R.S., ZHANG A.J., "Study on an end-milling generation surface model and simulation taking into account of the main axle tolerance", *Journal of Materials Processing Technology*, vol. 129, no. 1, pp. 86–90, 2002.

[LI 08] LI J.G., YAO Y.X., XIA P.J. *et al.*, "Extended octree for cutting force prediction", *International Journal of Advanced Manufacturing Technology*, vol. 39, nos. 9–10, pp. 866–873, 2008.

[LI 10] LI J.G., DING J.A., GAO D. *et al.*, "Quadtree-array-based workpiece geometric representation on three-axis milling process simulation", *International Journal of Advanced Manufacturing Technology*, vol. 50, no. 5-8, pp. 677–687, 2010.

[LI 14] LI Z., LIU Q., MING X.Z. *et al.*, "Cutting force prediction and analytical solution of regenerative chatter stability for helical milling operation", *International Journal of Advanced Manufacturing Technology*, vol. 73, nos. 1–4, pp. 433–442, 2014.

[LIA 94] LIANG S.Y., WANG J.J.J., "Milling force convolution modeling for identification of cutter axis offset", *International Journal of Machine Tools and Manufacture*, vol. 34, no. 8, pp. 1177–1190, 1994.

[LIU 06] LIU X.B., SOSHI M., SAHASRABUDHE A. *et al.*, "A geometrical simulation system of ball end finish milling process and its application for the prediction of surface micro features", *Journal of Manufacturing Science and Engineering – Transactions of the ASME*, vol. 128, no. 1, pp. 74–85, 2006.

[MAN 04] MANN B.P., BAYLY P.V., DAVIES M.A. *et al.*, "Limit cycles, bifurcations, and accuracy of the milling process", *Journal of Sound and Vibration*, vol. 277, nos. 1–2, pp. 31–48, 2004.

[MAN 05] MANN B.P., YOUNG K.A., SCHMITZ T.L. *et al.*, "Simultaneous stability and surface location error predictions in milling", *Journal of Manufacturing Science and Engineering – Transactions of the ASME*, vol. 127, no. 3, pp. 446–453, 2005.

[MAR 45] MARTELLOTTI M.E., "An analysis of the milling process, Part II: Down-milling", *Transactions of the ASME*, vol. 67, pp. 233–251, 1945.

[MAS 56] MASUKO M., "Fundamental researches on the metal cutting (2nd Report) - the theoretical equation of the indentation – force acting on a cutting edge and its experimental discussion", *Transactions of Japanese Society of Mechanical Engineers*, vol. 22, pp. 371–377, 1956.

[MER 44] MERCHANT M.E., "Basic mechanics of the metal - cutting process", *Journal of Applied Mechanics – Transactions of the ASME*, vol. 66, pp. A168–A175, 1944.

[MER 04] MERDOL S.D., ALTINTAS Y., "Multi frequency solution of chatter stability for low immersion milling", *Journal of Manufacturing Science and Engineering – Transactions of the ASME*, vol. 126, no. 3, pp. 459–466, 2004.

[MER 08] MERDOL S.D., ALTINTAS Y., "Virtual simulation and optimization of milling operations - Part I: Process simulation", *Journal of Manufacturing Science and Engineering – Transactions of the ASME*, vol. 130, p. 051004, 2008.

[MIN 90] MINIS I., YANUSHEVSKY T., TEMBO R. *et al.*, "Analysis of linear and nonlinear chatter in milling", *CIRP Annals – Manufacturing Technology*, vol. 39, pp. 459–462, 1990.

[NEE 95] NEE A.Y.C., WHYBREW K., KUMAR A.S., *Advanced Fixture Design for FMS*, Springer-Verlag, London, 1995.

[NEE 05] NEE A.Y.C., KUMAR A.S., TAO Z.J. *An Advanced Treatise on Fixture Design and Planning*, World Scientific, Singapore, 2005.

[NEL 65] NELDER J.A., MEAD R., "A simplex method for function minimization", *Computer Journal*, vol. 7, pp. 308–313, 1965.

[PAK 04] PAKSIRI C., PARNICHKUN M., "Geometric and force errors compensation in a 3-axis CNC milling machine", *International Journal of Machine Tools and Manufacture*, vol. 44, pp. 1283–1291, 2004.

[PAR 03] PARK S.S., ALTINTAS Y., MOVAHHEDY M., "Receptance coupling for end-mills", *International Journal of Machine Tools and Manufacture*, vol. 43, pp. 889–896, 2003.

[PAT 08] PATEL B.R., MANN B.P., YOUNG K.A., "Uncharted islands of chatter instability in milling", *International Journal of Machine Tools and Manufacture*, vol. 48, pp. 124–134, 2008.

[PIL 94] PILKEY W.D., WUNDERLICH W., *Mechanics of Structures: Variational and Computational Methods*, CRC Press, 1994.

[QIN 05] QIN G.H., ZHANG W.H., WAN M., "Modeling and application of workpiece stability based on the linear programming technique", *Chinese Journal of Mechanical Engineering* (in Chinese), vol. 41, no. 9, pp. 33–37, 2005.

[QIN 06a] QIN G.H., ZHANG W.H., WAN M., "Analysis and optimal design of fixture clamping sequence", *Journal of Manufacturing Science and Engineering – Transactions of the ASME*, vol. 128, no. 2, pp. 482–493, 2006.

[QIN 06b] QIN G.H., ZHANG W.H., WAN M., "A mathematical approach to analysis and optimal design of fixture locating scheme", *The International Journal of Advanced Manufacturing Technology*, vol. 29, pp. 349–359, 2006.

[QIN 07a] QIN G.H., ZHANG W.H., "Modeling and analysis of workpiece stability based on the linear programming method", *The International Journal of Advanced Manufacturing Technology*, vol. 32, nos. 1-2, pp. 78–91, 2007.

[QIN 07b] QIN G.H., ZHANG W.H., WU Z.X. *et al.*, "Systematic modeling of workpiece-fixture geometric default and compliance for the prediction of workpiece machining error", *Journal of Manufacturing Science and Engineering – Transactions of the ASME*, vol. 129, no. 4, pp. 789–801, 2007.

[QIN 08] QIN G.H., ZHANG W.H., WAN M., "A machining-dimension-based approach to locating scheme design", *Journal of Manufacturing Science and Engineering - Transactions of the ASME*, vol. 130, no. 5, 2008.

[RAO 06] RAO V.S., RAO P.V.M., "Tool deflection compensation in peripheral milling of curved geometries", *International Journal of Machine Tools and Manufacture*, vol. 46, no. 5, pp. 2036–2043, 2006.

[RAO 11] RAO S.S., *Mechanical Vibrations*, Prentice Hall, 5th edition, 2011.

[RAT 04a] RATCHEV S., LIU S., HUANG W. *et al.*, "A flexible force model for end milling of low-rigidity parts", *Journal of Materials Processing Technology*, vol. 153/154, pp. 134–138, 2004.

[RAT 04b] RATCHEV S., LIU S., HUANG W. *et al.*, "Milling error prediction and compensation in machining of low-rigidity parts", *International Journal of Machine Tools and Manufacture*, vol. 44, pp. 1629–1641, 2004.

[RAT 06] RATCHEV S., LIU S., HUANG W. *et al.*, "An advanced FEA based force induced error compensation strategy in milling", *International Journal of Machine Tools and Manufacture*, vol. 46, pp. 542–551, 2006.

[RON 99] RONG Y.M., ZHU Y.X., *Computer Aided Fixture Design*, Marcel Dekker, New York, 1999.

[RON 02] RONG Y.M., ZHU Y.X., LUO Z.B., *Computer Aided Fixture Design*, China Mechanical Press, 2002.

[RON 05] RONG Y.M., HUANG S.H., HOU Z.K., *Advanced Computer-Aided Fixture Design*, Elsevier, 2005.

[ROT 07] ROTH D., GRAY P., ISMAIL F. *et al.*, "Mechanistic modeling of 5-axis milling using an adaptive and local depth buffer", *Computer-Aided Design*, vol. 39, no. 4, pp. 302–312, 2007.

[RUD 76] RUDIN W., *Principles of Mathematical Analysis*, McGraw-Hill, 3rd edition, 1976.

[RYU 03] RYU S.H., LEE H.S., CHU C.N., "The form error prediction in side wall machining considering tool deflection", *International Journal of Machine Tools and Manufacture*, vol. 43, no. 14, pp. 1405–1411, 2003.

[RYU 05] RYU S.H., CHU C.N., "The form error reduction in side wall machining using successive down- and up-milling", *International Journal of Machine Tools and Manufacture*, vol. 45, nos. 12–13, pp. 1523–1530, 2005.

[SAD 03] SADEGHI M.H., HAGHIGHAT H., ELBESTAWI M.A., "A solid modeler based ball end milling process simulation", *International Journal of Advanced Manufacturing Technology*, vol. 22, nos. 11-12, pp. 775–785, 2003.

[SCH 00] SCHMITZ T., DONALDSON R., "Predicting high-speed machining dynamics by substructure analysis", *CIRP Annals – Manufacturing Technology*, vol. 49, no. 1, pp. 303–308, 2000.

[SCH 05] SCHMITZ T.L., DUNCAN G.S., "Three-component receptance coupling substructure analysis for tool point dynamics prediction", *Journal of Manufacturing Science and Engineering – Transactions of the ASME*, vol. 127, no. 4, pp. 781–790, 2005.

[SCH 07] SCHMITZ T.L., POWELL K., WON D. *et al.*, "Shrink fit tool holder connection stiffness/damping modeling for frequency response prediction in milling", *International Journal of Machine Tools and Manufacture*, vol. 47, no. 9, pp. 1368–1380, 2007.

[SCH 09] SCHMITZ T.L., SMITH K.S., *Machining Dynamics: Frequency Response for Improved Productivity*, Springer, 2009.

[SEE 99] SEETHALER R.J., YELLOWLEY I., "The identification of radial runout in milling operations", *Journal of Manufacturing Science and Engineering – Transactions of the ASME*, vol. 121, no. 3, pp. 524–531, 1999.

[SHA 01] SHAMPINE L.F., THOMPSON S., "Solving DDEs in Matlab", *Applied Numerical Mathematics*, vol. 37, no. 4, pp. 441–458, 2001.

[SHI 96] SHIRASE K., ALTINTAS Y., "Cutting force and dimensional surface error generation in peripheral milling with variable pitch helical end mills", *International Journal of Machine Tools and Manufacture*, vol. 36, no. 5, pp. 567–584, 1996.

[SHI 97] SHIN Y.C., WATERS A.J., "A new procedure to determine instantaneous cutting force coefficients for machining force prediction", *International Journal of Machine Tools and Manufacture*, vol. 37, no. 9, pp. 1337–1351, 1997.

[SIM 08] SIMS N.D., MANN B., HUYANAN S., "Analytical prediction of chatter stability for variable pitch and variable helix milling tools", *Journal of Sound and Vibration*, vol. 317, nos. 3–5, pp. 664–686, 2008.

[SOS 04] SOSHI M., LIU X.B., YAMAZAKI K. *et al.*, "Development of a simulation system for surface topographic features in 5-axis CNC machining process", *The 7th International Conference on Progress of Machining Technology*, Aviation Industry Press, 2004.

[SPE 94] SPENCE A.D., ALTINTAS Y., "A solid modeler based milling process simulation and planning system", *Journal of Engineering for Industry – Transactions of the ASME*, vol. 116, no. 1, pp. 61–69, 1994.

[SPE 00] SPENCE A.D., ABRARI F., ELBESTAWI M.A., "Integrated solid modeller based solutions for machining", *Computer-Aided Design*, vol. 32, no. 8-9, pp. 553–568, 2000.

[SRI 68] SRIDHAR R., HOHN R.E., LONG G.W., "A stability algorithm for the general milling process", *Journal of Engineering for Industry – Transactions of the ASME*, vol. 90, no. 2, pp. 330–334, 1968.

[SRI 06] SRIYOTHA P., SAHASRABUDHE A., YAMAZAKI K. *et al.*, "Geometrical modelling of a ball end finish milling process for a surface finish", *Proceedings of the Institution of Mechanical Engineers, Part B: Journal of Engineering Manufacture*, vol. 220, no. 4, pp. 467–477, 2006.

[STA 64] STABLER G.V., "The chip flow law and its consequences", in *Proceedings of the Fifth International Machine Tool Design and Research Conference*, Pergamon Press, pp. 243–251, 1964.

[STE 89] STEPAN G., *Retarded Dynamical Systems: Stability and Characteristic Functions*, Longman, Harlow, 1989.

[SUT 86] SUTHERLAND J.W., DEVOR R.E., "An improved method for cutting force and surface error prediction in flexible end-milling systems", *Journal of Engineering for Industry – Transactions of the ASME*, vol. 108, no. 4, pp. 269–279, 1986.

[THO 66] THOMSEN E.G., "Application of the mechanics of plastic deformation to metal cutting", *CIRP Annals – Manufacturing Technology*, vol. 14, pp. 113–123, 1966.

[TLU 81] TLUSTY J., ISMAIL F., "Basic non-linearity in machining chatter", *CIRP Annals – Manufacturing Technology*, vol. 30, no. 1, pp. 299–304, 1981.

[TOH 04] TOH C.K., "Surface topography analysis in high speed finish milling inclined hardened steel", *Precision Engineering*, vol. 28, no. 4, pp. 386–398, 2004.

[TOT 09] TOTIS G., "RCPM-A new method for robust chatter prediction in milling", *International Journal of Machine Tools and Manufacture*, vol. 49, nos. 3–4, pp. 273–284, 2009.

[TSA 99] TSAI J.S., LIAO C.L., "Finite-element modeling of static surface errors in the peripheral milling of thin-walled workpieces", *Journal of Materials Processing Technology*, vol. 94, nos. 2–3, pp. 235-246, 1999.

[WAN 94] WANG J.J.J., LIANG S.Y., BOOK W.J., "Convolution analysis of milling force pulsation", *Journal of Engineering for Industry - Transactions of the ASME*, vol. 116, no. 1, pp. 17–25, 1994.

[WAN 96] WANG J.J.J., LIANG S.Y., "Chip load kinematics in milling with radial cutter runout", *Journal of Engineering for Industry - Transactions of the ASME*, vol. 118, no. 1, pp. 111–116, 1996.

[WAN 01] WANG D.Y., ZHONG K.M., "Drilling jig of dual-cylinder position of one-sided oblique clamping", *New Technology and New Process*, vol. 12, pp. 12–13, 2001.

[WAN 03] WANG J.J.J., ZHENG C.M., "Identification of cutter offset in end milling without a prior knowledge of cutting coefficients", *International Journal of Machine Tools and Manufacture*, vol. 43, no. 7, pp. 687–697, 2003.

[WAN 05] WAN M., ZHANG W.H., QIU K.P., GAO T. *et al.*, "Numerical prediction of static form errors in peripheral milling of thin-walled workpieces with irregular meshes", *Journal of Manufacturing Science and Engineering – Transactions of the ASME*, vol. 127, no. 1, pp. 13–22, 2005.

[WAN 06a] WAN M., ZHANG W.H., "Calculations of chip thickness and cutting forces in flexible end milling", *International Journal of Advanced Manufacturing Technology*, vol. 29, nos. 7–8, pp. 637–647, 2006.

[WAN 06b] WAN M., ZHANG W.H., "Efficient algorithms for calculations of static form errors in peripheral milling", *Journal of Materials Processing Technology*, vol. 171, no. 1, pp. 156–165, 2006.

[WAN 07a] WAN M., ZHANG W.H., QIN G.H. *et al.*, "Efficient calibration of instantaneous cutting force coefficients and runout parameters for general end-mills", *International Journal of Machine Tools and Manufacture*, vol. 47, no. 11, pp. 1767–1776, 2007.

[WAN 07b] WAN M., ZHANG W.H., TAN G. *et al.*, "An in-depth analysis of the synchronization between the measured and predicted cutting forces for developing instantaneous milling force model", *International Journal of Machine Tools and Manufacture*, vol. 47, nos. 12–13, pp. 2018–2030, 2007.

[WAN 08] WAN M., ZHANG W.H., TAN G. *et al.*, "Systematic simulation procedure of peripheral milling process of thin-walled workpiece", *Journal of Materials Processing Technology*, vol. 197, nos. 1-3, pp. 122–131, 2008.

[WAN 09a] WAN M., ZHANG W.H., "Systematic study on cutting force modeling methods for peripheral milling", *International Journal of Machine Tools and Manufacture*, vol. 49, no. 5, pp. 424–432, 2009.

[WAN 09b] WAN M., ZHANG W.H., DANG J.W. *et al.*, "New procedures for calibration of instantaneous cutting force coefficients and cutter runout parameters in peripheral-milling", *International Journal of Machine Tools & Manufacture*, vol. 49, no. 14, pp. 1144–1151, 2009.

[WAN 10a] WAN M., ZHANG W.H., DANG J.W. *et al.*, "A novel cutting force modeling method for cylindrical end-mill", *Applied Mathematical Modeling*, vol. 34, no. 3, pp. 823–836, 2010.

[WAN 10b] WAN M., ZHANG W.H., DANG J.W. *et al.*, "A unified stability prediction method for milling process with multiple delays", *International Journal of Machine Tools and Manufacture*, vol. 50, no. 1, pp. 29–41, 2010.

[WAN 11] WAN M., WANG Y.T., ZHANG W.H. *et al.*, "Prediction of chatter stability for multiple-delay milling system under different cutting force models", *International Journal of Machine Tools & Manufacture*, vol. 51, no. 4, pp. 281–295, 2011.

[WAN 14] WAN M., PAN W.J., ZHANG W.H. *et al.*, "A unified instantaneous cutting force model for flat end mills with variable geometries", *Journal of Materials Processing Technology*, vol. 214, no. 3, pp. 641–650, 2014.

[WAN 15] WAN M., MA Y.C., ZHANG W.H. *et al.*, "Study on the construction mechanism of stability lobes in milling process with multiple modes", *The International Journal of Advanced Manufacturing Technology*, vol. 79, nos. 1–4, pp. 589–603, 2015.

[WEI 04] WEINERT K., DU S.J., DAMM P. *et al.*, "Swept volume generation for the simulation of machining processes", *International Journal of Machine Tools and Manufacture*, vol. 44, no. 6, pp. 617–628, 2004.

[WEI 10] WEI Z.C., WANG M.J., MA R.G. *et al.*, "Modeling of process geometry in peripheral milling of curved surfaces", *Journal of Materials Processing Technology*, vol. 210, no. 5, pp. 799–806, 2010.

[WU 97] WU N.H., CHAN K.C., LEONG S.S., "Static interactions of surface contacts in a fixture-workpiece system", *International Journal of Computer Applications in Technology*, vol. 10, nos. 3–4, pp. 133–151, 1997.

[XU 01] XU A.P., QU Y.X., LI W.M., "Generalized simulation model for milled surface topography – application to peripheral milling", *Chinese Journal of Mechanical Engineering*, vol. 14, no. 2, pp. 121–126, 2001.

[YAN 01] YAN B., ZHANG D.W., XU A.P. *et al.*, "Modeling and Simulation of ball end Milling Surface Topology", *Journal of Computer-Aided Design and Computer Graphics*, vol. 13, pp. 135–140, 2001.

[YAN 11] YANG Y., ZHANG W.H., WAN M., "Effect of cutter runout on process geometry and forces in peripheral milling of curved surfaces with variable curvature", *International Journal of Machine Tools & Manufacture*, vol. 51, no. 5, pp. 420–427, 2011.

[YAN 13] YANG Y., ZHANG W.H., WAN M. *et al.*, "A solid trimming method to extract cutter-workpiece engagement maps for multi-axis milling", *International Journal of Advanced Manufacturing Technology*, vol. 68, nos. 9–12, pp. 2801–2813, 2013.

[YAZ 94] YAZAR Z., KOCH K.F., .MERICK T. *et al.*, "Feed rate optimization based on cutting force calculations in 3-axis milling of dies and molds with sculptured surface", *International Journal of Machine Tools and Manufacture*, vol. 34, no. 3, pp. 365–377, 1994.

[YIP 06] YIP-HOI D., HUANG X.M., "Cutter/workpiece engagement feature extraction from solid models for end milling", *Journal of Manufacturing Science and Engineering – Transactions of the ASME*, vol. 128, no. 1, pp. 249–260, 2006.

[YUN 00] YUN W.S., CHO D.W., "An improved method for the determination of 3D cutting force coefficients and runout parameters in end milling", *International Journal of Advanced Manufacturing Technology*, vol. 16, no. 12, pp. 851–858, 2000.

[YUN 01] YUN W.S., CHO D.W., "Accurate 3D cutting force prediction using cutting-condition-independent coefficients in end milling", *International Journal of Machine Tools and Manufacture*, vol. 41, no. 4, pp. 463–478, 2001.

[ZAT 06] ZATARAIN M., MUNOA J., PEIGNE G. *et al.*, "Analysis of the influence of mill helix angle on chatter stability", *CIRP Annals – Manufacturing Technology*, vol. 55, no. 1, pp. 365–368, 2006.

[ZHA 01a] ZHANG Z.H., ZHENG L., LI Z.H. *et al.*, "Analytical model for end milling surface geometrical error with considering cutting force/torque", *Chinese Journal of Mechanical Engineering* (in Chinese), vol. 37, no. 1, pp. 6–10, 2001.

[ZHA 01b] ZHAO M.X., BALACHANDRAN B., "Dynamic and stability of milling process", *International Journal of Solid and Structures*, vol. 38, nos. 11–13, pp. 2233–2248, 2001.

[ZHA 03a] ZHANG W.H., DUYSINX P., "Dual approach using a variant perimeter constraint and efficient sub-iteration scheme for topology optimization", *Computers & Structures*, vol. 81, nos. 22–23, pp. 2173–2181, 2003.

[ZHA 03b] ZHAO X.M., HU D.J., ZHAO G.W., "Simulation of workpiece surface texture in 5-axis control machining", *Journal of Shanghai Jiaotong University*, vol. 37, no. 5, pp. 690–694, 2003.

[ZHA 08] ZHANG W.H., TAN G., WAN M., GAO T. *et al.*, "A new algorithm for the numerical simulation of machined surface topography in multiaxis ball end milling", *Journal of Manufacturing Science and Engineering – Transactions of the ASME*, vol. 130, no. 1, 2008.

[ZHA 11] ZHANG L.Q., "Process modeling and toolpath optimization for five-axis ball end milling based on tool motion analysis", *International Journal of Advanced Manufacturing Technology*, vol. 57, nos. 9–12, pp. 905–916, 2011.

[ZHE 97] ZHENG L., LIANG S.Y., "Identification of cutter axis tilt in end-milling", *Journal of Manufacturing Science and Engineering – Transactions of the ASME*, vol. 119, no. 2, pp. 178–185, 1997.

Index

Milling Simulation: *Metal Milling Mechanics, Dynamics and Clamping Principles*, First Edition. Weihong Zhang and Min Wan.

Other titles from

in

Numerical Methods in Engineering

2016

KERN Michel
Numerical Methods for Inverse Problems

2015

ANDRÉ Damien, CHARLES Jean-Luc and IORDANOFF Ivan
3D Discrete Element Workbench for Highly Dynamic Thermo-mechanical Analysis (Discrete Element Model and Simulation of Continuous Materials Behavior Set – Volume 3)

JEBAHI Mohamed, ANDRÉ Damien, TERREROS Inigo, IORDANOFF Ivan
Discrete Element Method to Model 3D Continuous Materials (Discrete Element Model and Simulation of Continuous Materials Behavior Set – Volume 1)

JEBAHI Mohamed, DAU Frédéric, CHARLES Jean-Luc, IORDANOFF Ivan
Discrete-continuum Coupling Method to Simulate Highly Dynamic Multi-scale Problems: Simulation of Laser-induced Damage in Silica Glass (Discrete Element Model and Simulation of Continuous Materials Behavior Set – Volume 2)

SOUZA DE CURSI Eduardo
Variational Methods for Engineers with Matlab®

2014

BECKERS Benoit, BECKERS Pierre
Reconciliation of Geometry and Perception in Radiation Physics

BERGHEAU Jean-Michel
Thermo-Mechanical Industrial Processes: Modeling and Numerical Simulation

BONNEAU Dominique, FATU Aurelian, SOUCHET Dominique
4-volume series
Hydrodynamic Bearings – Volume 1
Mixed Lubrication in Hydrodynamic Bearings – Volume 2
Thermo-hydrodynamic Lubrication in Hydrodynamic Bearings – Volume 3
Internal Combustion Engine Bearings Lubrication in Hydrodynamic Bearings – Volume 4

DESCAMPS Benoît
Physical Form Finding of Lightweight Structures

2013

YASTREBOV Vladislav A.
Numerical Methods in Contact Mechanics

2012

DHATT Gouri, LEFRANÇOIS Emmanuel, TOUZOT Gilbert
Finite Element Method

2011

CHINESTA Francisco *et al.*
Natural Element Method for the Simulation of Structures and Processes

DAVIM Paulo J.
Finite Element Method in Manufacturing Processes

POMMIER Sylvie, GRAVOUIL Anthony, MOËS Nicolas, COMBESCURE Alain
Extended Finite Element Method for Crack Propagation

2010

SOUZA DE CURSI Eduardo, SAMPAIO Rubens
Modeling and Convexity

2008

BERGHEAU Jean-Michel, FORTUNIER Roland
Finite Element Simulation of Heat Transfer

EYMARD Robert
Finite Volumes for Complex Applications V

FREY Pascal, GEORGE Paul-Louis
Mesh Generation – 2nd edition

GAY Daniel, GAMBELIN Jacques
Modeling and Dimensioning of Structures

2005

BENKHALDOUN Fayssal
Finite Volumes for Complex Applications IV